# Investigating the content and function of stress-induced extracellular vesicles in colorectal cancer




John Mason

Magdalen College
University of Oxford

A thesis submitted for the degree of
*Doctor of Philosophy*
Department of Physiology, Anatomy & Genetics
Trinity Term 2021

# Declaration

I confirm that the work presented in this thesis was performed by myself at the Department of Physiology, Anatomy and Genetics, University of Oxford, and Instituto de Biomedicina y Biotecnología, IBBTEC de Cantabria, Santander, Spain between October 2017 and March 2021. The collaborative aspects of this work in which additional parties have given their support have been duly acknowledged within the main text of this thesis. This thesis has been written by myself and has not been previously submitted for the award of a degree or other qualification at this university, or any other institution.

JD Mason
Magdalen College
Trinity Term 2021

# Acknowledgements

First of all, I would like to express my gratitude and appreciation to my scientific supervisor, Prof Deborah Goberdhan. I am incredibly grateful for the opportunity to spend the past three and half years working in her lab, for her dedication and support, and for her encouragement to develop and pursue my own research ideas and questions. I am also grateful for the support from my clinical supervisor, Prof Chris Cunningham. His advice was instrumental during the translational aspects of this thesis, as well as in securing additional funding for a future surgical research fellow to protect the legacy of this project. In addition to the input from my supervisors, I am enormously grateful for the insights and practical advice provided by Prof Clive Wilson, Prof Adrian Harris and Prof Freddie Hamdy throughout my DPhil.

Importantly, I would like acknowledge and thank CRUK for providing the fellowship that funded my DPhil. In particular I would like to express my thanks to Michael Youdell at the CRUK Oxford Centre, who was instrumental in helping me to secure a six-month extension following the COVID-19 lockdown during March-June 2020, which enabled me to complete vital experiments to conclude my thesis. I am also grateful to the Oxford Colon Cancer Trust (Occtopus) who funded the microRNA analysis of patient samples. I would also like acknowledge the Royal College of Surgeons of England who recognised my DPhil project with an honorary Surgical Research Fellowship (2017-18).

I am incredibly grateful to all members of the Goberdhan Group, both past and present. In particular, I would like to thank Shih-Jung Fan, who has provided me with almost daily advice and taught me the majority of the methods used throughout my DPhil. His rigorous approach to science is inspiring, and I wish him every success in his future career as a PI. A special thanks also to Kristie McCormick for her helpful guidance, and along with Matt Ellis, for your friendship outside of the lab. I wish both of you the best of luck as you begin your medical training, and hope to see you in general surgery in a few years' time...! I am also grateful to Hakimi Kassim for his insightful feedback during lab meetings, and to Cleidson Alves who taught me how to perform functional EV assays. Throughout my DPhil, I have had the enormous privilege to supervise two visiting students, Yaiza Ibáñez and Ewan Marks, which aside from being a rewarding experience, has led to significant contributions to my own research, for which I am immensely grateful. Specifically, thank you to Yaiza for the hospitality she showed me when I visited Santander in May 2019, and for sharing her expertise in the chick embryo model. To Ewan, thank you for your assistance in characterising the Caco-2 cell line, which led onto the interesting drug resistance data presented in this thesis.

I would also like to extend my thanks to members of the Wood Group: Ghulam Dar, Imre Mäger and Scott Bonner, for their invaluable practical support in repacking size exclusion chromatography columns, to Antonio Guerra for his help with nanosight tracking analysis, and also to Amarjit Bhomra and Britt Hanson for their sage advice and on demand loaning of reagents!

Beyond DPAG, I am also grateful to Errin Johnson for her help in generating the TEM images of EVs, and to Esther Bridges for sharing her expertise in immunohistochemistry.

Thank you also to Fenella Gross who quantified my EVs while our equipment was out of action for prolonged periods of time. I also extend my sincere gratitude to Simona Fourie and Heather Barnes at the Translational Gastroenterology Unit, who helped me to obtain clinical samples. Furthermore, I thank Naveed Akbar, for his advice regarding microRNA analysis of plasma EVs, as well as David Chambers from UK Bioinformatics Ltd who performed the microarray analysis. Subsequently, I am also incredibly grateful to Prof Francesca Buffa, Ryan Carter and Alessandro Barberis who undertook the bioinformatic analysis of this microRNA data.

Beyond the lab, I am of course grateful for the continued support from my parents who have always encouraged my ambition, even when this coincides with perpetual student status! Finally, and most importantly I would like to thank my wife Emma, for your love and unwavering support over the past three and a half years. The beginning and end of this DPhil has been marked with the arrival of our boys, Jasper and Woody. While lab work was challenging at times, three and a half years away from a busy surgical on call rota has provided time together as a family, which has been filled with precious memories that I will never forget.

# Abstract

Despite advances in detection and treatment, the incidence of colorectal cancer (CRC), particularly in those under 40 years of age is increasing, and survival from metastatic disease remains very low. Adaptation of tumour cells to microenvironmental stresses and anti-cancer therapies is a key mechanism driving tumour progression and resistance. Extracellular vesicles (EVs) are nanosized membrane-bound vesicles, which carry rich bioactive cargoes that are able to influence and reprogramme recipient cell behaviour. In CRC, EVs are known to be potent drivers of primary tumour growth and metastasis, and have also been shown to modulate response to treatment by promoting drug resistance. The Goberdhan Group has recently shown that glutamine depletion can lead to change in EV biogenesis, including an increase in Rab11a-exosomes formed in Rab11a-positive recycling endosomes through inhibition of the nutrient-sensing kinase complex, mechanistic Target of Rapamycin Complex 1 (mTORC1). These EVs have enhanced tumorigenic function in CRC cells. Therefore, my DPhil focussed on investigating the potential pro-tumorigenic properties of these “switched” EVs in CRC cell lines *in vitro* and also assessing the composition of EVs in CRC patient plasma.

Having validated size exclusion chromatography as a method to isolate and detect purified preparations of switched EVs from HCT116 CRC cells, I showed that hypoxia, which reduces mTORC1 signalling, also induces the secretion of Rab11a-exosomes. I also demonstrated that mTORC1 inhibition induces the EV switch in a panel of other CRC cell lines (Caco-2, SW480 and SW620) that are representative of the genetic heterogeneity observed in CRC. My work provided evidence that switched EVs from HCT116 cells preferentially increase tumour cell growth *in vitro* and within an *in vivo* chick-embryo model. This growth-promoting property is ERK-MAPK-dependent and can be blocked by selective neutralisation of the EGFR ligand, Amphiregulin (AREG), which is upregulated in switched EVs isolated from HCT116 and Caco-2 cells. Furthermore, switched EVs isolated from HCT116 cells (*KRAS* mutant) promote AREG-dependent resistance to EGFR monoclonal antibody therapy in Caco-2 (*KRAS* wild-type) cells. I also showed that switched EVs acted in an AREG-independent fashion to reduce tumour cell migration and invasion, potentially reflecting the mesenchymal-to-epithelial transition at distant sites during CRC metastasis.

My final results chapter focussed on EV-associated microRNA cargo within HCT116 and SW480 cells, as well as within a cohort of patients with rectal cancer treated with neoadjuvant chemoradiotherapy (nCRT). A comparative analysis of the miRNA cargo of non-switched and switched EVs showed that HCT116 and SW480 cells secrete EVs with distinct miRNA expression patterns, although both are enriched in miRNAs known to participate in pro-tumorigenic processes and signalling pathways. After validating a SEC-based method to isolate EVs from patient plasma, I showed that nCRT for rectal cancer is associated with altered EV-miRNA cargo. Furthermore, individuals who show a clinical response to nCRT appear to exhibit a different EV-miRNA profile when compared to non-responders, which may provide a novel method to predict response to treatment.

In summary, this thesis reveals mechanisms connecting microenvironmental stress to the release of pro-tumorigenic EVs, alongside insights into how treatment for CRC modulates EV cargo. It therefore highlights potential novel EV-associated biomarkers and therapeutic targets for future research.

# List of abbreviations

| Abbreviation | Description |
|---|---|
| 4E-BP1 | Eukaryotic translation initiation factor 4E-binding protein 1 |
| A1 | Annexin A1 |
| ADAM10 | A disintegrin and metalloproteinase domain containing protein 10 |
| Alix | ALG-2 interacting protein X |
| AMPK | 5’ AMP-activated protein kinase |
| APC | Adenomatous polyposis coli |
| APER | Abdominoperineal resection of the rectum |
| AREG | Amphiregulin |
| AREGab | Amphiregulin antibody |
| ATP | Adenosine triphosphate |
| BMI | Body mass index |
| BSA | Bovine serum albumin |
| CA9 | Carbonic anhydrase 9 |
| CAM | Chorioallantoic membrane |
| CRM | Circumferential resection margin |
| Cav-1 | Caveolin-1 |
| CEA | Carcinoembryonic antigen |
| CHMP | Charged multivesicular body protein |
| CIMP | CpG island methylator phenotype |
| CIN | Chromosomal instability |
| CRC | Colorectal cancer |
| CT | Computerised tomography |
| CTX | Cetuximab |
| CXCR4 | C-X-C chemokine receptor type 4 |
| DEPTOR | DEP domain-containing mTOR-interacting protein |
| DMEM | Dulbecco’s modified Eagle’s medium |
| DMSO | Dimethyl sulfoxide |
| DNA | Deoxyribonucleic acid |
| DPBS | Dulbecco’s phosphate-buffered saline |
| dUC | Differential ultracentrifugation |
| ECM | Extracellular matrix |
| EEA1 | Early endosome antigen 1 |
| EGFR | Epidermal growth factor receptor |

| | |
|---|---|
| eIF4E | Eukaryotic translation initiation factor 4E |
| EMEM | Eagle’s minimal essential medium |
| EMMPRIN | Extracellular matrix metalloproteinase inducer |
| EMR | Endoscopic mucosal resection |
| EMT | Epithelial-to-mesenchymal transition |
| ERK | Extracellular signal-regulated kinase |
| ESCRT | Endosomal sorting complexes required for transport |
| EV | Extracellular vesicle |
| FAP | Familial adenomatous polyposis |
| FBS | Foetal bovine serum |
| FFPE | Formalin-fixed paraffin-embedded |
| FIT | Faecal immunochemical test |
| FOLFOX | Folinic acid, fluorouracil and oxaliplatin |
| GATOR1, -2 | GAP activity towards Rags-1, -2 |
| gFOBT | Guaiac faecal occult blood test |
| Gln | L-glutamine |
| GTP | Guanosine triphosphate |
| HDL | High density lipoprotein |
| HIF-1α | Hypoxia-inducible factor 1-alpha |
| HLA-C | Human leukocyte antigen-C |
| HNPCC | Hereditary nonpolyposis colorectal cancer |
| HPF | High powered field |
| IBBTEC | Instituto de Biomedicina y Biotecnologia de Cantabria |
| IgG | Immunoglobulin G |
| ILV | Intraluminal vesicle |
| IP | Immunoprecipitation |
| IPTG | Isopropyl β-d-1-thiogalactopyranoside |
| ISEV | International society for extracellular vesicles |
| ITS | Insulin, transferrin and selenium |
| JAK | Janus kinase |
| KEGG | Kyoto Encyclopaedia or Genes and Genomes |
| LAR | Low anterior resection of the rectum |
| LDL | Low density lipoprotein |
| MDT | Multidisciplinary team |
| MET | Mesenchymal-to-epithelial transition |
| miRNA | MicroRNA |

| | |
|---|---|
| MISEV | Minimal information for studies of extracellular vesicles |
| MLH1 | MutL homolog 1 |
| mLST8 | Mammalian lethal with Sec13 protein 8 |
| MMP1 | Matrix metalloproteinase-1 |
| MMR | Mismatch repair |
| MRI | Magnetic resonance imaging |
| mRNA | Messenger ribonucleic acid |
| MSH2, -6 | MutS homolog-2, -6 |
| MSI | Microsatellite instability |
| mTOR | Mechanistic target of rapamycin |
| mTORC1/2 | Mechanistic target of rapamycin complex-1, -2 |
| MVB | Multivesicular body |
| nCRT | Neoadjuvant chemoradiotherapy |
| NSCLC | Non-small cell lung cancer |
| NTA | Nanoparticle tracking analysis |
| PAT4 | Proton-assisted amino acid transporter-4 |
| PBS | Phosphate buffered saline |
| PCA | Principle component analysis |
| PDCD4 | Programmed cell death protein 4 |
| PDRA | Postdoctoral research assistant |
| pEGFR | Phospho-epidermal growth factor receptor |
| pERK | Phospho-extracellular signal-regulated kinase |
| PET | Positron emission tomography |
| PI3K | Phosphatidylinositol 3-kinase |
| PIK3CA | Phosphatidylinositol-4,5-biphosphate 3-kinase catalytic subunit alpha |
| PRAS40 | Proline-rich Akt substrate of 40 kDa |
| PRISMA | Preferred reporting items for systematic reviews and meta-analyses |
| pS6 | Phospho-ribosomal protein S6 |
| PTEN | Phosphatase and tensin homolog |
| qRT-PCR | Quantitative real-time polymerase chain reaction |
| Raptor | Regulatory-associated protein with mTOR |
| rAREG | Recombinant amphiregulin |
| RBP | RNA binding protein |
| Rheb | Ras homolog enriched in brain |
| Rictor | Rapamycin insensitive companion of mTOR |
| RNA | Ribonucleic acid |

| | |
|---|---|
| S6K | Ribosomal protein S6 kinase |
| SEC | Size exclusion chromatography |
| shRNA | Short hairpin ribonucleic acid |
| SNAT | Sodium-coupled neutral amino acid transporter |
| SREBP | Sterol responsive element binding protein |
| Syn-1 | Syntenin-1 |
| TAMIS | Transanal minimally invasive surgery |
| TEM | Transmission electron microscopy |
| TEMS | Transanal endoscopic microsurgery |
| TFF | Tangential flow filtration |
| TfR | Transferrin receptor |
| TGF-β1 | Transforming growth factor-beta 1 |
| TGN46 | Trans-Golgi network integral membrane protein 46 |
| TNF | Tumour necrosis factor |
| TNM | Tumour, node, metastasis |
| TP53 | Tumour protein p53 |
| TRAIL | TNF-related apoptosis-inducing ligand |
| TSC1/2 | Tuberous sclerosis complex-1, -2 |
| Tsg101 | Tumour susceptibility gene 101 |
| UC | Ultracentrifugation |
| UF | Ultrafiltration |
| VEGF | Vascular endothelial growth factor |
| VLDL | Very-low-density lipoprotein |
| ZEB1 | Zinc finger E-box binding homeobox 1 |

# Table of Contents

**Declaration** ..... **1**
**Acknowledgements** ..... **2**
**Abstract** ..... **4**
**List of abbreviations** ..... **5**
**List of figures** ..... **15**
**List of tables** ..... **18**

**1. Introduction** ..... **20**
**1.1 Colorectal cancer** ..... **20**
1.1.1 Incidence and mortality ..... 20
1.1.2 Risk and preventive factors ..... 21
1.1.2.1 Modifiable factors ..... 21
1.1.2.2 Non-modifiable factors ..... 21
1.1.3 Pathogenesis ..... 23
1.1.4 Diagnosis ..... 25
1.1.4.1 Staging ..... 26
1.1.4.2 Screening ..... 28
1.1.8 Treatment ..... 29
1.1.9 Prognosis ..... 32
**1.2 Microenvironmental signalling** ..... **33**
1.2.1 mTORC1 signalling pathway ..... 33
1.2.2 Regulation of mTORC1 signalling ..... 34
1.2.3 mTORC1 signalling in CRC ..... 37
1.2.3.1 Targeting the mTORC1 pathway in CRC ..... 38
**1.3 Extracellular vesicles** ..... **39**
1.3.1 Defining extracellular vesicles ..... 39
1.3.2 Exosome biogenesis & secretion ..... 41
1.3.3 EV mediated signalling ..... 43
1.3.3.1 EV signalling during development and in normal physiology ..... 43
1.3.3.2 EV signalling in CRC cancer ..... 45
1.3.4 mTORC1 signalling and the EV switch ..... 48
**1.4 Research questions** ..... **49**

**2. Materials & methods** ..... **52**
**2.1 CRC cell characterisation** ..... **52**
2.1.1 Cell culture ..... 52

2.1.2 Comparison of culture media and modulation of mTORC1 signalling ..... 52
2.1.2.1 Growth analysis ..... 52
2.1.2.2 Glutamine depletion ..... 53
2.1.2.3 mTORC1 inhibition ..... 53
2.1.2.4 Hypoxia ..... 53
2.1.2.5 Cell viability measurement ..... 53
**2.2 Clinical samples ..... 54**
**2.3 Isolation & characterisation of EVs from CRC cell lines and patient plasma ..... 54**
2.3.1 Isolation conditions ..... 54
2.3.2 EV isolation methods ..... 55
2.3.2.1 Ultrafiltration ..... 57
2.3.2.2 Ultracentrifugation ..... 57
2.3.2.3 Size exclusion chromatography ..... 57
2.3.2.4 qEV column size exclusion chromatography ..... 58
2.3.3 EV characterisation ..... 58
2.3.3.1 EV normalisation ..... 59
2.3.3.2 Nanosight tracking analysis ..... 60
2.3.3.3 Transmission electron microscopy ..... 60
2.3.3.4 Western blot analysis ..... 60
2.3.3.5 Optiprep™ density gradient analysis ..... 63
2.3.3.6 Proteinase-K protection assay ..... 64
2.3.3.7 Co-immunoprecipitation ..... 64
**2.4 Functional analysis of CRC EVs *in vitro* and *in vivo* ..... 64**
2.4.1 Proliferation assays ..... 64
2.4.1.1 Determining serum assay conditions ..... 65
2.4.1.2 EV-dose response assays ..... 65
2.4.1.3 EV-depletion assays ..... 65
2.4.1.3.1 EV-pelleting assay ..... 65
2.4.1.3.2 CHMP5 knockdown ..... 66
2.4.1.4 Amphiregulin neutralisation assay ..... 66
2.4.1.5 EGFR-ERK signalling assay ..... 66
2.4.1.6 Cetuximab and EGFR kinase inhibitor assays ..... 67
2.4.1.7 Recombinant amphiregulin assay ..... 67
2.4.1.8 ELISA measurement of amphiregulin concentration ..... 67
2.4.2 Chick embryo HCT116 xenograft model ..... 68
2.4.2.1 Tumour-EV grafts ..... 68
2.4.2.2 Quantitative real-time PCR ..... 69

2.4.2.3 Immunohistochemistry ..... 69
2.4.3 Migration & invasion assays using HCT116 cells ..... 70
2.4.3.1 Scratch-wound assay ..... 70
2.4.3.2 Transwell migration and invasion assays ..... 71
2.4.3.3 Protein expression assays ..... 71
**2.5 EV cargo analysis ..... 72**
2.5.1 miRNA cargo analysis ..... 72
2.5.2 miRNA bioinformatic analysis ..... 72
**2.6 Statistical analysis ..... 72**

**3. Validation of SEC to isolate and study EV heterogeneity in CRC cell lines ..... 74**
**3.1 Introduction ..... 74**
3.1.1 EV isolation methods ..... 74
3.1.1.1 Ultrafiltration ..... 75
3.1.1.2 Ultracentrifugation ..... 75
3.1.1.3 Size exclusion chromatography ..... 77
3.1.2 The Minimal Information for Studies of Extracellular Vesicles (MISEV 2018) guidelines ..... 77
3.1.3 Aims and objectives ..... 79
**3.2 Results ..... 80**
3.2.1 Validation of SEC to study EV heterogeneity in HCT116 CRC cells ..... 80
3.2.2 Classical EV markers and the EV switch signature are detected throughout the SEC chromatogram ..... 87
3.2.2.1 Using the MISEV 2018 guidelines to investigate the non-EV peak fractions 89
3.2.2.2 Rab11a is located inside HCT116 cell EVs ..... 95
3.2.2.3 Proteomic analysis of switched EVs highlights increased loading of specific membrane proteins that exposes further detail of switched EV heterogeneity ..... 97
3.2.3 Hypoxia also induces the secretion of Rab11a exosomes in HCT116 cells .. 100
3.2.4 Using SEC to investigate EV switching in other CRC cell lines ..... 102
3.2.4.1 Determining cell culture conditions to isolate EVs from Caco-2, SW480, and SW620 cells ..... 103
3.2.4.2 Characterising EVs isolated from Caco-2, SW480, and SW620 cells ..... 106
3.2.4.3 Establishing glutamine-depletion and mTORC1 inhibition conditions to study EV switching in Caco-2, SW480, and SW620 cells ..... 109
3.2.4.4 Short term glutamine-depletion does not appear to induce EV switching in Caco-2, SW480 and SW620 cells ..... 112
3.2.4.5 mTORC1 inhibition induces EV switching in Caco-2, SW480 and SW620 cells ..... 114

**3.3 Discussion ..... 117**

3.3.1 SEC is a reproducible and valid method to isolate highly purified EV preparations containing Rab11a exosomes ..... 118

3.3.2 Rab11a and Cav-1 labelled EVs represent distinct EV subtypes secreted under microenvironmental stress ..... 120

3.3.3 Reduced mTORC1 activity is associated with the EV switch in a panel of CRC cell lines ..... 122

**4. Investigating the functional properties of stress-induced EVs in CRC ... 127**

**4.1 Introduction ..... 127**

4.1.1 EVs in cancer cell adaptation ..... 127

4.1.2 Studying the functional effects of EVs ..... 128

4.1.3 Aims and objectives ..... 129

**4.2 Results ..... 130**

4.2.1 Studying the effect of switched EVs on CRC cell growth *in vitro* ..... 130

4.2.1.1 Optimising conditions for an *in vitro* growth assay ..... 130

4.2.1.2 Switched EVs promote the dose-dependent growth of HCT116 recipient cells ..... 132

4.2.1.3 Amphiregulin is upregulated in switched EVs and is associated with increased EGFR/ERK signalling in recipient cells ..... 136

4.2.1.4 AREG inhibition blocks the ERK-dependent growth promoting property of switched EVs ..... 138

4.2.1.5 Switched EVs from SW480 and SW620 cells do not contain AREG and do not promote recipient cell growth ..... 142

4.2.1.6 The growth promoting property of switched EVs is transferrable to different CRC cell lines ..... 145

4.2.1.7 Switched EVs that contain AREG are more potent than non-EV associated AREG ..... 148

4.2.1.8 Switched EVs rescue cetuximab treated recipient cells via an AREG-dependent mechanism ..... 149

4.2.2 Studying the effect of switched EVs on tumour growth *in vivo* ..... 154

4.2.2.1 Switched EVs promote AREG-dependent tumour growth in an *in vivo* chick embryo model ..... 154

4.2.3 Studying the effect of switched EVs on colorectal cancer cell migration and invasion ..... 158

4.2.3.1 Switched EVs reduce recipient cell migration and invasion *in vitro* through an AREG-independent mechanism ..... 158

4.2.3.2 Studying the effect of switched EVs on HCT116 recipient cell invasion *in vivo* ..... 163

4.2.3.3 Switched EVs reduce the expression of mesenchymal protein markers *in vitro* and *in vivo* ..... 165

**4.3 Discussion ..... 168**

4.3.1 Nutrient depletion and hypoxia triggers the release of Rab11a-exosomes that promote AREG-dependent growth ..... 169
4.3.2 Switched EVs promote cetuximab resistance through an AREG-mediated competition or displacement mechanism ..... 173
4.3.3 Switched EVs are implicated in CRC metastasis by controlling migration and invasion through altered protein expression ..... 176
4.3.4 Updated model of microenvironmentally controlled EV secretion and the functional role of Rab11a-exosomes in CRC tumorigenesis ..... 179

**5. Investigating the EV-miRNA profile within CRC cell lines and within a rectal cancer patient cohort ..... 184**
**5.1 Introduction ..... 184**
5.1.1 EVs as biomarkers of disease ..... 184
5.1.2 EV-associated miRNAs as biomarkers of CRC ..... 185
5.1.3 Isolating EVs from plasma and serum ..... 186
5.1.3.1 UC-based methods for isolating EVs from plasma ..... 186
5.1.3.2 Precipitation-based methods for isolating EVs from plasma ..... 187
5.1.3.3 SEC-based methods for isolating EVs from plasma ..... 188
5.1.4 Aim and objectives ..... 189
**5.2 Results ..... 189**
5.2.1 Systematic review of EV-associated miRNAs in patients with CRC ..... 189
5.2.1.1 Data resources and search criteria ..... 189
5.2.1.2 Inclusion and exclusion criteria ..... 190
5.2.1.3 Overview of included studies ..... 190
5.2.2 Comparative analysis of EV-miRNA cargo in non-switched and switched EVs from HCT116 and SW480 CRC cells ..... 196
5.2.2.1 Data calibration and quality assessment ..... 196
5.2.2.2 HCT116 and SW480 CRC cells secrete EVs with distinct miRNA expression profiles ..... 199
5.2.2.3 Enrichment analysis of switched EV-miRNA cargoes ..... 206
5.2.3 Isolating EVs using qEV size exclusion columns ..... 215
5.2.3.1 Isolating EVs from cell culture media using qEV columns ..... 215
5.2.3.2 Isolating EVs from patient plasma using qEV columns ..... 218
5.2.4 Investigating plasma EV-miRNA cargoes in a cohort of patients with rectal cancer ..... 220
5.2.4.1 Patient cohort details ..... 220
5.2.4.2 Data calibration and quality assessment of plasma EV-miRNAs ..... 223
5.2.4.3 The plasma EV-miRNA profile of patients diagnosed with rectal cancer . 226
5.2.4.4 nCRT for rectal cancer is associated with changes in plasma EV-miRNA cargo ..... 227

5.2.4.5 Responders and non-responders to nCRT exhibit distinct EV-miRNA profiles ..... 231

**5.3 Discussion ..... 233**

5.3.1 Studies investigating EV-associated miRNAs in patients with CRC report highly heterogenous findings ..... 234

5.3.2 EV-miRNA data from CRC cell lines reveals differential loading of EV cargo under microenvironmental stress ..... 237

5.3.3 Altered miRNA loading in switched EVs from HCT116 cells may be due to increased levels of specific RNA loading proteins ..... 241

5.3.4 Changes in EV-miRNA cargo following nCRT may predict response to treatment ..... 242

**6. Research summary and future implications ..... 247**

**6.1 Summary of research aims ..... 247**

**6.2 Aim (i) Validating SEC to isolate and study EV switching in CRC cell lines ..... 248**

6.2.1 SEC can be used to isolate highly purified preparations of EVs ..... 248

6.2.2 Reduced mTORC1 signalling triggers the release of Rab11a-exosomes in a panel of CRC cell lines ..... 249

6.2.3 Clinical implications ..... 250

**6.3 Aim (ii) Investigating the functional role of switched EVs in CRC pathogenesis ..... 251**

6.3.1 Switched EVs promote AREG-dependent growth and drug resistance ..... 251

6.3.2 Switched EVs reduce recipient cell migration, invasion and mesenchymal protein expression ..... 252

6.3.3 Clinical implications ..... 253

**6.4 Aim (iii) Investigating EV-miRNA cargo in non-switched and switched EVs, and within a rectal cancer cohort ..... 255**

6.4.1 Microenvironmental stress modulates the miRNA content of EVs *in vitro* ..... 255

6.4.2 nCRT for rectal cancer is associated with changes in EV-miRNA profile and may differentiate responders from non-responders ..... 256

6.4.3 Clinical implications ..... 257

**6.5 Conclusions ..... 258**

**Appendix A – Fan *et al* (2020) EV switch study ..... 260**

**Appendix B – Uncropped western blot images ..... 287**

**Appendix C – Additional EV-miRNA data ..... 288**

**References ..... 291**

# List of figures

**Title** **Page**

1.1 Clinical and genetic differences between right sided versus left sided CRC ..... 25
1.2 Overview of mTORC1 activation ..... 36
1.3 Overview of EV heterogeneity ..... 40

2.1 Overview of the main EV isolation techniques ..... 56

3.1 SEC can be used to isolate EVs that exhibit the characteristics of exosomes ..... 81
3.2 SEC can be used for comparative analysis of switched EVs ..... 84
3.3 Classical EV markers and the the EV switch signature are detected throughout the SEC chromatogram ..... 89
3.4 NTA profiling of combined fractions show that the protein peak does not contain particles within the EV/exosome size range ..... 90
3.5 TEM demonstrates that EVs are primarily associated with the EV peak ..... 92
3.6 Co-localisation of EV markers is not observed in fractions outside of the EV peak ..... 94
3.7 Rab11a is an intravesicular exosome cargo and is not associated with vesicles in fractions outside of the EV peak ..... 96
3.8 Proteomic analysis reveals up-regulated of specific membrane proteins within switched EVs, which reveals further detail regarding EV heterogeneity ..... 99
3.9 Hypoxia also induces the secretion of Rab11a exosomes in HCT116 cells ..... 101
3.10 Establishing cell culture conditions to study EV switching in other CRC cell lines ..... 105
3.11 SEC enables the isolation of purified EV preparations from a panel of CRC cell lines ..... 108
3.12 Establishing mTORC1 suppression conditions to study EV switching in a panel of CRC cell lines ..... 110
3.13 Glutamine-depletion does not induce the EV switching in a panel of other CRC cell lines ..... 113
3.14 Torin1 induces the mTOR1-dependent EV switch in a panel of other CRC cell lines ..... 116

4.1 Developing an *in vitro* assay to measure the effect of switched EVs on recipient CRC cells growth ..... 131

4.2 Switched EVs promote the dose-dependent growth of HCT116 recipient cells in reduced serum conditions ..... 133
4.3 EV depletion results in loss of the growth promoting property of switched EVs ... 135
4.4 AREG is upregulated in switched EVs and is associated with increased EGFR and ERK phosphorylation in recipient cells ..... 137
4.5 The growth promoting property of switched EVs is AREG dependent ..... 139
4.6 Hypoxia and Torin1 also trigger the release of AREG-containing EVs that promote recipient cells growth ..... 141
4.7 Switched EVs from SW480 and SW620 cells do not contain AREG and do not promote recipient cell growth ..... 144
4.8 Switched EVs from HCT116 cells can promote the AREG-dependent growth of Caco-2 recipient cells ..... 146
4.9 EV-associated AREG is much more potent than recombinant AREG at promoting Caco-2 cell growth ..... 148
4.10 Sensitivity to cetuximab (CTX) is dependent on *KRAS* status ..... 150
4.11 Switched EVs isolated from HCT116 cells promote AREG-dependent cetuximab resistance in Caco-2 recipient cells ..... 152
4.12 AREG-containing EVs promote growth and drug resistance in recipient cells by binding to the EGFR receptor ..... 153
4.13 Switched EVs isolated from HCT116 cells promote AREG-dependent tumour growth *in vivo* ..... 155
4.14 Switched EVs promote recipient cell proliferation and nuclear localisation of activated ERK *in vivo* ..... 157
4.15 Switched EVs reduce recipient cell migration *in vitro* under serum-deplete but not serum-replete conditions ..... 159
4.16 Switched EVs isolated from HCT116 cells reduce the Transwell migration and invasion or recipient cells ..... 161
4.17 The switched EV-mediated reduction in recipient cell migration and invasion is AREG-independent *in vitro* ..... 163
4.18 Intravasation and distal CAM colonisation is affected by switched EVs *in vivo* and appears to be AREG-dependent ..... 164
4.19 Switched EVs increase E-cadherin expression and a reduce cell motility markers in recipient cells ..... 166
4.20 Switched EVs alter the expression of cellular motility markers in distal CAM secondary tumour deposits ..... 168

4.21 Proposed model to describe how the relationship between tumour heterogeneity and metabolic stress leads to the secretion of different EV-subtypes, which have distinct pro-tumorigenic properties ..... 181

5.1 PRISMA flow diagram for selection of studies ..... 191
5.2 Data calibration and quality assessment of EV-miRNAs isolated from HCT116 and SW480 CRC cells ..... 197
5.3 HCT116 and SW480 CRC cells exhibit distinct miRNA expression profiles ..... 200
5.4 The RNA-binding protein hnRNPA2B1 is increased in switched EVs secreted by HCT116 cells ..... 204
5.5 EV-miRNAs that show differential expression in switched EVs isolated from HCT116 cells are predicted to participate in a range of biological functions and cancer-related signalling pathways ..... 207
5.6 EV-miRNAs that show differential expression in switched EVs isolated from SW480 cells are predicted to participate in a range of biological functions and cancer-related signalling pathways ..... 213
5.7 qEV size exclusion columns can be used to isolate purified EV-preparations from HCT116 CRC cells ..... 217
5.8 qEV size exclusion columns can be used to isolate EVs from plasma ..... 219
5.9 Comparison of EVs isolated from healthy controls and patients pre- and post-nCRT ..... 223
5.10 Data calibration and quality assessment of plasma EV-miRNAs ..... 225
5.11 nCRT is associated with changes in EV-miRNA cargo ..... 228

# List of tables

**Title** **Page**

1.1 TNM classification of colonic adenocarcinoma ..... 27
1.2 Staging of colonic adenocarcinoma ..... 28

2.1 List of antibodies used for western blotting, co-immunoprecipitation and immunohistochemistry ..... 61

3.1 Overview of the MISEV guidelines ..... 79
3.2 Overview of the molecular and genetic characteristics of CRC cell lines selected for further study ..... 102

5.1 List of EV-miRNAs validated as biomarkers for CRC by studies included in systematic review ..... 192
5.2 List of miRNAs validated as a biomarker of CRC in more than one study ..... 193
5.3 EV-associated miRNAs that showed differential loading in switched EVs isolated from HCT116 CRC cells ..... 202
5.4 Differential expression of miRNAs isolated from HCT116 switched EVs that contain the hnRNPA2B1 binding motif ..... 204
5.5 EV-associated miRNAs that showed differential loading in switched EVs isolated from SW80 CRC cells ..... 205
5.6 Predicted gene targets within CRC pathways of miRNAs increased in switched EVs isolated from HCT116 CRC cells ..... 211
5.7 Predicted gene targets within CRC pathways of miRNAs increased in switched EVs isolated from SW480 CRC cells ..... 215
5.8 Patient demographics and clinical characteristics ..... 221
5.9 Healthy control demographics and clinical background ..... 222
5.10 EV-miRNAs that show differential expression in a cohort of patients with newly diagnosed rectal cancer ..... 226
5.11 Changes in EV-miRNA cargo following nCRT ..... 229
5.12 Changes in EV-miRNA cargo in patients that showed a complete clinical response to nCRT ..... 231
5.13 Changes in EV-miRNA cargo in patients that did not show a complete clinical response to nCRT ..... 232

# CHAPTER 1

## INTRODUCTION

# 1. Introduction

## 1.1 Colorectal cancer

### 1.1.1 Incidence and mortality

Colorectal cancer (CRC) accounts for approximately 10% of all annually diagnosed cancers worldwide (Dekker et al. 2019). Globally, in 2020, this equated to around 1.9-million new diagnoses and 935,000 CRC-related deaths (Globocan 2020). The highest rates of CRC are observed in developing countries, and alongside the increases within these nations, the incidence of CRC is predicted to rise to 2.5-million new cases per year by 2035 (Arnold et al. 2017; Globocan 2020). In the UK, CRC is the fourth most frequently diagnosed cancer overall, and the third most common in both men and women. In terms of mortality it is the second most common cause of cancer-related death, and the third most common in both men and women. The most recent statistics come from 2017, when there were 42,300 new cases of CRC and 16,600 deaths (CRUK 2017).

Increasing age is strongly associated with risk of disease, whereby approximately 88% of cases are diagnosed in people over the age of 50 (Siegel et al. 2020). However, despite this, numerous epidemiological studies have reported a worrying rise in cases of young-onset CRC over the past two decades. One study of 143 million people aged 20-49 across 20 European countries found that CRC incidence between 2004-2016 increased by 7.9% per year among 20-29-year olds, and 4.9% per year in 30-39-year olds (Vuik et al. 2019). Similar findings were reported by Chittleborough et al. (2020) who looked at all age groups, and found that increased incidence of young-onset CRC was observed despite overall rates of CRC remaining stable. The increased incidence of young-onset CRC does not correspond to an increase in CRC-related mortality within this age group (Vuik et al. 2019), which may be explained by the fact that almost 75% of these cancers are left-sided or rectal (P. Lu et al. 2019). These cancers are more likely to present with clinical features and physical symptoms, which would lead to someone seeking medical attention, and therefore

an earlier diagnosis. While the reasons driving this increase in young-onset CRC are not fully understood, the fact that it coincides with rising cases in developing countries highlights that this is likely to be driven, at least in part, by modifiable lifestyle and environmental factors.

### 1.1.2 Risk and preventive factors

#### 1.1.2.1 Modifiable factors

CRC risk can be attributed to modifiable and non-modifiable risk factors. The modifiable risk factors relate largely to lifestyle, and can be associated with increased as well as decreased risk. As with most other cancers, behaviours that increase the risk of poor health and disease in general, such as smoking and high alcohol intake are linked with an increased risk of developing CRC (Botteri et al. 2008; Cai et al. 2014). Obesity is also a known risk factor, whereby a BMI of over 30 almost doubles the risk of early-onset CRC compared with having a normal BMI of between 18.5-24.9 (P. H. Liu et al. 2019). In addition, dietary factors known to overlap with obesity, such as the consumption of large amounts of processed food and red meat, with minimal fruit and vegetable intake, also lead to an increased risk of CRC (Bradbury et al. 2020). In contrast, a healthy balanced diet, consisting of fruit, vegetables, dietary fibre and fish, alongside regular exercise has been shown to reduce risk (Bradbury et al. 2020; Dekker et al. 2019). Other preventative factors include the current and previous use of hormone-replacement therapy (Lin et al. 2012), and taking aspirin daily (Garcia-Albeniz and Chan 2011). By far the strongest preventative measure has been the uptake of national screening programmes using endoscopy, which has led to an increase in the removal of precancerous polyps leading to between a 20-30% reduction in CRC incidence and mortality in screened populations (Elmunzer et al. 2012).

#### 1.1.2.2 Non-modifiable factors

Non-modifiable risk factors for CRC can be split into hereditary and non-hereditary factors. Data from large epidemiological studies demonstrate that male sex and increasing age are

the most strongly associated non-modifiable, non-hereditary risk factors for CRC (Globocan 2020). Other important non-modifiable risk factors include inflammatory bowel disease, which is associated with young-onset CRC, and is modified by extent of chronic inflammation (Jess et al. 2012), as well as type-2 diabetes, which remains an important risk factor even after adjusting for obesity and diet (Dekker et al. 2019; Peeters et al. 2015).

CRC is known to have a substantial hereditary component, with positive family history featuring in up to 20% of cases (Henrikson et al. 2015). Twin studies indicate that 35% of CRC risk may be linked to heritable factors (Lichtenstein et al. 2000), although only around 5-10% can be attributed to known CRC syndromes (Valle et al. 2019). While large genome wide association studies continue to highlight single nucleotide polymorphisms associated with CRC, the associated risks are often minimal, and only partly explain a small proportion of hereditary risk (Montazeri et al. 2020).

Hereditary CRC syndromes arise in family pedigrees through Mendelian inheritance. They can be subdivided into hereditary non-polyposis and polyposis syndromes. Hereditary non-polyposis colorectal cancer (HNPCC) refers to a range an autosomal-dominant syndromes (including Lynch syndrome), which account for up to 4.2% of all CRC cases (J. Lee et al. 2017). These cancers are characterised by mutations in DNA mismatch repair (MMR) genes (MSH2,6 and MLH1), and are also associated with non-CRC malignancies, including endometrial, ovarian, gastric and small bowel cancer (Porkka et al. 2019). While patients with HNPCC are not at increased risk of developing colorectal polyps, the defective DNA repair mechanisms mean that if a polyp arises, malignant progression is almost inevitable, and often accelerated. The hereditary polyposis syndromes are also inherited autosomal dominantly, and account for approximately 5% of CRC cases (Hampel 2018). The most common polyposis syndrome is familial adenomatous polyposis (FAP), which is related to mutations in *adenomatous polyposis coli* (*APC*), a known tumour-suppressing protein, and is characterised by the growth of thousands of polyps throughout the entire colon. In

contrast to HNPCC, the risk of cancer within each polyp is not increased, however due to the sheer number of polyps, development of CRC is also inevitable (Half et al. 2009). In view of the known progression to CRC, national registries of affected families are maintained, with appropriate testing, surveillance and prophylactic surgery undertaken when required (Monahan et al. 2020).

### 1.1.3 Pathogenesis

Almost all CRCs arise from within a polyp, through a multistep process involving the progression of a premalignant lesion into invasive carcinoma. This sequence of events was initially described by Fearon and Vogelstein (1990), and is known as the adenoma-carcinoma pathway. This model describes how the transformation of the normal colorectal epithelium into a benign polyp, or adenoma, then progresses through the stepwise accumulation of genetic and epigenetic aberrations, leading to the development of invasive CRC. In sporadic cases of CRC, this sequence typically occurs over 10-15 years. Despite this common underlying sequence, the molecular and genetic pathophysiology of CRC is complex and heterogeneous. It is now understood that progression through this sequence is characterised by three major phenotypes: chromosomal instability (CIN), CpG island methylator phenotype (CIMP), and microsatellite-instability (MSI) (Nguyen and Duong 2018).

CIN is characterised by widespread aneuploidy and loss of heterozygosity, and is the most common type of genetic instability found in CRC, observed in over 70-80% of adenoma-carcinoma transitions (Pino and Chung 2010). The CIN phenotype most closely resembles the initial description of the adenoma-carcinoma sequence, and arises following mutations in *APC*, which are followed by activation of *KRAS* and inactivation of *TP53*. In contrast to this, the CIMP phenotype is associated with epigenetic instability, which arises through transcriptional inactivation by DNA hypermethylation at CpG promoter islands, leading to the silencing of tumour-suppressor genes as well as DNA repair genes, including MLH1.

This results in microsatellite stable and instable CRC, and is also associated with early *RAS* and *BRAF* mutations (Nguyen and Duong 2018). This sequence of events is commonly observed in serrated polyps, which are histologically and morphologically distinct from adenomas, and accounts for up 20% of sporadic cases of CRC (De Palma et al. 2019). MSI CRC accounts for approximately 10% of sporadic cases, and is considered to be a distinct phenotype based on its near diploid karyotype and association with a unique set of gene mutations involving the DNA MMR apparatus (Grady and Markowitz 2015). It is characterised by a high frequency of replication errors, which due to the failure of DNA repair mechanisms, results in progressive nucleotide insertions and deletions within the microsatellite sequence. This results in local immune cell infiltration, which is a common feature of MSI CRC (Dolcetti et al. 1999).

This genetic and molecular heterogeneity underlies observed differences between cancers arising in the right versus the left colon and rectum (Figure 1.1). These mechanisms are also clinically important, as they relate to prognosis and treatment response. For example, cancers arising from serrated polyps that exhibit a CIMP phenotype have a poor prognosis and do not respond to anti-EGFR therapies (De Sousa E Melo et al. 2013). Similarly, analysis of *KRAS* status is routinely undertaken in patients with metastatic CRC to determine eligibility for anti-EGFR therapy, which is ineffective in patients with *KRAS* mutations (S. H. Chen et al. 2019b). Clinically, MSI CRCs are categorised based on the level of instability as either MSI-high (MSI-H) or MSI-low (MSI-L) with the former being associated with improved prognosis (Popat et al. 2005). MSI-H has also been shown to predict response to irinotecan-based chemotherapy protocols (Bertagnolli et al. 2009). Furthermore, the degree of MSI positively correlates with density of tumour-infiltrating immune cells, which is also associated with a favourable prognosis (Galon et al. 2006).

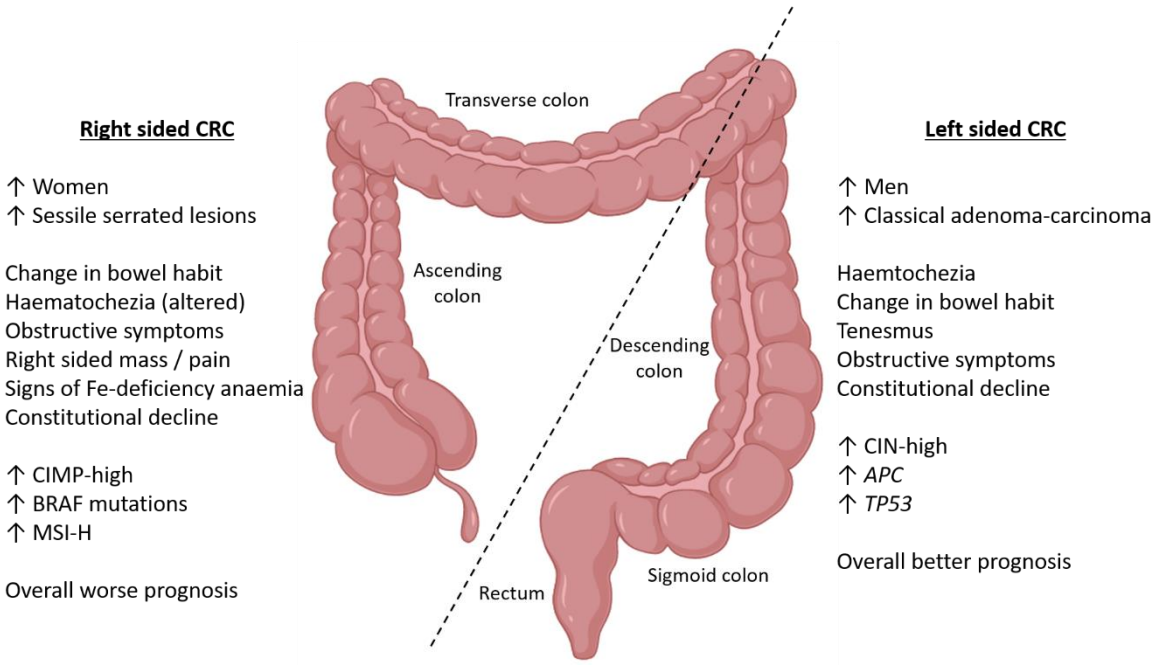



**Figure 1.1** Clinical and genetic differences between right sided versus left sided CRC. Image adapted from Dekker et al. (2019).

### 1.1.4 Diagnosis

In its early stages CRC is often asymptomatic. While there is considerable overlap between right and left sided CRC, the symptoms reported can provide clinical clues as to the site of disease (Figure 1.1), and often requires consideration within the context of additional patient-specific risk factors. New, onset rectal bleeding is the predominant red flag symptom prompting urgent referral for endoscopic investigation, which is the primary method used to diagnose CRC. While the detection of overt CRC by endoscopy is straight forward, specific quality indicators exist to benchmark endoscopists and endoscopy units to maximise the detection of pre-malignant lesions, particularly sessile polyps, which can be difficult to discern from the underlying bowel mucosa (Lanspa and Lynch 2010). Histopathological assessment of biopsies acquired during endoscopy forms the basis of diagnosis. Patients who are unable to undergo an index endoscopy are investigated by computer tomography (CT)-colonography, with large scale trials demonstrating similar sensitivity when compared with colonoscopy (Atkin et al. 2013).

Following the histopathological diagnosis of CRC, patients will need to undergo further investigations before progressing to treatment. Due to differences in anatomy and disease progression the diagnostic pathways for colonic and rectal cancer are distinct. In both cases, cross sectional imaging of the chest, abdomen and pelvis is required to rule out metastatic disease, which are detected in up to 20% of new cases of CRC (Brenner et al. 2014). The liver is the most frequent site of metastasis in CRC, and any suspicious lesions will need to be characterised by MRI. Detailed locoregional staging is also required in rectal cancer, which is undertaken by MRI, and is used to direct neoadjuvant treatment. While positron emission tomorgraphy (PET)-CT imaging may be used in select patients found to have metastatic disease, there is currently insufficient evidence to support its routine use during the diagnosis and staging of CRC (Rodríguez-Fraile et al. 2020). All patients diagnosed with CRC must also have their carcinoembryonic antigen (CEA) concentration checked. While this is not used to direct treatment, significantly elevated baseline CEA levels are associated with poor prognosis (Li Destri et al. 2015). Furthermore, it can be used following surgical resection to predict the presence of residual disease and as part of surveillance following treatment.

#### 1.1.4.1 Staging

Diagnostic information acquired from histopathological analysis and imaging are used to classify colorectal cancers according to the American Joint Committee on Cancer (AJCC) TNM classification (Amin et al. 2017), which provides detail on: local invasion depth (T stage), lymph node metastasis (N stage) and presence of metastatic disease (M stage, Table 1.1). These are then combined to provide an overall Union for International Cancer Control (UICC)/AJCC stage of disease (Table 1.2), which provides the basis for treatment allocation and correlates with prognosis. A drawback of this system is highlighted by the treatment of patients with stage II disease. Current guidelines recommend adjuvant chemotherapy for patients with high risk stage II (IIb) disease, although a significant proportion of patients do not gain any survival benefit from this (Fotheringham et al. 2019;

Kannarkatt et al. 2017). This highlights the need for further research to identify novel biomarkers to guide treatment allocations, which may need to focus more on individual patient-specific factors. Furthermore, the TNM staging system does not incorporate information acquired from the genetic and molecular analysis undertaken during histological assessment of a tumour, including MMR testing and *KRAS* status, which are now commonly used to inform treatment decisions.

| TNM CLASSIFICATION OF COLONIC ADENOCARCINOMA | |
|---|---|
| **T stage** | **Definition** |
| TX | Primary tumour not assessed |
| T0 | No evidence of primary tumour |
| Tis | Carcinoma *in situ* (intramucosal carcinoma) |
| T1 | Tumour invades submucosa (no involvement of muscularis propria) |
| T2 | Tumour invades muscularis propria |
| T3 | Tumour invades through muscularis propria into pericolorectal tissues |
| T4- | |
| T4a | Infiltration of the serosa into the visceral peritoneum |
| T4b | Tumour directly invades into adjacent organs and/or structures |
| **N stage** | |
| Nx | Regional lymph nodes not assessed |
| N0 | No evidence of regional lymph node metastasis |
| N1- | |
| N1a | Metastasis in 1 regional lymph node |
| N1b | Metastasis in 2-3 regional lymph nodes |
| N1c | No lymph node metastasis, but tumour deposits in non-peritonised tissues |
| N2- | |
| N2a | Metastasis in 4-6 regional lymph nodes |
| N2b | Metastasis in 7 or more regional lymph nodes |
| **M stage** | |
| M0 | No distant metastasis (as assessed on imaging) |
| M1- | |
| M1a | Metastasis confined to 1 organ or site without peritoneal metastasis |
| M1b | Metastasis to 2 or more organs or sites without peritoneal metastasis |
| M1c | Metastasis to the peritoneal surface with or without other organ metastasis |

**Table 1.1** AJCC TNM classification of colonic adenocarcinoma (8$^{th}$ Edition) (Amin et al. 2017).

| | T | N | M |
|---|---|---|---|
| Stage 0 | Tis | N0 | M0 |
| Stage I | T1-2 | N0 | M0 |
| Stage II | | | |
| Stage IIA | T3 | N0 | M0 |
| Stage IIB | T4a | N0 | M0 |
| Stage IIC | T4b | N0 | M0 |
| Stage III | | | |
| Stage IIIA | T1-T2 | N1/N1c | M0 |
| | T1 | N2a | M0 |
| Stage IIIB | T3-T4a | N1/N1c | M0 |
| | T2-T3 | N2a | M0 |
| | T1-T2 | N2b | M0 |
| Stage IIIC | T4a | N2a | M0 |
| | T3-T4a | N2b | M0 |
| | T4b | N1-N2 | M0 |
| Stage IV | | | |
| Stage IVA | Any T | Any N | M1a |
| Stage IVB | Any T | Any N | M1b |
| Stage IVc | Any T | Any N | M1c |

**Table 1.2** Staging of colonic adenocarcinoma. Based on UICC/AJCC TNM classification of colonic adenocarcinoma (8th Edition) (Amin et al. 2017)

#### 1.1.4.2 Screening

CRC is a life-threatening condition, and the burden of this disease is set to increase considerably over the next decade (Arnold et al. 2017). If detected early, over 90% of CRC-related deaths are avoidable (Simon 2016), although early stage disease is often asymptomatic. As CRC has a common precursor lesion (polyp), and development of cancer occurs over 10-15 years, detection and resection of these lesions can prevent progression to invasive CRC. Accordingly, national screening for CRC is an important aspect of public health in many developed countries.

In the UK, the Bowel Cancer Screening Program (BCSP) is population based, and is currently offered biannually to all adults between 50-74 years of age (Tepus and Yau 2020). Since its inception in 2006 it has undergone multiple changes, and continues to adapt to changing evidence and incidence patterns. Currently, screening is undertaken using faecal

immunochemical tests (FIT), which have replaced the guaiac faecal occult blood test (gFOBT). Both of these tests work by detecting trace amounts of haemoglobin, and those with positive tests are invited to undergo colonoscopy to look for, and remove, polyps. While gFOBT screening has not led to a significant reduction in CRC incidence, it is associated with a 16% reduction in CRC-related mortality, demonstrating its ability identify asymptomatic, yet clinically significant lesions before progression to life threatening invasive disease (Hewitson et al. 2008). However, the limitations of gFOBT include: poor sensitivity for detecting advanced colonic adenomas, requirement for repeat screening and dietary restrictions. Each of these limitations are overcome by FIT, which has the added advantage of being quantitative, enabling adjustment of cut-off values to adjust sensitivity and specificity accordingly to local resources (Schreuders et al. 2015). While the use of FIT has led to increased acceptance and participation in screening (Hol et al. 2010), important patient-based factors, including low acceptability of home testing, anxiety surrounding positive tests and the invasiveness of endoscopy, still prevent its uptake, particularly in the most deprived areas (Palmer et al. 2014). While non-faecal based tests exist for the detection of pre-malignant polyps, meta-analysis of existing trials fail to show effectiveness in the asymptomatic population (L. Song et al. 2017). Therefore, there is a need for further research to identify highly sensitive and specific plasma or serum-based biomarkers for use in CRC screening.

### 1.1.8 Treatment

Following the diagnosis of CRC, the subsequent management of CRC is assessed and undertaken by the CRC multidisciplinary team (MDT), which includes health professionals from: colorectal surgery, gastroenterology, oncology, pathology, radiotherapy and radiology, as well as specialist cancer nurses. In addition to this, there is a gradual move towards regional MDTs for complex disease, including low rectal cancers. The strength of the consensus-based decisions reached by the MDT is highlighted by a reduction in positive circumferential resection margins in rectal cancer (Burton et al. 2006), as well as an

increase in patients undergoing adjuvant chemotherapy for high risk disease, leading to increased survival, particularly in patients presenting with advanced disease (MacDermid et al. 2009; Munro et al. 2015).

Surgical resection of CRC remains the cornerstone of treatment with curative intent. Often resection alone is curative for patients diagnosed with stage I disease, which are often diagnosed within polyps biopsied during symptomatic investigations or screening. Recent advances in endoscopic treatment mean that T1 colonic tumours can be resected en bloc using endoscopic mucosal resection (EMR) or endoscopic submucosal dissection (ESD), which, in addition to transanal endoscopic microsurgery (TEMS) and transanal minimally invasive surgery (TAMIS), can also be used for stage I rectal cancer (Witjes et al. 2021). It is recommended that these complex procedures are undertaken at specialist centres to maximise oncological outcomes (Bhurwal et al. 2016). The presence of high-risk features in the resected tumour, including lymphatic invasion, and, or, deep and lateral margins are likely to prompt recommendation for further adjuvant surgery, including an appropriate lymphadenectomy (Dekker et al. 2019). Surgical resection of CRC is undertaken along embryological planes according to the principle of mesocolic excision. A laparoscopic approach is now standard practice in most developed countries, which is associated with improved post-operative outcomes without compromising long-term survival (Biondi et al. 2013; Y. M. Huang et al. 2020). Laparoscopic surgery for rectal cancer can be challenging due to accessibility within the pelvis, although advances in robot-assisted laparoscopic surgery can help to overcome this, which has led to its increased use to treat mid and low rectal cancer (Katsuno et al. 2020). Increasingly, surgery is being offered to patients with stage IV disease, particularly those with isolated, or low volume liver metastases. The timing of metastasectomy, alongside the benefits of neoadjuvant and adjuvant chemotherapy are debatable, without clear evidence to guide decisions, which highlights the important role of the MDT in directing the treatment of these patients (Chow and Chok 2019).

While not used in colonic cancer, neoadjuvant chemoradiotherapy (nCRT) has become standard for locally advanced rectal cancer, whereby treatment decisions are based on MRI staging. A typical nCRT treatment regime consists of a radiosensitising fluoropyrimidine and 45-50 Gy administered over 25-28 fractions, which results in oncological downsizing in the majority of patients (Feeney et al. 2019). Following neoadjuvant treatment, patients are reassessed endoscopically and by MRI prior to proceeding onto surgical resection, typically within 8-10 weeks (D. Du et al. 2018). Interestingly, up to 20% of patients undergoing nCRT demonstrate a complete clinical response when assessed by endoscopy and MRI. While long term data describing local recurrence in this subgroup of patients is not currently available, it appears safe to adopt a watch-and-wait strategy, using regular surveillance, although careful patient selection, followed by detailed discussion of the alternative treatments and risks are essential (Lopez-Campos et al. 2020; van der Valk et al. 2018).

Unless contraindicated, adjuvant chemotherapy is recommended in patients with stage III colonic cancer, where the standard regime includes a combination of folinic acid, fluorouracil and oxaliplatin (FOLFOX) (Andre et al. 2015). The use of FOLFOX in stage II patients is based on the presence of additional risk factors, including: pathological T4 stage, suboptimal lymph node resection (<12), lymphovascular or perineural invasion, poorly differentiated histology, persistently elevated CEA and positive margins, although even in these settings not all patients appear to benefit (Fotheringham et al. 2019; Kannarkatt et al. 2017). These same risk factors are used when recommending adjuvant chemotherapy for rectal cancer, although its benefit, particularly in those who have undergone nCRT is unclear (Poulsen et al. 2015). Often, FOLFOX also forms the basis of chemotherapy for CRC recurrence, and in disease control during palliative treatment. In addition to traditional chemotherapy drugs, biologics and immunotherapy are also now used in the targeted treatment of metastatic CRC. Anti-EGFR therapy, including cetuximab, is used in combination with three-agent chemotherapy regimens for *KRAS* wild-type metastatic CRC.

Immune checkpoint therapy using PD-L1 inhibitors is now being used in MMR-mutated and MSI-H CRC, where it is associated with a complete oncological response in select cases (Oliveira et al. 2019).

### 1.1.9 Prognosis

Despite the rising incidence of CRC, prognosis has steadily improved over the past four decades, although a clear discrepancy remains between high- and low-income countries. Whereas five-year survival is now between 60-65% in high income nations, it remains below 50% in low-income countries (Brenner et al. 2014; Sankaranarayanan et al. 2010). Reasons for the improvements in prognosis are multifactorial, and include: improved public understanding, access to, and increased uptake of national screening programmes, introduction of neoadjuvant and adjuvant therapies as well as improved surgical techniques (Bisschop et al. 2017; Elmunzer et al. 2012; Rentsch et al. 2016; Rubin and Weller 2013). Importantly, these developments have also led to an increase in quality of life following treatment for CRC (Dekker et al. 2019). Limited progress and access to each of these factors are also likely to explain why prognosis in poorer nations remains low.

While increasing age is associated with a reduction in survival from CRC (Brenner et al. 2014), by far the most significant factor is stage of disease at the time of diagnosis. This is characterised by five-year survival rates of over 90% for stage I cancers, decreasing to less than 15% for stage IV disease (Siegel et al. 2020). This stark difference highlights the need for further research to improve the early detection of CRC, particularly in younger patients, and to develop new treatment options for those with more advanced disease.

## 1.2 Microenvironmental signalling

### 1.2.1 mTORC1 signalling pathway

All cells reside in a microenvironment consisting of cellular and non-cellular components. Under normal physiological conditions, homeostatic mechanisms maintain and adapt to changes in the microenvironment through a complex range of interconnected intra and intercellular signalling pathways that regulate the balance between anabolic and catabolic processes. Indeed, disruption of these pathways are the hallmarks of many diseases, including cancer. Central to the ability of cellular adaptation to the microenvironment is the mechanistic target of rapamycin (mTOR) complex 1 (mTORC1) signalling hub. This plays essential roles in regulating growth and metabolism, and responds to a wide range of signals, including: growth factors, cellular energy levels, oxygen levels and nutrients (Dibble and Manning 2013).

mTOR is a highly conserved serine/threonine protein kinase, which was initially discovered in yeast 30-years ago (Heitman et al. 1991). Whereas, the yeast genome has two TOR genes (TOR1 and TOR2), eukaryotes only have one, which in mammals is the sole target of the macrolide antibiotic, rapamycin (Sabatini et al. 1994). mTORC1 is a multiprotein complex, comprising of activating and inhibitory components. The core activating machinery consists of: mTOR, regulatory-associated protein with mTOR (Raptor, involved in substrate recruitment) and mammalian lethal with Sec13 protein 8 (mLST8, involved in stabilising the mTOR catalytic domain). The inhibitory subunits are: proline-rich Akt substrate of 40 kDa (PRAS40) and DEP domain containing mTOR interacting protein (DEPTOR). mTOR can also form the rapamycin-insensitive mTORC2 complex by interacting with rapamycin insensitive companion of mTOR (Rictor) (Saxton and Sabatini 2017). Unlike mTORC1, mTORC2 activity is not regulated by oxygen and nutrient availability, but lies downstream of the growth factor regulated pathways such as the PI3K pathway (Smith et al. 2020). Despite this, the two mTOR pathways overlap, as an important

downstream effect of mTORC2 signalling is the activation of Akt, which regulates mTORC1 activity (J. Kim and Guan 2019).

Activation of mTORC1 signalling is synonymous with promoting downstream anabolic processes, particularly protein synthesis. The direct downstream targets of mTORC1 are: the eukaryotic initiation factor 4E (eIF4E) binding protein, 4E-BP1, and, the ribosomal S6 kinase (S6K). Inhibition of 4E-BP1 is a key effect of mTORC1, whereby phosphorylation leads to its release from eIF4E, leading to the translation of mRNA encoding ribosomal proteins and translation factors (Dibble and Manning 2013). In addition to its effects on protein synthesis, mTORC1-dependent S6K activity leads to activation of the sterol responsive element binding protein (SREBP) transcription factors, which promotes lipid and cholesterol biosynthesis, and regulates glucose metabolism (J. Kim and Guan 2019). Alongside promoting the synthesis of macromolecules, mTORC1 signalling also inhibits the catabolic process of autophagy by inhibiting several components of the autophagic machinery (Dossou and Basu 2019).

### 1.2.2 Regulation of mTORC1 signalling

As mTORC1 acts as a cellular sensor to a wide range of growth-related and metabolic signals, the upstream regulation of this signalling pathway is complex (Figure 1.2). Most of these inputs converge on the tuberous sclerosis complex (TSC), which is a heterotrimer of TSC1, TSC2 and TBC1D7. TSC negatively regulates mTORC1 signalling through its inhibitory effect on Ras homolog enriched in brain (Rheb), which is located on the late endosome or lysosomal membrane and is required for mTORC1 activation (Condon and Sabatini 2019). Growth factor signalling, which activates Akt phosphorylates TSC2 and PRAS40, both of which result in mTORC1 activation. Metabolic and other stresses, including those caused by hypoxia, DNA damage and, or, low levels of ATP also regulate mTORC1 signalling through 5’ AMP-activated protein kinase (AMPK) activation, which phosphorylates TSC leading to mTORC1 inhibition (Melick and Jewell 2020). AMPK-

mediated inhibition of mTORC1 is synonymous with a switch to catabolic cellular activity through the activation of autophagy.

mTORC1 activity is also regulated by amino acids via TSC-independent mechanisms, involving Rag GTPases. This amino-acid mediated control of mTORC1 activity is complex, involving a wide range of plasma membrane and intracellular transporters and sensors that respond to dynamic changes in specific amino acids (Goberdhan et al. 2016). The Rag family consists of four GTPases (Rag A, B, C and D) that form obligate heterodimers (Rag A or B pairing with C or D) that are anchored to the late endosomal or lysosomal membrane through interactions with the pentameric Ragulator scaffolding complex. Amino acid stimulation converts the Rag heterodimer to an active nucleotide-bound state, which enables them to bind to Raptor and recruit mTORC1 to the late endosome or lysosomal surface for activation by Rheb (Takahara et al. 2020). Other important components of this process are the lysosomal v-ATPase pump, as well as the multiprotein complexes GATOR1 and GATOR2, which are negative and positive respective regulators of Rag GTPase activity (J. Kim and Guan 2019).

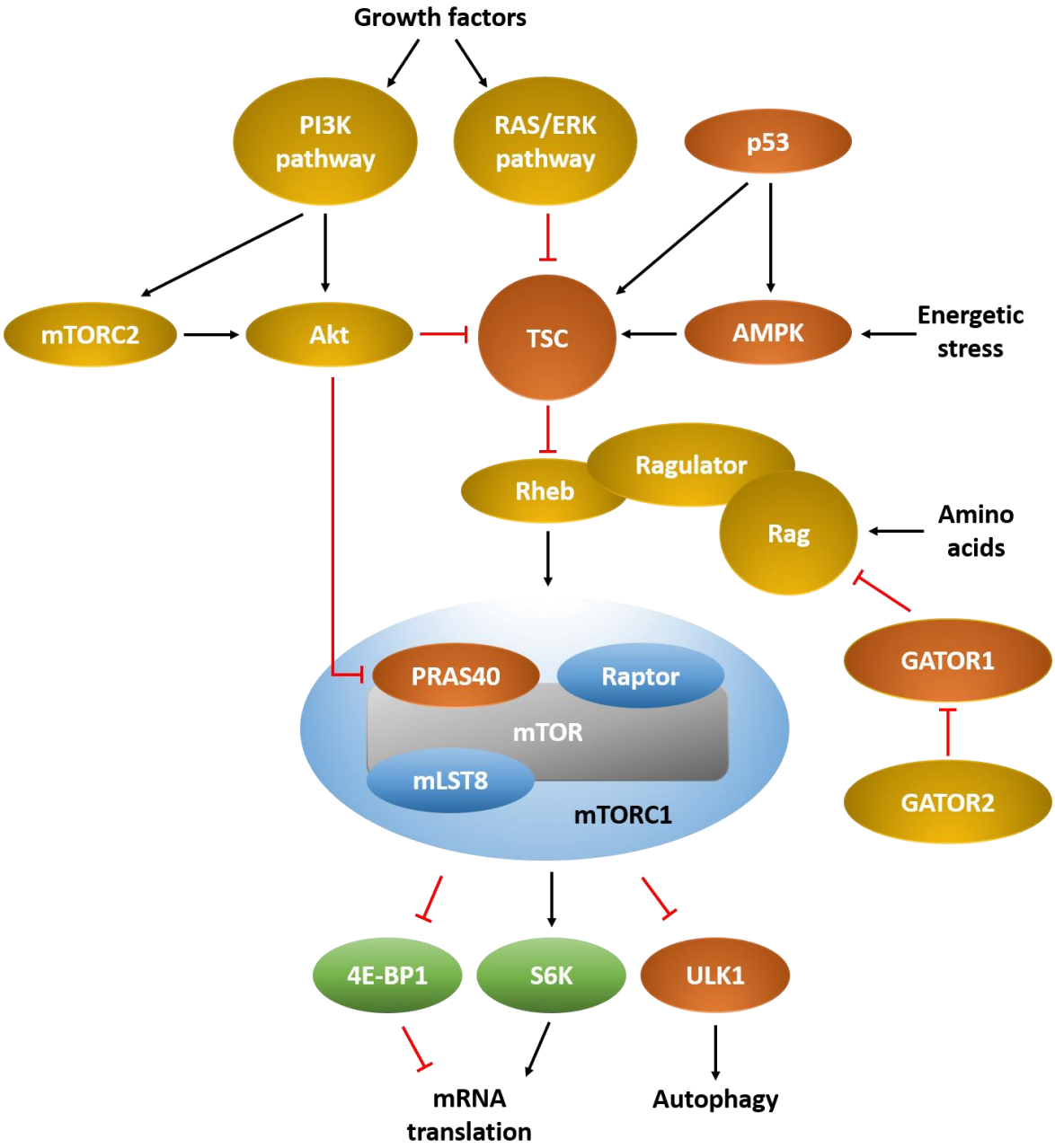



**Figure 1.2** Overview of mTORC1 activation. Growth factor signalling leads to phosphorylation and inactivation of the heterotrimer complex, TSC, removing its inhibitory effects on the mTORC1 activator Rheb, which is located on the late endosome or lysosomal membrane. An alternative pathway leading to Rheb, and subsequent mTORC1 activation involves amino acid sensing and stimulation. This converts Rag heterodimers to an activated state, which enables activation of Rheb and recruitment of the mTORC1 regulatory protein Raptor. Negative regulation of mTORC1 signalling is mediated by microenvironmental stress, including hypoxia and nutrient depletion, which leads to AMPK activation which activates TSC.

### 1.2.3 mTORC1 signalling in CRC

Aberrant mTORC1 signalling is common in most types of cancer (Populo et al. 2012). This arises due its regulation by upstream pathways, including EGFR/RAS/ERK and PI3K/Akt, which are themselves commonly mutated in cancer. This is particularly relevant in CRC, whereby an oncogenic mutation in at least one component of these two pathways is detected in almost every patient (De Roock et al. 2011). Furthermore, mTORC1 activity is attenuated during cancer through mutations in p53, which acts as a negative regulator by activation of AMPK and stabilisation of the TSC (Feng et al. 2005). Mutations in various molecular components of the mTORC1 pathway have also been associated with specific cancers, for example: TSC1/2 in the familial cancer syndrome tuberous sclerosis, GATOR1 complex in glioblastoma and RagC in follicular lymphoma (Saxton and Sabatini 2017). The resultant increase in mTORC1 signalling supports tumorigenesis by promoting anabolic processes such as mRNA translation and substrate synthesis for metabolism. In contrast to this, the downstream effects of reduced mTORC1 signalling are also associated with cancer cell survival and tumorigenesis. Microenvironmental stress, including hypoxia and nutrient depletion are commonly experienced by cancer cells, and these factors are known to suppress mTORC1 activity through a range of mechanisms including activation of AMPK. This is associated with the internalisation and degradation of extracellular proteins in order to release amino acids to feed metabolism and promote tumour cell survival (Palm et al. 2015).

While it is not a canonical pathway associated with CRC, overexpression of mTORC1 is a common feature (Francipane and Lagasse 2014). Immunohistochemical analysis of *ex vivo* tumours have shown that components of mTORC1 signalling, including mTOR and 4E-BP1, are highly active in adenomas exhibiting high grade dysplasia, and correlated with invasiveness of CRC (Y. J. Zhang et al. 2009). Activation of mTORC1 within intestinal polyps is known to be a β-catenin-independent effect of oncogenic *APC* mutations (Valvezan et al. 2014). Furthermore, stimulation of the mTOR pathway is associated with

the onset of CIN in polyps (Aoki et al. 2003), which alongside *APC* mutations are common molecular events during the adenoma-carcinoma sequence. Taken together, these findings suggest that activation of mTORC1 signalling is an important early event during CRC tumorigenesis. A subset of CRCs show marked upregulation of the mTORC1 component, Raptor, which is associated with increased translation of cyclin-dependent kinase substrates, which are required for cell cycle progression (T. Wang et al. 2020c). In addition, mTORC1 is also associated with advanced CRC, where it has been shown to have a role in regulating epithelial-to-mesenchymal transition through activation of pathways involved in cytoskeletal reorganisation and motility (Gulhati et al. 2011).

#### 1.2.3.1 Targeting the mTORC1 pathway in CRC

In view of the various pro-tumorigenic properties of mTORC1, there is ongoing interest in targeting its key components to design novel anticancer drugs. Based on its sensitivity to rapamycin, early therapies were known as rapalogs (temsirolimus and everolimus), although these were found to be largely ineffective, particularly in CRC (Tian et al. 2019). Reasons for this include the fact that the main downstream effect of mTORC1 signalling, phosphorylation of 4E-BP1, is insensitive to rapamycin, alongside the fact that inhibition of mTORC1 reverses a negative feedback loop on Akt activation, which paradoxically results in increased mTORC1 activation. Furthermore, short term exposure to rapamycin and rapalogs does not inhibit mTORC2, which also promotes mTORC1 activity through activation of Akt. Therefore, second-generation drugs have been developed that directly target the ATP-competitive mTOR catalytic domain (Torin1 and PP242), which simultaneously inhibit mTORC1 and mTORC2, and are currently being investigated in clinical trials. The loss of Akt activation that results from blocking mTORC2 activity underpins the parallel inhibition of mTORC1 activity. However, prolonged exposure to these second-generation inhibitors is associated increased PI3K signalling, which provides an alternative route for Akt activation (Saxton and Sabatini 2017).

Therefore, it is now accepted that monotherapy-based treatments that target mTOR activity are likely to be ineffective, and attention is now focussed on using them as part of combination therapies. This has been trialled in CRC, where the dual use of traditional rapalogs alongside a VEGF inhibitor was associated with delayed disease progression in metastatic disease during phase II studies (Wolpin et al. 2013). Furthermore, a combination of PP242, alongside the dual PI3K inhibitor NVP-BEZ232 can reduce the growth and survival in a range of CRC cell lines harbouring mutations in the EGFR/RAS/ERK and PI3K/Akt pathways (Blaser et al. 2012). Moreover, dual treatment with the ATP-competitive mTOR inhibitors, AZD8055 and OSI-027 was associated with prolonged reductions in 4E-BP1 phosphorylation and increased tumour cell apoptosis (H. N. Wang et al. 2020a). Finally, combining AZD8055 with low doses of the traditional chemotherapy drug, irinotecan, was more effective than full dose FOLFOX treatment at reducing liver metastases (Reita et al. 2019).

## 1.3 Extracellular vesicles

### 1.3.1 Defining extracellular vesicles

Extracellular vesicles (EVs) refer to a heterogenous group of nanometre-sized, lipid-membrane bound vesicles that are secreted by all cell types. While they were initially thought to represent a method for cells to eliminate waste products (Johnstone et al. 1987), they are now known to transport rich bioactive cargoes, containing lipids, proteins and nucleic acids, and are a vital component of intercellular signalling in normal development and physiology. Furthermore, it is now understood that aberrant EV signalling is implicated in the majority of pathological processes, including cancer (van Niel et al. 2018). There are two major categories of EVs: exosomes, which originate through the endosomal pathway and subsequent fusion with the plasma membrane, and microvesicles, which are shed directly from the plasma membrane. These distinct biogenesis and secretion pathways represent the primary method to distinguish these different EV subtypes, as the differences

in size, morphology, content and function between exosomes and microvesicles often overlap (Figure 1.3).

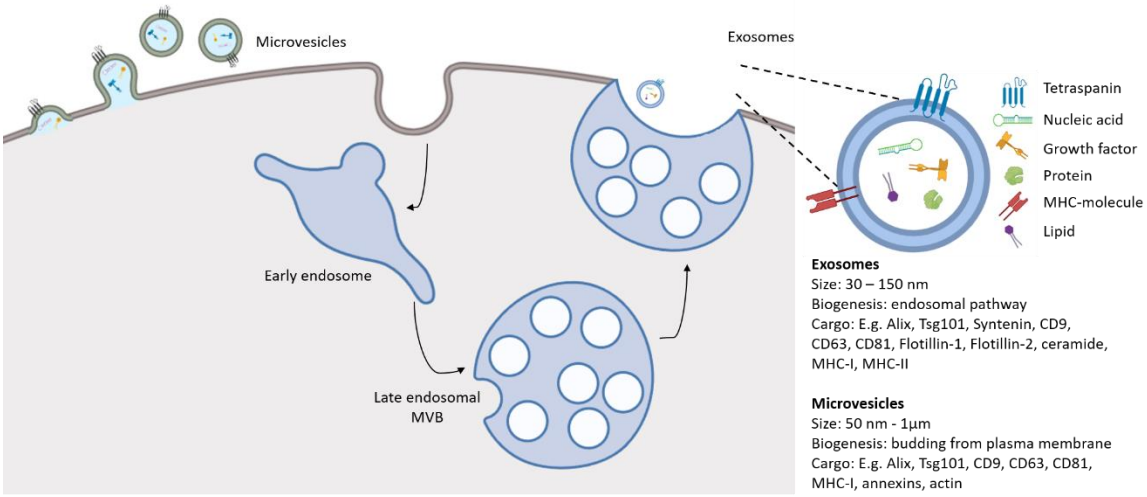



**Figure 1.3** Overview of EV heterogeneity. The two major categories of EV have distinct biogenesis at secretion pathways. Exosomes originate from within the endosomal pathway and subsequent fusion with the plasma membrane, while microvesicles are shed directly from the plasma membrane. There is considerable overlap in the biophysical properties (size and shape) and cargo of exosomes and microvesicles.

Exosomes are 30-150 nm in size and represent intraluminal vesicles (ILVs) formed within multivesicular bodies (MVBs), which are then secreted upon fusion of the MVBs with the plasma membrane. Microvesicles are 50 nm to 1 µm in size, and are secreted directly from the plasma membrane through a poorly understood mechanism of membrane budding (Veziroglu and Mias 2020). The proteomic and lipid profile of EVs is representative of these different biogenesis pathways, and alongside other methods, is used as a tool to characterise EVs isolated experimentally. Exosomes are formed by inward budding of the MVB limiting membrane during its maturation. This process involves the endosomal sorting complexes required for transport (ESCRT) machinery, and as such, components of this are detected in all exosomes. Examples of common ESCRT, or ESCRT accessory proteins used to identify exosomes include: Alix, Tsg101 and syntenin. Exosomes are also enriched in transmembrane proteins, specifically the tetraspanins, CD9, CD63 and CD81 (van Niel et al. 2018). As these proteins are present on the plasma membrane, they are also detected

within microvesicles. However, as microvesicles form by direct outward budding of the plasma membrane, in contrast to exosomes, they contain a higher concentration of specific cytosolic, and cytoskeletal proteins, which often contain post translational modifications, such as glycosylation and phosphorylation (Doyle and Wang 2019). Annexin A1 is known to be a specific marker for microvesicles that is undetected within exosomes (Jeppesen et al. 2019).

The overlap in size, morphology and composition represents a challenge when studying EV biology, and often the various terms are used interchangeably. Therefore, throughout this thesis the term EV will be used when referring to preparations of vesicles isolated from secreting cells or plasma, which are known to contain a heterogenous mix of different EV subtypes, whereas exosome will be used when specifically referring to vesicles secreted by the endosomal-MVB pathway.

### 1.3.2 Exosome biogenesis & secretion

Exosome biogenesis occurs within the endosomal pathway. Within this system, material internalised by endocytosis is delivered to the early endosome, where material is sorted and either labelled for recycling, or through a process of endosomal maturation, is transported into the late endosomal compartment. Early endosome-mediated recycling occurs either directly to the plasma membrane, or through transport into recycling endosomes, which enables intracellular processing (Grant and Donaldson 2009). In addition, intracellular material can also enter the early endosome via the trans Golgi-apparatus. MVBs are late endosomes that contain ILVs, which are generated by invaginations and budding of the limiting membrane into the lumen. From here, ILV cargo may undergo ubiquitination and degradation via MVB-lysosomal fusion, or are released into the extracellular space upon fusion with the plasma membrane (Hanson and Cashikar 2012). The mechanisms that control the balance between degradative and secretory MVB

pathways are poorly understood, but are known to be regulated by the specific components of the ESCRT machinery (Baietti et al. 2012).

The sorting of cargo into exosomes, as ILVs within the MVB lumen requires the ESCRT machinery, which are a group of evolutionary conserved protein subcomplexes (ESCRT-0, -I, -II, -III), that alongside accessory proteins, assemble into multiprotein complexes on the MVB limiting membrane, where they control protein sorting, membrane budding and membrane severing to generate ILVs (D'Souza-Schorey and Schorey 2018). The role of the ESCRT machinery in exosome biogenesis is summarised by Christ et al. (2017) and Juan and Furthauer (2018). Briefly, ESCRT-0 component HRS binds and clusters ubiquitinated proteins on the endosomal membranes, which then recruits ESCRT-I, through interaction with Tsg101, and ESCRT-II. Together, ESCRT-I and -II initiate the inward budding of the limiting membrane. Subsequently, ESCRT-III is recruited through the interaction between the ESCRT accessory protein Alix, and Tsg101, which then acts to constrict, and sever the neck of the developing membrane bud. Finally, ESCRT-III is disassembled by AAA-ATPase SKD1, and recycled for the next round of cargo sorting.

In addition to the ESCRT-dependent exosome biogenesis pathway, ILV formation also occurs via ESCRT-independent mechanism. The first evidence for this was provided in studies that detected the release of CD63-labelled exosomes following inactivation of the four ESCRT complexes (Stuffers et al. 2009). This alternative EV biogenesis pathway involves distinct lipid microdomains containing ceramide, which due to its cone-like structure, induce membrane curvature and budding. Similarly, tetraspanin clusters of CD9, CD81 and CD82 can also form cone-shaped microdomains that promote membrane budding (van Niel et al. 2018). The balance of activity between these distinct biogenesis pathways are likely to control the loading of specific EV cargoes and will vary between different cell types.

The transport and subsequent fusion of MVBs to the plasma membrane requires the interaction between Rab GTPases, the cytoskeleton (actin and microtubules), molecular motors (dynein, kinesins and myosin) and the membrane fusion apparatus (SNARE complex) (D'Souza-Schorey and Schorey 2018). Rab GTPases are known as the master regulators of intracellular membrane traffic, whereby distinct Rabs localise to specific membrane compartments and regulate transport by interacting with specific effector proteins (Zhen and Stenmark 2015). Specific Rabs implicated in the secretion of exosomes include: Rab27a, Rab27b, Rab7, Rab11 and Rab35. In particular, Rab27 and its associated proteins are reported to have a central role in controlling exosome secretion. Rab27b regulates the transport of MVBs towards the plasma membrane, while Rab27a coordinates cytoskeletal rearrangements that allows docking of the MVB to the plasma membrane (Ostrowski et al. 2010). Following arrival and docking, fusion with the plasma membrane occurs through the complimentary pairing of vesicular SNAREs and the target membrane SNARE to form the SNARE complex, which induces zipper-like fusion of the two opposing membranes and the release of exosomes into the extracellular space (Yue et al. 2020).

### 1.3.3 EV mediated signalling

#### 1.3.3.1 EV signalling during development and in normal physiology

Normal development and physiology are reliant on intercellular communication. EVs mediate cell-to-cell communication through the transfer of biologically active cargoes, both locally via autocrine and paracrine routes, as well as systemically between different organ systems. These factors highlight the critical role that EVs play during development and physiology, and it is important to study the biology of EVs during these processes in order to understand how aberrant EV signalling contributes to the onset of disease.

The importance of EVs during development are apparent during the very early stages of embryogenesis. Embryo survival depends on successful implantation into the uterine endometrium, and EV-mediated bidirectional communication appears to be critical for this

process (Ng et al. 2013). Following implantation, trophoblast cells secrete EVs that promote remodelling of the extracellular matrix (ECM) and induce angiogenesis, which is necessary for placental development (Atay et al. 2011). Subsequently, exosomes secreted by the placenta contain ligands such as TNF-related apoptosis-inducing ligand (TRAIL), which induces apoptosis in activated immune cells, and are therefore implicated in maintaining the immune-privileged microenvironment required for normal foetal development (Stenqvist et al. 2013). Finally, EVs secreted by the blastocyst, which gives rise to a whole embryo, are involved in establishing vital morphogen gradients that define the anatomical axes required for normal development (Cruz et al. 2018).

EVs are detected in all biological fluids (Raposo and Stoorvogel 2013), which provides compelling evidence that they play important physiological roles. EVs containing various procoagulant, anticoagulant and fibrinolytic properties are physiological components of blood, highlighting their role in maintaining haemostatic homeostasis (Yanez-Mo et al. 2015). Inflammatory and pathological processes associated with increased risk of thromboembolism coincide in alterations in the balance between EVs transporting prothrombotic and anticoagulant cargoes (Matsumoto et al. 2004). Following instances of thromboembolism, exosomes released by mesenchymal stem cells are potent inducers of angiogenesis and tissue regeneration within infarcted tissues (X. Teng et al. 2015). Within the liver, hepatocytes release EVs in response to drug-induced injury, which promote healing via the RNA-dependent activation of stellate cells (Royo et al. 2013). EVs secreted by oligodendrocytes within the central nervous system are enriched in myelin-associated proteins required for the maintenance of neurones (Kramer-Albers et al. 2007). Finally, EVs are also important mediators of both innate and acquired immunity. During innate immunity, macrophages release EVs containing cytokines and microRNAs (miRNAs) that promote myeloid cell proliferation and differentiation, while neutrophil-derived EVs have been shown to directly inhibit the growth of bacterial cells (Yanez-Mo et al. 2015). EVs contribute to

acquired immunity by transporting antigenic material to antigen presenting cells, which can activate specific T-cell responses (Mallegol et al. 2007).

#### 1.3.3.2 EV signalling in CRC cancer

The hallmarks of cancer include: sustaining proliferative signalling, insensitivity to antiproliferative signals, evasion of programmed cell death, replicative immortality, sustaining angiogenesis and tissue invasion and metastasis (Hanahan and Weinberg 2011). Fulfilling each of these requirements is dependent on the bidirectional communication between tumour cells and non-tumour cells, including immune and stromal cells, within the tumour microenvironment. It is now accepted that EVs are important mediators of this intercellular communication that drives tumorigenesis, which is often achieved through aberrant versions of EV-mediated signalling that occur during normal physiology. Indeed, tumour-derived EVs are now known to promote angiogenesis and inflammation, modulate the immune system, remodel parenchymal tissue locally and at sites metastasis and promote vascular and lymphatic invasion (Becker et al. 2016).

Sustained proliferation, despite opposing factors that would usually inhibit this process, is the central feature of all cancers, and arises due to increasing genetic instability. Coinciding with this genetic instability are alterations in EV cargo, which appear to further promote cancer cell growth. For example, mutant *KRAS* CRC cells export mutant *KRAS* in exosomes, which increases the proliferation of recipient cells (Demory Beckler et al. 2013). Conversely, cancer cells also use EVs to remove intracellular material that would otherwise suppress growth. This has been demonstrated for the removal of certain onco-suppressive miRNAs. miRNAs are short (average 22 nucleotides) non-coding RNAs that participate in post-transcriptional suppression of gene expression, and can have pro- and anti-tumorigenic properties (O'Brien et al. 2018). CRC cells have been shown to selectively sort onco-suppressive miR-193a into exosomes for disposal, which results in increased cell growth (Y. Teng et al. 2017). Uncontrolled cell proliferation is associated with

microenvironmental hypoxia, as tumour growth outstrips its blood supply. This triggers adaptive responses, including the release of cancer cell EVs that promote the differentiation of fibroblasts into pro-angiogenic cancer-associated fibroblasts (CAFs) (Ko et al. 2019; Webber et al. 2015). Moreover, hypoxia induces the release of CRC EVs containing Wnt4, which is associated with promoting angiogenesis through EV-mediated Wnt/β-catenin signalling in endothelial cells (Z. Huang and Feng 2017).

Uncontrolled cell growth and the resultant hypoxia promotes an inflammatory response that coincides with the recruitment of immune cells. Tumour progression is reliant on evading recognition from these immune cells and establishing an immunosuppressive microenvironment. EV-mediated mechanisms for achieving this have been described in CRC, which involves stimulating the expansion of negative regulators of the immune system, while also blocking the activity of CD8+ T-cells and natural killer cells (Mannavola et al. 2019). For example, CRC EVs have been shown to contain FasL and TRAIL, both of which induce apoptosis in CD8+ T-cells (Huber et al. 2005). With regards to immunosuppression, EVs containing TGF-β1 are able to upregulate T-regulatory cells (N. Yamada et al. 2016), while EVs transporting miR-145 promote M2 polarisation of monocytes into tumour-associated macrophages, which suppress the activity of cytotoxic T-cells (Shinohara et al. 2017). Indeed, circulating plasma EVs from patients with CRC that contain high amounts of TRAIL and miRNAs involved in promoting M2 polarisation have been shown to correlate with poor survival (Takano et al. 2017; N. Yamada et al. 2016).

CRC EVs also promote the differentiation of quiescent fibroblasts into CAFs that undertake ECM remodelling by upregulating matrix-remodelling proteins, such as MMP1, EMMPRIN and ADAM10 (Rai et al. 2019). This remodelling is required to enable tumour cells to invade through the epithelial basement membrane and enter the vascular and lymphatic circulation. Alongside these processes, cancer cells must undergo phenotypic changes in order to become circulating tumour cells. This process is known as epithelial-to-

mesenchymal transition (EMT) and is considered to be a precondition of metastatic potential (Heerboth et al. 2015). CRC EVs containing miR-210 have been shown to promote EMT, and subsequent growth in recipient cells. These cells also appear to be resistant to FOLFOX chemotherapy, which is known to be less effective at targeting mesenchymal tumour cells (Bigagli et al. 2016). Similarly, both EMT and chemoresistance are also induced following activation of Wnt/β-catenin signalling by EV-delivered miR-92a (J. L. Hu et al. 2019b). Tumour-derived EVs are now thought to be the key drivers of pre-metastatic niche formation, which is the process of priming tissue within a secondary organ to provide favourable conditions for the growth of metastatic cancer cells (Y. Guo et al. 2019). CRC EVs carrying miR-25-3 triggers VEGF expression in hepatic endothelial cells, leading to increased vascular permeability and angiogenesis, which is associated with increased number of metastasis in a mouse model (Zeng et al. 2018). In addition, Y. Shao et al. (2018b) found that CRC EVs promote the expression of the chemokine, CXCR4 within the liver, leading to the recruitment of immune and endothelial cells required for pre-metastatic niche formation. During this study the migration of CRC cells that usually exhibit low metastatic potential was also increased.

This role of EVs in priming the metastatic niche demonstrates the endocrine signalling capability of EVs, which is consistent with the fact that tumour-derived EVs can be detected in the blood of patients with CRC (Wei et al. 2020). Therefore, the detection of circulating cancer cell-derived EVs that carry specific pro-tumorigenic cargoes provides an attractive tool for novel biomarker discovery for diagnostic and prognostic applications, and, or, for predicting response to treatment. In addition, increased understanding of the intracellular mechanisms that control EV biogenesis and secretion, alongside identifying cancer-specific EV-cargoes may provide novel drug targets for future clinical use.

### 1.3.4 mTORC1 signalling and the EV switch

The precise molecular processes that control EV heterogeneity remain largely unknown, although it is believed to involve a combination of the different biogenesis pathways, involving ESCRT-dependent and -independent pathways, as well as specific Rab GTPases that coordinate their secretion. Work undertaken by the Goberdhan Group has revealed a novel mTORC1 signalling axis that regulates the secretion of EVs from a previously undescribed pathway, involving Rab11a-labelled recycling endosomes. The foundations of this discovery are reported in Fan et al. (2016), which describes a rapamycin-resistant form of mTORC1 in HCT116 CRC cells, which is located on the trans-Golgi network and is regulated by the upstream glutamine transporter/sensor, PAT4 (SLC36A4). Suppression of this PAT4-mTORC1 signalling axis via glutamine depletion, genetic manipulation or treatment with ATP-competitive mTOR inhibitors, triggers an intracellular switch in the biogenesis and profile of secreted EVs. This EV switch occurs due to increased protein trafficking through the recycling endosomes leading to the secretion of Rab11a-positive EVs, alongside a parallel reduction in EV biogenesis and secretion from the classical Rab7-labelled late endosomal pathway (Fan et al. 2020) (available in Appendix A). The EV switch is denoted on western blot by a decrease in CD63, signifying a reduction in EV biogenesis and secretion from Rab7-labelled compartments, and an increase in Rab11a, as well as the lipid raft protein Cav-1. In addition to HCT116 CRC cells, EV switching is also observed in prostate and cervical cancer cell lines.

The work by Fan et al. (2020) is the first study to demonstrate a direct role of mTORC1 in regulating the secretion of EVs. Glutamine is an important cancer cell metabolite, and its reduced availability is likely to represent a form of microenvironmental stress experienced by tumour cells (J. Zhang et al. 2017a). Therefore, it can be hypothesised that the secretion of switched EVs in response to microenvironmental stress, such as reduced glutamine, are capable of promoting adaptive changes in recipient cell behaviour within the tumour microenvironment, and thus driving tumorigenesis.

## 1.4 Research questions

The central hypothesis tested within this thesis is that microenvironmentally controlled EV switching is functionally important during tumorigenesis. The initial characterisation of switched EVs was undertaken in HCT116 CRC cells using EVs isolated by ultracentrifugation (UC). It is unknown whether other CRC cell lines also undergo EV switching, and whether other important stimuli of mTORC1 activity also triggers this response. These questions will be explored using EVs isolated using size exclusion chromatography (SEC), which overcomes some of the technical challenges associated with UC and is more appropriate for downstream functional analysis (Nordin et al. 2015). Previous studies that have investigated the role of EVs on tumorigenesis have highlighted effects on proliferation, as well as behaviours that drive metastasis, such as migration, invasion and phenotypic transformation. Therefore, the impact of switched EVs on each of these aspects of tumour biology will be investigated in the panel of CRC cell lines shown to undergo EV switching. EV-associated miRNAs are known to be important drivers of tumorigenesis, and studies comparing EV content in blood samples from healthy individuals and patients with CRC commonly report differences in miRNA cargo. Therefore, finally, the miRNA cargo of switched EVs will be explored alongside the EV-miRNA signature in a cohort of patients with newly diagnosed rectal cancer who have undergone nCRT.

In summary, the specific aims of this thesis are-

i. To validate size exclusion chromatography to isolate purified samples of non-switched and switched EVs, and to use this to investigate EV switching in other CRC cell lines (Chapter 3).
ii. To investigate the functional properties of switched EVs on CRC cell proliferation, migration and invasion, including the underlying mechanisms driving these behaviours (Chapter 4).

iii. To explore the differences in miRNA cargo between non-switched and switched EVs from different CRC cell lines, and to investigate whether this corresponds to miRNA changes following a diagnosis of CRC and, or, treatment with nCRT (Chapter 5).

# CHAPTER 2

## MATERIALS & METHODS

# 2. Materials & methods

## 2.1 CRC cell characterisation

### 2.1.1 Cell culture

The CRC cell lines used in this thesis were purchased from ATCC®. HCT116 cells were cultured in McCoy's 5A modified medium (Gibco®, Invitrogen), Caco-2 cells in EMEM (ATCC®), while SW480 and SW620 cells were maintained in DMEM GlutaMAX™ **(**Gibco®, Invitrogen). During normal cell culture, all media was supplemented with 10% (or 20% for EMEM) heat-inactivated foetal bovine serum (FBS; Gibco®, Invitrogen) and 100 U/ml penicillin-streptomycin antibiotic mix (Life Technologies). Cell lines were incubated at 37ºC with 5% $CO_2$ and were not used beyond passage 20.

### 2.1.2 Comparison of culture media and modulation of mTORC1 signalling

#### 2.1.2.1 Growth analysis

Cells were plated in a 12-well plate at a density of 200,000 cells per well in their full basal media and incubated overnight under standard conditions. The following day the culture media was replaced with either fresh full media, basal media supplemented with 1% insulin-selenium-transferrin mix (ITS; Gibco®, Invitrogen) without FBS, or DMEM/F12 (Gibco®, Invitrogen) plus 1% ITS. Analysis of growth was performed using the IncuCyte® ZOOM Live Cell Imager (Essen Bioscience), taking nine phase-contrast images every two hours for 48 hours. The IncuCyte® analysis software was used to detect cell edges and create a confluency mask, which was used to determine cell growth. Protein lysates were also collected after treatment with 60 µl RIPA (Sigma) supplemented by a cocktail of protease and phosphatase inhibitors (Sigma) to enable assessment of mTORC1 signalling using western blotting.

#### 2.1.2.2 Glutamine depletion

Cells were plated as per 2.1.2.1 and the following day replaced with DMEM/F12 without L-glutamine (Gibco®, Invitrogen) supplemented with 1% ITS. The first well was supplemented with 2mM of L-glutamine (Gibco®, Invitrogen), with subsequent serial dilutions down to 1.56% of physiological concentrations as well as a 0% control. Cells were then incubated for 24-hours, after which lysates were collected to assess mTORC1 signalling via western blotting. For HCT116 cells a glutamine concentration of 0.02 mM was used to prepare glutamine-depleted media (characterisation previously undertaken by Dr Shih-Jung Fan, (PDRA, Goberdhan Group; (Fan et al. 2020).

#### 2.1.2.3 mTORC1 inhibition

Cells were plated as per 2.1.2.1 and the following day replaced with DMEM/F12 supplemented with 1% ITS. Cells were treated with the mTOR inhibitor Torin1 (Cell Signalling) or rapamycin (Sigma) at the indicated concentrations, including a DMSO (Sigma) control. Treated cells were cultured for a further 24-hours, after which lysates were collected to assess mTORC1 signalling via western blotting.

#### 2.1.2.4 Hypoxia

Cells were plated at a density of 9 million cells per plate in 15 cm cell culture plates (Corning Life Sciences) in full basal media and incubated overnight under standard culture conditions. The following day the media was replaced with DMEM/F12 plus 1% ITS and incubated in a hypoxia chamber at 1% $O_2$ for 24-hours, after which cell lysates were collected to assess mTORC1 signalling via western blotting.

#### 2.1.2.5 Cell viability measurement

Cells were trypsinised and then resuspended in appropriate cell culture media. This was then mixed with trypan blue stain solution (Sigma) in a 1:1 ratio and cell viability assessed

by counting the number of non-stained cells using the LUNA-II™ Automated Cell Counter (Logos Biosystems, Inc).

## 2.2 Clinical samples

Between November 2017 and September 2019 plasma samples of 10 patients undergoing neoadjuvant chemoradiotherapy for newly diagnosed rectal cancer, and 10 healthy controls were provided by the Translational Gastroenterology Unit, NIHR Biomedical Research Centre, Oxford (REC reference no: 16/YH/0247). For the rectal cancer patients, plasma was collected before and after neoadjuvant chemoradiotherapy. Sample collection followed the standardised recommendations for downstream EV isolation and analysis (Witwer et al. 2013). Briefly, 10 ml of blood was collected by venepuncture in EDTA collection tubes and underwent centrifugation at 1300xg for 15 minutes. Plasma was aspirated into FluidX tubes (Brooks Life Sciences) and stored at -80 $^{o}$C until further analysis.

## 2.3 Isolation & characterisation of EVs from CRC cell lines and patient plasma

### 2.3.1 Isolation conditions

HCT116, Caco-2 and SW480 cells were plated at a density of 9 million cells per plate and SW620 cells at 15 million cells per plate in 15 cm cell culture plates in their full basal media. Cells were incubated overnight or until they reached 80% confluency and then the media was changed to EV-isolation media (glutamine-depleted DMEM/F12, or with added mTOR inhibitors) supplemented with 1% ITS. Cells were incubated overnight and the following day EVs were isolated using an appropriate method as described in 2.3.2.

### 2.3.2 EV isolation methods

EVs were isolated from cell culture media using ultrafiltration (UF), ultracentrifugation (UC) or size exclusion chromatography (SEC) as outlined in Figure 2.1. EVs were isolated from plasma using qEV size exclusion chromatography columns (Izon Sciences).

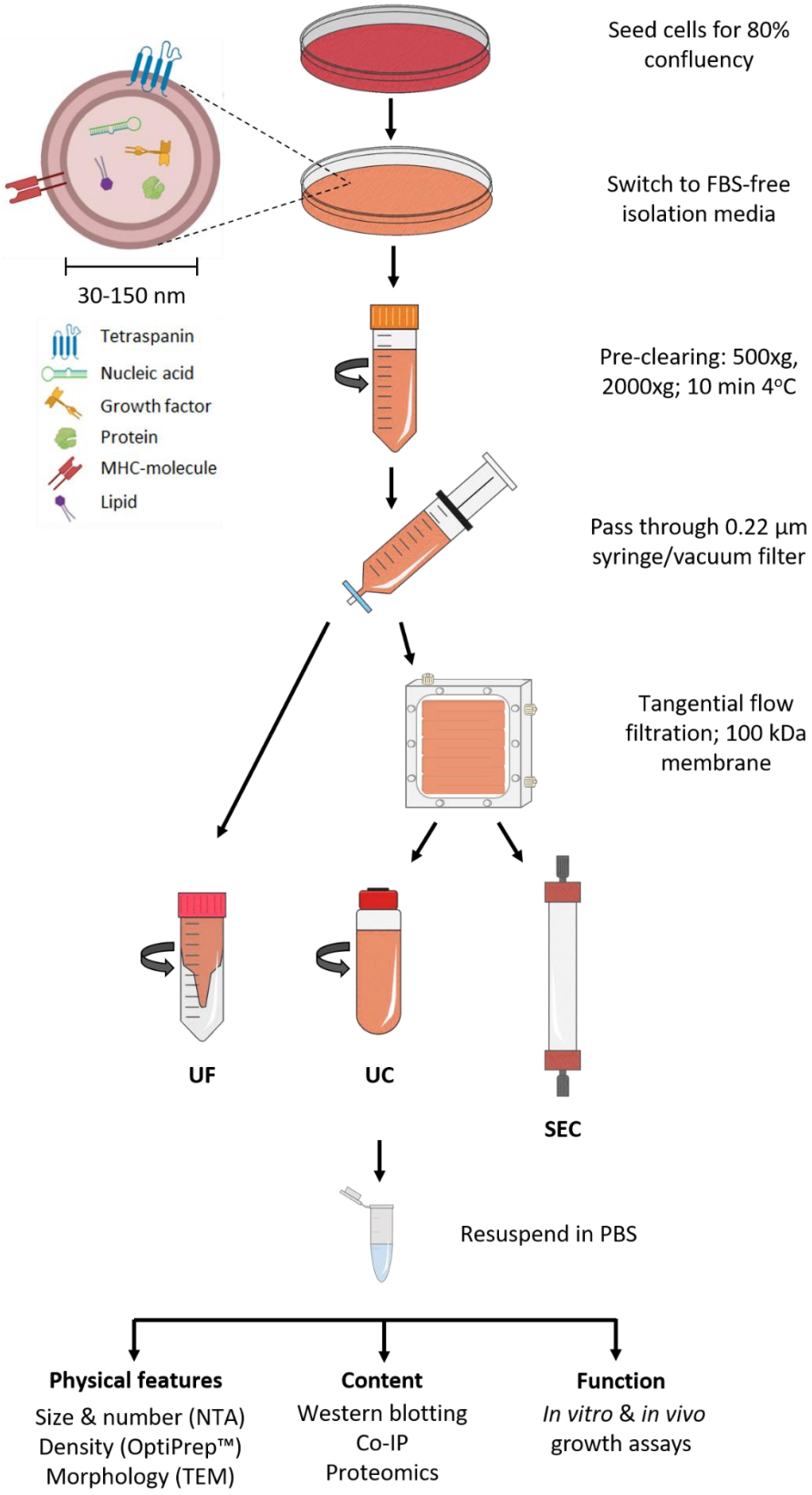



**Figure 2.1** Overview of the main EV isolation techniques. Image adapted from McCormick (2018)

#### 2.3.2.1 Ultrafiltration

Cells were plated as per 2.3.1 using three plates per experimental condition. Following 24-hours of cell growth in the relevant isolation conditions, the media was harvested and pre-cleared by centrifugation to remove whole cells and cell debris (500xg followed by 2000xg, each for 10-minutes at 4$^{o}$C). The supernatant was then syringe filtered through a 0.22 µm pore membrane to eliminate non-vesicular contaminants. Following this, the filtrate was concentrated using 100 kDa Amicon Ultra-15 UF units (Milex®) at 4000xg for 10-minutes at 4$^{o}$C. Finally, the ultrafiltrate was washed with PBS to minimise soluble protein contaminants and concentrated to a final volume of approximately 100 µl, and stored at -80$^{o}$C until further analysis.

#### 2.3.2.2 Ultracentrifugation

Cells were plated as per 2.3.1 using 15 plates per experimental condition and underwent the same pre-clearing spins used for UF-based isolations. Following this, the supernatant was vacuum filtered through a 0.22 µm pore membrane and then concentrated using tangential flow filtration (TFF) with a 100 kDa Vivaflow-50 membrane (Essen Bioscience) to a final volume of approximately 15 ml. The filtrate was then centrifuged at 100,000xg for 2-hours at 4$^{o}$C using a fixed angle Beckman 55.2Ti rotor (Beckman Coulter). Following this, the supernatant was discarded and the EV pellet resuspended in 15 ml of PBS and underwent further centrifugation at 100,000xg for 2-hours. Finally, the supernatant was discarded and the EV pellet resuspended in 100 µl of PBS and stored at -80 $^{o}$C until further analysis.

#### 2.3.2.3 Size exclusion chromatography

Cells were plated as per 2.3.1 using 15 plates per experimental condition and underwent pre-clearing centrifugation, vacuum filtration and concentration using TFF as described in 2.3.2.2. The filtrate then underwent UF at 4000xg for 10 minutes at 4$^{o}$C using a 100 kDa Amicon Ultra-15 UF ultrafiltration unit to a final volume of 1 ml. This was then injected onto

a 24 x 1 cm size exclusion chromatography column containing Sepharose® Fast Flow CL-4B resin, with a pore size of 84 nm (GE Healthcare Life Sciences) set up on an AKTA start purification system (GE Healthcare Life Sciences). The sample was eluted as 1 ml fractions in PBS, which were then combined according to the chromatogram and concentrated using UF to a final volume of 100 µl, which were stored at -80ºC until analysis.

#### 2.3.2.4 qEV column size exclusion chromatography

Cells were plated as per 2.3.1 using 3 plates per experimental condition, and underwent the pre-SEC concentrating stages as described in 2.3.2.3 to a final volume of 500 µl. Plasma samples were cleared of large non-particulate matter by sequential centrifugation at 1500xg followed by 10,000xg each for 10 minutes at 4ºC. EV isolation was undertaken using IZON qEV original 35 nm size exclusion columns as per the manufacturer's protocol, using a new column for each sample. Briefly, following priming of the qEV original column with PBS, 500 µl of EVs isolated from cell culture media or plasma was added to the top filter and allowed to enter the column, after which 10 ml of PBS was added to the top of the column. The first 3 ml represented the void volume, and EVs were eluted in the following 1.5 ml, collected as 3 x 500 µl fractions. EVs were then concentrated using UF to a final volume of approximately 150 µl and stored at -80ºC until further analysis.

### 2.3.3 EV characterisation

Due to the challenges of separating EVs from non-vesicular entities, EVs were characterised according to the International Society for Extracellular Vesicles Minimal Information for Studies of Extracellular Vesicles (MISEV) guidelines for defining EVs (Thery et al. 2018). These cover analysis of physical properties (size, density and morphology) as well as protein content of isolated EVs.

#### 2.3.3.1 EV normalisation

In order to compare changes in the protein content of EVs produced under different experimental conditions, a method of EV normalisation developed by Dr Shih-Jung Fan (PDRA, Goberdhan Group) was used. This is based on the equation for exponential cell growth-

$$\text{Log}(N) = \text{Log}(N0) + Kt$$

Where the increase in growth ($N$) is proportional to the number of cells plated at time zero ($N0$) plus the product of the growth constant (K) and experimental duration ($t$).

The rate of cell growth was determined indirectly using protein content of cells prior to changing from full basal media to the relevant EV-isolation media ($N0$) and then at 24-hours when the media is harvested prior to isolation. Practically, this involved plating an additional three plates at the beginning of an experiment to serve as $N0$ controls, which were then lysed before changing the remaining plates to EV-isolation media. After 24-hours growth, three plates per experimental condition ($N$) were also lysed once the media had been harvested. Average protein content was determined using a BCA protein assay kit (Thermo Fisher Scientific). As time was set at 24-hours, EV normalisation is determined by the ratio of the growth constants between the control ($Ka$) and experimental conditions ($Kb$)-

$$\underline{Ka = \text{Log}(Na) - \text{Log}(N0a)}$$

$$Kb = \text{Log}(Nb) - \text{Log}(N0b)$$

An equal volume of PBS was used to resuspend EVs during all isolation methods, meaning the above ratio could be applied directly to make adjustments for loading during western blot analysis, including protein band quantification, and functional experiments.

#### 2.3.3.2 Nanosight tracking analysis

The NS500 NanoSight® system (Malvern) was used to assess size and number of EVs. Samples underwent a 1/100 – 1/500 dilution in PBS and all measurements were performed using the same settings (detection threshold 5 and camera level 14) with the camera focus adjusted to ensure particles appeared as distinct dots. Image capture occurred during three 30-second video recordings using the script: PRIME, DELAY 7, CAPTURE 30, REPEAT 3. Particle movement was then assessed using NTA software 2.3 (NanoSight® Ltd) to generate graphs plotting EV concentration ($x10^8$ $ml^{-1}$) against particle size (nm).

#### 2.3.3.3 Transmission electron microscopy

TEM was undertaken in collaboration with Dr Errin Johnson (Sir William Dunn School of Pathology, University of Oxford). A 10 µl aliquot of purified EVs (≈0.2 µg/µl) was incubated on a glow discharged 300-mesh 3 mm carbon-coated copper grid (TAAB Laboratories) for 2-minutes. Following this the grid was blotted dry with filter paper and negatively stained with 2% uranyl acetate for 10-seconds. The grid was then blotted and air dried before imaging on a FEI Tecnai T12 transmission electron microscope (FEI UK Ltd) operated at 120 kV with a Gatan Oneview digital camera (Gatan Inc) at 120,000x magnification.

#### 2.3.3.4 Western blot analysis

Cell lysates were prepared by lysis in RIPA buffer supplemented with proteinase and phosphatase inhibitors and centrifuged at 14,000 rpm for 10-minutes at 4°C. Total protein content was measured using a BCA protein assay kit (Pierce, Thermo Scientific). Equal amounts of protein or EVs (based on EV normalisation outlined in 2.3.3.1) were mixed with reduced (containing 5% β-mercaptoethanol, Sigma) or non-reduced 4x Laemmli sample buffer for SDS-PAGE (Bio-Rad) and boiled at 95°C for 10-minutes. Samples were then separated by SDS-PAGE using 10% mini-PROTEAN® gels (Bio-Rad) at 140 V for approximately 1-hour, followed by wet-transfer onto a 0.22 µm pore size Immobilin®-FL

polyvinylidene difluoride (PVDF) membrane (Merck) at 100 V for 1-hour at 4ºC. Membranes were then blocked in 5% BSA (reduced conditions) or 5% skimmed milk (non-reduced) in TBS containing 1% Tween-20 (Sigma) (TBST) for 1-hour, before incubation with primary antibodies (Table 2.1) diluted in the same blocking buffer overnight at 4ºC. The following day membranes underwent three 10-minute TBST washes, followed by probing with the relevant secondary antibody (Table 2.1) for 1-hour at room temperature. The membranes then underwent a further three 20-minute washes with TBST before incubation in clarity solution (Bio-Rad) for 2-minutes and visualisation of protein bands using the ChemiDoc Touch Imaging System (Bio-Rad). Relative band intensities were quantified using ImageJ software (LOCI, University of Wisconsin).

| Technique | Antigen | Molecular weight* (kDa) | Species | Dilution | Company | Cat. no. |
|---|---|---|---|---|---|---|
| **WESTERN BLOTTNG** | 4E-BP1 (total) | 15-20 | Rabbit | 1:1000 | Cell Signaling | 9644S |
| | Albumin | 69 | Rabbit | 1:2000 | Abcam | ab213480 |
| | Annexin 1 | 38 | Rabbit | 1:500 | Cell Signaling | 32934S |
| | Akt (total) | 60 | Rabbit | 1:1000 | Cell Signaling | 9272S |
| | Alix | 96 | Mouse | 1:500 | Abcam | ab117600 |
| | Amphiregulin | 28 | Goat | 1:100 | R&D SYSTEMS | AF262 |
| | Calnexin | 90 | Rabbit | 1:500 | Cell Signaling | 2679S |
| | CD63 | 30-60 | Mouse | 1:500 | Santa Cruz | 556019 |
| | CD81 | 22-26 | Mouse | 1:500 | Santa Cruz | sc-23962 |
| | Caveolin-1 | 21-24 | Rabbit | 1:1000 | Cell Signaling | 3238S |
| | E-cadherin | 135 | Rabbit | 1.1000 | Cell Signaling | 3195S |
| | EEA-1 | 170 | Rabbit | 1:500 | Cell Signaling | 3288S |
| | EGFR (total) | 175 | Rabbit | 1:1000 | Cell Signaling | 4267S |
| | Erk (total) | 42-44 | Rabbit | 1:1000 | Cell Signaling | 4695S |
| | Fibronectin | 285 | Rabbit | 1:1000 | Abcam | ab2413 |
| | Flotillin-2 | 49-58 | Rabbit | 1:500 | Cell Signaling | 3436S |
| | GAPDH | 37 | Rabbit | 1:1000 | Cell Signaling | 2118S |
| | HIF-1$\alpha$ | 120 | Rabbit | 1:500 | Cell Signaling | 36169S |
| | HLA-C | 41 | Rabbit | 1:500 | Abcam | ab193432 |
| | N-cadherin | 110 | Rabbit | 1:1000 | Abcam | ab76057 |

| | | | | | | |
|---|---|---|---|---|---|---|
| | pAkt (S473) | 60 | Rabbit | 1:1000 | Cell Signaling | 4060S |
| | pEGFR (Y1068) | 175 | Rabbit | 1:500 | Cell Signaling | 3777S |
| | pErk (T202/Y204) | 42-44 | Rabbit | 1:1000 | Cell Signaling | 4370S |
| | pS6 (S240/244) | 32 | Rabbit | 1:1000 | Cell Signaling | 5364S |
| | Rab11a | 24 | Mouse | 1:500 | BD Biosciences | 610656 |
| | S6 (total) | 32 | Rabbit | 1:1000 | Cell Signaling | 2217S |
| | Syntenin-1 | 32 | Rabbit | 1:1000 | Abcam | ab133267 |
| | TGN46 | 51 | Rabbit | 1:1000 | Abcam | ab174280 |
| | Transferrin receptor | 84 | Rabbit | 1:500 | Abcam | ab84036 |
| | Tsg101 | 44 | Rabbit | 1:500 | Abcam | ab125011 |
| | α-Tubulin | 50 | Mouse | 1:2000 | Sigma | T6074 |
| | Vimentin | 54 | Rabbit | 1:500 | Abcam | ab92547 |
| | HRP-conj anti-goat IgG | - | Rabbit | 1:1000 | R&D SYSTEMS | HAF017 |
| | HRP-conj anti-mouse IgG | -- | Donkey | 1:10,000 | Promega | W4021 |
| | HRP-conj anti-rabbit IgG | - | Donkey | 1:10,000 | Promega | W4011 |
| **Co-IP** | HLA-C | - | Rabbit | 10 µg | Abcam | ab126722 |
| | Control mouse IgG | - | Rabbit | 10 µg | Cell Signaling | 5415S |
| | Control rabbit IgG | - | Rabbit | 10 µg | Cell Signaling | 2729S |
| | Transferrin receptor | - | Mouse | 10 µg | Abcam | ab1086 |
| | HRP-conj anti- mouse IgG (conformation specific) | -- | Rat | 1:2000 | Abcam | ab131368 |
| | HRP-conj anti-rabbit IgG (conformation specific) | | Mouse | 1:2000 | Cell Signaling | 5127S |

| | | | | | | |
|---|---|---|---|---|---|---|
| **IHC** | CA9 | - | Rabbit | 1:100 | BD Biosciences | M75 |
| | CD31 | - | Mouse | 1:100 | Dako | JC70 |
| | E-cadherin | - | Rabbit | 1:100 | Cell Signaling | 3195S |
| | Fibronectin | - | Rabbit | 1:100 | Abcam | ab2413 |
| | Ki-67 | - | Rabbit | 1:100 | Dako | M7240 |
| | N-cadherin | - | Rabbit | 1:100 | Abcam | ab76057 |
| | pErk (T202/Y204) | - | Rabbit | 1:100 | Cell Signaling | 4370S |
| | Vimentin | - | Rabbit | 1:100 | Abcam | ab92547 |
| | HRP-conj anti-mouse IgG | - | Goat | No dil. required | Dako | P0447 |
| | HRP-conj anti-rabbit IgG | - | Goat | No dil. required | Dako | P0448 |

Table 2.1 List of antibodies used for western blotting, co-immunoprecipitation and immunohistochemistry. Secondary antibodies are listed in rows highlighted in grey. *Denotes observed electrophoretic molecular weight.

#### 2.3.3.5 Optiprep™ density gradient analysis

Using 50 plates of HCT116 cells grown in either glutamine-replete or -depleted media for 24 hours, EVs were isolated using SEC and concentrated to a final volume of 750 µL. Iodixanol (Optiprep™, Sigma Aldrich) density media was prepared with PBS and $ddH_2O$ to generate discontinuous gradients (12%, 18%, 24%, 30% and 36%). EVs were mixed with the 36% Optiprep™ step, which was then added to the bottom of an ultracentrifuge tube, with decreasing Optiprep™ steps carefully layered on top to complete the gradient. These then underwent ultracentrifugation at 120,000xg for 15 hours at 4$^{o}$C using a SW41 Ti swinging-bucket rotor (Bechman Coulter). Starting from the top of the gradient, 12 x 1 ml fractions were then collected and weighted in order to calculate each fraction density. Each fraction was then concentrated using 100 kDa Amicon Ultra-4 filter units (4000xg at 4$^{o}$C for 4-10 minutes) to a final volume of approximately 70 µl and analysed using western blotting.

#### 2.3.3.6 Proteinase-K protection assay

Using 30-plates of HCT116 cells grown in glutamine-depleted media for 24-hours, EVs were isolated using SEC and resuspended in 200 µl of Dulbecco's Phosphate Buffered Saline (DPBS, Thermo Fisher Scientific). Equal volume of EVs were then mixed with either: 0.2 µl Proteinase-K (Thermo Fisher Scientific), 50 µl of 0.1% Triton-X 100 (Sigma) or both Proteinase-K and Triton-X 100 and along with an untreated sample of EVs were incubated for 1-hour at 37$^{o}$C. Next 2.5 µl of PMSF protease inhibitor (Thermo Fisher Scientific) was added to each sample and incubated for 10-minutes at 65$^{o}$C. Following this the samples were eluted in 7 µl of 4x Laemmli sample buffer and processed for western blotting.

#### 2.3.3.7 Co-immunoprecipitation

Using 30-plates of HCT116 cells grown in glutamine-depleted media for 24-hours, EVs were isolated using SEC and resuspended in 350 µl of PBS. Co-immunoprecipitation was performed using 50 µl of Protein-A magnetic Dynabeads™ (Invitrogen) per reaction. The beads were first washed in PBS, and then combined with 10 µg of the relevant primary antibody (Table 2.1) in 100 µl of PBS and incubated in a rotating mixer for 1-hour at 4$^{o}$C to allow conjugation. Following antibody-conjugation the beads were washed in PBS with 0.02% Tween-20, and plain PBS before overnight incubation with 140 µl of EVs on a rotating mixer at 4$^{o}$C. The next day the supernatant was aspirated and kept for analysis, and the beads underwent three PBS washes before elution in 20 µl of 4x Laemmli sample buffer for western blotting.

## 2.4 Functional analysis of CRC EVs *in vitro* and *in vivo*

### 2.4.1 Proliferation assays

Proliferation assays were undertaken in a 96-well plate with 8 technical repeats per experimental condition. HCT116 and SW480 cells were plated at a density of 2000 cells per well, while Caco-2 and SW620 cells were plated at a density of 4000 cells per well in

appropriate cell specific media. Analysis of growth was delayed by 12 hours to allow the cells to attach. Proliferation was measured using the IncuCyte® ZOOM Life Cell Imager, taking 4 phase-contrast images per well every 6 hours for 5 days. The IncuCyte® analysis software was used to detect cell edges to create a confluency mask, which was used to determine cell growth.

#### 2.4.1.1 Determining serum assay conditions

In order to determine appropriate serum-stressed conditions to assess cell growth, cells were plated and analysed as per 2.4.1 in their basal media with reducing FBS concentrations (5%, 2%, 1%, 0.5%, 0.25% and 0%).

#### 2.4.1.2 EV-dose response assays

Prior to plating, cells were incubated with fresh SEC-isolated EVs in reduced serum media (1% serum for HCT116 cells and 0.25% serum for Caco-2, SW480 and SW620 cells) for 30 minutes under standard culture conditions. Number of EVs were quantified using NTA, and added as number of EVs per cell (range 1000 – 16,000 EVs per cell). Following incubation, cells were plated and analysed as per 2.4.

#### 2.4.1.3 EV-depletion assays

##### 2.4.1.3.1 EV-pelleting assay

Following SEC, the fractions corresponding to the EV peak were combined and half the volume (1.5 ml) was concentrated using UF to a final volume of approximately 60 µl, while the remaining half underwent UC at 100,000xg for 2-hours at 4$^{o}$C using a fixed angle Beckman 55.2Ti rotor to pellet the EVs. The EV-depleted supernatant then underwent UF to a final volume of 60 µl. Each sample was then characterised using NTA and western blotting before testing their functional effect on proliferation as per 2.4.1 using an EV dose of 4000 EVs per cell.

#### 2.4.1.3.2 CHMP5 knockdown

As previously described by Fan et al. (2016), stably transduced HCT116 clones carrying IPTG-inducible lentiviral constructs that express a non-targeting (shNT, CAACAAGATGAAGAGCACCAA, SHC 202, Sigma) or CHMP5 targeting (shCHMP5, CTGGATGAAGATGATTTAGAA, Sigma, TRCN0000158654) shRNA were generated by Dr Shih-Jun Fan (PDRA, Goberdhan Group). Briefly, following generation of clones IPTG (100 µM, Sigma) was used to induce shRNA transcription. After three days, cells were plated as per 2.3.1 and EVs were isolated by SEC. EVs were quantified using NTA before testing their functional effect on proliferation as per 2.4.1 using an EV dose of 4000 EVs per cell.

### 2.4.1.4 Amphiregulin neutralisation assay

Amphiregulin (AREG) neutralising antibody experiments were undertaken in 96-well plates using 2000 HCT116 cells or 4000 Caco-2 cells treated with 4000 fresh SEC-isolated EVs per cell. Prior to mixing with recipient cells the EVs underwent incubation with either goat anti-AREG (R&D SYSTEMS #AF262) or a control goat anti-IgG (R&D SYSTEMS #AB-108-C) at a concentration of 4 µg/ml (Raimondo et al. 2019), in either McCoys 5A modified medium containing 1% FBS for HCT116 cells or EMEM containing 0.25% FBS for Caco-2 cells, for 2 hours at 37$^{o}$C. The EV-antibody mixture was then added to the recipient cells, also in reduced serum media, and allowed to incubate for a further 30 minutes prior to plating and analysis as per 2.4.1.

### 2.4.1.5 EGFR-ERK signalling assay

To assess EGFR and ERK activation upon EV treatment, HCT116 or Caco-2 cells were plated in 6-well plates in full basal media at a density of 400,000 cells per well. After 24 hours the cells were serum starved (0% FBS) overnight. The following day, freshly prepared EVs isolated using SEC were quantified using NTA and added at a concentration of 4000 EVs per cell. Following incubation (5 minutes for EGFR activation; 15 minutes for ERK

activation) cell lysates were collected for analysis by western blotting. In order to assess the role of EV-associated AREG in regulating changes in EGFR-Erk signalling, identical assays were performed by incubating EVs with 4 µg/ml of either goat anti-AREG or control goat anti-IgG in 0% serum media as described in 2.4.1.4 prior to being added to recipient cells.

#### 2.4.1.6 Cetuximab and EGFR kinase inhibitor assays

Cetuximab sensitivity was measured by adding increasing doses (1-30 µg/ml) of research grade cetuximab (R&D SYSTEMS #MAB9577) to HCT116 or Caco-2 cells in full or reduced serum media and measuring growth as per 2.4.1 or by generating cell lysates to measure EGFR-ERK signalling via western blotting. Subsequent cetuximab-EV co-treatment assays were performed in 96-well plates using Caco-2 recipient cells (4000 cells per well, 4000 EVs per cell) at a cetuximab dose of 30 µg/ml, with or without prior incubation with the AREG neutralising antibody. EGFR kinase inhibitor assays were undertaken by adding the inhibitors (AG1478 hydrochloride, TOCRIS #1276, or BMS599626, TOCRIS #5022) at a dose of 2.5 mM to recipient cells at the same time as freshly prepared EVs (4000 cells per well, 4000 EVs per cell) before plating and analysis as per 2.4.1.

#### 2.4.1.7 Recombinant amphiregulin assay

Caco-2 recipient cells (4000 per well) were incubated for 30 minutes with either freshly prepared EVs (4000 per cell) or recombinant human AREG protein (0.03-300 ng/ml, R&D SYSTEMS #262-AR-100) in reduced (0.25% FBS) media before plating in a 96-well plate and analysed as per 2.4.1.

#### 2.4.1.8 ELISA measurement of amphiregulin concentration

EVs were lysed in Cell Lysis Buffer 2 (R&D SYSTEMS) supplemented with protease inhibitors and incubated at room temperature for 30 minutes. EV-associated AREG was

measured using Quantikine ELISA-Human Amphiregulin Immunoassay (R&D SYSTEMS) according to the manufacturer's instructions.

### 2.4.2 Chick embryo HCT116 xenograft model

Chick embryo experiments were undertaken in collaboration with Dr Yaiza García Ibáñez, (Piero Crespo's group, Instituto de Biomedicina y Biotecnología, IBBTEC de Cantabria, Santander, Spain) during a visit made to IBBTEC in May 2019. This work was covered by a UK Home Office Personal License, category B and C to undertake relevant work in the UK and EU (issued February 2016).

#### 2.4.2.1 Tumour-EV grafts

Fertilised chick eggs were incubated in a rotating incubator at 37$^{o}$C and 65% humidity for nine days. On day nine, a window was generated to access the chorioallantoic membrane (CAM) using the protocol described by (Crespo and Casar 2016). Briefly, a 30-gauge needle was used to puncture a hole in the egg's air sack located at the blunt end of the egg. The allantoic vein was located using a light source, and a further hole made close to this using a Dremel® 100 rotary tool (Dremel®), taking care to remove the hard surface of the shell, while leaving the inner membrane intact as this is where the CAM attaches. A hooked 20-gauge needle was used to make a small hole in the inner shell membrane, and the CAM was "dropped" from the shell's hard membrane by application of a mild vacuum over the hole in the air sack. The Dremel® tool was then used to make the window large enough to access the CAM to inject tumour cell grafts.

Tumour-EV grafts consisted of 500,000 HCT116 cells and 4000 SEC-isolated EVs per cell were mixed in McCoys 5A modifiend medium containing 1% FBS and incubated for 30 minutes at 37$^{o}$C. Following this, the cell-EV suspension was grafted onto the CAM at a bifurcation in close proximity to the allantoic vein. Tumour-EV grafts were also generated

following pre-incubation of the EVs with 4 µg/ml of either goat anti-AREG or control goat anti-IgG in 1% serum media as described in 2.4.1.4. The window was then sealed with laboratory tape, and after 10 minutes the eggs were returned to a stationary incubator for 5 days. After 5 days, the tumours were excised and weighted, and sections of the distal CAM (area diametrically opposite to the CAM window), lungs and liver were harvested for DNA extraction or to be embedded in formalin fixed paraffin embedded (FFPE) blocks for histological analysis.

#### 2.4.2.2 Quantitative real-time PCR

Genomic DNA was extracted using the Gentra PureGene Tissue Kit (Qiagen) as per the manufacturer's instructions and quantified using the NanoDrop™ 2000c Spectrophotometer (Thermo Fisher Scientific). In order to detect human (HCT116) genetic material, quantitative real-time PCR (qRT-PCR) was undertaken using Power SYBR Green Master Mix (Applied Biosystems), with 30 ng of genomic DNA and human *Alu* sequence (299) primers (forward sequence: ACGCCTGTAATCCCAGGACTT; reverse sequence: TCGCCCAGGTGGCTGGGGCA). qRT-PCR was monitored using a StepOne™ Real-Time PCR console (Applied Biosystems). The number of metastasised human cells was determined by measurement of the triplicate $C_t$ values against a standard curve of DNA extracted from 100-100,000 HCT116 cells.

#### 2.4.2.3 Immunohistochemistry

Immunohistochemistry was undertaken in collaboration with Dr Esther Bridges (Adrian Harris's group, Weatherall Institute of Molecular Medicine, University of Oxford). FFPE blocks of the chick embryo xenograft tumours were sectioned onto positively charged slides (Vector) and a standard haematoxylin and eosin protocol was undertaken to assess morphology and necrosis. Following dewaxing and antigen retrieval at pH 6, immunohistochemistry staining was undertaken using the FLEX staining kit (Agilent). Endogenous peroxidase activity was blocked before staining with antibodies listed in Table

2.1 for 1 hour at 22°C. Slides were then incubated with the appropriate HRP-conjugated secondary antibody for 30 minutes at room temperature. Following this, slides were washed in FLEX Wash Buffer (Agilent) and 3,3'-Diaminobenzidine (Agilent) for 10 minutes. The slides were counterstained by immersing in FLEX-hematoxylin solution (Agilent) for 5 minutes, washed and air-dried before mounting using DEPEX Mounting Medium (Sigma). Secondary-only control staining was performed, and was consistently negative. Protein expression was quantified on whole sections using the Visiopharm® Integrator System (Visiopharm). The HDAB-DAB colour deconvolution band was used to detect positively stained cells. Threshold classification was used to identify necrotic and viable regions and to identify the number of positive-staining cells. Appropriate threshold levels were checked against control xenograft staining before being set and the xenografts from all groups were then analysed in the same way.

### 2.4.3 Migration & invasion assays using HCT116 cells

#### 2.4.3.1 Scratch-wound assay

HCT116 cells were plated at a density of 50,000 cells per well in full basal media in 96-well ImageLock plates (Essen Bioscience) at incubated overnight to reach 100% confluency. Following this, wound scratches were created using the 96-pin IncuCyte® WoundMaker tool (Essen Bioscience). The media was then aspirated, washed with PBS to remove detached cells, and replaced with reduced 1% FBS media mixed with fresh SEC-isolated EVs quantified with NTA at a concentration of 4000 EVs per cell. Migration was measured using the IncuCyte® ZOOM Life Cell Imager, taking 2 phase-contrast images per well every 2 hours for 48 hours. The IncuCyte® analysis software was used to detect wound edges to generate an initial scratch-wound mask, which was used to measure migration.

#### 2.4.3.2 Transwell migration and invasion assays

At a density of 50,000 cells per well, HCT116 cells were incubated with 4000 fresh EVs per cell in 0% serum media for 30 minutes at 37ºC. Following this, the HCT116-EV mixture was added to the top chamber within a 12-well Transwell plate (pore size 1 µm, Corning Life Sciences), with the bottom chamber containing full 10% serum media and then incubated under standard conditions. Invasion was assessed with the addition of 100 µl of a diluted Growth Factor Reduced Matrigel® Matrix (Corning Life Sciences) lining to the top side of the upper chamber (Matrigel® diluted in two parts serum free media). AREG neutralising assays for both migration and invasion were also undertaken by incubating EVs with 4 µg/ml of either goat anti-AREG or control goat anti-IgG in 0% serum media as described in 2.4.1.4 prior to being added to recipient cells. After 24 or 48 hours, migrated cells on the bottom side of the upper chamber were fixed with 4% paraformaldehyde (Sigma) for 10 minutes at room temperature, and then permeabilised with 0.25% Triton-X 100 for 15 minutes at room temperature. Non-migrated cells were removed from the top side of the membrane with a cotton swab, followed by staining of fixed cells with Hoechst (1:500 in BSA, Thermo Fisher Scientific). Images were captured using an inverted microscope at 5 random fields per well and analysed using ImageJ.

#### 2.4.3.3 Protein expression assays

To assess protein expression following EV treatment, HCT116 cells were plated in a 6-well plate in full basal media at a density of 400,000 cells per well. The media was changed after 24-hours to reduced 1% FBS media mixed with fresh SEC-isolated EVs quantified with NTA at a concentration of 4000 EVs per cell. The cells were incubated in this media for 72 hours, after which cell lysates were generated for western blotting.

## 2.5 EV cargo analysis

### 2.5.1 miRNA cargo analysis

EVs isolated from cell culture media using standard SEC, as described in 2.3.2.3, and from plasma using qEVoriginal columns as described in 2.3.2.4. microRNA (miRNA) was extracted using the miRNeasy Micro Kit (Qiagen) according to the manufacturer's protocol, and quantified using the NanoDrop™ ND-1000 Spectrophotometer (New Brunswick). miRNA analysis was undertaken by UK Bioinformatics Ltd, whereby miRNA representation was determined using the Bioanalyser (Agilent) and the GeneChip™ miRNA 4.0 array (ThermoFisher Scientific) as per the manufacturer's guidelines.

### 2.5.2 miRNA bioinformatic analysis

The miRNA analysis was undertaken in collaboration with Ryan Carter and Alessandro Barberis (Francesca Buffa's group, Department of Oncology, University of Oxford). Data was analysed in R (version 4.1) according to the protocol outlined by (Klaus and Reisenauer 2016) using the "maEndToEnd" Bioconductor package. Enrichment analysis was undertaken to predict the function and gene targets of miRNAs using the miRDB (Y. Chen and Wang 2020), and miRPathDB (Kehl et al. 2020) online databases.

## 2.6 Statistical analysis

The Shapiro-Wilk test was used to check whether datasets followed a normal distribution. Parametric data was analysed using a two-tailed unpaired Student's t-test, while the Kruskal-Wallis or Mann-Whitney U test was used for non-parametric data. Two-way analysis of variance (ANOVA) was used for multiple group comparisons. All data is presented as mean ± SD. A statistically significant difference was defined as *$p<0.05$, **$p<0.01$ or ***$p<0.001$. Data analysis was performed using GraphPad Prism version 8.3.1 (GraphPad Software, Inc).

# CHAPTER 3

## RESULTS

# 3. Validation of SEC to isolate and study EV heterogeneity in CRC cell lines

## 3.1 Introduction

### 3.1.1 EV isolation methods

The Goberdhan Group studies the relationship between the tumour microenvironment and EV biogenesis in CRC cells. They have recently shown that nutrient depletion leads to reduced signalling through the rapamycin-resistant PAT4-mTORC1 signalling axis, leading to a switch in EV biogenesis pathways. This EV switch is characterised by a reduction in exosomes secreted via the classical Rab7-CD63 labelled late endosomal pathway, and an increase in the biogenesis of EVs within the recycling endosome, leading to the secretion of Rab11a-exosomes (Fan et al. 2020; McCormick et al. 2020). The study of switched EVs may reveal novel mechanisms by which CRC cells adapt to microenvironmental stress, but in order to test this hypothesis, reliable and pure methods of EV isolation are required.

The term EV refers to two distinct types of vesicle: exosomes and microvesicles, which are distinguished by their different biogenesis pathways. Exosomes are generated through the endosomal pathway as ILVs within the late endosomal MVB, which are secreted upon fusion with the plasma membrane, whereas microvesicles are shed directly from the plasma membrane (Veziroglu and Mias 2020). A method of isolating purified samples of exosomes or microvesicles that is based on these different biogenesis pathways does not currently exist, meaning instead that isolation of EVs is based upon physical properties, including size and density. As the physical properties of EV subtypes overlap, these different isolation methods produce preparations of heterogeneous EVs (Gardiner et al. 2016). The three main methods used to isolate EVs from cell culture media are: ultrafiltration (UF), ultracentrifugation (UC) and size exclusion chromatography (SEC). All three methods rely on the same prior centrifugation and filtration steps to remove particles over 220 nm. While

each method has its own strengths and limitations, the choice of isolation method should be informed by the downstream research question or application.

#### 3.1.1.1 Ultrafiltration

UF is the simplest isolation method and is based on EV size. During this method, separation of vesicles by the use of membranes with a specific pore-diameters (10-100 kDa) is achieved through high-speed centrifugation, and often sequential rounds of UF are required to ensure maximal elimination of non-vesicular contaminants and to concentrate the sample. This method is often combined with the other EV isolation methods as a means of concentrating samples prior to or following isolation (Konoshenko et al. 2018). While in theory it is possible to vary the pore size to isolate specific EV subtypes, the recovery of vesicles is also dependent on the type of membrane used within the filter. Cellulose-based membranes with a pore size of 10 kDa are the most efficient, whereas recovery rates of less than 40% observed with other types of filter (Vergauwen et al. 2017). When used as a method of isolation by itself, UF is associated with high levels of contamination, mainly due to the formation of protein aggregates that are unable to pass through the UF membrane. Furthermore, the UF membrane acts as a binding surface for EVs, which also form aggregates and cause pore blockage (Sidhom et al. 2020). These factors reduce the purity of isolated EVs. In particular, when compared with UC, UF results in suboptimal RNA (including miRNA) quality (Alvarez et al. 2012). However, despite these limitations, and due to its speed, UF is an effective technique to use during initial EV characterisations, or to assess the potential impact of a treatment on EV cargo, which can then be validated using either UC or SEC.

#### 3.1.1.2 Ultracentrifugation

UC is the most widely used method to isolate EVs (Gardiner et al. 2016), and was the method used during the initial work that was undertaken to characterise the EV switch in HCT116 CRC cells. The most common protocol involves differential UC (dUC), whereby

different EV subtypes have been shown to pellet at different centrifugal forces. For example, large EVs (up to 1 μm, including apoptotic bodies) are pelleted at 2000 x g, other microvesicles at 10,000-20,000 x g and exosomes at forces of 100,000-200,000 x g (Szatanek et al. 2015). Studies characterising the EVs pelleted at these differential speeds have shown that ESCRT proteins and tetraspanins are enriched within the exosome pellet, but not the microvesicular pellet (Willms et al. 2018). EV yield following UC can vary considerably, and is closely related to several variables including: acceleration, rotor type (swinging bucket or fixed angle), sample viscosity and time (Konoshenko et al. 2018). While UC enables EV enrichment, co-sedimentation of non-vesicular contaminants is known to occur, which threatens sample purity (Thery et al. 2006). This limitation has been party addressed by the use of density gradient UC. This method separates particles based upon their post-centrifugation position in a density gradient of sucrose or iodixanol. Particle migration is influenced by size, shape and density, meaning membrane-bound structures containing lipids will float towards the top of the gradient, whereas protein aggregates will sediment within the bottom of the gradient (P. Li et al. 2017a). Due to this, it is often used as a method in its own right to help characterise EVs following their isolation by an alternative method. Density gradient UC has been used successfully to study exosome heterogeneity, identifying subpopulations of vesicles within the exosomal size range (Jeppesen et al. 2019). However, as with dUC this method still relies UC speeds that are associated with high sheer forces that lead to aggregation, morphological disruption and even EV rupture (Linares et al. 2015; Sidhom et al. 2020). Furthermore, high levels of inter-user and experimental variability are common (Torres Crigna et al. 2021). This is a particular issue encountered when using dUC to isolate switched EVs, which often led to an inability to detect Rab11a. Collectively, these factors prohibit the subsequent functional analysis of switched EVs, which is dependent on purified samples of intact vesicles.

#### 3.1.1.3 Size exclusion chromatography

While UC is the method most commonly used to isolate EVs, there has been a gradual move away from this technique, most likely due to technical advancements in other methods, particularly SEC, which overcome most of the UC-specific limitations (Boing et al. 2014; Gardiner et al. 2016). During SEC, EVs are separated based upon size, which effects their rate of migration through a column containing a tightly packed porous resin. The resin contains beads with a defined pore size, such that particles that can enter the beads will have a longer passage time through the column. Following the various pre-clearing and filtration stages, EVs represent the largest remaining component within the sample and are too big to enter the beads. Therefore, following injection onto a SEC column, the EVs elute ahead of the remaining protein present within the sample, producing a highly purified sample of functionally intact vesicles (Mol et al. 2017). However, the high purity that is provided by SEC can come at the cost of overall yield, particularly from cell culture media where a large amount of starting material is often required (Guerreiro et al. 2018), although combining SEC with UF in order to concentrate the eluted EVs has been shown to address this limitation (Nordin et al. 2015). In particular, RNA yield is known to be impacted, although this is more of an issue when isolating EVs from plasma or serum, and should be balanced alongside the fact that it can be reliably associated with EVs as opposed to representing cell-free nucleic acids (Buschmann et al. 2018). Unlike UC based methods, SEC is passive, which produces highly reproducible results (Konoshenko et al. 2018). Moreover, various adaptations to the SEC platform have enabled the isolation of purified EVs from a range of biological fluids, including: plasma, serum, milk, urine, seminal fluid, saliva, cerebrospinal fluid and synovial fluid (Sidhom et al. 2020).

### 3.1.2 The Minimal Information for Studies of Extracellular Vesicles (MISEV 2018) guidelines

The realisation that EVs are important mediators of intercellular signalling in normal physiology and many disease processes has led to a rapid rise in the number of studies undergoing peer review and publication. This includes publications in high-impact journals

that propose exciting functional roles of EVs. However, different EV isolation methods alter the resultant EV preparations, and furthermore, it is technically challenging to obtain highly purified samples that are free from non-vesicular contaminants. Therefore, without clear recommendations there is a danger of incorrectly attributing biological function to EVs, or specific EV subtypes, and experts within the field have raised concern over major conclusions not being supported by appropriate methods to accurately characterise isolated EVs and validate their supposed roles. This is particularly true of the term exosome, which is often inappropriately used to describe any EV subtype (Lotvall et al. 2014). Therefore, based on expert consensus, the International Society for Extracellular Vesicles (ISEV) have developed a comprehensive set of minimum reporting guidelines, known as the Minimal Information for Studies of Extracellular Vesicles (MISEV 2018) guidelines (summarised in Table 3.1) (Thery et al. 2018). By providing editors and researchers with clear recommendations, the primary aim of these guidelines is to promote reliability and reproducibility of published EV results.

| Minimal information for studies of extracellular vesicles (MISEV 2018) guidelines |
|---|
| **EV characterisation-** |
| *a) General characterisation of content should include-*<br>i. At least three positive EV protein markers, including at least one-<br>• transmembrane/lipid-bound protein<br>• cytosolic protein<br>ii. At least one negative EV marker |
| *b) Characterisation of single vesicles, using two different techniques-*<br>i. Electron / atomic force microscopy<br>ii. Single particle tracking<br>iii. Density gradient analysis |
| **Functional studies should include-** |
| *a) Dose-response studies*<br>*b) Suitable negative controls to rule out influence of serum components*<br>*c) Assays to demonstrate activity is intrinsic to EVs, including-*<br>i. EV depletion to remove activity, or-<br>ii. EV/cell labelling |

**Table 3.1** Overview of the MISEV guidelines (Thery et al. 2018).

As the biophysical properties of different EV subtypes overlap, the MISEV 2018 guidelines mandate a multi-technique approach to characterising EV preparations, including an assessment of EV size, morphology and content. They also provide a useful tool to assist with the design of functional assays. Therefore, throughout this thesis adherence to the MISEV 2018 guidelines will be maintained, and where possible supplemented with additional techniques to validate specific findings.

### 3.1.3 Aims and objectives

As stated, the EV switch was initially characterised in EVs isolated using UC. This method is limited by the presence of non-vesicular impurities and EV rupture (Sidhom et al. 2020;

Thery et al. 2006), as well as high inter-user and experimental variability (Torres Crigna et al. 2021). SEC has been promoted as a method to overcome these limitations. Therefore, the central aim of this chapter was to investigate whether SEC can be used to isolate highly purified EV preparations from CRC cells exposed to microenvironmental stress. If validated, this will enable the comparative analysis of the downstream functional roles of switched EVs to be investigated within recipient cells. The specific objectives were-

i. To use the recommendations outlined in the MISEV 2018 guidelines to determine whether SEC can be used to isolate EVs, and characterise the EV switch, initially in HCT116 cells.
ii. To investigate whether other microenvironmental factors known to influence mTORC1 signalling also induce EV switching in HCT116 CRC cells.
iii. To investigate whether microenvironmental stress also induces the biogenesis and secretion of Rab11a-exosomes in other CRC cell lines.

## 3.2 Results

### 3.2.1 Validation of SEC to study EV heterogeneity in HCT116 CRC cells

In order to determine whether SEC could be used to isolate EVs from HCT116 cells, prepared media was injected onto a column containing Sepharose® Fast Flow CL-4B resin with a pore size of 84 nm and 30 x 1 mL fractions collected. The resulting chromatogram (Figure 3.1A) shows an initial UV peak, suggested to correspond to isolated EVs within the exosome size-range (30-150 nm), followed by a large distinct protein peak. The fractions corresponding to the EV peak (fractions 2-5) were combined, and western blot analysis was used to assess sample purity by comparing known EV-enriched proteins in the EV sample to those in whole cell lysate (Figure 3.1B). Reassuringly, the combined fractions were enriched in the membrane bound EV markers CD63, CD81, and contained proteins involved in EV biogenesis and secretion (Alix, Tsg101 and Syn-1). Co-enrichment of CD63 and CD81 alongside CD9 (also detected but not shown here) is indicative of preparations

enriched in EVs with a size of less than 100 nm, which includes exosomes (Kowal et al. 2016). Importantly, early endosomal marker EEA1, the trans-Golgi network integral membrane protein TGN46 and endoplasmic reticulum marker calnexin were not detected within the EV preparation, supporting the purity of the sample, and absence of contaminating proteins.

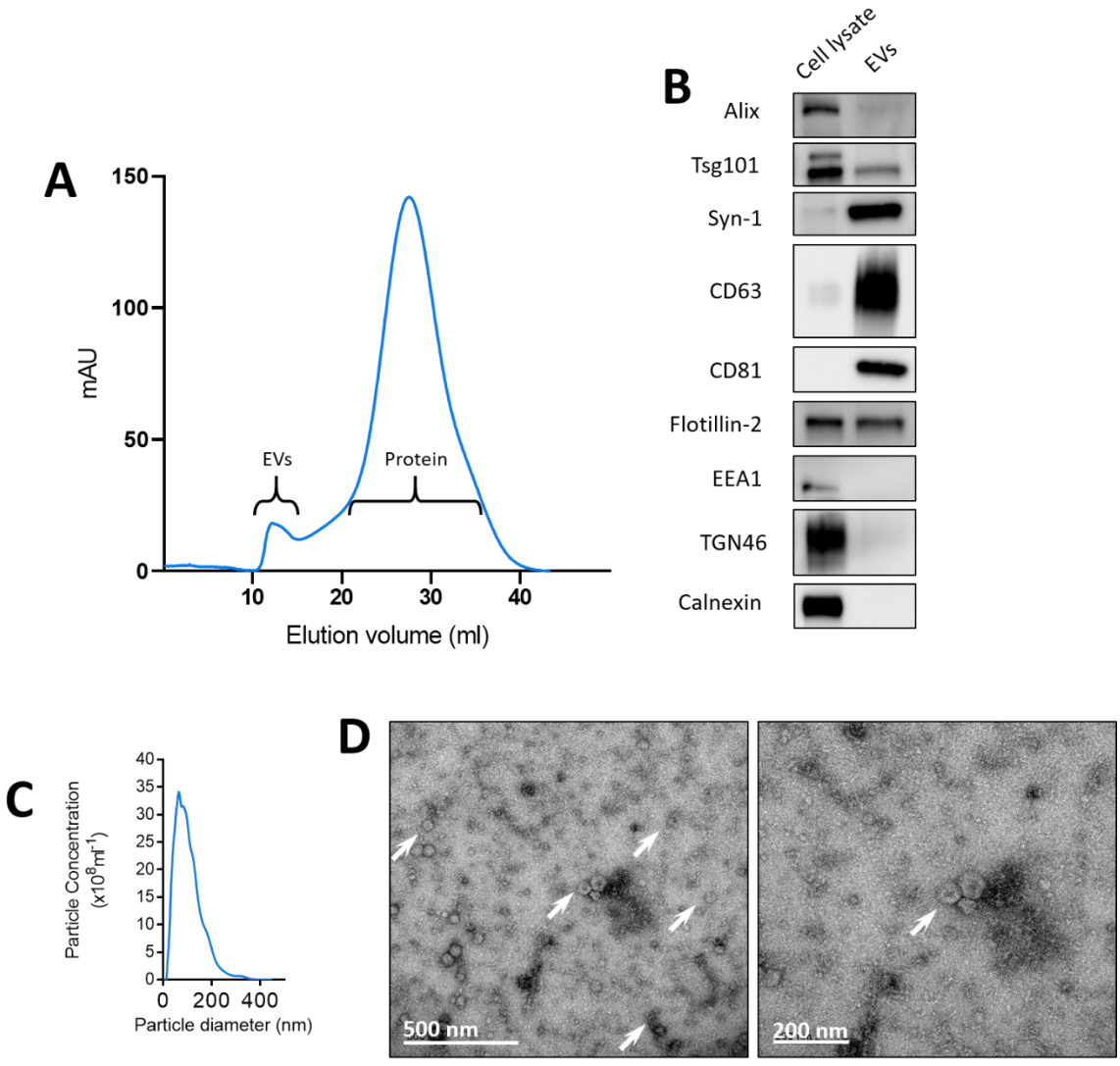



**Figure 3.1** SEC can be used to isolate EVs that exhibit the characteristics of exosomes. (A) Cell culture media (devoid of FBS and instead supplemented with ITS) was harvested from HCT116 CRC cells and injected onto a SEC column. The resulting chromatogram shows clear separation between the initial EV peak and subsequent protein peak. (B) Western blot comparing SEC isolated EVs against an equivalent amount of protein from the HCT116 secreting cells. EVs are enriched in tetraspanins (CD63 and CD81), including ESCRT accessory proteins (Syn-1), but devoid of intracellular markers associated with the endolysosomal pathway (EEA1, TGN46 and calnexin). (C) NTA profile of isolated EVs, showing a median particle size of 105 nm. (D) TEM images of isolated vesicles demonstrating the classic “cup” shape morphology of EVs.

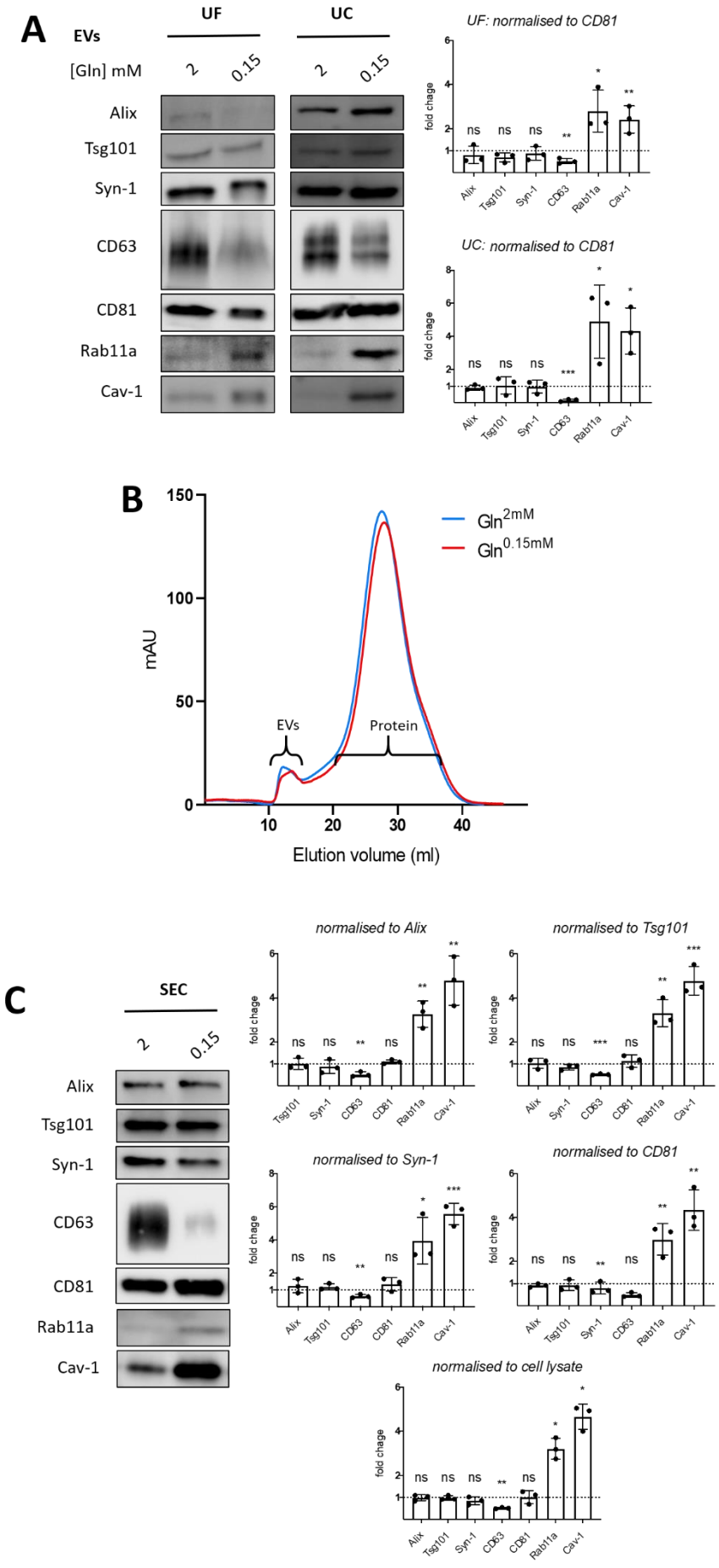
Further evidence for the purity of the SEC isolated EVs is provided by NTA (Figure 3.1C) and TEM (Figure 3.1D). NTA revealed a major peak of isolated vesicles with an average size of 105 ± 57 nm, consistent with the NTA profiles from UF and UC-isolated EVs (data not shown; (Fan et al. 2020) and within the exosome size range. Images acquired by TEM demonstrate the classical “cup” shape morphology of exosomes, and within the 30 – 150 nm size range. Furthermore, the images (Figure 3.1D) show only a low amount of contaminating particles and are completely devoid of particles, including vesicles, measuring over 200 nm, which typically includes apoptotic bodies and liposomes.

Next, SEC was undertaken to determine whether it could be used to study the EV switch. Consistent with UF and UC (Figure 3.2Ai-ii), EVs isolated using SEC from HCT116 cells grown in glutamine-replete and -depleted conditions for 24 hours have similar chromatogram profiles (Figure 3.2B) and clearly demonstrate the EV switch signature (Figure 3.2C). The method for comparing protein expression in EVs isolated under different conditions is complex and controversial. EV preparations contain a complex mixture of microvesicles, exosomes and protein aggregates (Jeppesen et al. 2019), and no specific protein is known to evenly distribute between different EV subtypes. Moreover, exposing cells to different experimental conditions is likely to alter the balance of EVs isolated downstream in a way that cannot be understood by measuring a single protein. Previously, CD81 was selected as the loading control to normalise protein express in EVs isolated from different conditions, as it had been shown to denote a broad population of tetraspanin-labelled EVs (Kowal et al. 2016). However, pulldown experiments undertaken by Dr Shih-Jung Fan (PDRA, Goberdhan Group) have shown that most Rab11a-labelled exosomes are not consistently associated with CD81 (Fan et al. 2020).

Therefore, the initial analysis included normalisation using the other EV markers (Alix, Tsg101, Syn-1 and CD81) that all appear to be unchanged following 24 hours of glutamine

depletion. While the EV switch signature was maintained at statistical significance regardless of the protein used for normalisation there was a considerable variability in the fold changes observed for CD63, Rab11a and Cav-1. When analysing Rab11a, the increase ranged from a 3.1 – 5.5 fold change when Syn-1 was used for normalisation, compared to a 2.2 – 3.3 fold change when using CD81. Similarly, for Cav-1 the increase ranged from 2.9 – 5.8 fold change when Alix was used for normalisation, compared to 4.3 – 5.5 fold change when using Tsg101. This variability highlights the fact that the different proteins are unlikely to be evenly distributed between non-switched and switched EVs.

An alternative method for loading EVs is based on the cell number or protein mass of the EV secreting cells (normalisation to cell lysate). Using this method, EVs isolated from cells of an equivalent protein mass are compared. This method has been promoted by several leaders in the EV field (Baietti et al. 2012), and is particularly useful when comparing EVs secreted from the same cell line. When normalising to total cell lysate, there was a 3.2 ± 0.5 ($p=0.03$) and a 4.6 ± 0.6 ($p=0.03$) fold average increase in Rab11a and Cav-1 respectively, and a 1.9 ± 0.1 ($p=0.005$) fold decrease in CD63, while Alix, Tsg101 and Syn-1 expression was broadly equal between conditions. Consequently, this method for normalising protein content in EVs is used in all subsequent analysis.


A
EVs
UF
UC
[Gln] mM
2
0.15
2
0.15
Alix
Tsg101
Syn-1
CD63
CD81
Rab11a
Cav-1
UF: normalised to CD81
UC: normalised to CD81
fold chage
ns
ns
ns
**
*
**
***
*
*
Alix
Tsg101
Syn-1
CD63
Rab11a
Cav-1
B
150
100
50
0
mAU
Gln2mM
Gln0.15mM
EVs
Protein
10
20
30
40
Elution volume (ml)
C
SEC
2
0.15
Alix
Tsg101
Syn-1
CD63
CD81
Rab11a
Cav-1
normalised to Alix
normalised to Tsg101
normalised to Syn-1
normalised to CD81
normalised to cell lysate
fold chage
ns
**
***
*
Tsg101
Syn-1
CD63
CD81
Rab11a
Cav-1

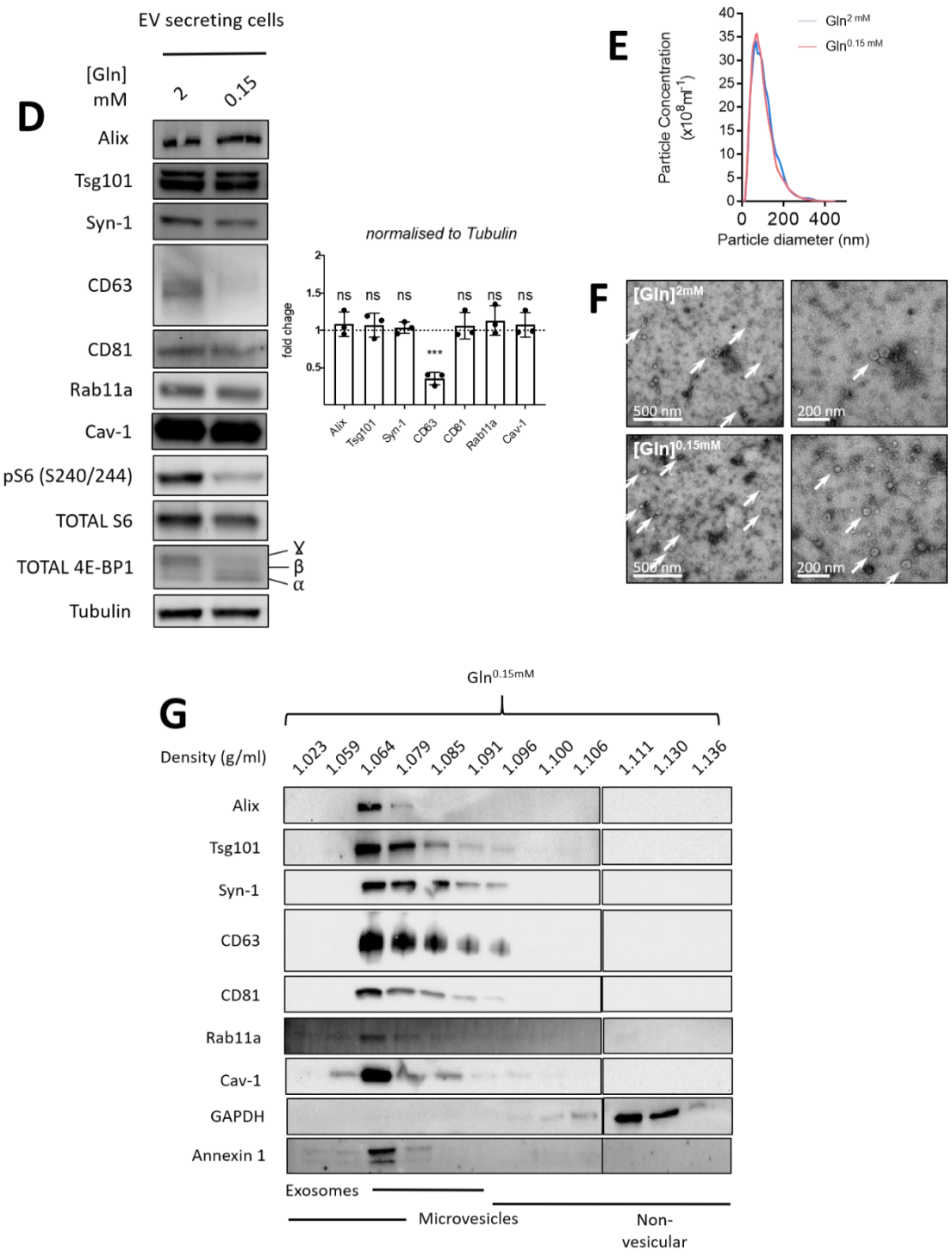



**Figure 3.2** SEC can be used for comparative analysis of switched EVs. (A) Western blots of EVs isolated using UF (Ai) and UC (Aii) demonstrating the EV switch signature, denoted by a decrease in CD63 and an increase in Rab11a and Cav-1. (B) Cell culture media (devoid of FBS, supplemented with ITS) was harvested from glutamine-replete ($Gln^{2mM}$) and –deplete ($Gln^{0.15mM}$) HCT116 CRC cells and injected onto a SEC column. The resulting chromatogram shows clear separation of the EV and protein peaks under both conditions, and the EV switch signature is clearly demonstrated on western blot (C). (D) Western blot of EV markers and mTORC1 activity within the secreting cells. (E) NTA profile comparing

the size distribution, and (F) TEM images comparing the morphology of non-switched (median size 105 nm) and switched EVs (median size 101 nm), which are typical exosome sizes. (G) EV preparations from glutamine-deplete HCT116 CRC cells were separated on an Optiprep™ density gradient. The western blot shows that Rab11a co-migrates with the other canonical exosome markers within the exosome density range, and does not overlap with non-vesicular markers (GAPDH). Bar graphs show the mean ± SD of three biological replicates.

The reduction in CD63 positive EVs is thought to partially relate to the corresponding reduction in CD63 observed in EV secreting cells following glutamine depletion (Figure 3.2D), while the other EV markers are unchanged. Figure 3.2D also demonstrates the changes in mTORC1 signalling that are thought to precede EV switching, whereby glutamine depletion causes a reduction in both phosphorylated S6 (p-S6) and hyperphosphorylated 4E-BP1.

Following this the physical properties of switched EVs were analysed using NTA (Figure 3.2E) and TEM (Figure 3.2F), which showed that they were of a similar size to non-switched EVs (105 ± 57 nm, non-switched vs. 101 ± 55 nm, switched) and exhibited the typical collapsed vesicle “cup” shape morphology. In addition, to this switched EVs were separated on an Optiprep™ density gradient to ensure that the increased Rab11a following glutamine-depletion is associated with a subpopulation of EVs, as opposed to a non-EV artefact (Figure 3.2G). Reassuringly, Rab11a exhibited the same fractionation pattern as the canonical exosome markers, as opposed to the microvesicular marker Annexin 1 (A1) and non-vesicular GAPDH. Interestingly, Cav-1 also co-localises with Rab11a and the other exosome markers, although it is also present with the less dense fractions alongside A1. While Cav-1 is known to be associated with exosomes, it is also commonly found in microvesicles (H. Lee et al. 2019; Ni et al. 2020). It is therefore, unclear whether Rab11a-exosomes also contain Cav-1, or whether the increased Cav-1 is associated with an additional effect of glutamine depletion. The resolution of the Optiprep™ gradient shown here was not broad enough to show clear separation of microvesicles and exosomes.

Consistent with this the A1 expression is also strongest in the exosome containing fractions, despite the fact that it is a distinct marker for microvesicles (Jeppesen et al. 2019).

In summary, these results fulfil the MISEV 2018 guidelines for identifying EVs, and demonstrates that SEC can be used to isolate highly purified preparations of non-switched and switched EVs from HCT116 cells with consistent efficiency required for comparative analysis.

### 3.2.2 Classical EV markers and the EV switch signature are detected throughout the SEC chromatogram

The average size of particles eluted within the EV peak (fractions 2-5) was 105 ± 57 nm. This size range, combined with the protein markers shown by western blotting indicate that the EV preparations are enriched with exosomes. As exosomes cover a broad size range of 30-150 nm, it is possible that smaller exosomes could be eluted in later fractions. Indeed, it is likely that a significant proportion of exosomes would be smaller than the SEC columns 84 nm pore size, meaning their passage through the SEC column would be delayed as they enter into and interact with the Sepharose® beads.

In order to investigate this, the SEC fractions were combined and concentrated according to Figure 3.3A and analysed by western blotting (Figure 3.3B). Interestingly, while the classical EV markers Alix, Tsg101, Syn-1, CD63 and CD81 were enriched within the fractions corresponding to the EV-peak (fraction 2-5), they were also detectable in other fractions and throughout the protein-peak. Furthermore, when comparing EVs from control and glutamine-depleted conditions, the EV switch signature was also observed throughout each of the compared fractions. The decrease in CD63 that underpins part of the EV switch signature was significantly decreased in all combined fractions (Figure 3.3C). While the increase in Rab11a and Cav-1 was observed in each of the combined fractions it was not always statistically significant throughout the so-called protein peak.

This unexpected finding may reveal additional detail about the EV switch. The majority of Cav-1 appears to be located within the fraction 2-5, whereas Rab11a appears to be more concentrated in fraction 9-12. This may be because Rab11a and Cav-1 label two separate subpopulations of EVs, which are both up-regulated in response to glutamine deprivation. An alternative explanation could be that these findings are produced by EV damage or rupture, leading to EV protein cargo eluting within the protein peak. It is important to undertake a detailed characterisation of these later fractions to determine whether or not these are enriched in intact EVs, as this will underpin downstream functional and cargo-based analysis of switched EVs.

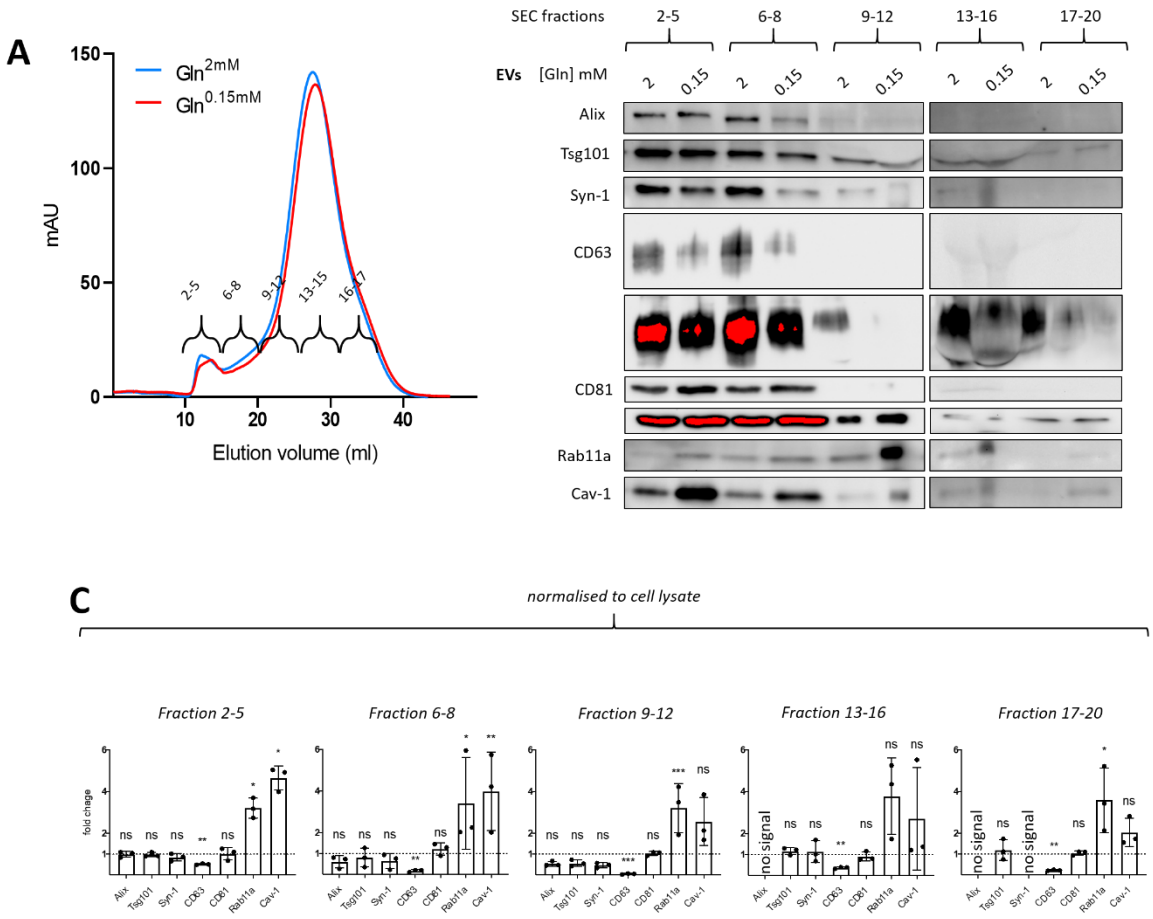



**Figure 3.3** Classical EV markers and the the EV switch signature are detected throughout the SEC chromatogram. (A) Cell culture media (devoid of FBS, supplemented with ITS) was harvested from glutamine-replete ($Gln^{2mM}$) and –deplete ($Gln^{0.15mM}$) HCT116 CRC cells and injected onto a SEC column. The resulting fractions were combined as illustrated on the chromatogram, and examined using western blotting (B), which shows propagation of the EV markers and EV switch signature beyond the fractions corresponding to the EV peak (fraction 2-5) and throughout the entire chromatogram (C). Bar graphs show the mean ± SD of three biological replicates.

### 3.2.2.1 Using the MISEV 2018 guidelines to investigate the non-EV peak fractions

The methods outlined in the MISEV 2018 guidelines to investigate the physical properties of EVs were undertaken for each of the combined fractions. NTA showed that fraction 6-8, which corresponds to the plateau between the EV and protein peak, had a typical EV profile (Figure 3.4). The average size of particles in fraction 6-8 was smaller than those isolated in the EV peak (70 ± 39 nm, non-switched vs. 69 ± 47 nm, switched), consistent with a separation method based on size. There is a significant drop off in the concentration of measured particles in fraction 9-12, although the size range is still consistent with EVs (88

± 50 nm, non-switched vs. 96 ± 53 nm, switched). Beyond fraction 9-12 the classical EV profile produced by NTA is lost, as shown by a broader size range in measured particles (90-350 nm). As these later fractions correspond to the middle of the protein peak it is likely that these NTA profiles are the result of measured protein aggregates, possibly including ruptured EVs. This underpins one of the main limitations of NTA, which uses light scattering and Brownian motion to measure particles and not just EVs. Furthermore, NTA has been shown to be inaccurate at measuring particles below 60 nm (Bachurski et al. 2019). Therefore, it is important to combine NTA with other more direct methods of investigating EVs to determine whether the later fractions also contain functional EVs.

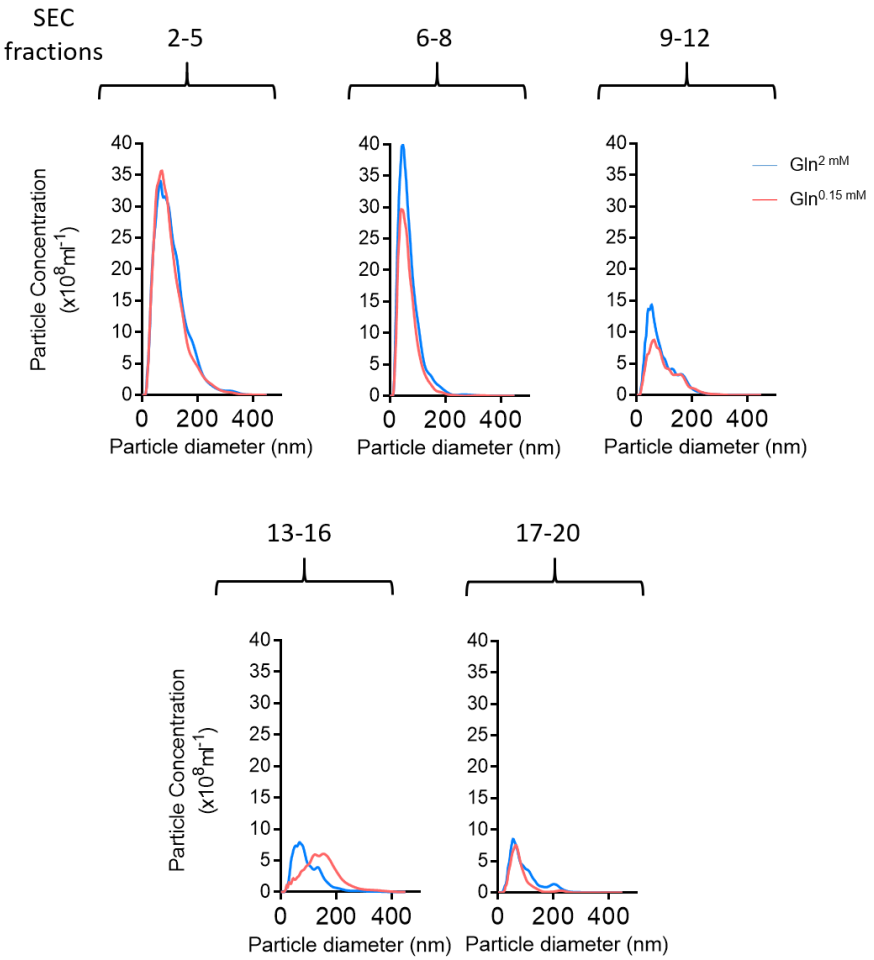



**Figure 3.4** NTA profiling of combined fractions show that the protein peak does not contain particles within the EV/exosome size range. Fractions throughout the SEC chromatogram were combined as per Figure 3.3A and compared using NTA. Aside from the typical EV profile exhibited in fraction 2-5 (corresponding to the EV peak), particles within fraction 6-8

fell within the EV size range (median size 70 nm non-switched EVs, 69 nm switched EVs). Beyond fraction 6-8 there is a significant decrease in particle concentration, and the size of particles beyond fraction 12 ranged widely from 90-350 nm, most likely resembling non-vesicle protein aggregates.

Next, TEM was undertaken on fresh SEC fractions isolated from glutamine-depleted HCT116 cells to provide a direct visualisation of whether the later fractions contain typical EV shaped particles (Figure 3.5). The wide field views clearly show that fraction 2-5 (EV peak) is enriched in EVs, which demonstrate the “cup” morphology typical of exosomes. While there is a clear reduction in the number, fraction 6-8 also contained morphologically distinct EVs. TEM images from fraction 9-12 did not contain more than one EV-like particle per view, which often displayed irregular morphology as shown in the higher magnification image. Fraction 13-16 was entirely devoid of any EVs.

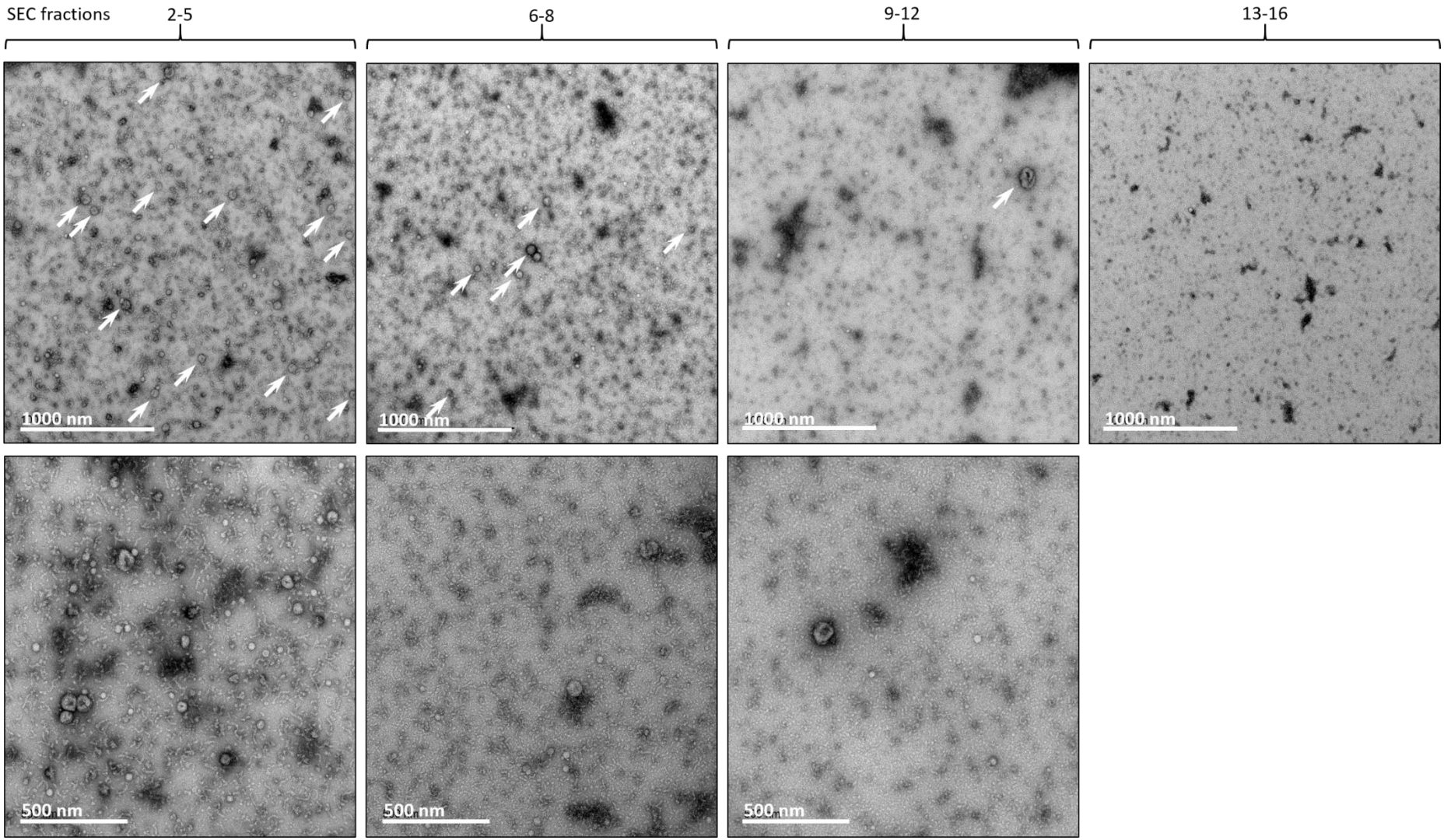

SEC fractions
2-5
6-8
9-12
13-16
1000 nm
1000 nm
1000 nm
1000 nm
500 nm
500 nm
500 nm

**Figure 3.5** TEM demonstrates that EVs are primarily associated with the EV peak. Fractions throughout the SEC chromatogram were combined as per Figure 3.3A and imaged using TEM. While fraction 2-5 (corresponding to the EV peak) is enriched is ”cup” shaped exosomes, a small number are also shown within fraction 6-8, as well as a single abnormally shaped vesicle in fraction 9-12.

Grouped SEC fractions isolated from glutamine-depleted HCT116 cells were also separated on Optiprep™ density gradients and analysed by western blotting (Figure 3.6). The gradients for each set of fractions were broadly similar, which allows comparisons to be made. The EV peak (fraction 2-5) density gradient shows strong co-localisation of the switched EV markers Rab11a and Cav-1 alongside each of the other classical exosome markers at 1.069 g $ml^{-1}$. This co-localisation is then lost in fraction 6-8 and 9-12, whereby Alix and Tsg101, as well as Rab11a and Cav-1 are shifted into the more dense, non-vesicular region of the density gradient. This provides strong evidence that EV protein detected outside of the EV peak reflects protein cargo shed from EV rupture. Even following EV rupture, CD63 and CD81 (both membrane proteins), along with Syn-1 (a membrane associated protein) may still be embedded within phospholipid bilayers, explaining why they continue to be detected within the exosome density range, although in fraction 9-12 non-vesicular CD63 can also be detected.

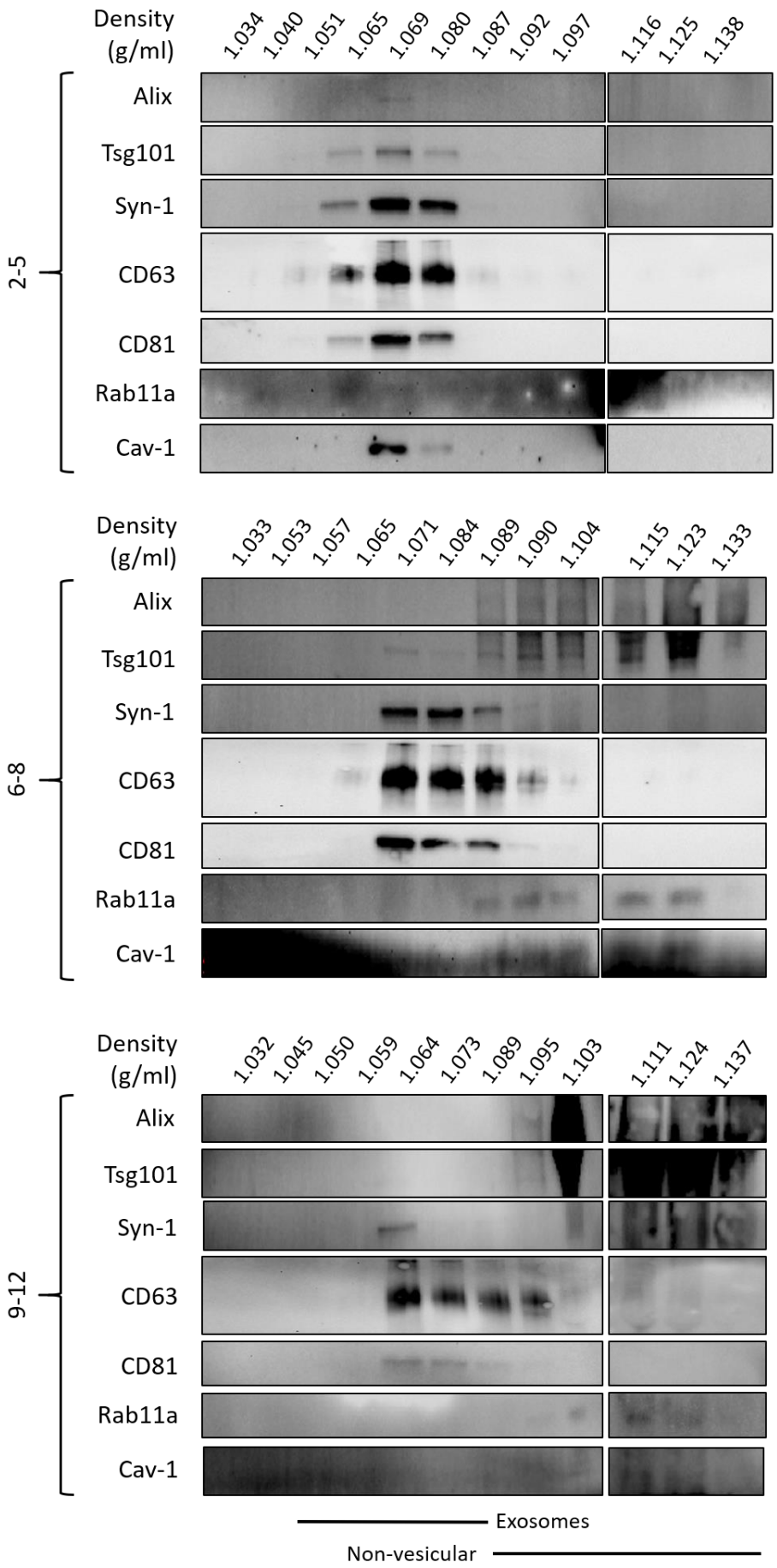

Density (g/ml)
1.034
1.040
1.051
1.065
1.069
1.080
1.087
1.092
1.097
1.116
1.125
1.138
Alix
Tsg101
Syn-1
CD63
CD81
Rab11a
Cav-1
2-5
Density (g/ml)
1.033
1.053
1.057
1.065
1.071
1.084
1.089
1.090
1.104
1.115
1.123
1.133
Alix
Tsg101
Syn-1
CD63
CD81
Rab11a
Cav-1
6-8
Density (g/ml)
1.032
1.045
1.050
1.059
1.064
1.073
1.089
1.095
1.103
1.111
1.124
1.137
Alix
Tsg101
Syn-1
CD63
CD81
Rab11a
Cav-1
9-12
Exosomes
Non-vesicular

**Figure 3.6** Co-localisation of EV markers is not observed in fractions outside of the EV peak**.** Fractions throughout the SEC chromatogram were combined as per Figure 3.3A and underwent separation on Optiprep™ density gradients. While Rab11a co-localises with the other canonical EV markers within fraction 2-5 (corresponding to the EV peak), this co-localisation is lost from fraction 6 onwards. The most likely explanation for this is vesicular rupture.

The combined findings from NTA, TEM and density gradient analysis provide robust evidence that intact EVs are isolated in purified preparations in fraction 2-5 only. While there may be a degree of "spill over" of intact EVs into the adjacent fractions, this only represents a tiny fraction of detectable EV related protein that is detected outside of the EV peak. Therefore, it is likely that EV markers that are detected outside of the EV peak, and particularly within the protein peak, originate from non-functional ruptured EVs.

#### 3.2.2.2 Rab11a is located inside HCT116 cell EVs

The observation that the Rab11a signal is consistently stronger outside of the EV peak needs to be explored further. One explanation could be that switched EVs are more fragile than non-switched EVs, meaning that they are more likely to rupture during isolation. Alternatively, instead of being a true exosome marker, it could represent a contaminant that is not entirely eliminated during the isolation process. Therefore, to investigate this further EVs isolated from glutamine-depleted HCT116 cells were subjected to proteinase K digestion in the absence or presence of the detergent Triton-X (Figure 3.7). In fraction 2-5 (EV peak), Rab11a is protected from digestion from Proteinase K in the absence of Triton X-100, and is only fully digested in the presence of both enzyme and detergent. This is in contrast to CD81, which is partially exposed on the surface of the exosome membrane, making it vulnerable to proteinase K digestion. Therefore, this provides evidence that Rab11a is an internal exosome marker, as it demonstrates the same digestion pattern as the known intravesicular proteins, Tsg101 and Syn-1.

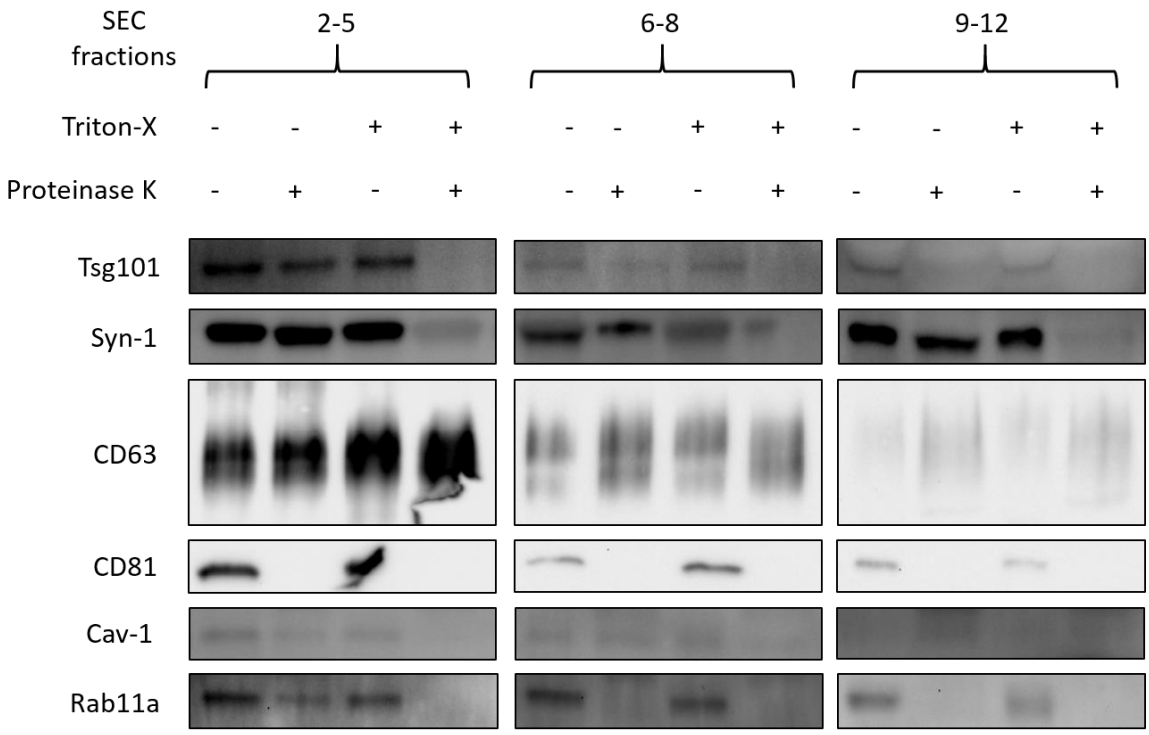



**Figure 3.7** Rab11a is an intravesicular exosome cargo and is not associated with vesicles in fractions outside of the EV peak. Cell culture media (devoid of FBS, supplemented with ITS) was harvested from glutamine-deplete ($Gln^{0.15mM}$) HCT116 CRC cells and underwent SEC. Fractions were combined as per Figure 3.3A and were subjected to proteinase K digestion, with, and without the addition of the detergent Triton-X. Rab11a was protected from digestion in fraction 2-5 (corresponding to the EV peak) providing evidence that it is an intravesicular cargo. Beyond the EV peak, Rab11a was digested indicating it is not associated within EVs within these fractions.

In contrast to the EV peak, Rab11a undergoes complete digestion in the proteinase K alone condition in fraction 6-8 and 9-12, suggesting that it is not associated with EVs within these fractions. A small amount of Tsg101 appears to be protected from digestion in fraction 6-8, but not 9-12, consistent with the findings from NTA and TEM that suggest low numbers of EVs may be detected in the fractions adjacent to the EV peak, although these are unlikely to be Rab11a containing exosomes. While CD63 was protected from digestion in all conditions, and within each fraction, it has been shown to undergo degradation in the presence of more potent detergents (Fan et al, 2020), suggesting that Triton X-100 is unable to fully disrupt its protein structure, and, or, lipid interactions. It is unclear why Syn-1 remains protected from digestion in fractions 6-8 and 9-12. As a membrane associated

protein, its vulnerable domains may be protected from digestion by continued interaction with phospholipid bilayers, even if these are not present as intact vesicles. This explanation would coincide with the finding that following separation on an Optiprep™ density gradient, Syn-1 continues to strongly co-localise with exosomal CD63 and CD81 in fraction 9-12.

#### 3.2.2.3 Proteomic analysis of switched EVs highlights increased loading of specific membrane proteins that exposes further detail of switched EV heterogeneity

A proteomic analysis of UC-isolated non-switched and switched EVs undertaken by Dr Shih-Jung Fan (PDRA, Goberdhan Group) in collaboration with Dr Roman Fischer (Target Discovery Institute, University of Oxford) showed significant differences in the protein cargoes between these two sets of EVs. Over 100 proteins were found to be increased in switched EVs, including HLA-C and the Transferrin Receptor (TfR), both of which are membrane bound proteins. The increase in both of these proteins was validated using switched EVs isolated by SEC (Figure 3.8A), while levels in the glutamine-depleted secreting cells are unchanged (Figure 3.8B).

These up-regulated membrane bound proteins are of experimental value, as they provide a tool for pulling down switched EVs for further characterisation using co-immunoprecipitation (Co-IP). As shown in Figure 3.8C, Co-IP pull down of EVs using HLA-C or TfR conjugated beads was only observed in fraction 2-5 (EV peak), providing further indirect evidence that the later fractions do not contain large quantities of intact EVs. Non-specific binding and strong signal intensity caused by binding of the secondary antibody to the Ig heavy and light chains necessitated a tight crop of the western blot images to highlight the Rab11a bands. This was observed despite the use of a conformation specific secondary antibody. Therefore, uncropped versions of these western blots are provided in Appendix B.

While Co-IP was initially used as an additional method to investigate whether the non-EV peak fractions, it also revealed an additional level of detail regarding switched EV heterogeneity. Co-IP using HLA-C pulled down Rab11a containing EVs, but not Cav-1 (Figure 3.8Ci), while TfR pulled down Cav-1 EVs, but not Rab11a-exosomes (Figure 3.8Cii). This provides evidence that Rab11a containing EVs are distinct from those expressing Cav-1, suggesting that the EV switch results in the biogenesis and secretion of at least two different populations of EVs. While the pull-down efficiency in these initial experiments is low (as demonstrated by low signal in the anti-HLA-C/TfR IP lane and only a minor reduction in amount of Rab11a/Cav-1 within the respective supernatants), if optimised, it would provide a powerful method to study the biology of the different populations EVs secreted under microenvironmental stress, including glutamine.

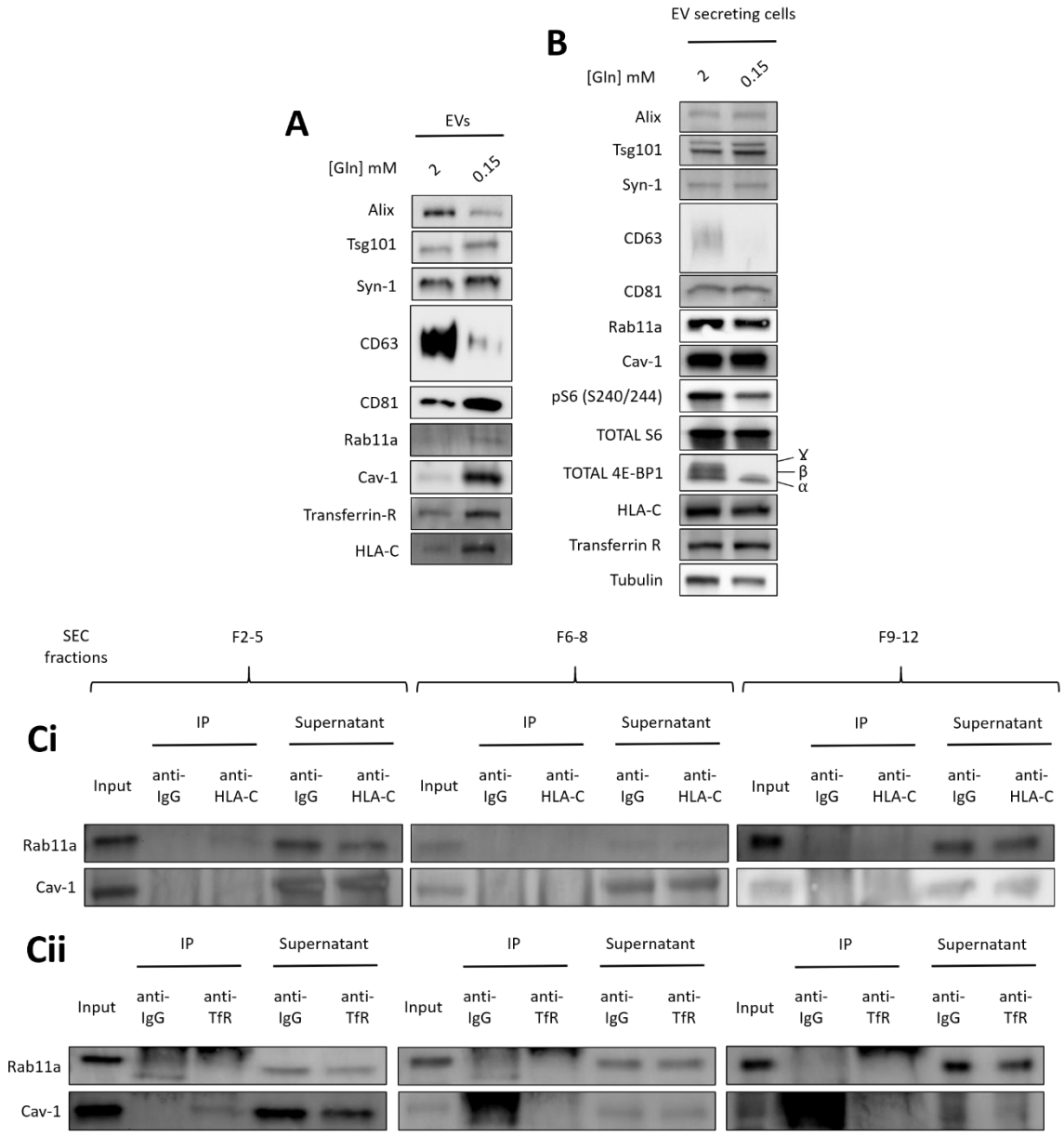



**Figure 3.8** Proteomic analysis reveals upregulation of specific membrane proteins within switched EVs, which reveals further detail regarding EV heterogeneity. A proteomic analysis of UC-isolated EVs from glutamine-replete (2 mM, non-switched) and –deplete (0.15 mM) HCT116 CRC cells was undertaken by Dr Shih-Jung Fan (PDRA, Goberdhan Group) in collaboration with Dr Roman Fischer (Target Discovery Institute, University of Oxford), which showed that over 100 proteins were up-regulated within the switched EVs, including HLA-C and TfR. (A) Western blot confirming upregulation of these membrane-bound proteins in EVs isolated using SEC, which were found to be unchanged within the secreting cells (B). Based on this finding and following the separation of cell culture media from glutamine-deplete HCT116 cells using SEC, the fractions were combined according to Figure 3.3A and underwent Co-IP with HLA-C (Ci) or TfR (Cii) conjugated beads. Despite poor pull-down efficiency, this showed that Rab11a and Cav-1 represent separate EV subtypes. Furthermore, vesicle pulldown was only observed within fraction 2-5 (corresponding to the EV peak), indicating that the subsequent fractions do not contain switched EVs.

### 3.2.3 Hypoxia also induces the secretion of Rab11a exosomes in HCT116 cells

The validation of SEC to isolate and comparatively analyse purified EVs from HCT116 cells enables the investigation of how other forms of microenvironmental stress affects EV biogenesis and secretion. In our switched EV model, glutamine depletion results in reduced signalling through the PAT4-mTORC1 signalling axis, leading to the secretion of Rab11a and Cav-1 EVs and a reduction in CD63 EV secretion (Fan et al. 2020). Interestingly, a previous study has reported an increase in EVs enriched with Cav-1 under hypoxic conditions (Kucharzewska et al. 2013), which is known to be an important suppressor of mTORC1 activity. Therefore, SEC was used to isolate EVs from HCT116 cells grown under standard culture conditions and hypoxia (1% $O_2$) to test the hypothesis that hypoxia can also induce EV switching.

Following 24 hours of growth under hypoxic conditions cell viability was similar in both conditions (91.8 ± 0.9%, control vs. 89.9 ± 1.4%, 1% $O_2$, p=0.115) consistent with viability levels reported following glutamine depletion. Hypoxia led to a reduction in mTORC1 signalling, as demonstrated by a loss of 4E-BP1 hyperphosphorylation and pS6 phosphorylation (Figure 3.9A). As expected under hypoxic conditions, there is also upregulation of HIF-1α, which is known to be associated with the hypoxia-induced suppression of mTORC1 signalling (Cam et al. 2010). In contrast to glutamine-depletion, hypoxia does not reduce intracellular CD63, although CD81 is up-regulated – the precise reason for this is unclear. Similarly, western blot analysis of the EVs also showed that CD63 levels were unchanged following hypoxia, although Rab11a and Cav-1 were increased, consistent with the EV switch phenotype observed following glutamine depletion (Figure 3.9B). Interestingly, a similar EV phenotype is observed in LNCaP prostate cancer cells following glutamine depletion (unchanged CD63 and increased Rab11a) (Fan et al. 2020; McCormick 2018), suggesting that nutrient depletion and hypoxic stress alter EV secretion via a common mTORC1-centered pathway.

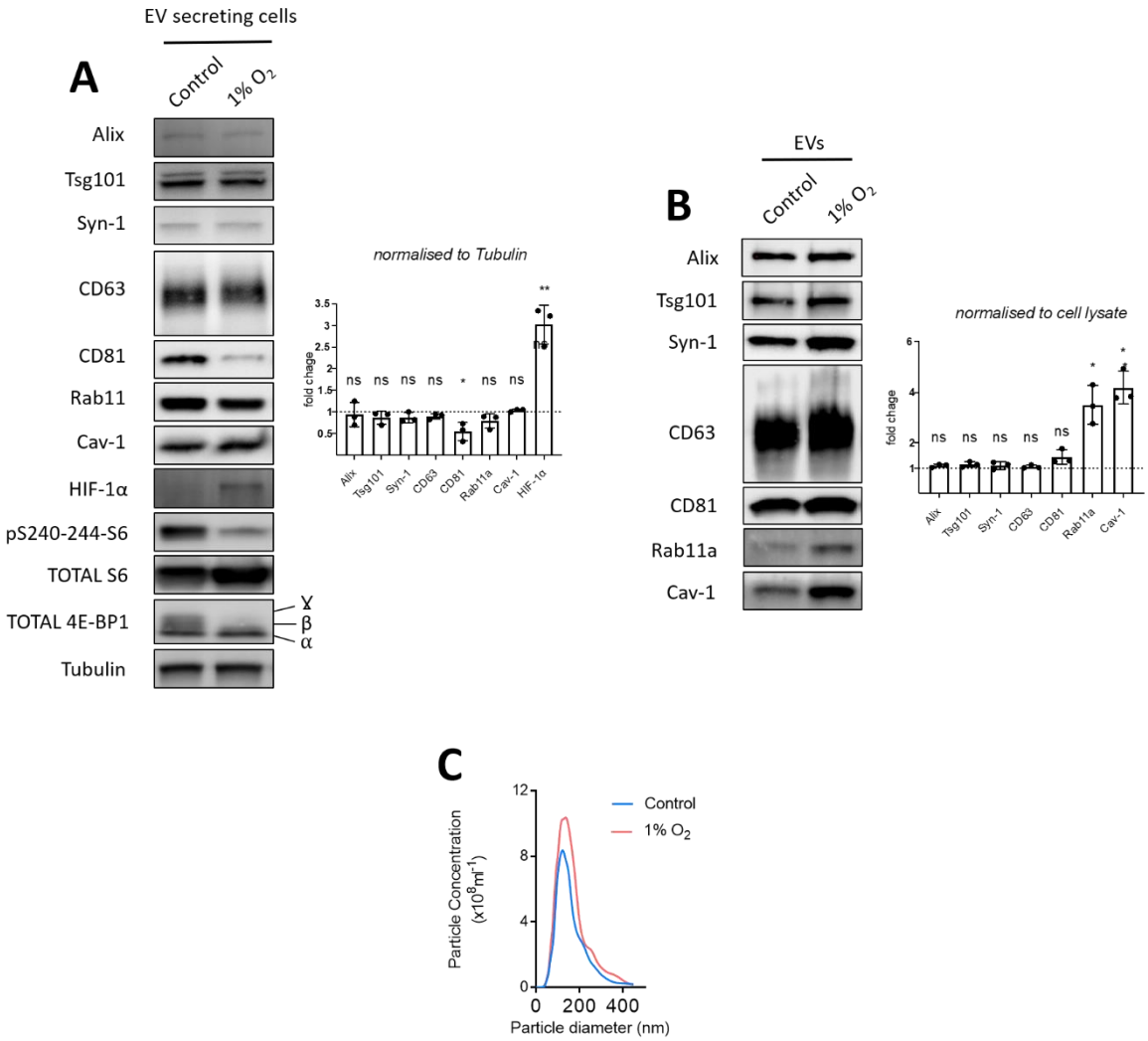



**Figure 3.9** Hypoxia also induces the secretion of Rab11a exosomes in HCT116 cells. (A) Western blot comparing EV markers and mTORC1 signalling in HCT116 CRC cells following 24 hours of growth under standard culture and hypoxic (1% $O_2$) conditions. Following 24 hours of growth under these conditions, EVs were isolated using SEC and compared by western blot (B) and NTA (C). Bar graphs show the mean ± SD of three biological replicates.

NTA revealed that the EVs were of similar size (140 ± 67 nm, control vs. 137 ± 62 nm, 1% $O_2$), although hypoxia stimulated the secretion of approximately 30% more vesicles (Figure 3.9C). Therefore, given the unchanged levels of intracellular and EV-associated CD63, hypoxia may stimulate the secretion of multiple subtypes of EVs (including Rab11a and Cav-1), as opposed to mimicking the glutamine-depletion induced EV switch.

### 3.2.4 Using SEC to investigate EV switching in other CRC cell lines

Since the EV switch was first described in HCT116 cells, it has also been reported in breast (MDA-MB-231), cervical (HeLa) and prostate (C4-2B and LNCaP) cancer cell lines. However, to date it has not been investigated in other CRC cell lines. The validation of SEC to isolate EVs from cell culture media, and to provide reproducible comparative results, provides a basis for using it to investigate whether microenvironmental stress induces EV switching in other CRC cancer cells. Therefore, a panel of cell lines (Table 3.2) representative of the molecular and genetic heterogeneity observed in CRC was selected for further study.

| Cell line | Derived from | MSI status | CIMP status | CIN status | KRAS | BRAF | PIK3CA | p53 |
|---|---|---|---|---|---|---|---|---|
| HCT116 | Primary tumour | MSI | + | - | G13D | wt | H1047R | wt |
| Caco-2 | Primary tumour | MSS | + | + | wt | wt | wt | E204X |
| SW480 | Primary tumour | MSS | - | + | G12V | wt | wt | R273H; P309S |
| SW620 | Lymph node metastasis | MSS | + | + | G12V | wt | wt | R273H; P309S |

**Table 3.2** Overview of the molecular and genetic characteristics of CRC cell lines selected for further study. MSI: microsatellite instability; MSS: microsatellite stability; CIMP: CpG island methylator phenotype; CIN: chromosomal instability pathway; X: stop codon. Table adapted from Ahmed et al. (2013).

HCT116 cells are typical of proximal, or right-sided tumours (Figure 1.1). These are mid-gut derivative cancers that typically exhibit MSI and high CpG island methylation phenotype. Common mutations occur in the *KRAS* and *BRAF*, while *TP53* mutations are less common when compared to more distal cancers. In contrast, Caco-2 and SW480 cells are from left-sided or hind-gut derived tumours, that are often MSS (with or without epigenetic instability), exhibit aneuploidy (CIN) and follow the classical adenoma-to-carcinoma pathway, frequently involving *TP53* mutations. Caco-2 cells are particularly interesting, because they possess a wild type EGFR/RAS/ERK pathway. Mutations in this pathway are known to lead to aberrant signalling leading to the co-activation of the PI3K-

Akt-mTOR axis. Therefore, determining whether Caco-2 cells also secrete switched EVs in response to microenvironmental stress-induced downregulation of mTORC1 signalling may provide further insights into whether EV switching is a cancer specific (i.e. dependent on certain mutational phenotypes), or a general physiological response to adverse growth conditions. To date EV switching has only been investigated in cell lines derived from primary tumours, so it is unknown whether metastatic cells also secrete switched EVs. This will be investigated in SW620 cells, which are derived from a metastatic lymph node and are matched with the SW480 cell line that originate from the primary tumour.

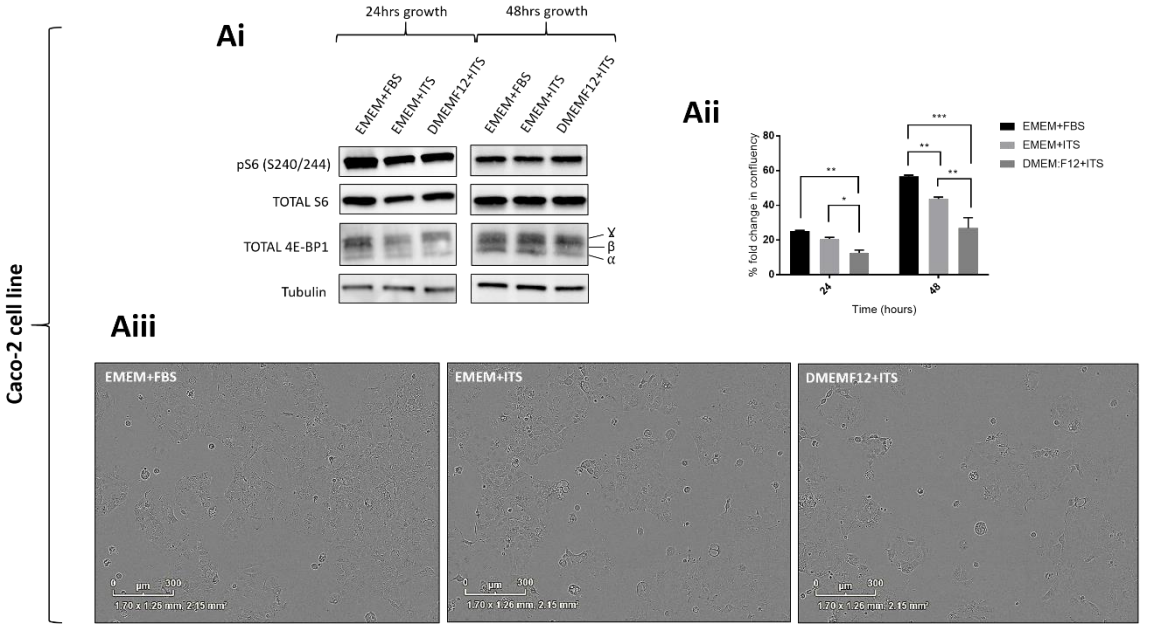
#### 3.2.4.1 Determining cell culture conditions to isolate EVs from Caco-2, SW480, and SW620 cells

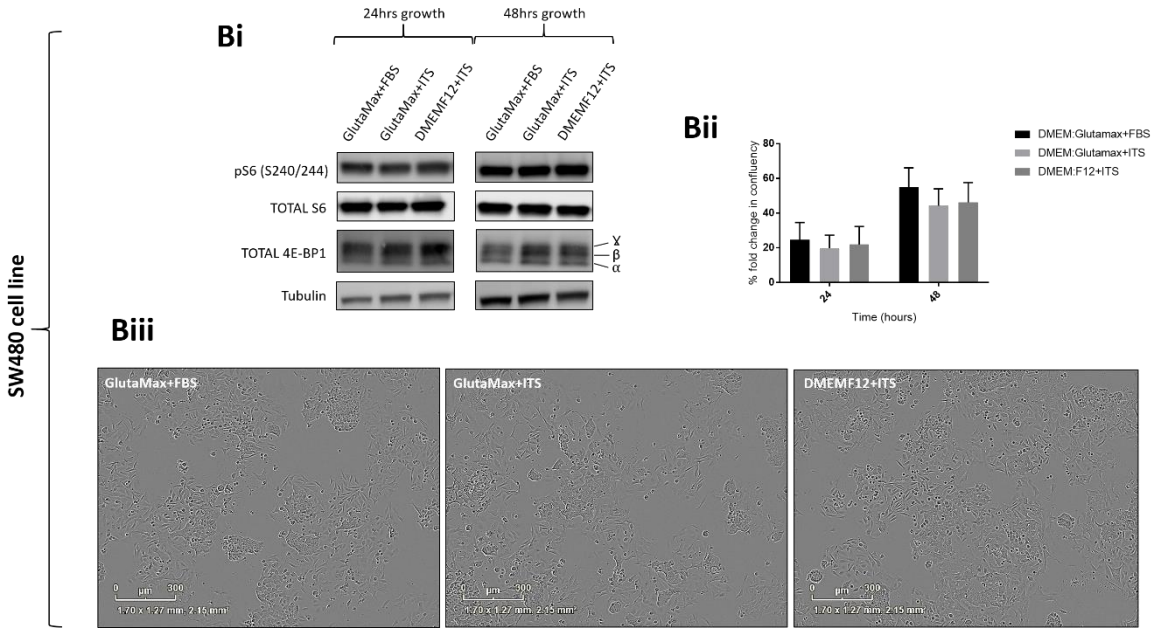
Under standard culture conditions, cells are maintained in the manufacturers recommended cell culture media supplemented with FBS. However, FBS is enriched in bovine-derived EVs, meaning that alternative, serum-free, cell culture conditions that maintain growth and cell signalling must be established before attempting EV isolation. Importantly, in order to investigate EV switching, mTORC1 signalling should not be affected by the serum-free culture conditions. Therefore, Caco-2, SW480 and SW620 cells were cultured for up to 48 hours in either: basal media plus FBS, basal media plus ITS or DMEM/F12 plus ITS. DMEM/F12 has been specifically formulated to culture cells in low-serum conditions, and ITS is added to maintain mTORC1 signalling (Tauro et al. 2012). Cell lysates were collected at 24 and 48 hours to monitor mTORC1 signalling, and growth was monitored using the IncuCyte® ZOOM Live Cell Imager (Figure 3.10).

While mTORC1 signalling was maintained in Caco-2 cells for up to 48 hours in DMEM/F12 plus ITS (Figure 3.10Ai), there were clear differences in the rate of cell growth (Figure 3.10Aii). After 24 hours there was a general trend towards lower rates of growth when Caco-2 cells were cultured in serum-depleted media (EMEM), with significantly less growth observed in the DMEM/F12 condition. This effect is more pronounced at 48 hours, whereby

even the use of serum-depleted EMEM resulted in an approximate 20% reduction in growth, while DMEM/F12 resulted in an almost 50% reduction. Despite this, cell morphology was unchanged after 48 hours by the choice of media (Figure 3.10Aiii), although the differences in cell growth are clear. Therefore, 24-hour incubation in EMEM plus ITS was selected to isolate EVs from Caco-2 cells.

SW480 cells maintained mTORC1 signalling for up to 24-hours when cultured in DMEM/F12 plus ITS (Figure 3.10Bi). While pS6 is unchanged after 48 hours, there appears to be a shift in 4E-BP1 hyperphosphorylation in the DMEM/F12 plus ITS condition. Reassuringly, cell growth and morphology were unaffected by the choice of culture media (Figure 3.10Bii-iii). Similarly, DMEM/F12 plus ITS was sufficient to maintain mTORC1 signalling in SW620 cells for 24-hours, and there was a shift in 4E-BP1 hyperphosphorylation after 48 hours (Figure 3.10Ci). The significance of this shift in 4E-BP1 hyperphosphorylation is unclear, as a similar pattern was observed for basal media plus FBS, meaning it may be related to cellular stress secondary to high confluency. While the choice of culture media did not affect the rate of cell growth after 24 hours, there was approximately 20% less growth after 48 hours when DMEM/F12 was used (Figure 3.10Cii-iii). SW480 and SW620 cells are both known to be fast growing cells (Ahmed et al. 2013), meaning that 24 hours of culture in DMEM/F12 plus ITS should be sufficient to enable EV isolation, while maintaining adequate mTORC1 signalling and so this culture condition was employed.


Caco-2 cell line
Ai
24hrs growth
48hrs growth
EMEM+FBS
EMEM+ITS
DMEMF12+ITS
pS6 (S240/244)
TOTAL S6
TOTAL 4E-BP1
Tubulin
γ
β
α
Aii
% fold change in confluency
Time (hours)
EMEM+FBS
EMEM+ITS
DMEM:F12+ITS
Aiii
EMEM+FBS
EMEM+ITS
DMEMF12+ITS


SW480 cell line
Bi
24hrs growth
48hrs growth
GlutaMax+FBS
GlutaMax+ITS
DMEMF12+ITS
pS6 (S240/244)
TOTAL S6
TOTAL 4E-BP1
Tubulin
γ
β
α
Bii
% fold change in confluency
Time (hours)
DMEM:Glutamax+FBS
DMEM:Glutamax+ITS
DMEM:F12+ITS
Biii
GlutaMax+FBS
GlutaMax+ITS
DMEMF12+ITS

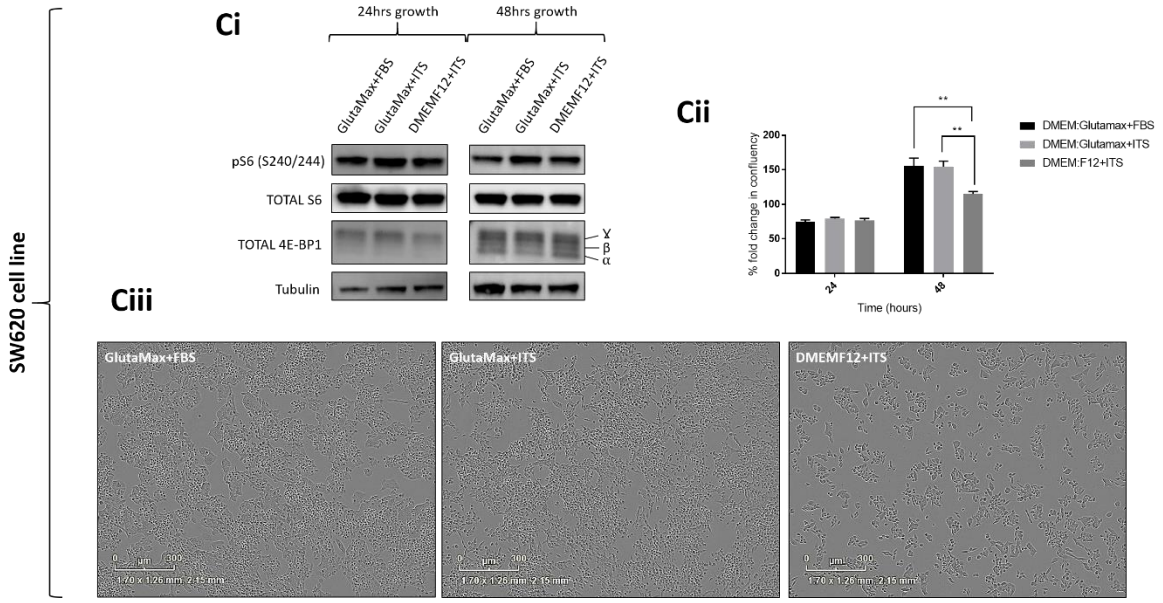



**Figure 3.10** Establishing cell culture conditions to study EV switching in other CRC cell lines. CRC cells were cultured in the indicated media for between 24-48 hours before the effects on mTORC1 signaling (Ai-Ci), rate of cell growth (Aii-Cii) and cell morphology (Aiii-Ciii) were compared. Rate of cell growth was assessed using the IncuCyte® ZOOM Live Cell Imager. Bar graphs show the mean ± SD (n=8 per condition).

### 3.2.4.2 Characterising EVs isolated from Caco-2, SW480, and SW620 cells

Using the conditions described in Section 3.2.4.1, SEC was used to isolate EVs from Caco-2, SW480 and SW620 cells. Figure 3.11Ai-Ci show the chromatograms for each cell line, demonstrating clear separation between the initial EV peak and subsequent protein peak. The fractions corresponding to the EV peak were combined and analysed by western blotting, NTA and TEM to confirm sample purity for each cell line according to the MISEV 2018 guidelines. Western blots comparing cell lysate and EVs showed that for each cell line, the combined EV fractions were enriched in the tetraspanins (CD63 and CD81), and also contained Syn-1 and Tsg101, which are involved in MVB and EV biogenesis (Figure 3.11Aii-Cii). Importantly, the EVs were consistently devoid of EEA-1, TGN46 and Calnexin, providing evidence that the EV fractions were not contaminated by vesicles from non-EV producing compartments.

The NTA profiles are shown in Figure 3.11Aiii-Ciii, which reveal a major peak within the exosome size range for each cell line (Caco-2: 131 ± 53 nm; SW480: 117 ± 58 nm and SW620: 115 ± 57 nm). Interestingly, SW480 cells were found to consistently secrete up to 25% more EVs than the paired metastatic SW620 cell line. This may suggest that EV biogenesis and secretion reduces as cancer cells acquire a more stem like phenotype, which is a feature of circulating tumour cells, and within metastases (Mani et al. 2008). Finally, TEM images revealed a heterogeneous mixture of EV-shaped particles, consistent with EV preparations that are enriched in exosomes (Figure 3.11Aiv-Civ). Taken together, these results indicate that SEC can be used to isolate purified preparations of EVs from Caco-2, SW480 and SW620 cells.

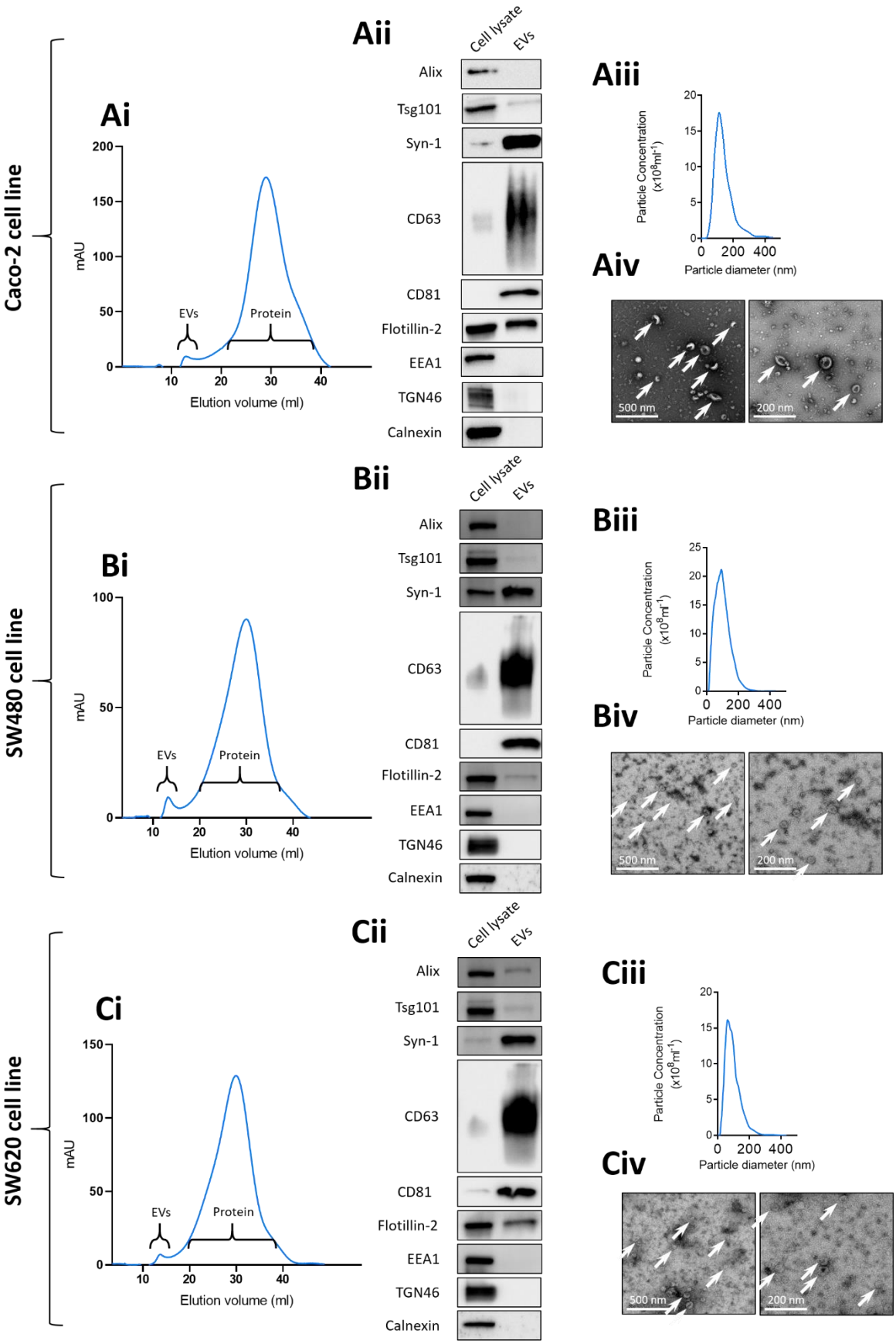

Caco-2 cell line
Ai
mAU
EVs
Protein
Elution volume (ml)
Aii
Cell lysate
EVs
Alix
Tsg101
Syn-1
CD63
CD81
Flotillin-2
EEA1
TGN46
Calnexin
Aiii
Particle Concentration (x10⁸ml⁻¹)
Particle diameter (nm)
Aiv
500 nm
200 nm
SW480 cell line
Bi
Bii
Biii
Biv
SW620 cell line
Ci
Cii
Ciii
Civ

**Figure 3.11** SEC enables the isolation of purified EV preparations from a panel of CRC cell lines. EVs were isolated from (A) Caco-2, (B) SW480 and (C) SW620 CRC cells using SEC. (Ai-Ci) For each cell line there was clear separation between the EV peak and subsequent protein peak. (Aii-Cii) Fractions corresponding to the EV peak for each cell line were combined and compared against an equivalent amount of protein from the respective secreting cells. These show enrichment of EV marker proteins and an absence of intracellular endolysosomal markers. (Aiii-Ciii) NTA exhibits a typical exosome profile for each cell line, and (Aiv-Civ) TEM images are enriched in ”cup” shaped vesicles typical of exosomes.

### 3.2.4.3 Establishing glutamine-depletion and mTORC1 inhibition conditions to study EV switching in Caco-2, SW480, and SW620 cells

EV switching in HCT116 cells is believed to occur through reduced signalling via the PAT4-mTORC1 signalling pathway, leading to reduced EV biogenesis via the classical MVB pathway, and increased secretion via the Rab11a-labelled recycling endosome pathway. Experimentally, this is induced by glutamine-depletion (as PAT4 is a glutamine/serine amino acid transporter) or mTOR inhibition with the drug, Torin1. Therefore, glutamine-depletion and Torin1 drug assays were undertaken to establish conditions to investigate whether Caco-2, SW480 and SW620 cells also undergo EV switching in response to microenvironmental stress.

Following 24 hours of growth under standard culture conditions, the media was changed to either the EV isolation media for each cell line as described in Section 3.2.4.1 (for Torin1 inhibition) or the equivalent glutamine-free media (for glutamine-depletion assays). For the glutamine-depletion assay, L-glutamine was added at 100% of physiological concentrations (2 mM) and serial diluted to 0%, while the Torin1 dose-response ranged from 0-300 nM. After a further 24 hours, the effects on mTORC1 and mTORC2 signalling were analysed by western blotting (Figure 3.12).

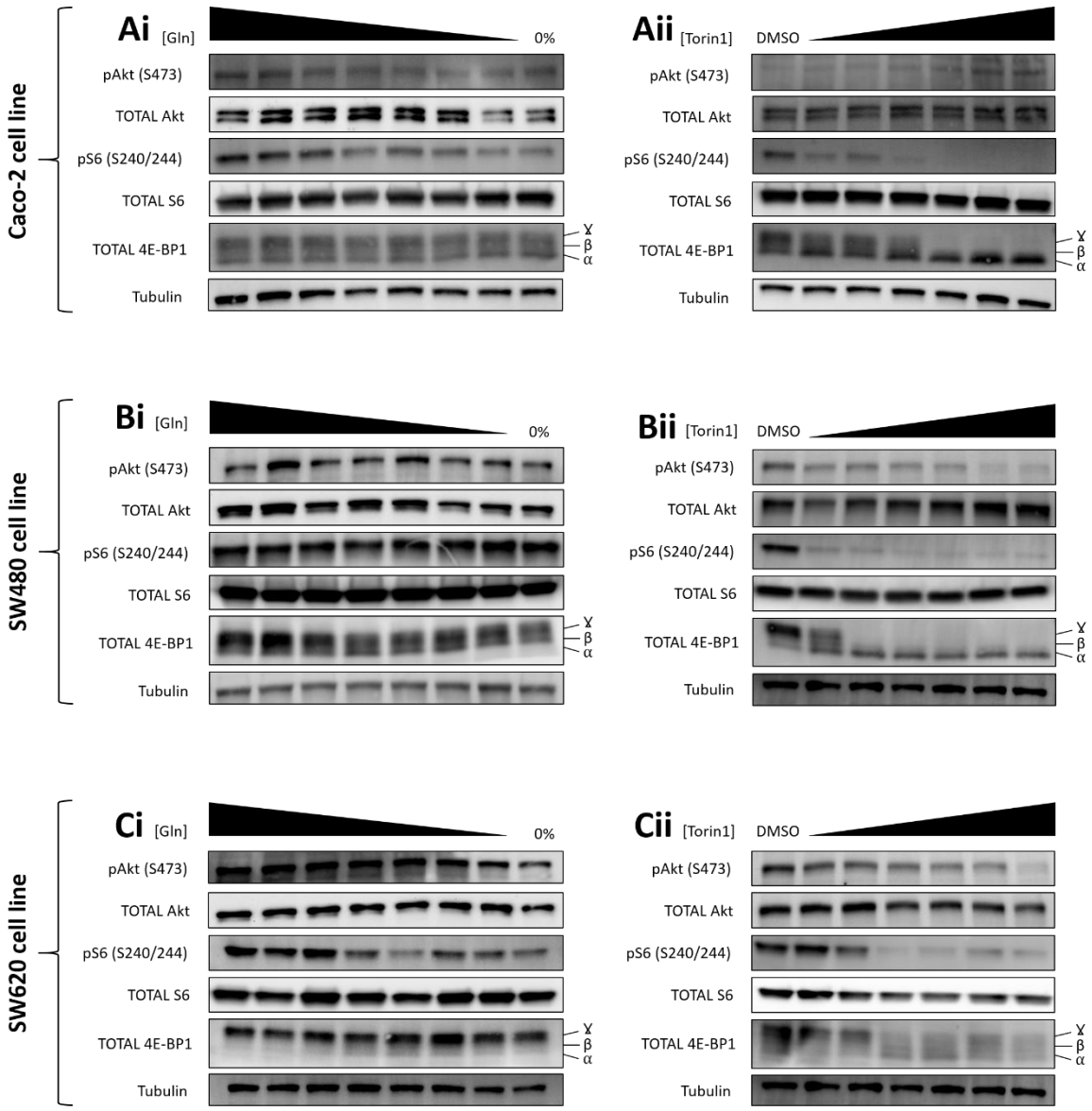



**Figure 3.12** Establishing mTORC1 suppression conditions to study EV switching in a panel of CRC cell lines. (A) Caco-2, (B) SW480 and (C) SW620 CRC cells were subjected to glutamine-depletion (Ai-Ci) or Torin1 treatment (Aii-Cii) for 24-hours and the effect on mTORC1 signaling investigated via western blotting. Conditions used for glutamine-depletion ranged from 2 mM, serial diluted to 0.03 mM and Torin1 treatment doses (nM): 300, 250, 200, 150, 100 and 50.

None of the additional CRC cell lines tested appeared to show the same sensitivity to glutamine-depletion in terms of mTORC1 and mTORC2 activity as observed in HCT116 cells (Fan et al. 2016). While there appears to be slight reduction in pS6 and a shift in 4E-BP1 hyperphosphorylation in Caco-2 cells (Figure 3.12Ai) this does not follow the stronger reduction in mTORC1 signalling observed in HCT116 cells that leads to the EV switch (Fan

et al. 2020). A similar 4E-BP1 phosphorylation pattern is observed in SW480 cells, although some hyperphosphorylation is still evident even at 0% glutamine, and pS6 appears to be completely unaffected (Figure 3.12Bi). Hyperphosphorylation of 4E-BP1 in SW620 cells is clearly insensitive to glutamine-depletion even at 0% glutamine, although there is a small reduction in pS6 (Figure 3.12Ci). Similarly, pAkt (mTORC2 activity) was also maintained at low glutamine concentrations. Before drawing any conclusions, it is important to remember that the cells were only depleted of glutamine for 24 hours, which is a timescale that may lack relevance in true cancer development. It does however highlight interesting differences in mTOR signalling between different CRC cell lines.

Torin1 is a second-generation ATP-competitive mTOR inhibitor that blocks the activation of all mTOR-containing complexes, including mTORC1 and mTORC2 (Saxton and Sabatini 2017). Treatment with Torin1 resulted in the complete blockade of mTORC1 activity, marked by a total loss of pS6 and 4E-BP1 hyperphosphorylation in each of the analysed CRC cell lines (Figure 3.12Aii-Cii). While mTORC2 activity also appeared sensitive, pAkt was still detectable when mTORC1 signalling was inhibited, indicating that mTORC1 is more sensitive to Torin1 in these cells. Based on these findings the Torin1 doses chosen to investigate EV switching were: Caco-2, 150 nM; SW480, 100 nM and SW620 150 nM.

Therefore, based on these findings it was hypothesised that: 1) short term glutamine-depletion does not stimulate the secretion of switched EVs in Caco-2, SW480 and SW620 cells, while, 2) mTORC1 inhibition with Torin1 will induce these cell lines to undergo EV switching. HCT116 cells are known to undergo EV switching when treated with Torin1, although this coincides with an approximate 50% reduction in particle number alongside a general reduction in all EV markers, particularly CD63. In contrast to this, Torin1 also induces the EV switch in LNCaP prostate cancer cells, but is associated with a slight increase in the number of EVs produced (Fan et al. 2020).

### 3.2.4.4 Short term glutamine-depletion does not appear to induce EV switching in Caco-2, SW480 and SW620 cells

EVs were isolated from Caco-2, SW480 and SW620 cells grown in glutamine-replete and -depleted media using SEC, to test the hypothesis that short-term glutamine-depletion does not stimulate the EV-switch in these cell lines. As serial dilution of glutamine did not result in any gradual reduction in 4E-BP1 hyperphosphorylation or pS6 levels (as observed in HCT116 cells), initial experiments tested 0.04 mM glutamine (2% of physiological glutamine concentration) and did not result in the detection of an EV switch (data not shown). To ensure that glutamine sensitivity was not observed at extremely low concentrations, subsequent EV isolations tested 0% glutamine (Figure 3.13), which provided further evidence that Caco-2, SW480 and SW620 cells do not undergo EV switching in response to short term glutamine-depletion. Cell viability was not significantly lowered by 24 hours of glutamine-depletion in any of the tested cell lines (Caco-2: 80.2 ± 2.3%, control vs. 75.8 ± 4.2%, 0% glutamine, $p=0.182$; SW480: 87.1 ± 1.1%, control vs. 83.2 ± 3.6%, 0% glutamine, $p=0.144$; SW620: 91.8 ± 1.1%, control vs. 90.1 ± 1.1%, 0% glutamine, $p=0.136$). There were no significant differences in any of the classical exosome markers, Alix, Tsg101, Syn-1, CD63 or CD81, and each cell line appeared to secrete Rab11a vesicles under both glutamine-replete and -depleted conditions (Figure 3.13Aii-Cii). NTA profiles showed that Caco-2 cells secreted approximately 20% less vesicles following glutamine-depletion, which were also slightly larger than those secreted by cells grown in glutamine-replete media (141 ± 70 nm, control vs. 165 ± 79 nm, 0% glutamine) (Figure 3.13Aiii). EV size and concentration was unaffected by glutamine-depletion in SW480 (125 ± 65 nm, control vs. 121 ± 62 nm, 0% glutamine) and SW620 cells (120 ± 47 nm, control vs. 122 ± 46 nm, 0% glutamine) (Figure 3.13Biii-Ciii). Finally, CD63 expression in the secreting cells was unchanged following 24 hours of glutamine-depletion (Figure 3.13Aiv-Civ).

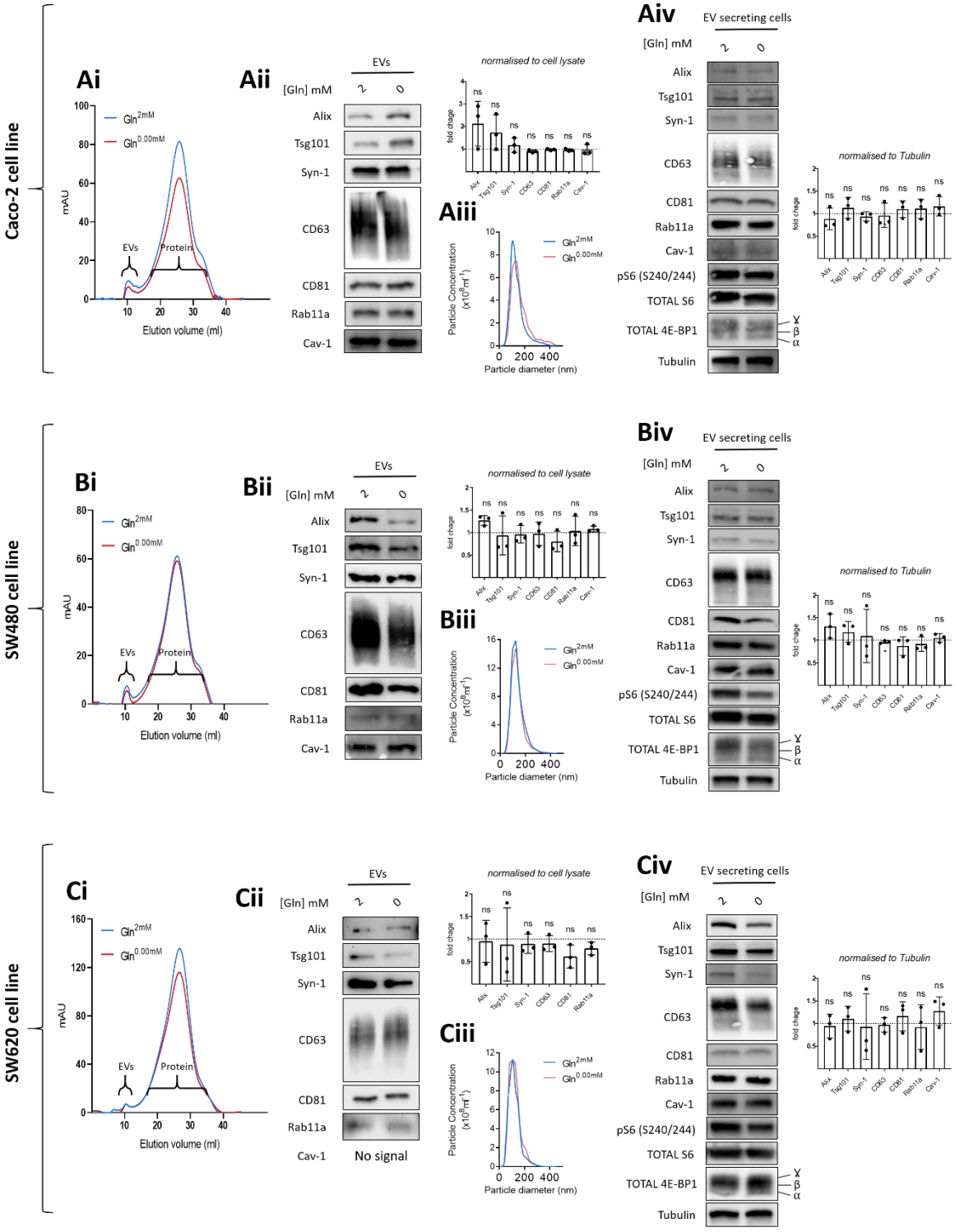



**Figure 3.13** Glutamine-depletion does not induce the EV switching in a panel of other CRC cell lines. EVs were isolated from (A) Caco-2, (B) SW480 and (C) SW620 CRC cells grown under glutamine-replete (2mM) and –deplete (0mM) conditions using SEC. (Ai-Ci) The SEC chromatograms were similar for each condition, and showed clear separation between the EV and protein peaks. (Aii-Cii) Western blots of isolated EVs, which show that glutamine-depletion does not induce EV switching in these cell lines. (Aiii-Ciii) NTA profiles for each cell line, which show that glutamine-depletion does not significantly alter the number of secreted EVs, which fall within the exosome size range. (Aiv-Civ) Western

blot of EV markers and mTORC1 activity within the EV secreting cells, which were unaffected by glutamine-depletion. Bar graphs show the mean ± SD of three biological replicates.

### 3.2.4.5 mTORC1 inhibition induces EV switching in Caco-2, SW480 and SW620 cells

Caco-2, SW480 and SW620 cells each demonstrated sensitivity to Torin1, leading to the hypothesis that mTORC1 inhibition can induce the EV switch in these cell lines. To test this hypothesis, EVs were isolated from each cell line following 24 hours of Torin1 treatment using the doses outlined in section 3.2.4.3. Figure 3.14 demonstrates that each cell line underwent an EV switch, which was accompanied by clear inhibition of mTORC1 signalling.

EVs isolated from Caco-2 cells demonstrate the classical decrease in CD63, and increase in Rab11a labelled exosomes, although Cav-1 was unchanged by Torin1 treatment (Figure 3.14Aii). As co-immunoprecipitation data indicate that Rab11a and Cav-1 labelled EVs are two distinct populations (section 3.2.2.3), this may indicate that mTORC1 inhibition primarily promotes the secretion of Rab11a exosomes. Further evidence for the existence of two distinct populations of switched EVs is provided by SW620 cells, as Cav-1 was not detectable in control or switched EVs, although there was still a clear CD63 decrease and increase in Rab11a following mTORC1 inhibition (Figure 3.14cii). While similar findings have been reported in LNCaP cells, which do not express Cav-1, intracellular Cav-1 was detected in SW620 cells (Figure 3.14Civ). mTORC1 inhibition induced an EV switch in SW480 cells that most closely resembled the switch in HCT116 cells (Figure 3.14Bii), whereby the decrease in CD63 was accompanied by a significant increase in both Rab11a and Cav-1 labelled EVs. However, unlike HCT116 secreting cells, intracellular CD63 was unaffected by Torin1 treatment in SW480 cells (Figure 3.14Biv). This was also observed in SW620 secreting cells (Figure 3.14Civ), although Caco-2 cells did exhibit the intracellular decrease in CD63 following mTORC1 inhibition (Figure 3.14Aiv). The EV and intracellular expression of the other exosome markers, Alix, Tsg101, Syn-1 and CD81 was unaltered by mTORC1 inhibition in each cell lines. The NTA data shown in Figure 3.14Aiii-Ciii show that

there was an approximate 20-25% reduction in EV secretion following Torin1 treatment in each cell line, which is also seen in HCT116 cells treated with Torin1 (Fan et al. 2020). Despite the differences in EV secretion, Torin1 did not significantly alter the size of secreted vesicles (Caco-2: 139 ± 58 nm, control vs. 143 ± 57 nm, Torin1; SW480 149 ± 55 nm, control, vs 150 ± 49 nm Torin1; SW620 111 ± 54 nm, control vs. 109 ± 54, Torin1).

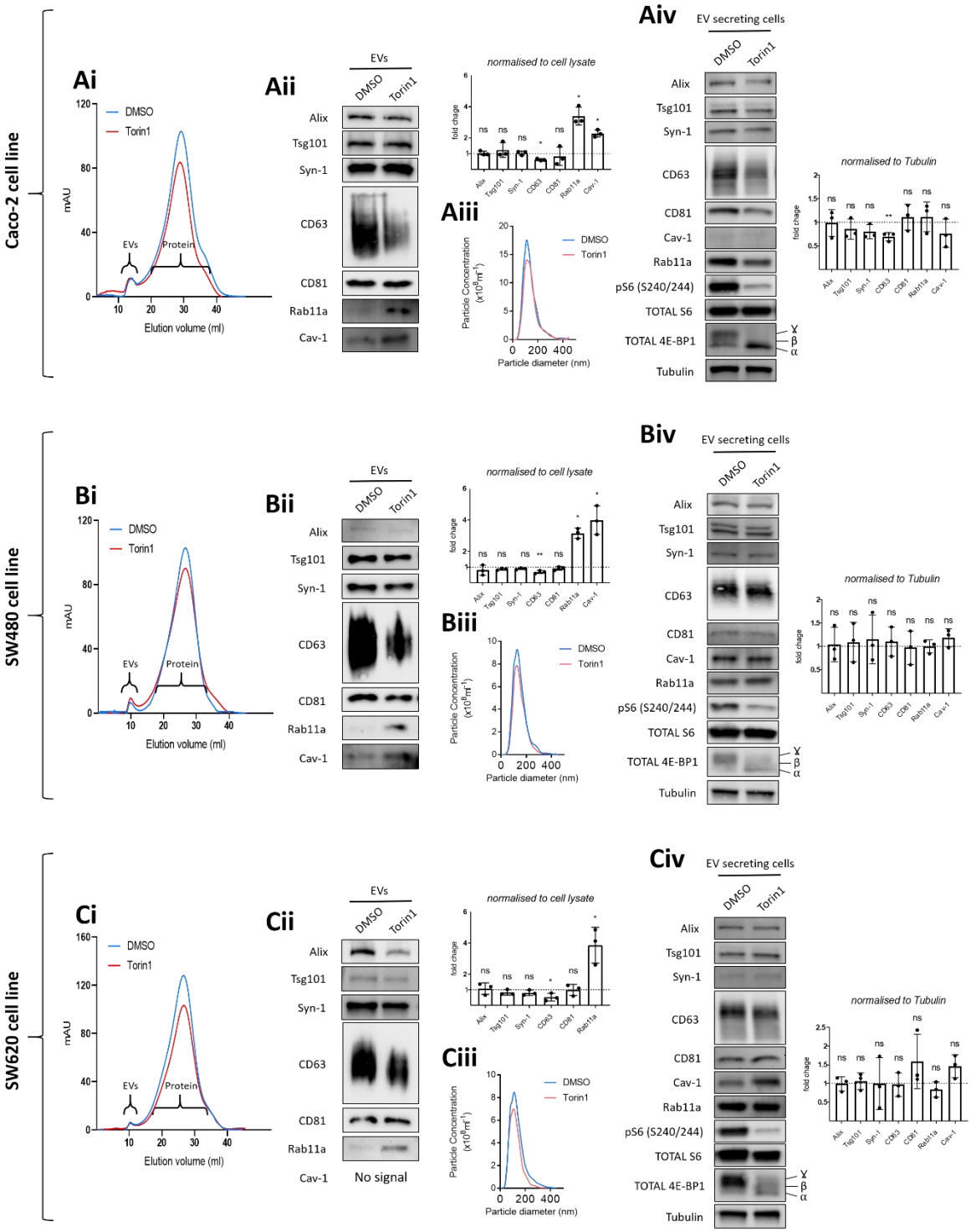



**Figure 3.14** Torin1 induces the mTOR1-dependent EV switch in a panel of other CRC cell lines. Following 24 hours of exposure to either vehicle (DMSO) or Torin1, EVs were isolated from (A) Caco-2, (B) SW480 and (C) SW620 CRC cells using SEC. (Ai-Ci) The chromatograms were similar for each condition, and showed clear separation between the EV and protein peaks. (Aii-Cii) Western blots of isolated EVs, which show that mTORC1 inhibition by Torin1 induces the secretion of switched EVs in each of these cell lines. (Aiii-Ciii) NTA profiles for each cell line, which show that while Torin1 treatment does not effect

the size of secreted vesicles, it is associated with decreased EV secretion (by up to 25%). (Aiv-Civ) Western blot of EV markers and mTORC1 activity within the secreting cells. Torin1 doses: Caco-2 = 150 nM, SW480 = 100 nM and SW620 150 nM. Bar graphs show the mean ± SD of three biological replicates.

In summary, these results provide further evidence that the mTORC1 pathway regulates the EV switch, particularly when compared with the glutamine-depletion data for Caco-2, SW480 and SW620 cells, which did not exhibit the reduction in 4E-BP1 hyperphosphorylation and pS6 caused by Torin1.

## 3.3 Discussion

EVs are vital mediators of intercellular signalling in normal physiology and pathological processes, including cancer. However, the mechanisms by which EV biogenesis and subsequent signalling are affected by microenvironmental stress are poorly understood. The Goberdhan Group's discovery of the EV switch provides novel insights into how cancer cells adapt to nutrient depletion and possibly other forms of mTORC1-sensed microenvironmental stress. However, in order to investigate the importance of stress-induced EV heterogeneity, including the functional role of switched EVs, reliable and pure methods of EV isolation are required. Therefore, the central aim of this chapter was to validate SEC as an isolation method to study EV heterogeneity. Initially this was investigated in HCT116 CRC cells, which are known to have enhanced secretion of Rab11a exosomes in response to glutamine-depletion. SEC was shown to be a reproducible and valid method to isolate EVs and to detect the EV switch. Through use of the MISEV 2018 guidelines, these EVs were found to be purified exclusively within the EV peak of the chromatogram, and this data is included in the EV switch study by Fan et al. (2020) (Appendix A). Based on this, SEC was used to show that hypoxia also promotes the mTORC1-dependent release of Rab11a exosomes, and that reduced mTORC1 activity promotes an EV switch in a panel of other CRC cells.

### 3.3.1 SEC is a reproducible and valid method to isolate highly purified EV preparations containing Rab11a exosomes

The initial work undertaken to isolate EVs following glutamine-depletion used UC, which is known to suffer from non-vesicular macromolecule contamination, as well as EV aggregation and rupture (Linares et al. 2015; Sidhom et al. 2020; Thery et al. 2006). Furthermore, a high level of inter-user and experimental variability is associated with large variations in the resultant EV yield (Torres Crigna et al. 2021), particularly for Rab11a-labelled vesicles, which represents a major challenge for any subsequent comparative downstream functional analysis. Indeed, the unpredictable detection of Rab11a raises doubt over its identity as a marker of the EV switch. SEC has been promoted as an alternative isolation method and is associated with less contamination and provides reproducible results (Boing et al. 2014; Gardiner et al. 2016). In contrast to the technical difficulties frequently experienced when using UC, SEC was found to be an effective method to study the EV switch. The high purity of isolated vesicles that is associated with SEC is often achieved by compromising EV yield (Guerreiro et al. 2018). This can be overcome by undertaking UF prior to SEC, as was done during this work, which can separate different EV populations at high yields and with intact functional properties (Nordin et al. 2015). As isolating EVs from cell culture media requires a large amount of starting material (typically 300 ml of media), the harvested media was concentrated using tangential flow filtration (TFF) prior to undergoing UF (Busatto et al. 2018). TFF is an efficient and scalable method to concentrate EVs that prevents vesicle aggregation and rupture, both of which would be likely to occur through the repeated rounds of centrifugation that would be required to concentrate such a large volume of media using UF alone. Using this adapted SEC-based protocol, EVs including Rab11a-exosomes were consistently detected within the EV peak in a pattern that could be predicted according to the glutamine status of the secreting cells. Furthermore, isolated vesicles were characterised using the MISEV 2018 guidelines, and fulfilled each of the required recommendations, which shows that the EV preparations were highly purified.

The strength of the MISEV 2018 guidelines as an experimental tool for studying EVs was highlighted following the unexpected detection of EV markers, including the EV switch signature throughout the remaining SEC fractions. If confirmed to represent intact vesicles this would undermine the validity of SEC to separate EVs from the protein content of the media. However, application of the MISEV 2018 guidelines provided a robust method to dismiss this concern. Despite, NTA and TEM images showing a small degree of “spill over” of EV-like particles in the fractions immediately adjacent to the EV peak, the fractions corresponding to the protein peak did not demonstrate any of the physical characteristics of intact EVs. While the strength of this investigation comes from the use of multiple different methods, probably the most striking proof of this is provided by the TEM images, which show that the protein peak is entirely devoid of any vesicular-like structures. Using a Rab11a-antibody alongside cryogenic-electron microscopy (cryo-EM) would have been the gold standard method to investigate whether the non-EV peak fractions contain intact vesicles (Chuo et al. 2018), although was not feasible during this investigation. The MISEV 2018 guidelines highlight the strengths of cryo-EM for characterising EVs, which include: perseveration of EV structure and size, ability to image all particles in a given volume as opposed to just those adherent to the imaging grid and ability to label and quantify specific EV subtypes (Thery et al. 2018). In addition to the methods outlined within the MISEV 2018 guidelines, proteinase K and Co-IP assays provided strong evidence that the Rab11a, and other EV markers detected outside of the EV peak was not associated with intact vesicles. These findings are consistent with the Optiprep™ density gradient analysis of the non-EV peak fractions that showed detection of Rab11a within the dense, non-vesicular region of the gradient, and loss of co-localisation with the canonical EV markers. Therefore, while the processing of harvested media appears to be associated with a degree of unavoidable EV rupture, SEC is highly effective at separating these from intact vesicles, leading to the isolation of highly purified EV preparations.

While EV rupture is the most likely explanation for the detection of EV protein throughout the SEC chromatogram, the possibility that this is related to a distinct subset of functional extracellular nanoparticles cannot be excluded. H. Zhang et al. (2018) describe a non-membranous class of extracellular nanoparticles, termed exomeres, which are less than 50 nm in size and are produced via a non-endolysosomal, yet undiscovered biogenesis pathway. Exomeres were initially discovered using the non-classical EV isolation technique, asymmetric flow field-flow fractionation, although they can also be isolated using UC (Q. Zhang et al. 2019b). Interestingly, proteomic profiling of exomeres reveals that they are enriched in metabolic enzymes and proteins that are related to glycolysis and mTOR signalling, which are also known to be upregulated in CRC exosomes (X. Wang et al. 2020d; E. Yang et al. 2020). Importantly, exomeres are also associated with known EV proteins, including CD81 and Syn-1 (Q. Zhang et al. 2019b), which may indicate that the detection of these EV markers outside of the EV peak could be related to exomeres. As SEC separates particles based on size, this is feasible, as the isolation of particles below 50 nm would be expected in the later fractions, although this is below the reliable threshold for detection by NTA (Bachurski et al. 2019). Moreover, exomeres have a non-distinct appearance on TEM, and are difficult to distinguish from the typical appearance of protein aggregates such as those detected in the SEC fractions corresponding to the protein peak. Unique exomeres-associated proteins, including IDH1 and hexokinase I have been recommended for use during exomere characterisation (H. Zhang et al. 2018). Therefore, these should be investigated within the SEC fractions, to determine whether the later fractions are enriched in these markers, and whether these are affected by glutamine-depletion.

### 3.3.2 Rab11a and Cav-1 labelled EVs represent distinct EV subtypes secreted under microenvironmental stress

The EV switch is characterised by a decrease in the secretion of CD63-labelled EVs and an increase in the secretion of Rab11a-exosomes. Immunocapture experiments reveal that

CD63- and Rab11a-labelled exosomes are distinct populations of EV, which have been shown to have different endolysosomal biogenesis pathways (Fan et al. 2020). The reduction in CD63-labelled EVs arises due to a decrease in biogenesis and secretion from the Rab7-labelled classical late endosomal MVB pathway, whereas the increase in Rab11a-exosomes is due to increased biogenesis of EVs within the recycling endosome, which was not previously known to represent a site of EV biogenesis. Alongside *in vitro* work this was demonstrated using EV-labelling techniques and super-resolution imaging within secondary cells of the *Drosophila* accessory gland, which is analogous to the mammalian prostate gland. This showed that Rab11-labelled compartments within the secondary cells generate ILVs that undergo subsequent fusion with the plasma membrane. Furthermore, this process was ESCRT-dependent, and was inhibited by knockdown of ESCRT-components that specifically control the secretion of exosomes, and not microvesicles.

The EV switch is also associated with an increase in the lipid raft protein Cav-1. Cav-1 acts as a scaffolding protein and participates in a complex range of interrelated and distinct cellular processes, including: signalling, trafficking and cellular adhesion. It is often upregulated in cancer, where it correlates with stage of disease, and appears to be involved in promoting tumour cell migration and invasion (Campos et al. 2019). Cav-1 is also known to participate in the biogenesis of exosomes and microvesicles, coordinating: EV cargo sorting and transportation, as well as EV uptake by recipient cells. In particular, it appears to play a crucial role in the loading of miRNA into both exosomes and microvesicles (Ni et al. 2020; Robinson et al. 2021). With regards to the EV switch, the significance and origin of increased Cav-1 is not fully understood. Rab11a knockdown in HCT116 cells was still associated with an increase in Cav-1 containing EVs under glutamine-depleted conditions (Fan et al. 2020), suggesting that its secretion involves an alternative, unidentified biogenesis pathway. Indeed, while the release of stress-induced EVs labelled with Cav-1 has been previously described under hypoxia and metabolic stress (Crewe et al. 2018;

Kucharzewska et al. 2013), the origin of these vesicles has not been defined. Furthermore, not all cell lines express Cav-1, and even in some of those that do, it is not always detected in EVs. For example, Cav-1 is not expressed by the prostate cancer cell line LNCaP, but these cells do secrete Rab11a-labelled exosomes in response to glutamine-depletion (Fan et al. 2020; McCormick 2018). In contrast to this, while SW620 CRC cells do express Cav-1 and undergo EV switching following inhibition of mTORC1 signalling, it was not detected in either EV subtype.

During the characterisation of SEC-isolated EVs from HCT116 cells, Optiprep™ density gradient analysis showed strong co-localisation of Cav-1 alongside Rab11a and the other EV markers, although it was also detected within the less-dense, typically microvesicle-associated fractions. An unexpected outcome of this characterisation process led to robust evidence to prove that Rab11a and Cav-1 denote separate EV subtypes. This was initially proposed as an explanation for the propagation of the EV switch signature throughout all the SEC fractions, although this was excluded through use of the MISEV 2018 guidelines. However, the subsequent Co-IP experiments provided the clearest indication that they represent separate EV subtypes, whereby HLA-C immunocapture was associated with Rab11a EVs, while TfR pulled down Cav-1-containing EVs. HLA-C is a MHC-I receptor, which are associated with both exosomes and microvesicles (van Niel et al. 2018), whereas TfR is associated with exosomes but is absent in microvesicles (Muralidharan-Chari et al. 2010). Following optimisation of the Co-IP efficiency, this could be used as an effective method to separate the two stress-induced EV subtypes, which would allow their individual functional roles to be explored.

### 3.3.3 Reduced mTORC1 activity is associated with the EV switch in a panel of CRC cell lines

The EV switch arises due to reduced signalling through the PAT4-mTORC1 signalling pathway. As PAT4 is a glutamine transporter, the majority of work so far has focussed on glutamine depletion as the main trigger of the EV switch. Aside from this, the EV switch has

also been demonstrated using non-physiological triggers, such as treatment with ATP-competitive mTOR inhibitors (Torin1), and PAT4 knockdown, which induces the EV switch in LNCaP and VCaP prostate cancer cells (McCormick 2018). Hypoxia is a ubiquitous feature of almost all developing tumours, and is known to modulate mTORC1 signalling through a range of mechanisms that ultimately lead to its decreased activity (Melick and Jewell 2020). During this chapter, hypoxia was shown to induce a partial EV switch. This was characterised by an increase in Rab11a and Cav-1 labelled EV secretion, although there was no reduction in intracellular or EV-associated CD63. It is unlikely that this partial EV switch signature is a hypoxia-specific feature, as an identical response is exhibited in EVs isolated from glutamine-depleted LNCaP prostate cancer cells (Fan et al. 2020). It is also feasible that higher levels or prolonged periods of hypoxia would eventually result in a decrease in the biogenesis and secretion of CD63-labelled EVs. These findings do however provide further evidence that the different EV subtypes have distinct biogenesis pathways. It also suggests that mTORC1 can modulate EV secretion through a PAT4-independent pathway, as it is unlikely that hypoxia would alter intracellular amino acid transport. As previously reported (C. Shao et al. 2018a), hypoxia led to an increase in the number of secreted EVs, which are likely to have downstream affects on promoting angiogenesis and recipient cell adaptation. This increased secretion is mediated in part by HIF-1α, which has been shown to increase the expression of Rabs, including Rab27a, that drive EV secretion (Bister et al. 2020). Furthermore HIF-1α has also been shown to increase expression of miR-210, a canonical miRNA involved in the EV-mediated stress response to hypoxia in a range of solid cancers, including CRC (Zonneveld et al. 2019).

Using SEC, a panel of three other CRC cell lines were also found to undergo EV switching following treatment with Torin1. These cell lines were chosen carefully in order to reflect the important genetic heterogeneity that is observed in CRC, which is clinically important as it underlies prognosis and response to treatment (Dekker et al. 2019). While no rectal cancer cell line was investigated, often these cancers follow the classical adenoma-to-

carcinoma pathway and are therefore represented by Caco-2 and SW480 cells. The fact that EV switching was observed in each of these cell lines, which included the metastatic cell line, SW620, alongside its known occurrence in cervical and prostate cancer cell lines (Fan et al. 2020), provides strong evidence that this is a general adaptive mechanism that cells undertake in response to microenvironmental stress. Despite this, emerging work from the Goberdhan Group has highlighted cancer-specific functions of switched EVs, including the induction of anti-androgen resistance in prostate cancer (McCormick et al. 2020). It is likely that these arise due to cancer-specific switched EV cargoes.

Unlike HCT116 cells, short-term glutamine depletion did not affect mTORC1 signalling, or trigger the EV switch in Caco-2, SW480 or SW620 cells. It is unknown whether these findings arose due to methodological limitations or whether it reflects the underlying biology of these cell lines. In order to isolate EVs from cell culture media, the secreting cells are cultured in serum-free media, which is necessary because FBS contains high concentrations of bovine-derived EVs. To maintain mTOR signalling in the absence of FBS, ITS was used to supplement the media. However, analysis of mTORC1 signalling at 48-hours shows that the cells were starting to exhibit a stress response, most likely due to the lack of other essential serum-based nutrients, which would confound any downstream analysis of EVs. Therefore, it is possible that these cell lines are sensitive to glutamine and do undergo the EV switch, but the required reduction mTORC1 activity takes longer than 24-hours to develop. This could be investigated by using EV-depleted FBS, which is available commercially, or can be prepared by pelleting the EVs using UC (Kornilov et al. 2018), and would allow longer periods of incubation prior to EV isolation.

If this finding was not related to the methodology, and is instead reflective of biological differences between HCT116 cells and the other CRC cell lines, then this is unexpected. Under the microenvironmental stress experienced by rapidly dividing cancer cells, glutamine is known to be converted to α-ketoglutarate, an essential substrate in the citric

acid cycle, as well as being a nitrogen donor for the synthesis of non-essential amino acids (Wise and Thompson 2010). This metabolic switch is necessary due to the parallel metabolic re-programming in glucose metabolism (Warburg effect), which favours glycolysis instead of the oxidative phosphorylation pathway. This has led to glutamine being considered as an essential amino acid in cancer growth (J. Zhang et al. 2017a). A possible explanation for the differences in glutamine sensitivity between HCT116 cells and the other CRC cell lines studied may relate to their mutational heterogeneity. Hao et al. (2016) show that cells harbouring *PIK3CA* mutations (including HCT116 cells) are more sensitive to glutamine deprivation compared with *PIK3CA* wild-type cells (including Caco-2, SW480 and SW620 cells). The key determinant of glutamine sensitivity in *PIK3CA* mutant tumours is glutamate pyruvate transaminase 2 (GPT2), which converts glutamate to α-ketoglutarate. Consequently, significantly higher concentrations of α-ketoglutarate are found in *PIK3CA* mutant clones, and α-ketoglutarate is able to rescue cells from cell death under glutamine-depleted conditions. An alternative explanation could be related to the expression of other amino acid transporters within these cell lines. For example, SNAT2 is involved in the transport of small neutral amino acids, and, like PAT4, has important regulatory roles in coordinating mTORC1 activity. However, unlike PAT4, SNAT2 has been shown to activate mTORC1 signalling during amino acid starvation (Fan and Goberdhan 2018). Moreover, amino acid starvation leads to increased SNAT2 expression, which promotes resistance to glutamine-depletion and hypoxia (Morotti et al. 2019). Therefore, the expression levels of SNAT2 in each of the investigated CRC cell lines should be compared to investigate whether this could account for the variation in glutamine sensitivity. Regardless of the underlying explanation, it is important to remember that unlike cell culture, *in vivo* tumours consist of many cancer cell clones, each undergoing their own malignant expansion, so it is possible that all developing cancers will exhibit a degree of sensitivity to glutamine-depletion.

# CHAPTER 4

## RESULTS

# 4. Investigating the functional properties of stress-induced EVs in CRC

## 4.1 Introduction

### 4.1.1 EVs in cancer cell adaptation

Under normal physiological conditions, cell growth is closely regulated by the microenvironment, and factors such as hypoxia and nutrient depletion trigger intracellular signalling responses that lead to cell cycle arrest, or even apoptosis (Goda et al. 2003; Semenza 2011). Therefore, cancer cells must implement adaptive strategies to survive the inevitable microenvironmental stress that will arise due to the uncontrolled cell growth, which is a fundamental feature of all cancers. Historically, this was thought to arise primarily through genetic instability, which promoted adaptation and growth through reconfiguring intracellular signalling pathways. However, as our understanding of cancer biology has increased, it is now clear that adaptation occurs through complex crosstalk between different cancer cell colonies, as well as stromal and immune cells. Accumulated evidence indicates that cancer cells actively release EVs into the tumour microenvironment, and are important in promoting adaptation to microenvironmental stress during tumorigenesis (E. Yang et al. 2020). Beyond adaptation, EVs are also implicated in virtually all aspects of primary tumour growth and metastasis (Becker et al. 2016).

The mechanisms through which EVs can promote tumour cell adaptation are diverse. In CRC, EVs secreted under microenvironmental stress have been reported to stimulate the upregulation of glycolytic enzymes to promote the metabolic switch to non-oxidative glucose metabolism (X. Wang et al. 2020d). EV-mediated upregulation of glycolytic mechanisms have also been suggested to promote drug resistance to platinum-based chemotherapies, and enable cancer cells to escape immune surveillance by cytotoxic T-cells (E. Yang et al. 2020). Furthermore, hypoxia triggers the release of cancer cell EVs

that appear to promote angiogenesis through the transfer of VEGF, and activation of Wnt/β-catenin signalling in endothelial cells (Z. Huang and Feng 2017; Ko et al. 2019). CRC EVs also promote evasion from the immune system by triggering ligand mediated apoptosis of cytotoxic T-cells (Huber et al. 2005), while simultaneously promoting the expansion of immunosuppressive macrophages and T-regulatory cells (Shinohara et al. 2017).

mTORC1 signalling is known to be an important regulator of the cellular response to microenvironmental stress (Cam et al. 2010). Work undertaken by the Goberdhan Group has shown that a microenvironmental-mediated reduction in mTORC1 signalling leads to the release of Rab11a-exosomes (Fan et al. 2020). The fact that these switched EVs are secreted as part of a cellular stress-response suggests that they may play a role in promoting tumour cell adaptation, and could be drivers of tumorigenesis. If this is the case then it would shed further light on the complexity of mTORC1 signalling during the pathogenesis of cancer, as it is generally accepted that tumorigenesis is synonymous with increased mTOR activity due its role in promoting protein synthesis (Populo et al. 2012). Furthermore, it may provide a novel explanation for the limited therapeutic efficacy of mTOR-inhibitor monotherapy (Saxton and Sabatini 2017).

### 4.1.2 Studying the functional effects of EVs

The initial work that led to the discovery of the EV switch was undertaken using UC. However, the high sheer forces associated with UC leads to EV rupture and damage to the surface molecules of isolated vesicles. It is also associated with EV aggregation and morphological changes (Sidhom et al. 2020). This loss of integrity may render the EVs ineffective at binding to recipient cells and exerting their biological effects, which presents a major challenge for the downstream functional analysis of EVs on recipient cells. These challenges are even more significant when the aim is to investigate the function of specific EV subtypes. SEC has been highlighted an alternative approach for isolating EVs for functional analysis, which when compared to UC, results in higher yields of isolated EVs

with preserved biophysical and functional properties (Nordin et al. 2015). In the previous chapter, SEC was shown to be a reliable method for the isolation of purified non-switched and switched EVs from a range of CRC cell lines.

In addition to providing guidance on the characterisation of EVs, the MISEV guidelines also outline a series of recommendations for undertaking functional studies (Thery et al. 2018). These cover three broad areas of experimental design. Firstly, a validated method of EV normalisation should be undertaken to enable appropriate dose-response studies to be performed. Second, negative or background controls must always be included, using cell media that has not been conditioned by cells. Thirdly, control experiments should be undertaken to assess the possible confounding influence of soluble, non-EV components. Therefore, these guidelines were used as a framework during the investigation of the function of switched EVs in CRC tumorigenesis.

### 4.1.3 Aims and objectives

The aim of this chapter was to investigate the impact of EV heterogeneity on CRC tumorigenesis, with a focus on determining whether stress-induced switched EVs play a role in cancer cell adaptation and survival under microenvironmental stress. The specific objectives were-

i. To develop an assay to measure the effect of switched EVs on CRC cell growth.
ii. To investigate the potential pro-metastatic role of switched EVs by focussing on EV-mediated migration and invasion.
iii. To use a recently performed proteomic analysis of switched EVs (undertaken by Dr Shih-Jung Fan, PDRA, Goberdhan Group) to investigate the potential mechanisms underlying any EV-mediated effects on growth and cell motility.

## 4.2 Results

### 4.2.1 Studying the effect of switched EVs on CRC cell growth *in vitro*

#### 4.2.1.1 Optimising conditions for an *in vitro* growth assay

One of the most widely reported effects of EVs on cancer cells is their ability to promote growth (L. Han et al. 2019; Xavier et al. 2020). Therefore, to investigate the role of switched EVs on CRC cell growth, an assay was developed whereby EVs were isolated from glutamine-replete and -depleted HCT116 secreting cells using SEC, quantified using NTA and then mixed with recipient HCT116 cells before plating (Figure 4.1A). The MISEV guidelines state that the most appropriate method for normalising "EV dose" will depend on the downstream question (Thery et al. 2018). As EVs carry a highly heterogeneous mix of protein, lipids and nucleic acids, and in the absence of any preceding knowledge of switched EV cargo, total EV number was chosen as the most appropriate measurement. Recipient cell growth was measured using the IncuCyte® ZOOM Live Cell Imager for five days. Initially these assays used an EV concentration of 10,000 EVs per recipient cell in media containing the standard 10% FBS used to culture these cells. Under these conditions, neither EV-subtype had an effect on growth when compared to a PBS control (Figure 4.1B), with all conditions exhibiting a classical sigmoid pattern of proliferation. Therefore, next HCT116 growth and morphology was assessed in reducing FBS concentrations (Figure 4.1C-D), as a tumour *in vivo* will not grow in conditions akin to those in cell culture conditions supplemented with high amounts of FBS. Furthermore, these conditions would not promote the release of stress-induced EVs. Under 5% serum conditions, cells still exhibited a sigmoid-type growth pattern, although the logarithmic growth phase was absent below concentrations of 2% FBS (Figure 4.1C). While cells continued to grow in very low serum concentrations, cellular morphology was markedly disrupted at 0.25% FBS (Figure 4.1D), indicative of cellular death.

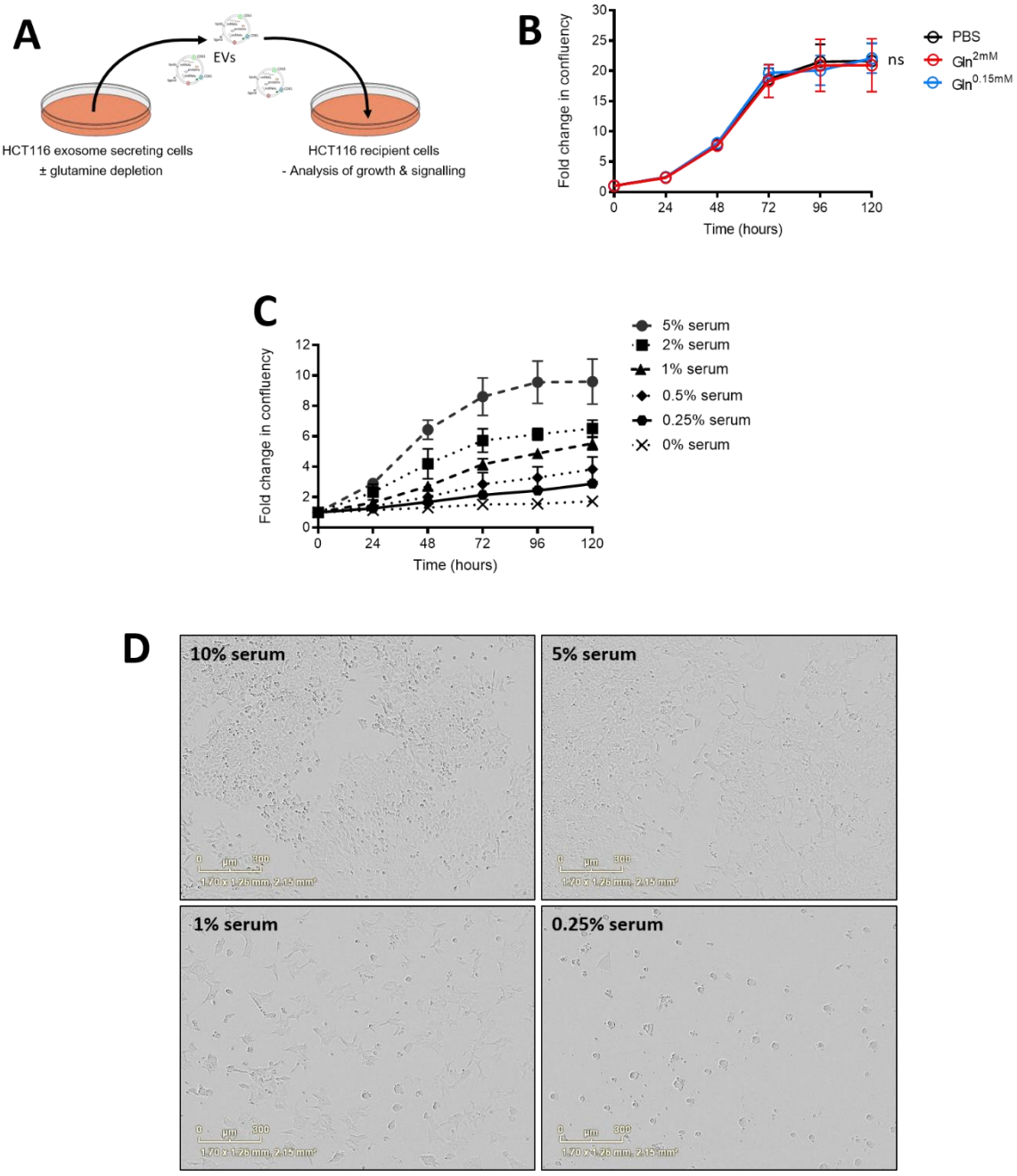



**Figure 4.1** Developing an *in vitro* assay to measure the effect of switched EVs on recipient CRC cells growth. (A) EVs were isolated by SEC from glutamine-replete or –depleted HCT116 cells, quantified using NTA and added to recipient HCT116 cells. Growth was measured using the IncuCyte® ZOOM Live Cell Imager. (B) Initial growth curve comparing effect of EVs isolated from glutamine-replete (2 mM, non-switched), –depleted (0.15 mM, switched) or vehicle (PBS) conditions on recipient cells grown in media containing 10% FBS. Fold change in confluency is a measure of cell area occupied within a well relative to time zero, as measured by the IncuCyte® software (n=8 per condition). (C) Growth curve comparing rate of HCT116 cell growth in media containing reducing concentrations of FBS. (D) Images from the IncuCyte® ZOOM Live Cell Imager showing HCT116 morphology in reducing concentrations of FBS.

#### 4.2.1.2 Switched EVs promote the dose-dependent growth of HCT116 recipient cells

Next growth assays were undertaken in reduced serum conditions (0.5% and 1% FBS) using an increasing number of EVs per recipient cell (1000 – 16,000 EVs /cell). These assays showed that switched EVs selectively stimulated recipient cell growth at concentrations above 4000 EVs per cell (Figure 4.2A), and that this positive effect on growth was dose-dependent (Figure 4.2B). EVs isolated from glutamine-replete cells did not significantly alter recipient cell growth compared to a PBS control. Through undertaking biological repeats of these assays, those performed in 1% serum using an EV concentration of 4000 EVs per recipient cell were found to be the most reproducible (Figure 4.2C). Interestingly, this EV concentration is roughly consistent with studies that have attempted to quantify the number of EVs released following MVB fusion with the plasma membrane per day (Bebelman et al. 2020; Veziroglu and Mias 2020). Therefore, unless stated otherwise, these conditions were utilised in all subsequent experiments.

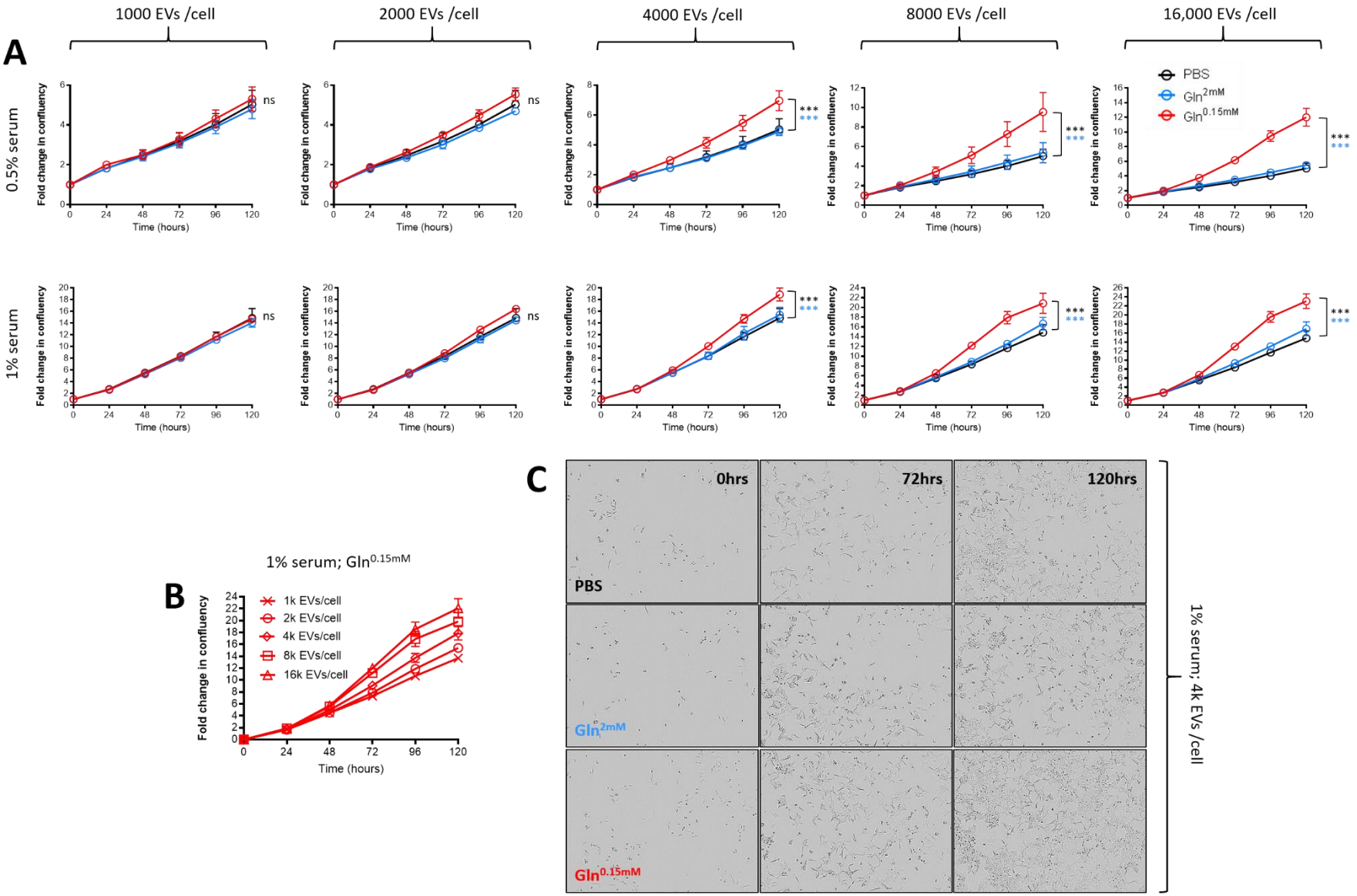

A
1000 EVs /cell
2000 EVs /cell
4000 EVs /cell
8000 EVs /cell
16,000 EVs /cell
0.5% serum
1% serum
Fold change in confluency
Time (hours)
ns
***
PBS
Gln2mM
Gln0.15mM
B
1% serum; Gln0.15mM
1k EVs/cell
2k EVs/cell
4k EVs/cell
8k EVs/cell
16k EVs/cell
C
0hrs
72hrs
120hrs
PBS
Gln2mM
Gln0.15mM
1% serum; 4k EVs /cell

**Figure 4.2** Switched EVs promote the dose-dependent growth of HCT116 recipient cells in reduced serum conditions. (A) Growth curves for HCT116 recipient cells in reduced serum (1% and 0.5%) conditions with increasing doses of non-switched ($Gln^{2mM}$), switched ($Gln^{0.15mM}$) EVs, or vehicle (PBS). (B) Combined growth curve demonstrating the dose-dependent growth promoting property of switched EVs on HCT116 recipient cell growth. (C) Images from the IncuCyte® ZOOM Live Cell Imager illustrating proliferative effect of switched EVs on recipient cell growth. The colour of the asterisks denotes significant increase in growth relative to culture in just PBS (black) or EVs from glutamine-replete secreting cells (blue). Growth curves show the mean ± SD (n=8 per condition) and are representative of results from three biological replicates.

When investigating the functional role of EVs, the MISEV guidelines stipulate that any observed activity must be proven to be EV-mediated, rather than secondary to other non-vesicular serum components (Thery et al. 2018). To do this, EVs isolated by SEC were pelleted using UC, and then compared with the supernatant, which was concentrated using UF to the same final volume as the resuspended EVs. The supernatant was devoid of the EV markers, including the EV switch signature (Figure 4.3A), and did not contain any EV-like structures on NTA (Figure 4.3B). Reassuringly, only the resuspended switched EVs promoted the growth of recipient cells (Figure 4.3C). In addition to this, parallel work undertaken by the Goberdhan Group, focussing on the intracellular mechanisms that control the secretion of Rab11a-exosomes has found that this process is dependent on the accessory ESCRT-III subcomplex component, CHMP5. Based on this finding, Dr Shih-Jung Fan (PDRA, Goberdhan Group) generated stably transduced HCT116 clones carrying an inducible lentiviral construct that expresses a shRNA targeting *CHMP5*, and found that induction of *CHMP5* knockdown under glutamine-deplete conditions selectively reduced Rab11a-exosome production (unpublished data). Consistent with this, shRNA knockdown of *CHMP5* reverses the growth promoting properties of Rab11a-exosomes (Figure 4.3D). This simultaneously provides evidence that the growth promoting property is EV-mediated, and is specific to the Rab11a-exosomes.

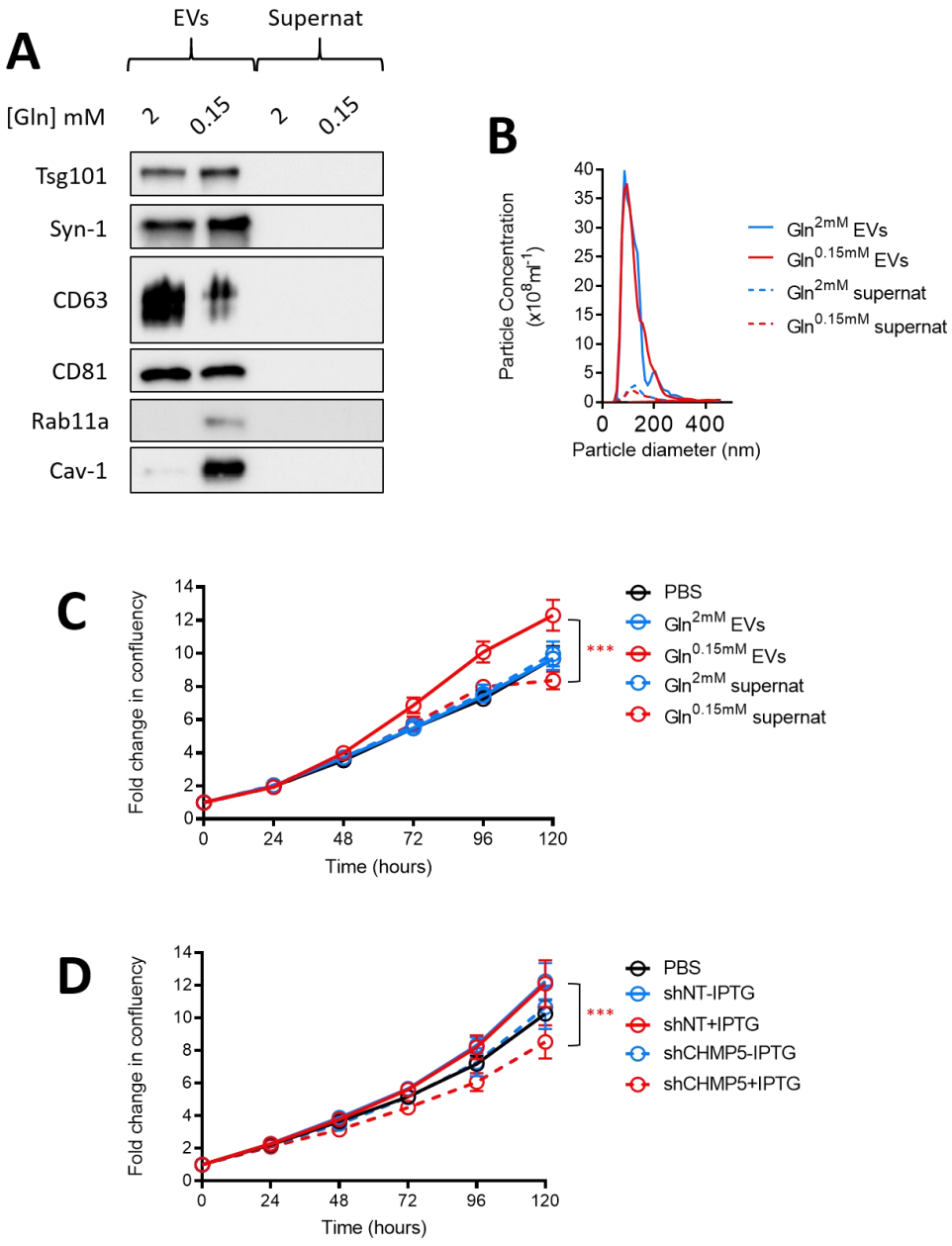



**Figure 4.3** EV depletion results in loss of the growth promoting property of switched EVs. (A) EVs were isolated from glutamine-replete (2 mM, non-switched) and –deplete (0.15 mM, switched) HCT116 cells using SEC, and then pelleted using UC. The EV pellet was resuspended in PBS, and the UC-supernatant underwent concentration using UF down to an equivalent volume. Western blot shows loss of the EV markers and EV switch signature in the concentrated UC-supernatant. (B) NTA showing that the UC supernatant was devoid of particles within the EV size range. (C) Growth curve comparing HCT116 recipient cell growth in response to treatment with EVs or the corresponding UC-supernatant, showing that EV depletion is associated with loss of the growth promoting properties of switched EVs. The colour of the asterisks denotes significant increase in growth relative to culture in just PBS (black), EVs from glutamine-replete secreting cells (blue) or the glutamine-replete UC-supernatant (red). (D) EVs were isolated from glutamine-depleted HCT116 cells carrying an inducible lentiviral construct expressing a shRNA targeting CHMP5 (generated by Dr Shih-Jung Fan), which is required for the secretion of Rab11a-exosomes. Induction

of CHMP5 knockdown was associated with loss of the growth promoting properties of switched EVs. Growth assays were undertaken using 4000 EVs per recipient cell in media containing 1% FBS and show (n=8 per condition).

#### 4.2.1.3 Amphiregulin is upregulated in switched EVs and is associated with increased EGFR/ERK signalling in recipient cells

Having shown that switched EVs are able to promote the growth of recipient HCT116 cells, attention was next directed towards investigating the mechanisms underlying this effect. A comparative proteomic analysis of non-switched and switched EVs isolated by UC, undertaken by Dr Shih-Jung Fan (PDRA, Goberdhan Group) indicated that the EGFR-ligand Amphiregulin (AREG) was upregulated in switched EVs. EGFR signalling is known to be important in the development of CRC cancer, whereby aberrant signalling has been correlated with advanced disease and poor prognosis (Spano et al. 2005). Furthermore, AREG is known to be expressed by HCT116 cells (Nagathihalli et al. 2014), and has been shown to be packaged into CRC-derived exosomes (Higginbotham et al. 2011). This finding was validated by western blotting, whereby glutamine depletion increased expression of a 26 kDa membrane-associated form of AREG in both EVs isolated using SEC and cell lysates (Figure 4.4A-B). Based on this finding, it was hypothesised that switched EVs could increase growth factor signalling via the EGFR signalling pathway. To test this, HCT116 recipient cells were serum starved overnight and then incubated with non-switched or switched EVs for between 5-15 minutes to assess EGFR and ERK phosphorylation (Figure 4.4C). The addition of EVs from glutamine-depleted cells enhanced the phosphorylation of EGFR and ERK under serum starved conditions, indicating that the growth promoting property of switched EVs is mediated via this signalling pathway.

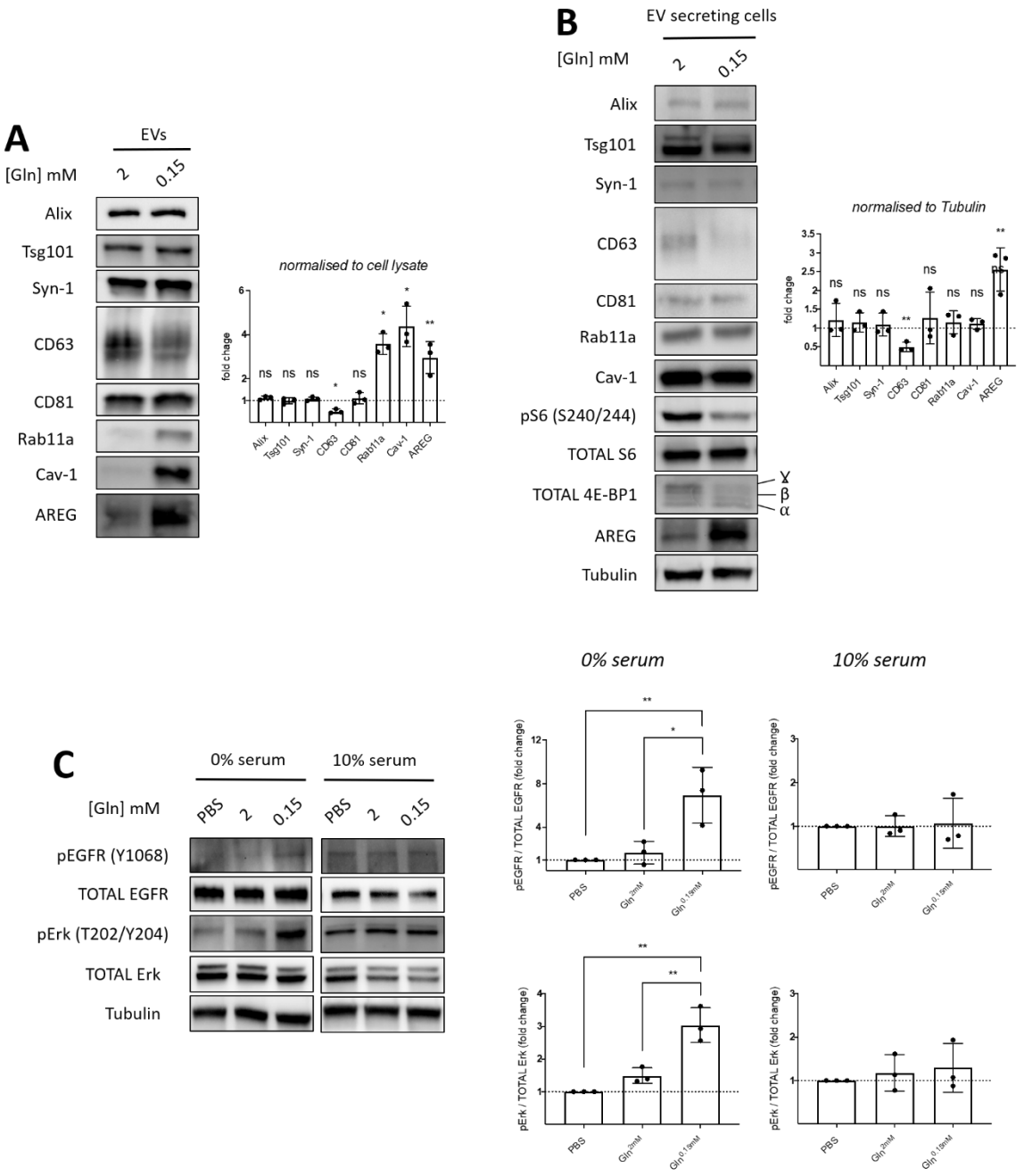



**Figure 4.4** AREG is upregulated in switched EVs and is associated with increased EGFR and ERK phosphorylation in recipient cells. (A) Western blot showing AREG levels in EVs isolated from glutamine-replete (2 mM, non-switched) or –deplete (0.15 mM, switched) HCT116 cells. (B) Western blot showing AREG levels are also increased within EV secreting cells grown under glutamine–depleted conditions for 24 hours. (C) Western blot of signalling assays undertaken in serum-starved (0% FBS) and serum-replete (10% FBS) HCT116 recipient cells, comparing phosphorylation of EGFR and ERK in response to treatment with PBS, non-switched or switched EVs (4000 EVs per recipient cell). Consistent with the growth promoting properties of switched EVs, activation of EGFR-ERK signalling was only observed in reduced serum conditions. Bar graphs show the mean ± SD of three biological replicates.

#### 4.2.1.4 AREG inhibition blocks the ERK-dependent growth promoting property of switched EVs

Previous studies into EV-associated AREG have also reported on its function as a potent activator of the EGFR pathway in recipient cells (Higginbotham et al. 2011; Raimondo et al. 2019; Q. Zhang et al. 2019b). Raimondo *et al* (2019) found that AREG was enriched in multiple myeloma-derived exosomes, and is able to promote the EGFR-dependent differentiation of osteoclasts, involved the development of osteolytic bone disease, which is one of the hallmarks of this malignancy. To validate this finding, the authors treated the exosomes with a neutralising anti-AREG monoclonal antibody, which reversed the effect on osteoclast differentiation. Therefore, similar experiments were undertaken to validate the role of AREG in promoting the ERK-dependent growth of HCT116 recipient cells. Reassuringly, incubating EV preparations from glutamine-depleted and control cells with the neutralising AREG antibody blocked the growth-promoting property of switched EVs (Figure 4.5A), and suppressed ERK activation in target cells (Figure 4.5B). Unfortunately, despite attempting multiple iterations of the method it was not possible to demonstrate suppression of EGFR phosphorylation using the AREG neutralising antibody. The reasons for this are unclear, as the signalling assays described in the previous section clearly show EGFR phosphorylation is enhanced by the switched EVs (Figure 4.4C), although the antibody staining was poor quality.

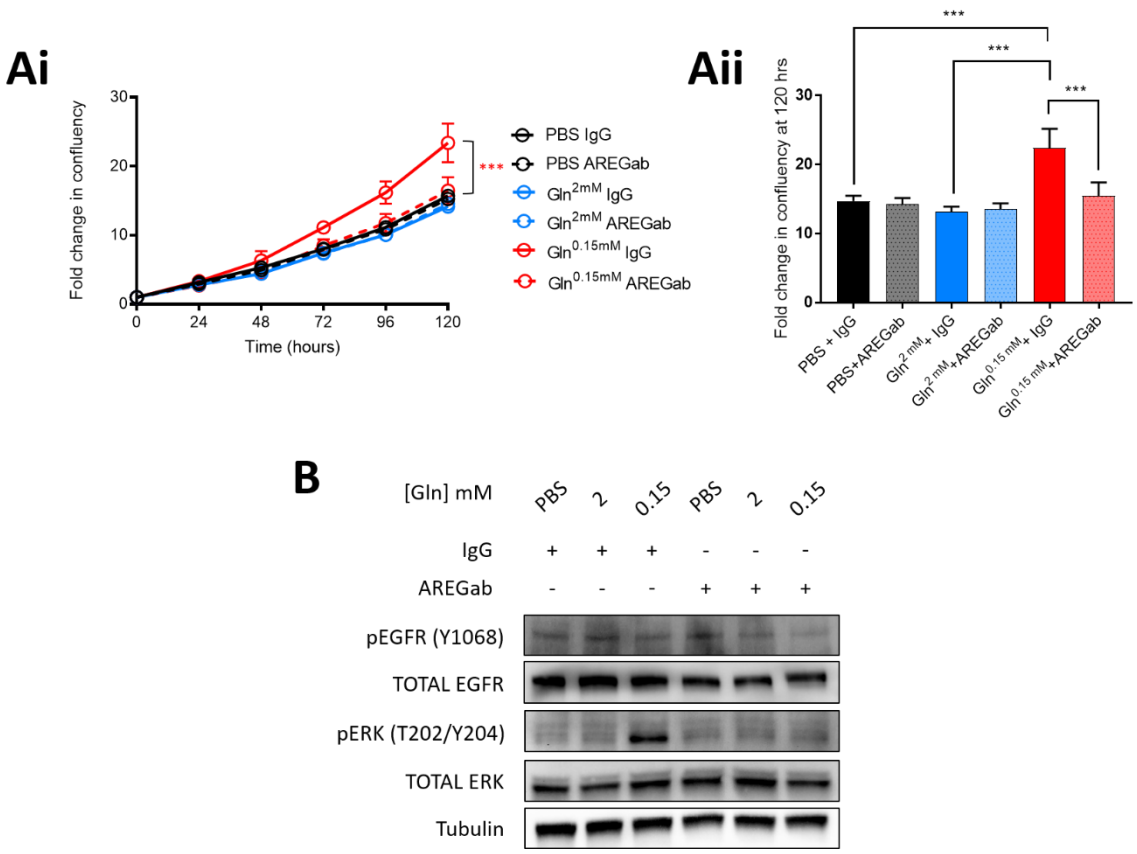



**Figure 4.5** The growth promoting property of switched EVs is AREG dependent. (Ai) Growth curve and (Aii) bar chart comparing proliferation of HCT116 recipient cells pre-treated with vehicle (PBS), non-switched ($Gln^{2mM}$) or switched ($Gln^{0.15mM}$) EVs, which themselves had been either pre-incubated with an AREG neutralising monoclonal antibody (AREGab) or a control IgG. The colour of the asterisks denotes significant increase in growth relative to culture in just PBS (black), EVs from glutamine-replete secreting cells (blue) or following pre-incubation with AREGab (red). (B) Western blot of EGFR and ERK phosphorylation in HCT116 recipient cells pre-treated with PBS, non-switched or switched EVs, with or without pre-incubation with AREGab or control IgG. Growth assays used 4000 EVs per recipient cell in media containing 1% FBS. Growth curves and bar graphs show the mean ± SD (n=8 per condition) and are representative of results from three biological replicates.

So far all of the functional data presented is based on EVs isolated from HCT116 cells grown in either glutamine-replete or -depleted conditions. To provide wider evidence for the role of switched EVs in promoting CRC cell growth, EVs isolated from HCT116 cells grown under hypoxic conditions, as well as Torin1 treated Caco-2 cells were also investigated. AREG expression was increased in EVs isolated from HCT116 cells grown in 1% $O_2$ (Figure 4.6A), with a corresponding AREG-dependent effect on recipient cells grown in reduced

serum conditions (Figure 4.6B). While these switched EVs did promote recipient cell growth, the relative extent of this increase was less when compared to switched EVs isolated from glutamine-depleted cells. It is possible that this is because hypoxia does not cause the reduction in CD63-positive EVs that is observed with glutamine depletion. These CD63-positive EVs may counteract some of the activity of the Rab11a-AREG containing exosomes.

Similarly, Caco-2 cells treated with Torin1 also produce switched EVs with increased levels of AREG (Figure 4.6C). While Caco-2 cells are usually cultured in high serum concentrations (20%), they still continued to grow at much lower concentrations (Figure 4.6D), without compromising morphology. While optimising the conditions for the growth assays it was found that the growth promoting property of switched EVs was only observed when serum concentrations for the recipient cells were as low as 0.25%, suggesting this cell line is much more resistant to nutrient depletion. This may also explain why glutamine depletion does not induce an EV switch in Caco-2 cells (Figure 3.13A). Caco-2 recipient cells also required double the concentration of switched EVs than are required by HCT116 recipient cells to produce a significant increase in growth (8000 EVs per cell as opposed to 4000 EVs per cell). Furthermore, the growth promoting property did not appear to be dose-dependent, although it was reversed by neutralising AREG (Figure 4.6F). The increased amount of EVs required to promote recipient cell growth may relate to the amount of AREG present on the EVs.

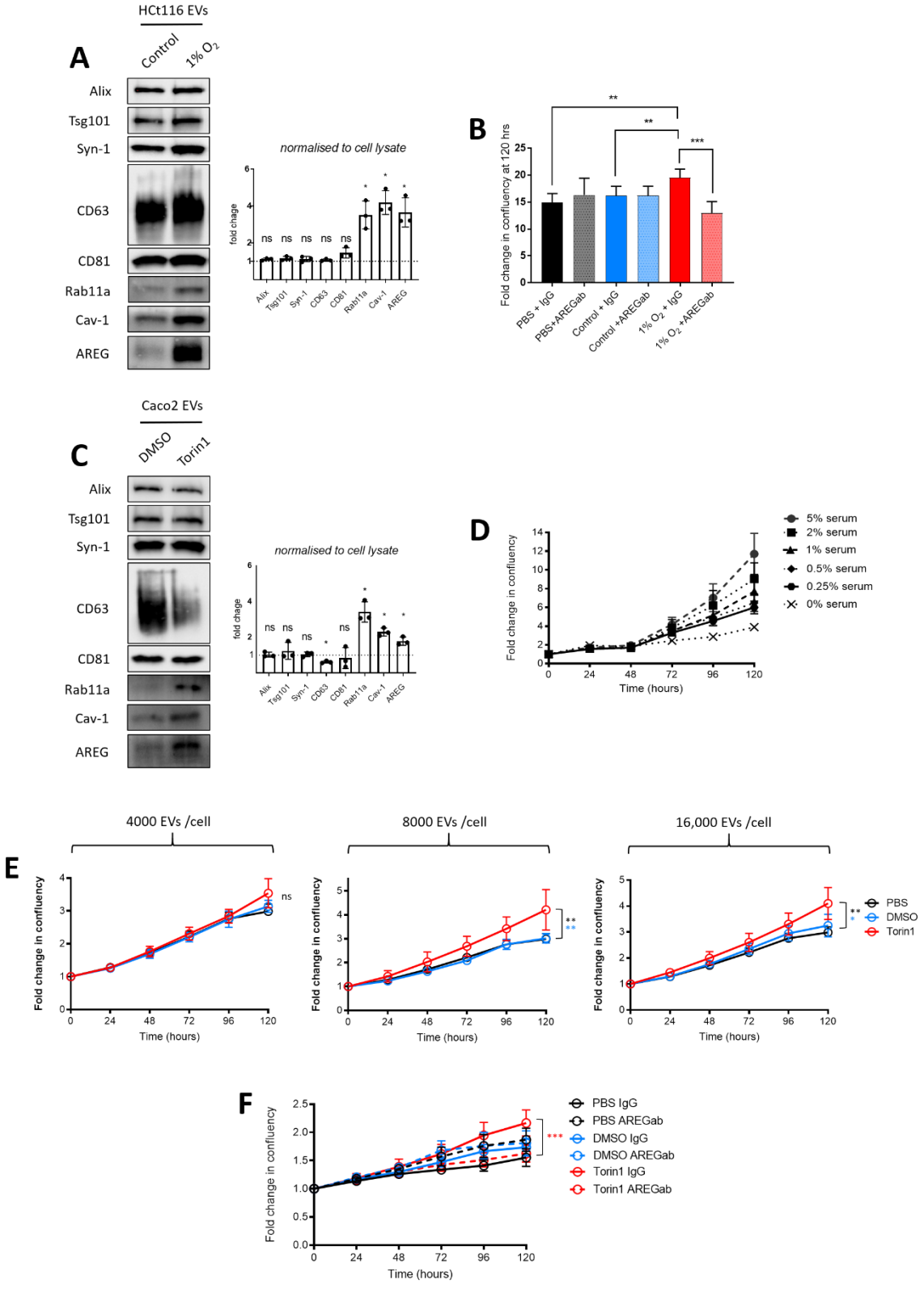



**Figure 4.6** Hypoxia and Torin1 also trigger the release of AREG-containing EVs that promote recipient cells growth. (A) Western blot showing AREG levels in EVs isolated from HCT116 secreting cells grown under control or hypoxic (1% $O_2$) conditions. (B) Bar chart bar comparing proliferation of HCT116 recipient cells (in 1% FBS) pre-treated with EVs isolated from secreting cells grown under standard culture or hypoxic conditions, which

themselves had been either pre-incubated with an AREG neutralising monoclonal antibody (AREGab) or a control IgG. (C) Western blot showing AREG levels in EVs isolated from Caco-2 secreting cells exposed Torin1 or vehicle (DMSO). (D) Growth curve comparing rate of Caco-2 cell growth in media containing reducing concentrations of FBS. (E) Caco-2 recipient cell growth in reduced serum (0.25%) conditions with increasing doses of non-switched (DMSO), switched (Torin1) EVs, or vehicle (PBS). The colour of the asterisks denotes significant increase in growth relative to culture in just PBS (black) or EVs from DMSO treated secreting cells (blue). (F) Growth curve comparing proliferation of Caco-2 recipient cells (in 0.25% FBS) pre-treated with PBS, non-switched (DMSO) or switched (Torin1) EVs, which themselves had been either pre-incubated with AREGab or a control IgG. The colour of the asterisks denotes significant increase in growth relative to EVs from Torin1 treated secreting cells that were pre-incubated with AREGab (red). Unless otherwise stated, growth assays used 4000 EVs per recipient cell, show the mean ± SD (n=8 per condition) and are representative of results from three biological replicates.

Collectively, this sequence of results provides strong evidence that microenvironmental stress induces the secretion of Rab11a EVs containing AREG, which play a pivotal role in the growth enhancing activity of switched EVs.

#### 4.2.1.5 Switched EVs from SW480 and SW620 cells do not contain AREG and do not promote recipient cell growth

Like Caco-2 cells, SW480 and SW620 cells also secrete Rab11a-positive exosomes when treated with Torin1. Surprisingly, despite this, EVs from both SW480 and SW620 cells do not contain AREG (Figure 4.7A) and also appear to express very low intracellular levels (Figure 4.7B), which are reduced under microenvironmental stress, including glutamine-depletion, which does not trigger an EV switch in these cell lines. This finding demonstrates the complexity of the intracellular mechanisms that underpin the EV switch, and is the focus of ongoing investigation by members of the Goberdhan Group.

Similar to Caco-2 cells, both SW480 and SW620 cells also maintain cell growth at very low serum concentrations (0.25%, Figure 4.7C). However, growth assays using control or switched EVs from SW480 and SW620 cells, including EVs isolated under glutamine-replete and -depleted conditions, and added to either SW480 or SW620 recipient cells did not exhibit any growth promoting properties that were specific to the stress-induced EVs

(Figure 4.7D). To exclude a dose-dependent response, this was checked using higher EV concentrations (up to 16,000 EVs per recipient cell), although no EV-subtype specific effect was observed. This negative finding provides further evidence that AREG is an essential stress-induced EV cargo required for promoting growth in recipient cells.

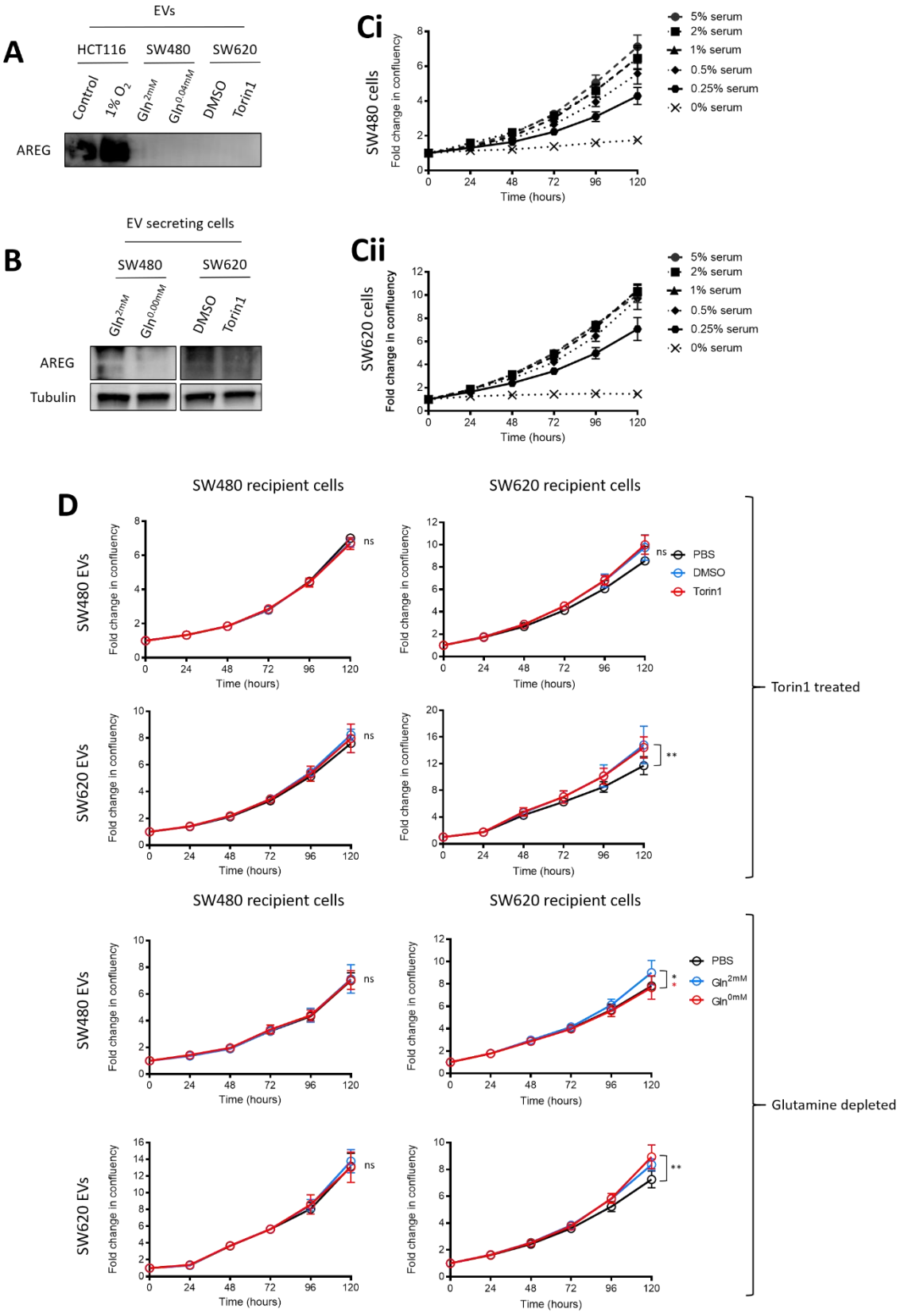



**Figure 4.7** Switched EVs from SW480 and SW620 cells do not contain AREG and do not promote recipient cell growth. (A) Western blot comparing AREG levels in non-switched and switched EVs from HCT116, SW480 and SW620 cells. (B) Western blot of AREG level expression in glutamine-replete (2 mM) or –deplete (0 mM) SW480 cells and in vehicle

(DMSO) or Torin1 treated SW620 cells. (Ci) SW480 and (Cii) SW620 cell growth in media containing reducing concentrations of FBS. (D) Growth curves showing SW480 and SW620 recipient cell growth (in 0.25% FBS) pre-treated with EVs isolated from either glutamine-replete or –depleted; or vehicle (DMSO) or Torin1 treated SW480 or SW620 secreting cells. Growth assays used up to 16,000 EVs per recipient cell, show the mean ± SD (n=8 per condition) and are representative of results from three biological replicates.

#### 4.2.1.6 The growth promoting property of switched EVs is transferrable to different CRC cell lines

As tumours represent the expansion of multiple different clones, tumorigenesis is likely to involve EV-mediated paracrine signalling between these genetically distinct cells (Xavier et al. 2020). To test this, switched EVs from HCT116 cells were added to Caco-2 recipient cells growing in reduced serum conditions (Figure 4.8A). As with HCT116 recipient cells, Caco-2 cell growth was strongly promoted by HCT116 Rab11a-positive exosomes (Figure 4.8B), although this effect did not appear to be dose responsive. An explanation for this may be that Caco-2 cells are in fact more sensitive to the growth promoting properties of HCT116 EVs, whereby the proliferative effect is already acting at its peak at 4000 EVs per cell, and that the dose response is demonstrated at lower EV concentrations. Interestingly, in contrast to HCT116 recipient cells, Caco-2 cells were also sensitive to high concentrations of non-switched EVs, whereby a small, yet significant decrease in proliferation was observed at 16,000 EVs per cell. It is possible that HCT116 cell growth is also reduced by non-switched EVs, although due to differences in sensitivity, higher EV concentrations are required for this to be observed. Further growth assays should be undertaken in Caco-2 recipient cells at higher EV concentrations to determine whether this inhibitory effect on growth is dose responsive.

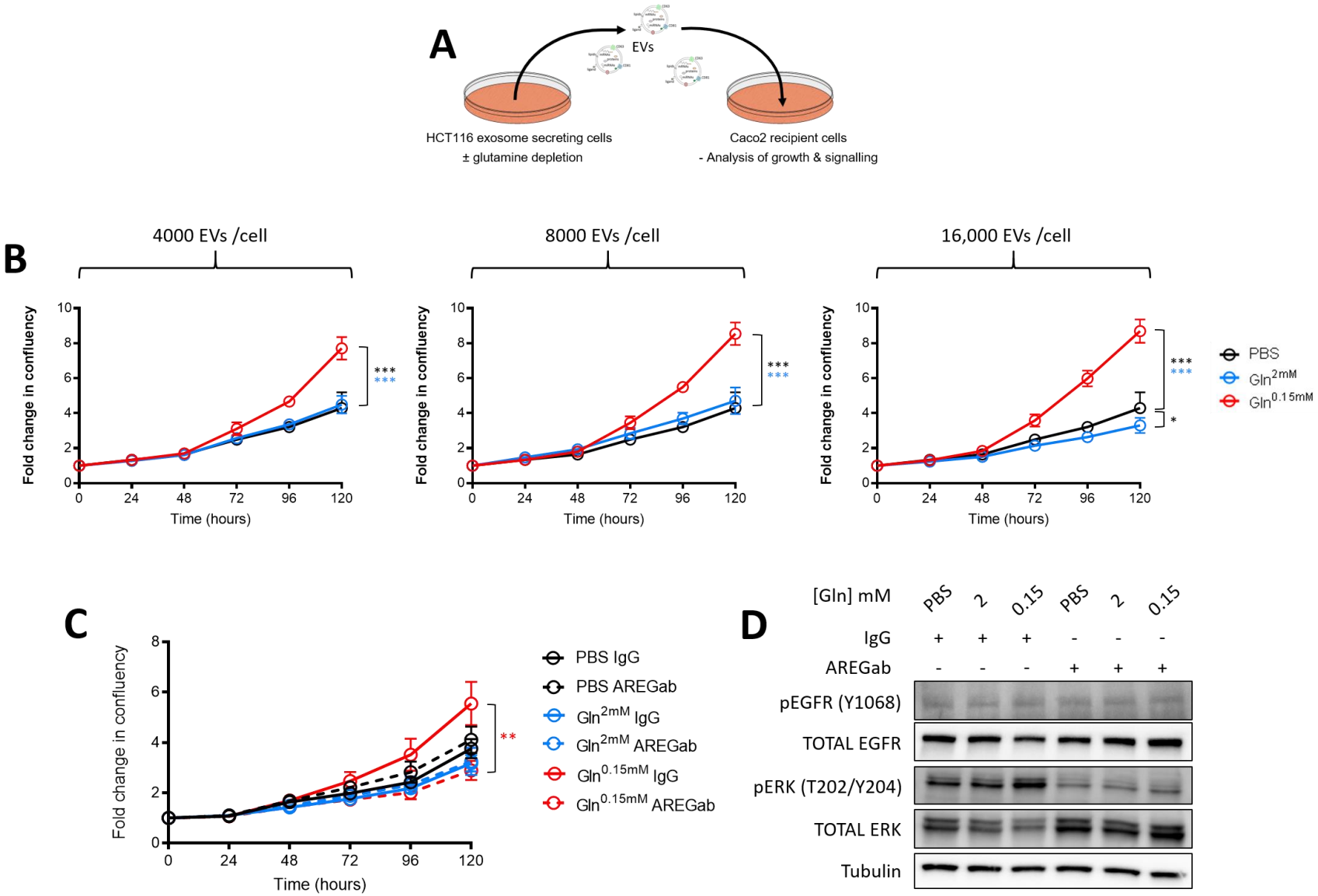

A
EVs
HCT116 exosome secreting cells
± glutamine depletion
Caco2 recipient cells
- Analysis of growth & signalling
B
4000 EVs /cell
8000 EVs /cell
16,000 EVs /cell
Fold change in confluency
Time (hours)
PBS
Gln2mM
Gln0.15mM
C
PBS IgG
PBS AREGab
Gln2mM IgG
Gln2mM AREGab
Gln0.15mM IgG
Gln0.15mM AREGab
D
[Gln] mM
PBS
2
0.15
IgG
AREGab
pEGFR (Y1068)
TOTAL EGFR
pERK (T202/Y204)
TOTAL ERK
Tubulin

**Figure 4.8** Switched EVs from HCT116 cells can promote the AREG-dependent growth of Caco-2 recipient cells. (A) EVs were isolated by SEC from glutamine-replete (2 mM, non-switched) or –depleted (0.15 mM, switched) HCT116 cells, quantified using NTA and added to recipient Caco-2 cells grown in reduced serum (0.25%) containing media. (B) Growth curves of Caco-2 recipient cell growth following exposure to increasing doses PBS, non-switched or switched HCT116 EVs. The colour of the asterisks denotes significant difference in growth relative to culture in just PBS (black) or EVs from glutamine-replete secreting cells (blue). (C) Caco-2 recipient cell growth, and (D) western blot of EGFR/ERK phosphorylation, following pre-treatment with PBS, non-switched or switched EVs from HCT116 cells (4000 EVs per recipient cell), which themselves had been either pre-incubated with an AREG neutralising monoclonal antibody (AREGab) or a control IgG. The colour of the asterisks denotes significant increase in growth relative to culture in just PBS (black), EVs from glutamine-replete secreting cells (blue) or following pre-incubation with AREGab (red). Growth curves show the mean ± SD (n=8 per condition) and are representative of results from three biological replicates.

As observed in HCT116 recipient cells, the growth promoting property of switched EVs in Caco-2 cells was also AREG dependent. Neutralisation of AREG led to a reversal of the proliferative effects of switched EVs (Figure 4.8C), and suppressed phosphorylation of ERK in target cells (Figure 4.8D). Unfortunately, as encountered during the HCT116 signalling assays, it was not possible to demonstrate any AREG-sensitive changes in EGFR activation. Interestingly, AREG neutralisation always resulted in a small, yet non-significant decrease in recipient cell growth when compared to a PBS control condition. These assays were undertaken using an EV dose of 4000 EVs per recipient cell, which was not a high enough dose of CD63 EVs to reduce the growth of target cells in the dose response experiments (Figure 4.8B). This highlights the fact that EV preparations contain a mixture of non-switched and switched EVs, the predominant subtype depending on the secreting cells mTORC1 signalling status. Upon neutralisation of AREG, the antiproliferative effects of CD63-positive EVs may begin to exert a greater effect on cell growth, which is highlighted during these assays due to the possible increased sensitivity of Caco-2 cells when compared with HCT116 target cells.

#### 4.2.1.7 Switched EVs that contain AREG are more potent than non-EV associated AREG

A previous study that investigated the transfer of pro-tumorigenic properties of AREG containing exosomes to different breast cancer recipient cells noted that these EVs were five times more potent than soluble AREG (Higginbotham et al. 2011). Subsequently, the same authors went onto demonstrate that extremely low concentrations of EV-associated AREG is required to activate EGFR signalling and enhance the growth of colonic tumour organoids (Q. Zhang et al. 2019b). Consistent with these results, ELISA measurements have shown that the AREG concentration transported by the dose of switched EVs required to promote recipient cell growth is extremely low, at approximately 1.4 pg/ml (Fan et al. 2020). To explore this further, Caco-2 recipient cells were exposed to either switched EVs, or increasing concentrations of recombinant AREG (rAREG, Figure 4.9). This revealed the potency of EV-associated AREG, whereby a dose of 30-300 ng/ml of rAREG was required to exert the same proliferative effect as that triggered by EV-associated AREG. The reasons underpinning this dramatic, more than 20,000 – 200,000 times greater activity are unclear, but may relate to the specific arrangement or conformation of AREG within the switched EVs, resulting in a stronger or more prolonged effect on EGFR. This highlights the therapeutic importance of targeting vesicle associated processes.

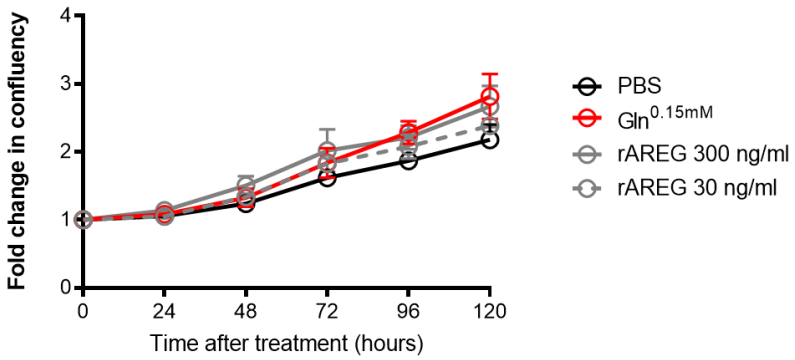



**Figure 4.9** EV-associated AREG is much more potent than recombinant AREG at promoting Caco-2 cell growth. Growth curve of Caco-2 recipient cells in reduced (0.25%) serum conditions that were exposed to switched EVs ($Gln^{2mM}$) from HCT116 secreting cells,

or increasing doses of rAREG (n=8 per condition). A dose of between 30-300 ng/ml of rAREG was required to increase recipient cell growth to the same level observed by adding 4000 EVs per recipient cell (equivalent to approximately 1.4 pg/ml of AREG).

#### 4.2.1.8 Switched EVs rescue cetuximab treated recipient cells via an AREG-dependent mechanism

EGFR-targeted monoclonal antibodies, such as cetuximab, are used in combination with traditional chemotherapy regimes in the treatment of *RAS* wild-type metastatic colorectal cancer, where it has been shown to improve progression free survival, overall survival and quality of life (Jonker et al. 2007). However, approximately 40% of patients have *KRAS* mutations, and 3% have *NRAS* mutations, rendering anti-EGFR therapies ineffective (S. H. Chen et al. 2019b). To demonstrate this HCT116 cells (*KRAS* mutant) and Caco-2 cells (*KRAS* wild-type) were treated with increasing doses of research grade cetuximab to determine its effect on growth and EGFR signalling. As predicted, HCT116 cell growth was unaffected in both full (10% FBS) and reduced (1% FBS) serum conditions (Figure 4.10A), whereas there was a dose-dependent decrease in Caco-2 cell proliferation under both serum conditions (Figure 4.10B). Similarly, EGFR-ERK signalling was reduced in Caco-2 cells treated with cetuximab, but was unaffected in HCT116 cells (Figure 4.10C).

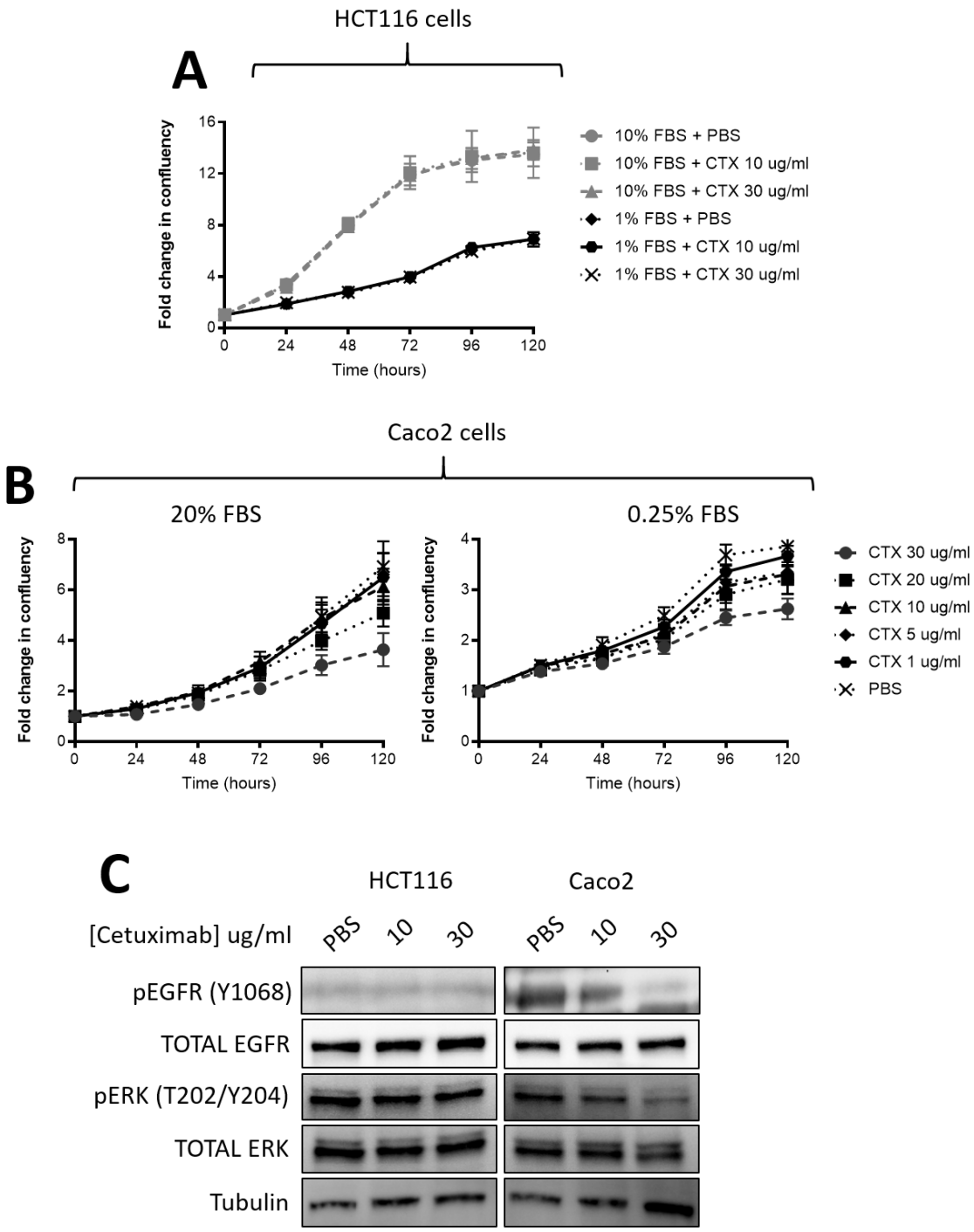



**Figure 4.10** Sensitivity to cetuximab (CTX) is dependent on *KRAS* status. (A) HCT116 (*KRAS* mutant) and (B) Caco-2 (*KRAS* wild-type) growth curves under full and reduced serum conditions with increasing doses of cetuximab (CTX, n=8 per condition). (C) Western blot comparing EGFR and ERK signalling in HCT116 and Caco-2 cells grown in full serum conditions with increasing doses of CTX.

Unfortunately, even in the relatively small proportion of patients that are sensitive to anti-EGFR therapies, most of these go on to develop drug resistance, which emerge through a

range of mechanisms, including: alterations in EGFR gene copy number, downstream mutations in RAS or BRAF and, or, activation of interconnected pathways, such as the PIK3/Akt or JAK/STAT signalling pathway (Sforza et al. 2016). However, current understanding of resistance mechanisms only accounts for approximately 35-50% of nonresponsive patients (B. Zhao et al. 2017a), although there is emerging evidence highlighting the role of cell-cell communication within the tumour microenvironment as potential drug resistance pathways, which may involve EV signalling (Giallombardo et al. 2016). Indeed, exosomes isolated from cetuximab-resistant CRC cells have previously been demonstrated to promote resistance in *KRAS* wild-type cells (S. Zhang et al. 2017b). Therefore, it was hypothesised that switched EVs isolated from glutamine-depleted HCT116 cells could block the growth inhibitory effect of cetuximab treated Caco-2 recipient cells. To test this, growth assays were undertaken by incubating Caco-2 cells with either cetuximab, stress-induced EVs from HCT116 cells, or both (Figure 4.11A). As observed in HCT116 recipient cells, switched EVs only promoted the growth of Caco-2 recipient cells in reduced serum conditions, and the growth inhibitory effect of cetuximab was clearly demonstrated in both conditions (Figure 4.11Bi-ii). This inhibitory effect was partially reversed by co-treatment with switched EVs (Figure 4.11Ci-ii). Interestingly, the switched EVs had an effect in both full serum and reduced serum conditions, although the degree of rescue was greater in the reduced serum conditions. Furthermore, this restorative effect on growth was itself reversed by pre-incubating EVs with the AREG neutralising antibody in both serum conditions (Figure 4.11Di-ii).

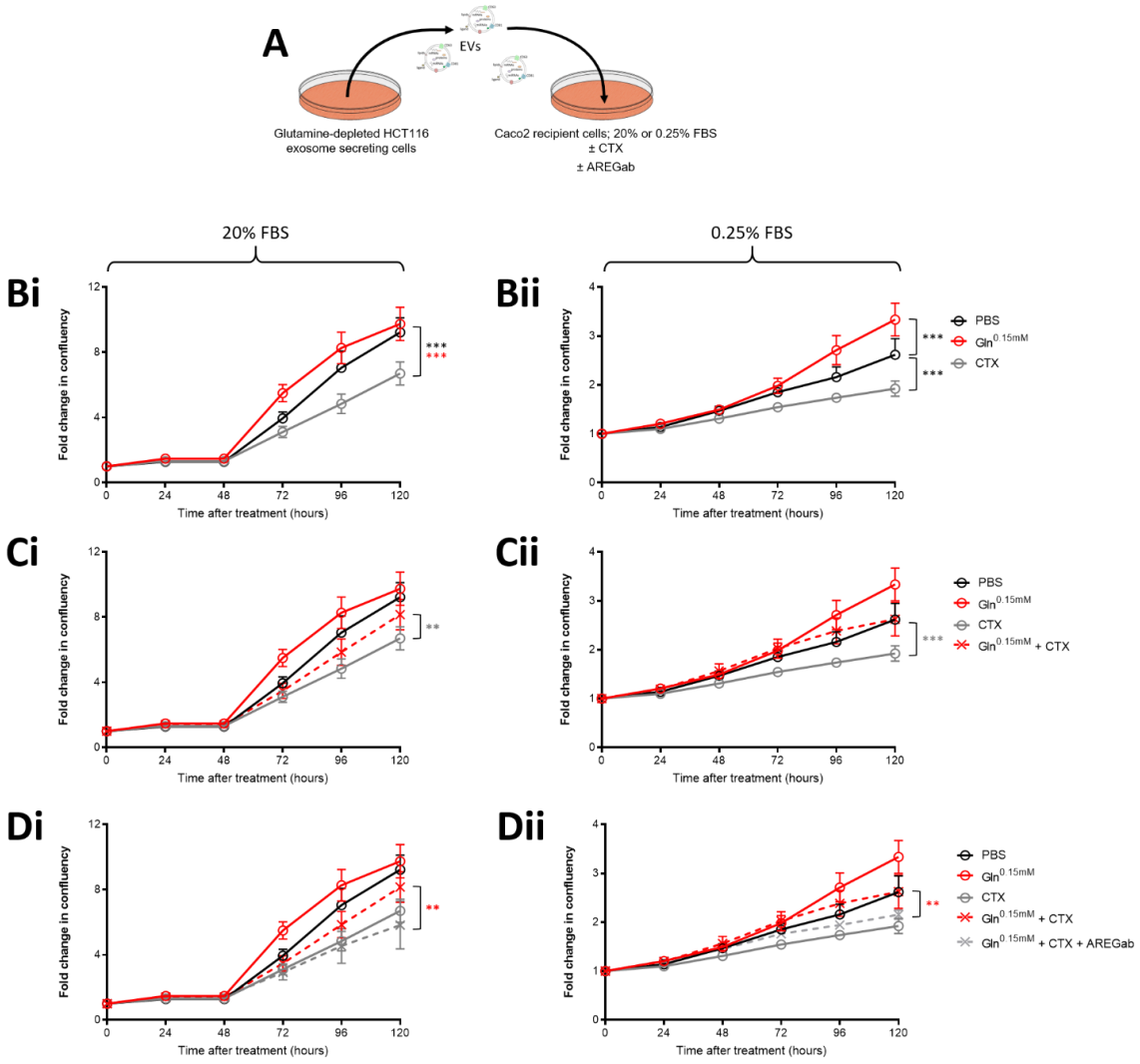



**Figure 4.11** Switched EVs isolated from HCT116 cells promote AREG-dependent cetuximab resistance in Caco-2 recipient cells. (A) Caco-2 recipient cells cultured in either full (20% FBS) or reduced (0.25% FBS) serum conditions were treated with either cetuximab (30 µg/ml, CTX), switched EVs ($Gln^{0.15mM}$) from HCT116 secreting cells with or without pre-treatment with an AREG neutralising monoclonal antibody (AREGab). (B-D) Sequential graphical build-up of Caco-2 growth curves following exposure to each experimental condition in either 20% FBS (Bi-Di) or 0.25% FBS (Bii-Dii). (B) CTX inhibits the growth of Caco-2 cells in both serum conditions. The colour of the atserisks denotes significant difference in growth relative to culture in just PBS (black) or also in the presence EVs from glutamine-deplete secreting cells (red). (C) Co-treatment with switched EVs partially reverses the growth inhibitory effect of CTX. (D) Switched EV-induced CTX resistance is reversed by pre-incubating EVs with AREGab. The growth curves were generated using an EV dose of 4000 EVs per recipient cell, show the mean ± SD (n=8 per condition) and are representative of three biological repeats.

Since an anti-AREG antibody can block the effect of the stress-induced EVs on cetuximab mediated inhibition of Caco-2 cell growth, this raised the question of whether this vesicle-

mediated effect was mediated through the EGFR, via a receptor-ligand competition or displacement mechanism, or via an alternative pathway. The best way to investigate this would be to undertake further signalling assays to measure changes in EGFR activation using western blotting, but it was not possible to optimise these assays despite multiple attempts. Therefore, an alternative approach was employed, based on testing whether the switched EVs could suppress the effects of inhibitors that target the downstream EGFR catalytic domain (EGFR kinase). Caco-2 cells grown in full serum were treated with the selective and potent EGFR kinase inhibitors AG1478 and BMS599626 (Ashar et al. 2020; Soria et al. 2019), both of which exhibited inhibitory effects on proliferation within 48-hours (Figure 4.12A-B). The switched EVs were unable to suppress the effects of either inhibitor, supporting the hypothesis that EV-mediated cetuximab rescue occurs via AREG acting on the cell surface via EGFR.

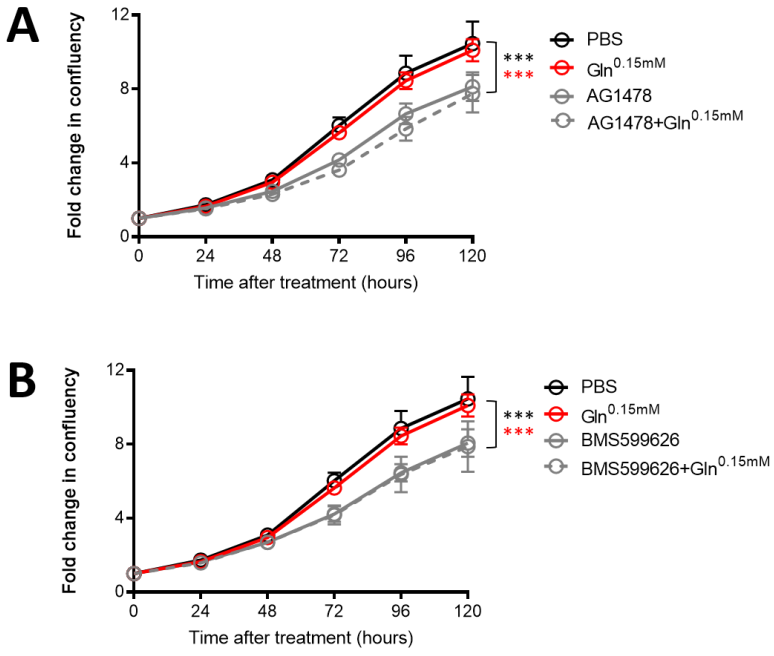



**Figure 4.12** AREG-containing EVs promote growth and drug resistance in recipient cells by binding to the EGFR receptor. (A) Caco-2 cell growth in 20% FBS following exposure to the EGFR inhibitors AG1478 and (B) BMS599626 with or without pre-treatment with switched EVs isolated from HCT116 secreting cells ($Gln^{0.15mM}$, 4000 EVs per recipient cell, n=8 per condition). The colour of the asterisks denotes significant difference in growth relative to culture in just PBS (black) or EVs from glutamine-deplete secreting cells (red).

### 4.2.2 Studying the effect of switched EVs on tumour growth *in vivo*

#### 4.2.2.1 Switched EVs promote AREG-dependent tumour growth in an *in vivo* chick embryo model

To test whether the growth promoting properties of switched EVs could be replicated *in vivo*, a series of HCT116 xenograft experiments were undertaken using a chick embryo model (Crespo and Casar 2016). These experiments were performed in collaboration with Dr Yaiza García Ibáñez, (Crespo Group, Instituto de Biomedicina y Biotecnología, IBBTEC de Cantabria, Santander, Spain). This model involves grafting tumour cells onto the chorioallantoic membrane (CAM) that surrounds the chicken embryo inside the fertilised egg. Within three to five days an organised tumour structure develops, including vascularisation and extracellular matrix formation, recapitulating features found within the tumour microenvironment (B. T. Vu et al. 2018). Tumour development occurs within days, which is in contrast to the much longer durations required to grow tumours in mice (weeks to months). Moreover, these experiments are much less expensive when compared to other animal models as they are undertaken before the maturation of the embryos immune system, negating the need to breed specific immunodeficient lines. Therefore, this model overcomes many of the limitations of other animal models.

Using a similar method utilised during *in vitro* assays, HCT116 recipient cells were incubated with either control or switched EVs and grafted onto the CAM of nine-day old chick embryos. After five days of growth, tumours were harvested for analysis. Switched EVs increased recipient cell growth, resulting in tumours that were on average 50% larger than tumours grown under control and non-switched EV treated conditions (Figure 4.13A). Furthermore, consistent with the results of *in vitro* experiments, this growth promoting property was reversed by incubating switched EVs with an AREG neutralising antibody (Figure 4.13B). In addition, the macroscopic features of the tumours appeared different (Figure 4.13C), whereby switched EVs promoted the development of larger tumours that had an exophytic, lobular appearance. This was in contrast to the flat, sessile-like tumours

grown when recipient cells were incubated with non-switched EVs or a PBS control. The exophytic growth pattern was also reversed when AREG was neutralised.

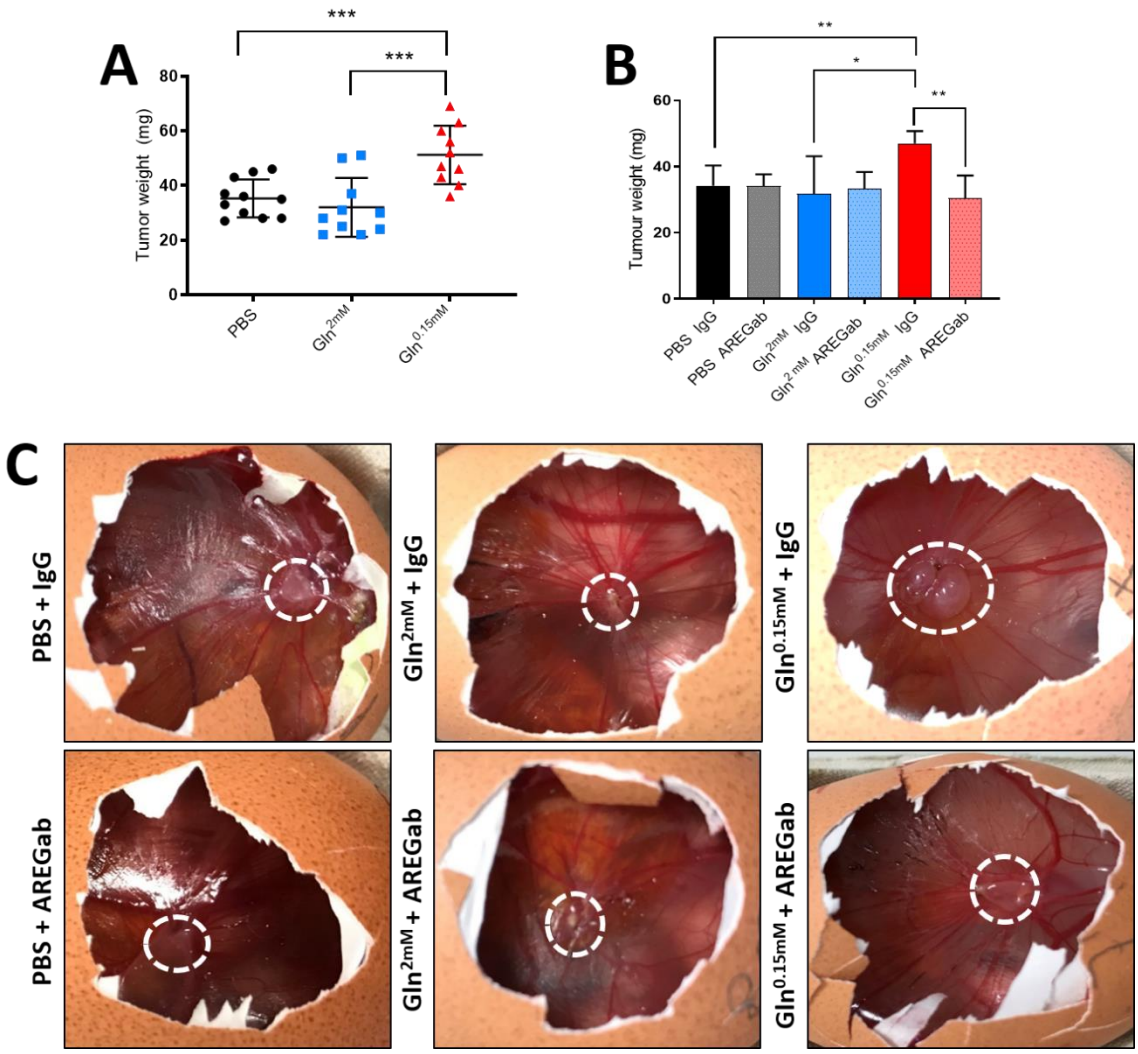



**Figure 4.13** Switched EVs isolated from HCT116 cells promote AREG-dependent tumour growth *in vivo*. (A) Scatter plot comparing tumour weight of HCT116-xenografts generated by mixing recipient cells with either PBS, non-switched ($Gln^{2mM}$) or switched ($Gln^{0.15mM}$) EVs prior to grafting onto the chick embryo CAM ($n \geq 3$ per condition). (B) Bar chart and (C) photographs comparing tumour weight and size of HCT116-xenografts pre-treated with PBS, non-switched or switched EVs, which themselves had been either pre-incubated with an AREG neutralising monoclonal antibody (AREGab) or a control IgG. HCT116-xenografts used 4000 EVs per recipient cell and for the assays that did not test the effect of adding AREGab, are representative of results from three biological replicates.

The microscopic features of the tumours were also examined using immunohistochemistry, which was undertaken in collaboration with Dr Esther Bridges (Weatherall Institute of

Molecular Medicine, University of Oxford). Consistent with larger tumours, treatment with switched EVs was associated with increased expression of the proliferation marker Ki-67 (Figure 4.14A). Ki-67 is expressed by all dividing cells, and accumulates in cells rapidly progressing through S, G2 and M phases of the cell cycle (Miller et al. 2018). A meta-analysis of 6180 patients found that high Ki-67 expression correlates with poor overall and disease-free survival in CRC (Luo et al. 2019). The *in vitro* growth signalling assays showed that switched EVs increased phosphorylation of ERK, and histologically this coincides with increased nuclear localisation of activated ERK, where it promotes the expression of genes driving cellular proliferation (Figure 4.14B). Additional staining for markers of hypoxia (CA9) and angiogenesis (CD31) were undertaken, but did not reveal any significant changes (data not shown).

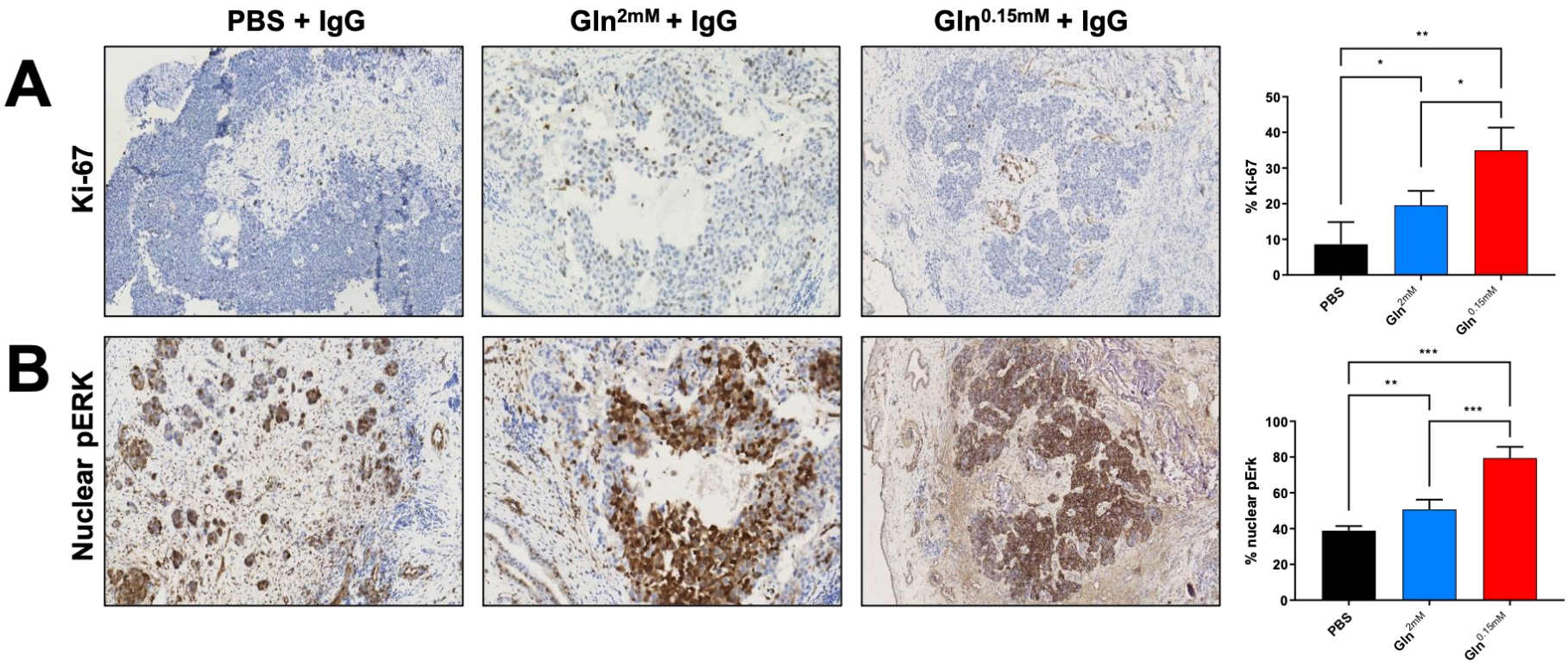

PBS + IgG
Gln2mM + IgG
Gln0.15mM + IgG
A
Ki-67
% Ki-67
PBS
Gln2mM
Gln0.15mM
B
Nuclear pERK
% nuclear pErk

**Figure 4.14** Switched EVs promote recipient cell proliferation and nuclear localisation of activated ERK *in vivo*. (A) Sections immunostained for the cellular proliferation marker, Ki67, and, (B) nuclear localisation of phospho-ERK within primary HCT116-xenograft tumours five days after pre-treatment with vehicle (PBS), non-switched ($Gln^{2mM}$) or switched ($Gln^{0.15mM}$) EVs. Bar graphs show the mean ± SD and are were generated from the analysis of sections from at least three tumours per condition.

### 4.2.3 Studying the effect of switched EVs on colorectal cancer cell migration and invasion

#### 4.2.3.1 Switched EVs reduce recipient cell migration and invasion *in vitro* through an AREG-independent mechanism

Metastasis is the leading cause of cancer-related mortality (van Zijl et al. 2011). The early stages of this multistep process include changes in tumour cell phenotype, leading to increased cellular motility, local infiltration into adjacent tissue and invasion into local blood and lymphatic vessels (Fares et al. 2020). There is growing evidence highlighting the role of EVs in driving these phenotypic changes through a range of inter and intracellular communication mechanisms (H. Zhao et al. 2018). Therefore, alongside experiments exploring the EV-mediated effects on CRC cell growth, parallel experiments investigating the effects on migration and invasion were also undertaken. Initially, migration was examined in HCT116 recipient cells using a scratch-wound assay. Once fully confluent, wounds were created using the IncuCyte® WoundMaker tool and then fresh reduced serum (1% FBS) media was added containing EVs isolated from glutamine-replete or depleted secreting cells, or a PBS control. EVs were added at a dose of 4000 EVs per recipient cell. Migration into the wound was then measured using the IncuCyte® ZOOM Live Cell Imager. As cell migration and invasion are associated with increased EGFR/ERK signalling (Higginbotham et al. 2011), which is promoted by AREG-containing EVs, it was hypothesised that treatment with switched EVs would promote both of these processes. However, surprisingly, there was a significant reduction in the migration of recipient cells treated with switched EVs as demonstrated by an average relative wound density after 48-hours of 46.8%, compared with 55.2% (PBS control) and 58.8 (non-switched EVs, Figure 4.15A-B). Similarly, as was also the case during growth assays, this effect was not

observed in full serum conditions (Figure 4.15C), suggesting that the switched EV-mediated reduction in migration is also an adaptive response to a nutrient depleted microenvironment.

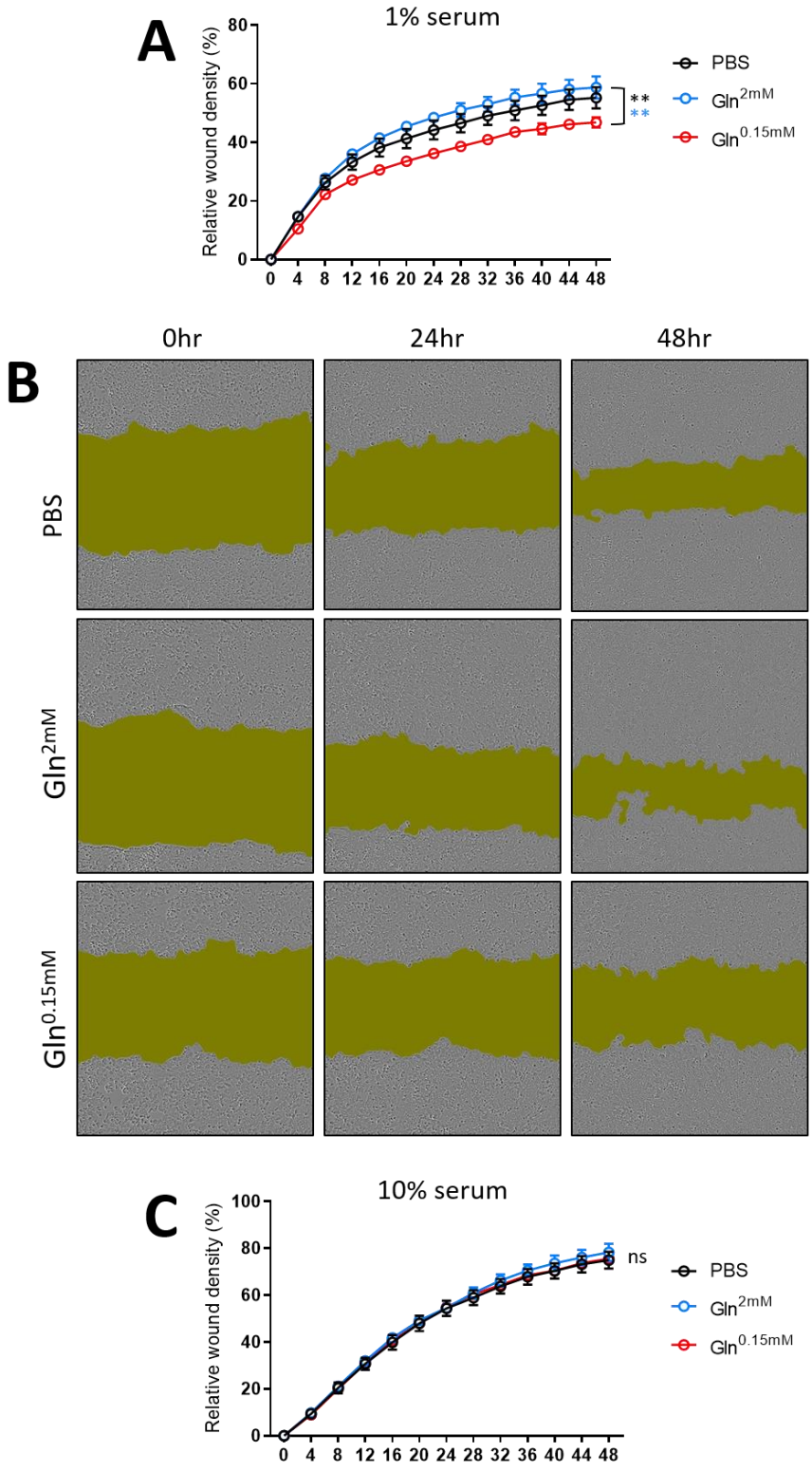


**Figure 4.15** Switched EVs reduce recipient cell migration *in vitro* under serum-deplete but not serum-replete conditions. (A) Relative wound density curves, and, (B) images comparing HCT116 recipient cell migration after 48 hours in reduced serum (1% FBS) following treatment with PBS or EVs isolated from glutamine-replete (2mM, non-switched) or –depleted (0.15mM, switched) HCT116 cells. (C) The switched-EV mediated reduction in recipient cell migration was not replicated in full serum (10% FBS) conditions. The colour of the asterisks denotes significant decrease in migration relative to culture in just PBS (black) or EVs from glutamine-replete secreting cells (blue). Scratch-wound assays show the mean ± SD (n=8 per condition) and those performed using 1% FBS are representative of results from three biological replicates.

A limitation of using the scratch-wound assay to measure migration is the confounding effect of proliferating cells at the wound edge. This is particularly relevant for HCT116 cells, which have a doubling time of less than 24-hours (Ahmed et al. 2013), and are resistant to drugs, such as mitomycin C, which are commonly used during these assays to inhibit proliferation (Willson et al. 1984). However, it could be argued that these factors provide additional support for the EV-mediated reduction in cell migration, as switched EVs also increase recipient cell proliferation, meaning that the actual reduction in migration may be even larger than was observed. To explore this further, an alternative migration assay was subsequently undertaken using the Boyden (transwell) chamber assay (H. C. Chen 2005). This technique uses a hollow plastic chamber, sealed at one end with a porous membrane to which recipient cells are added in serum-depleted (0% FBS) media. This chamber is suspended over a larger well containing serum-replete media (10% FBS), which promotes the migration of cells through the pores to the contralateral side of the membrane (Figure 4.16A). Consistent with the results of the scratch-wound assays, switched EVs reduced recipient cell migration by up to 50% after 24-hours, and up to 35% after 48-hours (Figure 4.16B). Additional assays were undertaken to explore invasion, whereby a Matrigel® layer was added on top of the porous membrane to replicate the extracellular matrix that is traversed by invasive tumour cells. Similarly, switched EVs led to a significant reduction in recipient cell invasion after 24-hours (Figure 4.16C). Future experiments should focus on whether this reduction in migration and invasion is dose-dependent, which may also reveal a role of the non-switched EVs.

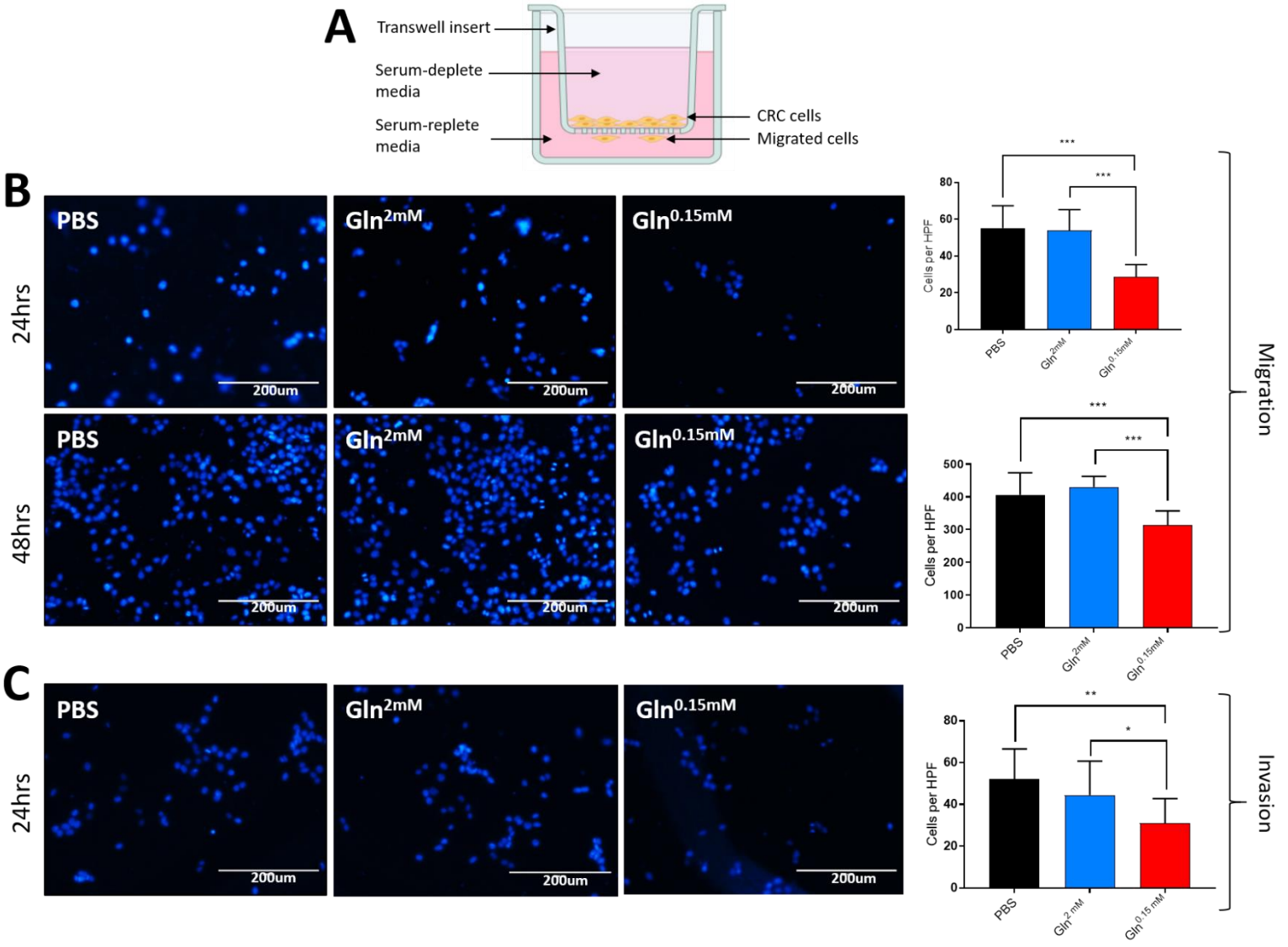

A
Transwell insert
Serum-deplete media
Serum-replete media
CRC cells
Migrated cells
B
24hrs
48hrs
PBS
Gln2mM
Gln0.15mM
200um
Cells per HPF
Migration
C
Invasion
***
**
*

**Figure 4.16** Switched EVs isolated from HCT116 cells reduce the Transwell migration and invasion or recipient cells. (A) Boyden chamber assays were undertaken using HCT116 recipient cells, which were mixed with PBS, non-switched ($Gln^{2mM}$) or switched ($Gln^{0.15mM}$) EVs in 0% serum and added to the top chamber of a transwell plate, which contains a porous membrane (with the addition of a Matrigel® layer for invasion assays), and suspended within a larger well containing full (10%) serum. (B) Migration or (C) invasion were assessed after 24-48 hours by counting the number of HCT116 cells per high power field (HPF) that had traversed the porous membrane to the contralateral side. Treatment with switched EVs was associated with significantly reduced migration and invasion. Bar graphs show the mean ± SD (n=3 per condition with five random HPFs assessed per well) and is representative of three biological repeats.

Previous studies have highlighted the role of exosomes containing AREG in controlling cancer cell migration and invasion. Higginbotham *et al* (2011) showed that AREG-containing exosomes increase the invasiveness of breast cancer recipient cells by up to four-fold compared with control EVs. This result is clearly in contrast to the data presented here, which shows that switched EVs lead to a significant reduction in recipient cell migration and invasion. Therefore, to explore this further, additional Boyden chamber assays were undertaken whereby EVs were pre-incubated with an AREG neutralising antibody prior to being added to recipient cells. In contrast to proliferation, inhibition of AREG did not reverse the effect of switched EVs on migration or invasion (Figure 4.17A-B), suggesting that this is an AREG-independent phenomenon. This finding underlies the fact that EVs contain rich bioactive cargoes, which can impact different cellular behaviours through a range of distinct mechanisms.

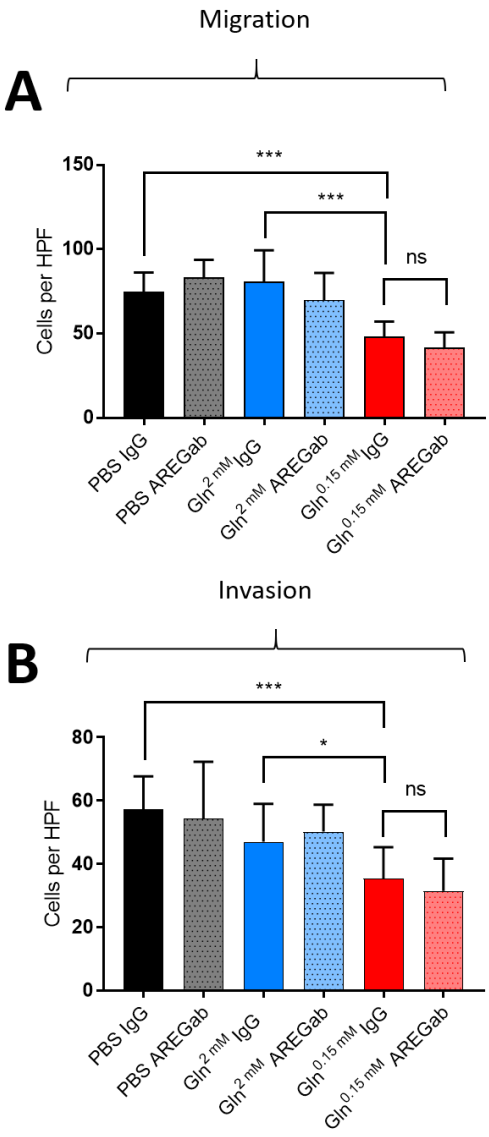



**Figure 4.17** The switched EV-mediated reduction in recipient cell migration and invasion is AREG-independent *in vitro.* (A) Transwell migration and (B) invasion assays were performed by mixing HCT116 recipient cells pre-treated with PBS, non-switched ($Gln^{2mM}$) or switched ($Gln^{0.15mM}$) EVs, which themselves had been either pre-incubated with an AREG neutralising monoclonal antibody (AREGab) or a control IgG (n=3 per condition with five random HPFs assessed per well). Unlike proliferation, the EV-mediated effects on migration and invasion were not AREG-dependent. Bar graphs show the mean ± SD.

### 4.2.3.2 Studying the effect of switched EVs on HCT116 recipient cell invasion *in vivo*

The chick embryo model can also be utilised to investigate the invasiveness of cancer cells (Crespo and Casar 2016). This is done by harvesting a section of the distal CAM, which lies diametrically opposite the site where tumours cells were initially grafted (Figure 4.18A). Colonisation of the distal CAM requires tumour cells to have invaded into the dense

capillary network of the CAM (intravasation), where they can then travel within the CAM vasculature and develop secondary tumour deposits, or metastases. These can then be measured using qRT-PCR by amplifying human *Alu* sequences expressed by the HCT116 cells. Consistent with *in vitro* assays, switched EVs significantly reduced distal CAM colonisation when compared with a PBS control, although this reduction was not significant when compared with non-switched EVs (Figure 4.18B). However, in contrast to the *in vitro* experiments this reduction in intravasation did appear to be AREG-dependent.

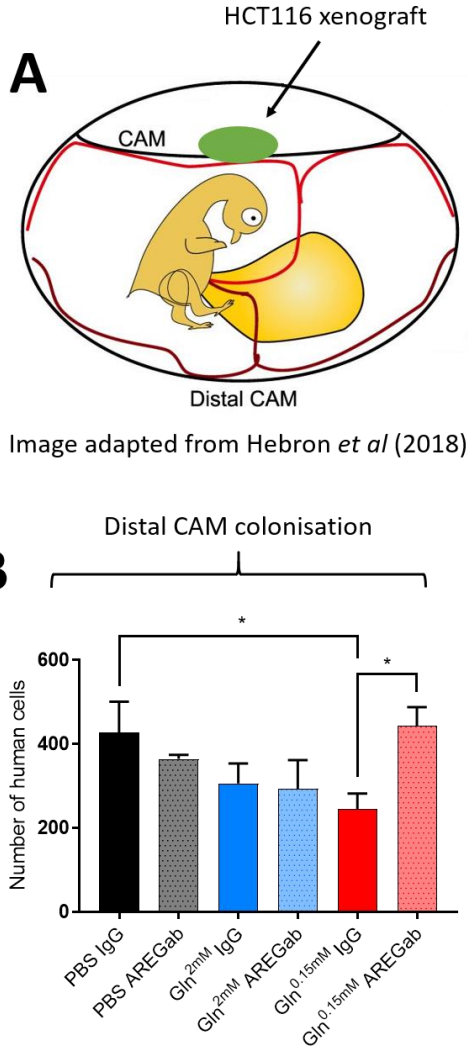



**Figure 4.18** Intravasation and distal CAM colonisation is affected by switched EVs *in vivo* and appears to be AREG-dependent. (A) In the chick embryo model, the area diametrically opposite the site of tumour cell grafting is known as the distal CAM. Tumour cells may intravasate into the CAMs rich blood supply and spread to the distal CAM, leading to the development of secondary tumour deposits, or metastases. Image adapted from Hebron et

al. (2018). (B) Bar chart comparing distal CAM colonisation of xenograft cells generated by pre-treating HCT116 recipient cells with PBS, non-switched ($Gln^{2mM}$) or switched ($Gln^{0.15mM}$) EVs, which themselves had been either pre-incubated with an AREG neutralising monoclonal antibody (AREGab) or a control IgG ($n \geq 3$ per condition). Bar graphs show the mean ± SD.

Once cancer cells have undergone intravasation into the dense vascular network of the CAM they have direct access to the developing embryo where metastases can also develop. Lung and liver metastases were also investigated during these experiments, with widespread tumour deposits detected in each, although there were no significant differences between the various conditions (data not shown). Despite this, it is not possible to make any conclusions based on this set of results because the model was initially used to study primary tumour growth, and was not optimised to study metastasis. This was reflected by the harvested organs containing very high quantities of human DNA that exceeded the standard curves limits for accurate measurement.

#### 4.2.3.3 Switched EVs reduce the expression of mesenchymal protein markers *in vitro* and *in vivo*

The processes that underpin metastasis, including intravasation of tumour cells into the blood or lymphatic system, and subsequent exit (extravasation) at a distant site, requires a reciprocal two-way phenotypic transformation (Figure 4.19A). During tumorigenesis, certain primary cancer cells will develop changes in their morphology, characterised by loss of epithelial features and concomitant gain of mesenchymal gene expression (epithelial-to-mesenchymal transition, EMT). At a protein level, EMT is characterised by downregulation of E-cadherin, which is an essential component of adherence junctions that bind epithelial cells together. Coinciding with this is the increased expression of vimentin, fibronectin and N-cadherin, which leads to cytoskeletal rearrangements and increased cell mobility (van Zijl et al. 2011). Cancer cells that have undergone EMT are able to invade through the epithelial ECM and intravasate into the blood and lymphatic systems, ultimately leading to metastatic spread. The process of EMT is then reversed at the site of secondary tumour

development (mesenchymal-to-epithelial transition, MET), whereby circulating tumour cells reacquire epithelial features and establish cell-to-cell adherence junctions.

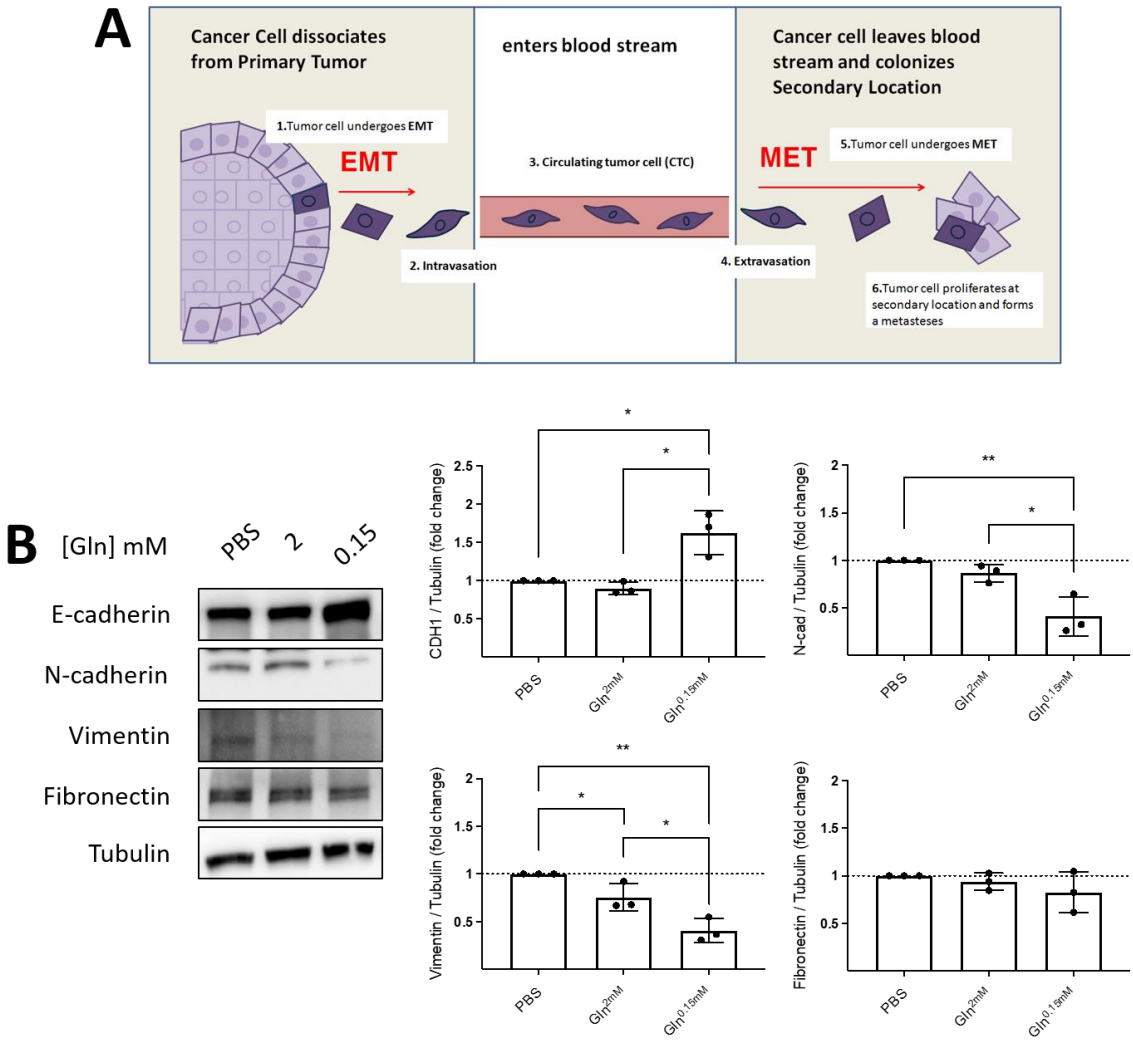



**Figure 4.19** Switched EVs increase E-cadherin expression and a reduce cell motility markers in recipient cells. (A) Metastasis of epithelial-derived cancers, such as CRC, requires the two-way process of epithelial-to-mesenchymal transition (EMT) and mesenchymal-to-epithelial transition (MET). Cancer cells within the primary tumour must detach from surrounding cells, including the basement membrane and acquire mesenchymal characteristics (EMT), such as increased motility, which enables with intravasation into the blood and lymphatic circulation. This process is reversed at a secondary location, whereby circulating tumour cells reacquire epithelial features such as anchorage to neighbouring cells (MET) which leads to the formation of metastases. (B) Western blots of HCT116 recipient cell gene expression profiles following 72-hours of incubation with either vehicle (PBS), or EVs isolated from glutamine-replete (2 mM) or –deplete (0.15 mM) secreting cells. Treatment with switched EVs was associated with a MET-like phenotype. Bar graphs show the mean ± SD of three biological replicates.

As with the other properties of cancer cells investigated in this chapter, EVs have also been implicated as important mediators in driving EMT (L. Han et al. 2019; H. Kim et al. 2020a), although there are no reports of their involvement in MET. Despite this, reduced mTORC1 signalling has previously been associated with the process of MET in CRC cells (Gulhati et al. 2011). Therefore, given the ability of switched EVs to reduce recipient cell migration and invasion, it was hypothesised that this would coincide with a MET-like protein expression profile. HCT116 recipient cells were grown in reduced serum (1% FBS) media for 24-hours and then exposed to either non-switched EVs, switched EVs or a PBS control. Cell lysates were collected after 72-hours to determine the effects on protein expression (Figure 4.19B). Consistent with reduced migration and invasion, recipient cells treated with switched EVs exhibited significantly higher E-cadherin expression, while N-cadherin and vimentin expression was downregulated. Fibronectin expression was unchanged.

As switched EVs also reduced HCT116 cell intravasation when compared with PBS in the chick embryo model, protein expression of secondary tumour deposits in the distal CAMs was analysed by immunohistochemistry (Figure 4.20). While switched EVs did not significantly impact E-cadherin expression, the expression of N-cadherin and vimentin was markedly reduced by exposure to switched EVs. Interestingly exposure to non-switched EVs significantly increased N-cadherin expression, which may indicate an *in vivo* role of this subtype of EVs in opposing the roles of switched EVs, possibly in promoting EMT within the primary tumour. To explore this further, additional *in vitro* dose-response experiments, followed by optimisation of the chick embryo model to study these behaviours are required.

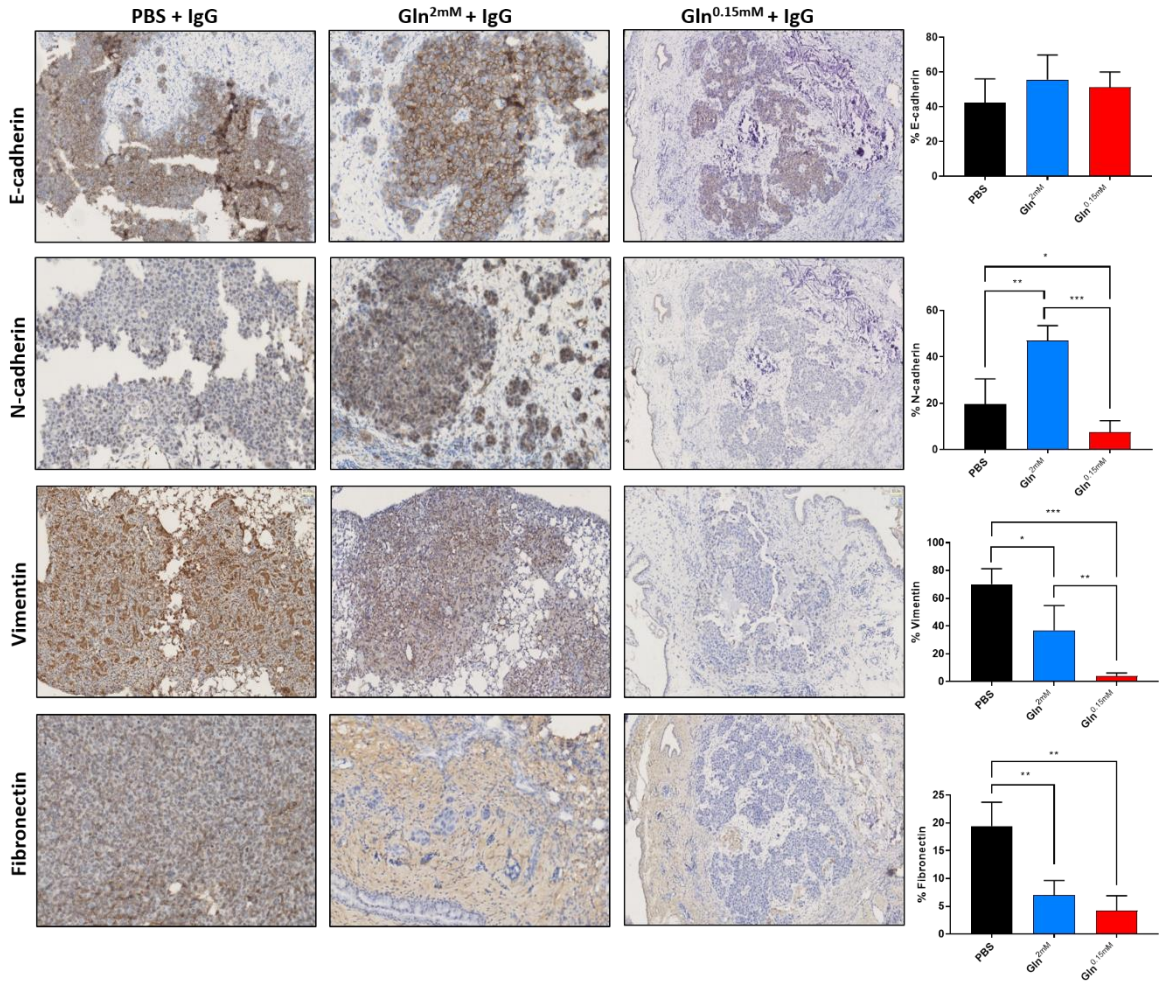



**Figure 4.20** Switched EVs alter the expression of cellular motility markers in distal CAM secondary tumour deposits. Sections immunostained for EMT/MET markers within the distal CAMs of HCT116-xenografts five days after pre-treatment with vehicle (PBS), non-switched ($Gln^{2mM}$) or switched ($Gln^{0.15mM}$) EVs. Bar graphs show the mean ± SD and are were generated from the analysis of sections from at least three tumours per condition.

## 4.3 Discussion

Over the past decade there has been growing interest in the pro-tumorigenic roles of EVs. Tumours are complex structures, consisting of multiple different expanding cancer clones, each responding to different external microenvironmental signals and stressors. These factors control EV biogenesis and can trigger the release of different EV subtypes, including Rab11a-labelled exosomes. Therefore, the aim of this chapter was to investigate the functional roles of these different EV-subtypes, focussing on the potential pro-tumorigenic properties of switched EVs. Briefly, switched EVs were shown to promote the AREG-

dependent growth of recipient cells *in vitro* and *in vivo*, and can partially reverse the inhibitory effects of EGFR antagonists, such as cetuximab. This work was undertaken in accordance with the recommendations outlined in the MISEV guidelines (Thery et al. 2018). The *in vitro* data demonstrating the AREG-dependent growth promoting properties of switched EVs is reported in Fan et al. (2020) (Appendix A). In addition, switched EVs reduce cancer cell migration and invasion, which appears to be AREG-independent, and downregulates proteins involved in cell motility. These findings will now be considered in more detail, including their context within the existing literature, concluding with a proposed model that describes how the tumour microenvironmental regulation of EV secretion promotes CRC tumorigenesis.

### 4.3.1 Nutrient depletion and hypoxia triggers the release of Rab11a-exosomes that promote AREG-dependent growth

Uncoordinated tumour growth will eventually outgrow its blood supply, resulting in hypoxia and nutrient depletion. This hostile microenvironment exerts selective pressures that promote the expansion of genetically unstable and aggressive cancer cell clones, ultimately leading to disease progression (Petrova et al. 2018). Reduced mTORC1 signalling is known to be an important component in regulating the cellular response to hypoxia, leading to activation of HIF-1α, which promotes angiogenesis and metabolic reconfiguration (Cam et al. 2010). In addition, EVs are well recognised mediators of tumour adaptation, and sustained cell proliferation under hostile conditions (E. Yang et al. 2020). Therefore, the stress-induced release of Rab11a-labelled exosomes, triggered by a reduction in rapamycin-resistant mTORC1 signalling reveals important and novel insights into EV-mediated adaptation.

Glutamine is known to be an important cancer cell metabolite, switching from a non-essential to an essential amino acid, required to sustain increased protein and nucleotide synthesis, and by acting as a surrogate metabolite in the TCA cycle (J. Zhang et al. 2017a).

It is also a known to activate mTORC1 signalling (Goberdhan et al. 2016). The results presented here demonstrate that glutamine-depleted CRC cells secrete EVs that are enriched in the EGFR ligand, AREG, which promote the ERK-dependent proliferation of recipient cells. Similarly, drug-induced inhibition of mTORC1 replicates this response in CRC cells that are insensitive to glutamine-depletion, and EVs isolated from secreting cells grown under hypoxic conditions also produces equivalent findings. The hypoxic stimulation of pro-tumorigenic EVs from a range of CRC cell lines have been previously reported (Endzelins et al. 2018; X. Hu et al. 2020; Z. Huang et al. 2018), although this has not been associated with changes in mTORC1 signalling until now. The ability of cancer cell-derived EVs to promote ERK-dependent growth has also been previously reported in CRC (B. Wang et al. 2019), as well as in lung and gastric adenocarcinoma (Qu et al. 2009; X. Song et al. 2016). Additional evidence that elevated ERK signalling underlies the growth promoting property of switched EVs was revealed by treating recipient cells with the potent ERK inhibitor (SCH772984) for 24 hours prior to exposure to EVs, which completely blocked the extra growth induced by these vesicles (Fan et al. 2020).

EVs are known to participate in autocrine, paracrine and even endocrine signalling, triggering phenotypic changes in different cell types (Maia et al. 2018). A recent study by Oszvald et al. (2020) demonstrates the ability of colonic fibroblast-derived EVs to promote AREG-dependent CRC cell proliferation. Consistent with these findings, switched EVs from HCT116 cells were also able to promote the AREG-dependent growth of Caco-2 recipient cells. Moreover, it appeared that Caco-2 cells may be more sensitive to the activity of HCT116 EVs, which may be linked to genetic differences between these two cell lines. HCT116 cells possess an activating mutation in *KRAS*, meaning activation of the EGFR signalling pathway is not dependent on upstream EGFR phosphorylation. In contrast, Caco-2 cells do not possess mutations in any component of the EGFR/RAS/ERK or PI3K/Akt pathways, meaning EGFR signalling operatives via largely wild-type conditions. Therefore, persistent paracrine activation of EGFR via EV-associated AREG will be a strong driver of

proliferation in these recipient cells. An alternative explanation may be linked to the amount of AREG transported in switched EVs from different cell lines. AREG upregulation in switched EVs isolated from Caco-2 secreting cells appeared less than that demonstrated in HCT116 EVs, and associated with this was the finding that a higher dose of switched EVs from Caco-2 cells was required to promote a significant increase in recipient cell growth. Treating Caco-2 cells with EVs isolated from HCT116 secreting cells also revealed a possible role of non-switched EVs in negatively controlling cell growth. This was also highlighted in growth assays following the inducible knockdown of CHMP5, which inhibits the biogenesis and secretion of Rab11a-exosomes. Inducible knockdown of CHMP5 was associated with a significant reduction in recipient cell growth, possibly due to the unhindered action of non-switched EVs.

The finding that EVs isolated from SW480 and SW620 cells did not contain AREG was surprising, although reassuringly, there are no studies in the literature that have detected AREG within these cell lines either. Furthermore, it was also reassuring that switched EVs from these cell lines were unable to promote recipient cell growth as this serves as a negative validator, strengthening the evidence that the proliferative properties of switched EVs from HCT116 and Caco-2 cells are AREG-dependent. This finding underlies the complexity of EV biogenesis, and in particular EV switching. Isolated EV preparations are known to consist of a mixture of different vesicle subtypes, including non-switched and switched EVs. While Rab11a is the canonical marker of the EV switch, which coincides with upregulated EV-associated AREG in HCT116 and Caco-2 cells, it is possible that they represent two distinct EV populations, which require similar microenvironmental cues to trigger their secretion. This would account for the fact that SW480 and SW620 cells produce Rab11a-exosomes, but not AREG-labelled EVs. This could be investigated using co-immunoprecipitation as AREG is located within the EV membrane. If AREG is located within a distinct population of exosomes, it would be expected that immunocapture of AREG-labelled EVs would not be labelled with Rab11a and vice-versa.

The AREG-dependent growth promoting properties of switched EVs were validated in a chick embryo model, which at the time of writing is the first time this model has been used to specifically study the role of EVs during tumorigenesis. Treatment with switched EVs resulted in larger morphologically distinct tumours, which coincided with increased histological markers of proliferation and the nuclear localisation of activated ERK. This compliments the *in vitro* growth signalling data by showing that increased ERK phosphorylation coincides with its cellular re-localisation to its site of transcriptional control. Further immunohistological analysis is required to determine whether this effect is reversed by inhibiting AREG, as well as investigating upstream EGFR phosphorylation, which was not feasible during the *in vitro* experiments. The activities of EVs isolated from glutamine-depleted HCT116 cells have also been investigated in a mouse xenograft model, whereby HCT116 xenografts underwent serial EV injections during the exponential tumour growth phase (Fan et al. 2020). By providing long term exposure to EVs, which more accurately resembles the true biology, this experimental design overcomes an important limitation of the *in vitro* work and chick embryo experiments, whereby recipient cells only received a single dose of EVs. Consistent with the data presented so far, switched EVs led to higher levels of cellular proliferation, although this coincided with increased levels of hypoxia and necrosis, so that there was no overall difference in tumour size. As previously reported (Sheldon et al. 2010), injection of EVs into xenografts resulted in an increase in overall vessel number, which was observed for both non-switched and switched EVs. However, vessel lumen size was significantly increased in xenografts injected with switched EVs. It seems likely that these observations are all interconnected, whereby the switched EVs increase recipient cell proliferation leading to increased hypoxia and necrosis, which subsequently promotes angiogenic adaptations. It would be interesting to follow-up by investigating whether these phenotypic differences are AREG-dependent. Future work should also focus on generating orthotopic xenografts, which would also enable the potential metastatic roles of EVs to be investigated.

The incorporation of AREG into EVs is associated with a significant increase in its potency, despite its very low concentration (1.4 pg/ml). This was highlighted by comparative assays using rAREG, which showed that a dose of between 30-300 ng/ml of rAREG is required to reproduce the proliferative effect of switched EVs. Similar findings have been reported by Q. Zhang et al. (2019b), who show that AREG-containing exosomes led to prolonged EGFR signalling and dramatically increased the growth of CRC organoids at 1:1000$^{th}$ the concentration of rAREG. The explanation underlying this large difference in potency is unclear. It has been estimated that a single EV contains on average 24 AREG molecules per vesicle, and is higher in EVs isolated from CRC cells with a mutant *KRAS* allele (Higginbotham et al. 2011). It is likely that this is even higher in switched EVs, where AREG expression is increased. Perhaps the distinct conformation of AREG within the EV membrane leads to increased affinity and binding to EGFR. This may explain how switched EVs are able to increase EGFR and ERK phosphorylation in HCT116 cells, which would not be expected to respond to stimulation from AREG due to the negative feedback caused by the activating mutation in *KRAS*. Importantly, this central role of EV-associated AREG in driving the proliferative effects of switched EVs was validated using an AREG neutralising monoclonal antibody. While this method has been utilised in other studies that investigated the role of EV-associated AREG (Oszvald et al. 2020; Raimondo et al. 2019), the possibility that binding of the anti-AREG antibody to AREG-containing EVs also indirectly interferes with other important functions of these vesicles cannot be eliminated.

### 4.3.2 Switched EVs promote cetuximab resistance through an AREG-mediated competition or displacement mechanism

Intercellular EV-mediated communication within the tumour microenvironment has been suggested to promote chemotherapy resistance in a range of different cancers (S. Li et al. 2020b). This includes studies that demonstrate the ability of CRC-derived exosomes to promote chemoresistance to commonly used agents, including: 5-flurouracil and oxaliplatin

(Gu et al. 2019; Y. Hu et al. 2015), as well as monoclonal antibody-based therapies, such as bevacizumab (Ko et al. 2019). Cetuximab is used in patients with metastatic CRC, whose tumours express wild-type *KRAS* and who have developed resistance to other first line chemotherapy agents, or where these drugs are contraindicated. While its use has been associated with improved survival and quality of life (Jonker et al. 2007), eventual drug resistance develops in virtually all patients (B. Zhao et al. 2017a). Current understanding of these resistance pathways only explains around 50% of cases, and is focused on intrinsic cellular responses, such alterations in gene copy number and the activation of alternative growth factor signalling pathways (Sforza et al. 2016).

A recent study demonstrated the ability of exosomes isolated from *KRAS* mutant, cetuximab-resistant CRC cells to promote cetuximab resistance in Caco-2 cells, which are *KRAS* wild-type and therefore cetuximab sensitive (S. Zhang et al. 2017b). These findings were replicated by treating Caco-2 recipient cells with Rab11a-exosomes isolated from glutamine-depleted, cetuximab resistant HCT116 cells. Switched EVs were able rescue cetuximab treated Caco-2 cells, restoring proliferation close to or just above that observed under control conditions. Moreover, this effect was AREG-dependent, but was eliminated by inhibition of the downstream EGFR kinase domain, providing strong evidence that resistance is mediated by binding to the EGFR receptor. This ability is likely to be linked to the increased potency of EV-associated AREG, which may act as a reservoir of AREG, strongly binding to the EGFR receptor, and possibly also displacing cetuximab. Despite these interesting findings, the external validity of this EV-mediated drug resistance mechanism is unclear. Cetuximab is used in metastatic CRC, at which point tumour growth is unlikely to be reliant on the adaptive changes such as those promoted by switched EVs. Furthermore, following the induction of angiogenesis, sustained vascular growth and remodelling within the tumour is likely to lead to reduced tumour hypoxia and nutrient depletion, which would likely coincide with a reduction in switched EV secretion.

In CRC patients with *KRAS* wild-type tumours, there is a significant positive correlation between the expression of EGFR ligands, including AREG and epiregulin (EREG) and overall survival (Stahler et al. 2020). Similarly, expression of AREG and EREG is positively correlated with response to anti-EGFR therapies, including cetuximab (Bormann et al. 2019; Khambata-Ford et al. 2007). Conversely, cetuximab resistance in CRC is known to be associated with low AREG gene expression levels. A study of 220 patients with metastatic CRC treated with cetuximab found that *KRAS* wild-type patients with low AREG expression responded like those with *KRAS* mutant tumours, and was associated with cetuximab resistance (Jacobs et al. 2009). These studies indicate that low expression of AREG may characterise tumours that are less dependent on EGFR signalling, making them particularly susceptible to developing cetuximab resistance (B. Zhao et al. 2017a). While these findings may be difficult to reconcile alongside a resistance mechanism that is mediated by AREG-containing EVs, the concentration of AREG within these vesicles has been shown to be very low, with its potent activity thought to be related to its arrangement within the vesicle membrane. Furthermore, the studies described above measured mRNA levels of AREG to quantify its expression within tumours. This is unlikely to correlate with the AREG content of switched EVs. Furthermore, as EVs participate in endocrine signalling, AREG-containing EVs could originate from outside of the tumour, and are delivered via the bloodstream. Therefore, an EV-associated AREG resistance mechanism is compatible with the reported negative correlation between AREG expression and cetuximab resistance.

In addition to the RAS/ERK pathway, EGFR also activates PI3K/Akt signalling, and cetuximab inhibits both pathways. In the study by S. Zhang et al. (2017b), they found that the cetuximab resistance conferred by EVs isolated from *KRAS* mutant cells was associated with inactivation of PTEN and increased Akt phosphorylation. Akt is required for the activation of mTORC1 signalling, and its inhibition has been shown to trigger the release of Rab11a-labelled exosomes (Fan et al. 2020). This may reveal an autocrine loop resistance mechanism, whereby the cetuximab-induced reduction in PI3K signalling leads

to reduced mTORC1 activity and the secretion of switched EVs, which contain highly potent AREG, leading to cetuximab resistance. This should be investigated in cetuximab treated Caco-2 cells, to assess the impact on mTORC1 signalling, followed by EV isolations to determine whether cetuximab triggers the EV switch.

### 4.3.3 Switched EVs are implicated in CRC metastasis by controlling migration and invasion through altered protein expression

In contrast to what was expected due to the potent activity of AREG-containing EVs that are promoted under glutamine depleted conditions, switched EVs were found to significantly reduce the *in vitro* migration and invasion of recipient cells. These findings were partly replicated in the chick embryo model, whereby distal CAM colonisation was reduced by treatment with switched EVs compared with a PBS control, but not when compared to non-switched EVs. Histological analysis of distal CAM tumour deposits revealed treatment with switched EVs was associated with a reduction in the cell motility markers, N-cadherin and vimentin, which is consistent with the process of MET. Similar findings were found during *in vitro* assays, in which increased expression of the epithelia junctional protein E-cadherin was also observed. In contrast to the *in vitro* data, which measured protein expression within recipient cells grown in standard cell culture plates, the *in vivo* data provides convincing evidence that switched EVs are involved in the phenotypic changes that drive metastasis, as tumour cells will have had to actually undergo the two-way process of EMT to intravasate into the CAMs vasculature, followed by MET within the distal CAM to establish a secondary deposit.

Despite the initial hypothesis to the contrary, the reduction in migration and invasion triggered by switched EVs could be reconciled following the finding that, at least *in vitro*, this is AREG-independent. Previous *in vitro* studies have shown that AREG-containing exosomes increase the invasiveness CRC cells, where similar to its effect on proliferation, it is significantly more potent than soluble AREG (Higginbotham et al. 2011). Similarly,

AREG-mediated activation of EGFR/ERK signalling has been shown to promote migration and EMT in breast cancer (N. Yang et al. 2012). However, further complexity is added by the finding that the association between switched EVs and decreased distal CAM colonisation was AREG-dependent. While this may reflect biological differences between *in vitro* and *in vivo* activity, important questions surrounding the underlying mechanism by which switched EVs alter recipient cell motility remain. Alternatively, it is possible that the Cav-1 EVs mediate the differences in migration and invasion. Indeed, Cav-1 containing EVs have been shown to be important mediators of migration and invasion in breast cancer, although they were associated with an increase in both of these behaviours (Campos et al. 2018). This could be explored further by undertaking Rab11a, and, or CHMP5 knockdown studies to determine which subgroup of EVs are involved.

Tumour migration and invasion are closely linked to the two-way process of EMT and MET. While EVs have been linked to driving tumour EMT (H. Kim et al. 2020a), this is the first report that directly implicates EVs in promoting MET-like changes in CRC. Interestingly, Gulhati et al. (2011) found that MET was induced in CRC cells following the knockdown of mTORC1, although this was not linked to the biogenesis and secretion of switched EVs. As EMT and MET are interlinked, an understanding of the EV-mediated processes that promote EMT may reveal possible mechanisms for EV-driven MET. EV-mediated release of the Zinc finger E-box-binding homeobox 1 (ZEB1) has been highlighted as an important EMT-inducing event in prostate cancer (Nam et al. 2016). ZEB1 is known as the master orchestrator of EMT, and acts both as a transcriptional suppressor, reducing E-cadherin levels, while also promoting N-cadherin and vimentin expression (H. T. Wu et al. 2020a). Interestingly, this corresponds to previous work by members of the Goberdhan Group, which showed that switched EVs led to a decrease in *ZEB1* mRNA in recipient cells, which would be consistent with a MET phenotype (unpublished data). Indeed, exosomal miR-101 has been shown to reverse EMT by targeting ZEB1 in ovarian cancer (F. Guo et al. 2014). EV-mediated mechanisms of EMT often involve the activity of miRNAs, and the

downstream effects of these often overlap with the processes that regulate EV switching. For example, miR-92a in fibroblast EVs has been shown to activate Wnt/β-catenin signalling, leading to EMT in CRC cells (J. L. Hu et al. 2019b). This miRNA has also been shown to activate PIK3/Akt signalling by targeting PTEN (C. Lu et al. 2017), which would be associated with downstream mTORC1 signalling, and, therefore, reduced switched EV secretion. Similarly, miR-21-containing EVs have been shown to be important mediators of EMT in oral squamous cell cancer, where it also targets PTEN (L. Li et al. 2016b). These studies suggest that EVs that promote EMT are likely to coincide with intracellular signalling that downregulates the secretion of Rab11a-exosomes and favours the biogenesis and secretion of CD63-labelled EVs.

Future work should investigate the role that switched EVs play on non-cancer cells that contribute to the tumour microenvironment. Many studies have highlighted the importance of EV-mediated communication with CAFs and immune cells, and how these modulate tumour cell migration and invasion, which ultimately leads to metastasis (Tao and Guo 2020). EV signalling can reprogramme fibroblasts to undertake remodelling of the ECM and increased vascular leakiness, which lead to increased invasiveness (Sidhu et al. 2004). These processes are also important in priming of the premetastatic niche at sites of secondary spread, and may also explain the observed organotropism of specific cancers. Hoshino et al. (2015) showed that exosomes isolated from primary tumours have distinct integrin expression patterns, meaning they preferentially fuse with resident cells within the predicted secondary organs. Furthermore, uptake into the recipient cells was associated with the activation of signalling pathways involved ECM remodelling. Therefore, it is feasible that while switched EVs appear to reduce autologous cell migration and invasion, they may have pro-metastatic properties through their effects on neighbouring and distant non-cancer cells.

Future work should also investigate the potential metastatic roles of non-switched EVs. Treatment with non-switched EVs increased N-cadherin expression in distal CAM metastases, and proliferation data suggests that they may reduce tumour cell growth. This combination of findings would be consistent with an EMT phenotype. Moreover, the fact that previous studies investigating EV-mediated EMT show that this is also associated with increased mTORC1 signalling, which would lead to increased secretion of CD63-labelled EVs, provides further evidence to support the possible pro-metastatic role these EVs. If true, this suggests that non-switched and switched EVs promote tumorigenesis through opposing actions. This is consistent with the known proliferation-migration trade-offs that arise due to tumour heterogeneity, whereby migration is favoured over proliferation at the tumour edge, and vice versa within the tumour core (Gallaher et al. 2019; Hausser and Alon 2020). This also overlaps with how microenvironmental factors control EV switching, as cancer cells at the tumour edge are likely to have an adequate blood supply, which would favour non-switched EV secretion, leading to EMT and increased migration. In contrast, interior hypoxia and nutrient depletion would promote the biogenesis and secretion of Rab11a-labelled exosomes, leading to decreased migration and increased proliferation.

### 4.3.4 Updated model of microenvironmentally controlled EV secretion and the functional role of Rab11a-exosomes in CRC tumorigenesis

In the previous results chapter, hypoxia was shown to induce EV switching in HCT116 cells, and treatment with the ATP-competitive mTOR inhibitor, Torin1, promoted the secretion of switched EVs in SW480, SW620 and Caco-2 cells. This coincides with similar findings in cervical, breast and prostate cancer cell lines (Fan et al. 2020; McCormick et al. 2020), showing how EV signalling is closely regulated by metabolic stress and mTORC1 activity. During this chapter, stress-induced Rab11a-exosomes were shown to promote tumour growth and drug resistance via an AREG-dependent mechanism, as well as triggering phenotypic changes that are characteristic of metastatic cells. In addition, preliminary evidence suggests that non-switched EVs may also drive tumorigenesis, largely by

promoting the opposite effects to those triggered by switched EVs. Therefore, the data presented in this chapter reveals how tumour heterogeneity and metabolic stress are interlinked, leading to the secretion of EVs with a range of different pro-tumorigenic properties (Figure 4.21).

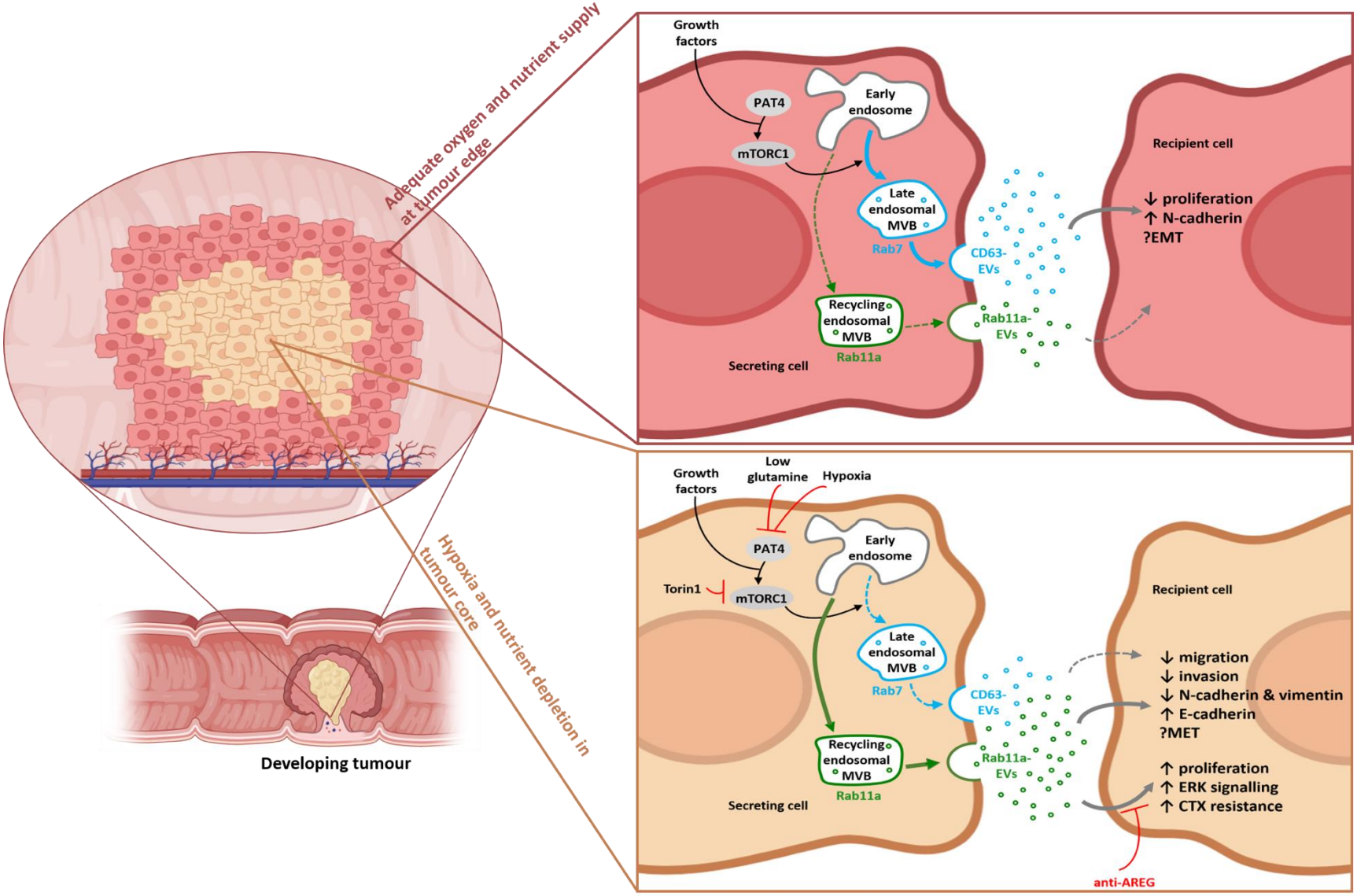

Adequate oxygen and nutrient supply at tumour edge
Growth factors
PAT4
mTORC1
Early endosome
Late endosomal MVB
Rab7
CD63-EVs
Recycling endosomal MVB
Rab11a
Rab11a-EVs
Secreting cell
Recipient cell
↓ proliferation
↑ N-cadherin
?EMT
Hypoxia and nutrient depletion in tumour core
Low glutamine
Hypoxia
Torin1
↓ migration
↓ invasion
↓ N-cadherin & vimentin
↑ E-cadherin
?MET
↑ proliferation
↑ ERK signalling
↑ CTX resistance
anti-AREG
Developing tumour

**Figure 4.21** Proposed model to describe how the relationship between tumour heterogeneity and metabolic stress leads to the secretion of different EV-subtypes, which have distinct pro-tumorigenic properties. Cancer cells around the tumour edge are unlikely to experience hypoxia or nutrient-depletion, which will promote the secretion of non-switched (CD63) EVs. Peripheral cancer cells are known to favour migration over proliferation (REF), and this is consistent with preliminary data demonstrating the role of non-switched EVs. In contrast, hypoxia within the core of the tumour would lead to a reduction in mTORC1 signaling, and the secretion of switched (Rab11a) EVs, which promote AREG-dependent proliferation and drug resistance, as well as reducing cancer cell migration and invasion.

# CHAPTER 5

## RESULTS

# 5. Investigating the EV-miRNA profile within CRC cell lines and within a rectal cancer patient cohort

## 5.1 Introduction

### 5.1.1 EVs as biomarkers of disease

EVs are secreted by all cell types and contain diverse bioactive cargoes that are specific to the secreting cell. This cargo is reflective of the function and physiological status of the secreting cell. This is in contrast to the majority of existing biomarkers used in clinical medicine, which are mostly circulating proteins (e.g. CEA in CRC) that do not contain specific information about the cell or tissue of origin. In addition, EVs are detected in all body fluids and their contents are protected from degradation due to encapsulation within a lipid membrane. These factors make EVs promising targets to investigate novel liquid biopsy-based biomarkers for disease. Indeed, EV-associated biomarkers have been identified in a wide range of pathological processes, including autoimmune diseases (Xu et al. 2020), cardiovascular disease (Dickhout and Koenen 2018), dermatological disorders (McBride et al. 2017), diabetes (Garcia-Contreras et al. 2017), neurodegenerative disease (Thompson et al. 2016) and cancer (Lane et al. 2018).

In cancer there has been considerable interest in exploring the use of plasma and serum tumour-derived EVs for diagnostic purposes, as well as for predicting survival and response to treatment (Dai et al. 2020). Diagnostically, tumour-EVs have been shown to aid early disease detection, for example, in acute myeloid leukaemia (AML), whereby AML-EVs are detected within the blood before malignant cells (Hornick et al. 2015). Therefore, it is possible that CRC-derived EVs may be detectable within blood before these lesions are picked up by existing screening tools (gFOBT and FIT) or the onset of symptoms. The value of EV-associated biomarkers is likely to be applicable in most types of cancer, as highlighted by Hurwitz et al. (2016) who profiled 60 different cancers and found that the EV

proteomes reflected the cancer cell proteome and transcriptome and could be segregated based on tissue type. This correlation could be particularly valuable in cancers, including those affecting the central nervous system, where tissue biopsy is often not feasible (Lane et al. 2018). Moreover, as tumorigenesis progresses this is associated with detectable changes in EV cargo, which have been found to correlate with prognostic parameters, including: invasion depth, TNM stage and resistance to treatment (Kosaka et al. 2019).

### 5.1.2 EV-associated miRNAs as biomarkers of CRC

Dysregulation of miRNA expression in cancer is now known to contribute to each of the hallmarks of cancer (Y. Peng and Croce 2016). miRNAs are known to be transported in EVs, where they form tissue specific expression patterns. EV-associated miRNAs appear to promote tumorigenesis through two mutually exclusive mechanisms. Firstly, EVs can deliver intact miRNAs to target cells resulting in upregulation of oncogenic genes, while also preventing the translation of tumour suppressive mRNA. In contrast to this, cancer cells have also been shown to actively load tumour suppressive miRNAs into EVs, which are then removed from the cell following fusion of the MVB with the plasma membrane (Y. Teng et al. 2017).

The first study to investigate circulating exosomal miRNAs as biomarkers in CRC was undertaken by Ogata-Kawata et al. (2014), who found that serum levels of seven EV-miRNAs (let-7a, miR-21, miR-23a, miR-150, miR-223, miR-1229 and miR-1246) were significantly elevated in patients with early stage CRC when compared to healthy controls, and that circulating levels of these were reduced following surgical resection. In addition to being able to predict diagnosis, EV-miRNA biomarkers have been reported as a means of predicting the presence of metastases, estimating prognosis in patients who have undergone surgery, undertaking surveillance and follow-up following surgery as well as predicting response to chemo- and radiotherapy (Alves Dos Santos et al. 2020). Despite this there is a large degree of variation in the miRNAs reported between different studies,

including those focussing on the same outcomes. It is unclear whether this is representative of individual study limitations, including the isolation methods used, or whether the range of possible EV-miRNA biomarkers is reflective of the genetic and molecular heterogeneity observed in CRC.

### 5.1.3 Isolating EVs from plasma and serum

Unlike cell culture media, plasma and serum contain vast quantities of additional particles and protein aggregates whose physical properties overlap with EVs. Furthermore, with the isolation methods currently available, a degree of contamination from these additional components is inevitable, and there is no single recommendation to guide study design (Kang et al. 2017). Therefore, decisions regarding the most appropriate isolation method need to be made in the context of the intended downstream analysis of EVs. As with cell culture media, the MISEV guidelines should be used to provide evidence that vesicles isolated form plasma or serum are EVs (Thery et al. 2018).

However, before selecting an isolation method it is important to decide whether plasma or serum will be studied. Serum is acquired after the process of clotting. This involves the activation of platelets, which includes the release of large quantities of EVs. In contrast to this, plasma is acquired prior to clotting and is considered to be the physiological medium of EVs within the blood (Witwer et al. 2013). For this reason, plasma was selected to study EV-miRNA in this chapter. The three main methods used to isolate EVs from plasma are: UC, precipitation-based methods and SEC. A number of studies comparing these methods found important quantitative and morphological differences between the isolated vesicles (Brennan et al. 2020; Buschmann et al. 2018; Lobb et al. 2015).

#### 5.1.3.1 UC-based methods for isolating EVs from plasma

As with cell culture media, UC-based methods for isolating EVs from plasma include dUC and density-gradient UC. The benefits of using dUC on plasma is that the sample can

undergo sequential UC at increasing speeds to gradually remove larger particles and cell debris. However, aside from being time consuming, the repeated rounds of UC reduce the overall EV yield (Lobb et al. 2015), and is still associated with high protein contamination as measured by the presence of albumin impurities (Baranyai et al. 2015). Density-gradient UC is increasingly used to isolate EVs from plasma. The main advantage of this method is its ability to separate similar sized vesicles that differ in terms of their density (e.g. exosomes and low-density lipoproteins, LDLs) (Liangsupree et al. 2021). A study by Brennan et al. (2020) that compared isolation methods found that density gradient-UC yielded the greatest number of particles with a size range of 60-150 nm, although this also coincides with the detection of various non-EV proteins. Other studies investigating the addition of a second purification stage using UC of the EV enriched density-gradient fractions still resulted in the co-isolation of small amounts of LDLs, chylomicrons, albumin and fibrinogen (Onodi et al. 2018). Finally, when used to isolate EVs from plasma or serum, density-gradient UC is associated with suboptimal EV yields of between 10-50% (Coumans et al. 2017).

#### 5.1.3.2 Precipitation-based methods for isolating EVs from plasma

The growing interest in isolating in EVs for clinical use has resulted in the emergence of precipitation-based methods for their isolation. These methods do not rely on prior experience of working with EVs and do not require any expensive equipment, such as a UC or SEC apparatus. Isolation is based on the aqueous two-phase system that underlies many of the separation protocols utilised in molecular biology. Many companies have now produced EV-precipitations kits, e.g. ExoQuick exosome precipitation, (Systems Biosciences) and Total exosome isolation precipitating agent, (Invitrogen), and while the precise details of the reagents are not disclosed, most utilise a mixture of polyethylene glycol and dextran (Kang et al. 2017). Following complete mixing of the sample and two-phase solution, the mixture undergoes centrifugation, whereby EVs move into the dextran phase. A study comparing various commercial EV-precipitation kits showed that this

method could be used to isolate EVs enriched in known EV-associated miRNAs, although there were no differences in yield between the different kits or equivalent laboratory reagents (Andreu et al. 2016). While recovery of EVs using these methods has been found to exceed 75% (J. Kim et al. 2015), they are also the least purified when compared with UC and SEC, whereby contamination of EVs has been shown to include a wide range of plasma components, including: albumin and other extracellular proteins, lipoproteins, immunoglobulins and immune complexes (Konoshenko et al. 2018).

#### 5.1.3.3 SEC-based methods for isolating EVs from plasma

SEC has many features that are advantageous for isolating EVs from plasma and serum. In contrast to UC and precipitation-based methods SEC only requires a small amount of starting material. It is less time consuming, which enables more efficient processing of samples, as well as being a more passive less user-dependent process (Gaspar et al. 2020). Furthermore, commercial SEC columns have also been produced that are optimised for isolating EVs from biological fluids. EV recovery can be up to 90% (Coumans et al. 2017), without significant albumin contamination (Baranyai et al. 2015). The reusable SEC column used to isolate EVs from cell culture media in the previous two chapters is not suitable for isolating EVs from plasma, particularly when downstream miRNA analysis is planned (Kreimer and Ivanov 2017). Single use SEC columns prepared by packing an appropriately sized syringe with agarose beads have been used to isolate biologically active exosomes from the plasma of patients with AML (Hong et al. 2016). Alternatively, commercially available SEC columns are available, which are advantageous in improving consistency between isolations. The most commonly used of these are the IZON qEV original size exclusion columns, which contain Sepharose® CL-2B resin. These columns have been shown to outperform precipitation-based methods in terms of EV purity, as determined by adherence to the MISEV guidelines (Lobb et al. 2015; Stranska et al. 2018). Recently, qEV size exclusion columns have been used successfully to study plasma-

derived EVs in non-alcoholic fatty liver disease (Povero et al. 2020), as well as EV-miRNAs in patients with NSCLC (Shukuya et al. 2020).

### 5.1.4 Aim and objectives

The aim of this chapter was to investigate the EV-miRNA content within two of the CRC cell lines studied in the previous two chapters as well as within a rectal cancer patient cohort. As each isolation method produces slightly different EV preparations (Buschmann et al. 2018), and in order to ensure consistency with the work undertaken throughout the rest of this thesis, EVs were isolated from plasma using SEC with qEV original size exclusion columns. The specific objectives were-

i. To undertake a systematic review of studies investigating plasma and serum-derived EV-associated miRNAs in patients diagnosed with CRC.
ii. To investigate and compare the EV-miRNA profiles of non-switched and switched EVs from HCT116 and SW480 CRC cells.
iii. To validate IZON qEV original size exclusion columns for the isolation of EVs from human plasma.
iv. To undertake a pilot study to investigate and compare the EV-miRNA profiles of patients with a new diagnosis of rectal cancer against healthy controls, and to explore how nCRT changes the miRNA content of EVs.

## 5.2 Results

### 5.2.1 Systematic review of EV-associated miRNAs in patients with CRC

#### 5.2.1.1 Data resources and search criteria

In order to identify miRNAs of interest, a systematic review of studies investigating plasma or serum-derived EV-associated miRNAs from CRC patients was undertaken according to the Preferred Reporting Items for Systematic Review and Meta Analyses (PRISMA) guidelines (Moher et al. 2009). The use of these guidelines during clinical studies are

mandated by many journals, and provide a framework for designing reviews that maximise coverage of the literature, as well as recommendations for the transparent reporting of combined outcomes across multiple studies. The literature search was conducted using: Embase (1974 to present), MEDLINE (including, Epub Ahead of Print, In-Process & Other Non-Indexed Citations) and PubMed Central. For each database, four domains of exploded MeSH keyword terms were combined using relevant Boolean operators. These search terms were: colorectal cancer OR colonic cancer OR colon cancer OR rectal cancer OR bowel cancer; (AND) plasma OR serum OR blood; (AND) extracellular vesicle OR vesicle OR EVs OR exosomes OR exosom*; (AND) microRNA OR miRNA OR miR*. Where a keyword mapped to further subject headings, those considered relevant were exploded and also included in the search. Coverage of the grey literature included searching reference lists of relevant review articles and included studies, searching Bioarchive and studies highlighted by weekly PubMed e-mail alerts. Studies were restricted to those undertaken in humans, and only studies available in English were included. The last search date was 27th October 2020.

#### 5.2.1.2 Inclusion and exclusion criteria

Primary studies reporting EV-associated miRNAs isolated from the plasma or serum of patients with CRC were included if they were investigating these miRNAs as biomarkers for diagnosis, prognosis or response to treatment. Studies were excluded if they were conducted exclusively in cell lines or animal models, reported alternative types of RNA (including, lncRNA or circular RNA) or were based on a secondary analysis of a previous study. Review articles and conference abstracts were also excluded.

#### 5.2.1.3 Overview of included studies

The primary search identified 434 records. Following the removal of duplicates and screening of titles, 133 abstracts were reviewed for relevance, which highlighted 84 full-texts for in-depth consideration. Full-text review excluded 35 studies, while cross-

referencing identified an additional four studies for consideration. At the end of the process 53 studies were included for review (Figure 5.1).

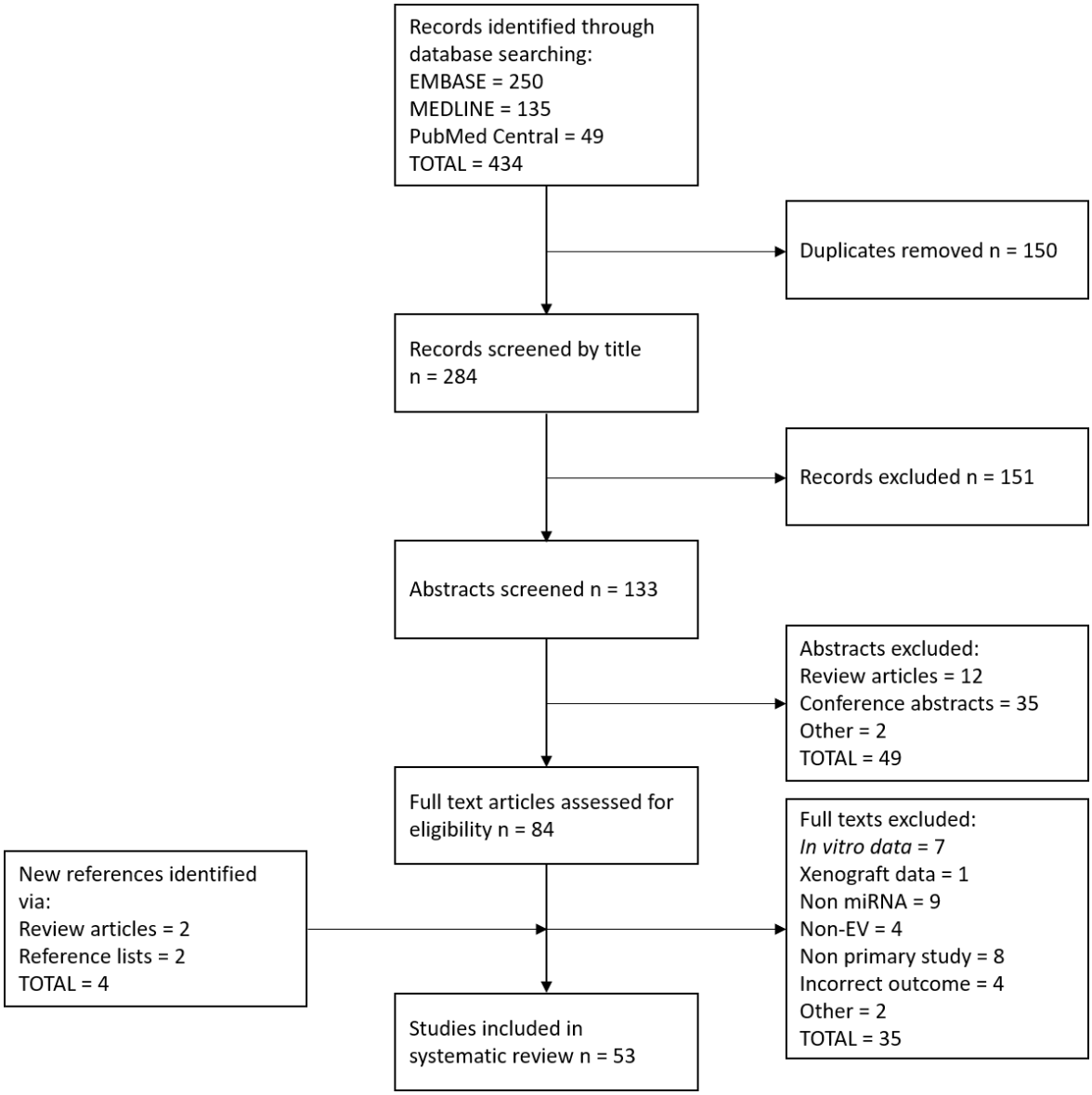



**Figure 5.1** PRISMA flow diagram for selection of studies.

Nine (17%) studies focussed on colonic cancer, four (8%) focussed on rectal cancer, while the remaining 40 studies included all types of CRC. Seventeen (32%) of the studies isolated EVs using dUC, 35 (66%) used commercial EV precipitation kits and one (2%) study used SEC (qEV columns). Eighteen (34%) studies isolated EVs from plasma, while the remaining studies isolated EVs from serum. In total, these studies identified 66 EV-associated

miRNAs (46 up-regulated, 20 down-regulated, Table 5.1) as potential biomarkers for the diagnosis of CRC (23 studies), or for predicting prognosis (24 studies) or response to treatment (8 studies). Of these miRNAs, 22 were cited in more than one study (Table 5.2).

| Outcome | Up-regulated hsa-miR- | Down-regulated hsa-miR- |
|---|---|---|
| Diagnostic | let-7a*; let-7b-3p; 16-5p*‡; 17-5p*‡; 18a/b-5p‡; 19a*‡; 20a*‡; 21‡; 23a/b-3p*; 27a/b-3p*‡; 30b/c-5p; 92a*‡; 122‡; 125a-3p; 130a‡; 141-3p*‡; 145-3p; 150*‡; 181a-5p*‡; 196b-5p*‡; 217; 221-3p*‡; 222-3p*‡; 223; 301a; 320c/d*‡; 425-5p; 1229*‡; 1246*‡; 4435; 6803-5p‡ | 92b; 99b-5p; 139-3p; 193a-5p |
| Prognostic | let-7g; 15b; 19a*‡; 21*‡; 25-3p; 27a*‡; 92a*‡; 106-3p; 122‡; 130a‡; 141-3p*‡; 155; 199a/b-3p‡; 199a/b-5p‡; 200c*‡; 203; 222-3p*‡; 320c/d*‡; 328; 375; 1229-5p*‡; 6803-5p‡ | 150-5p*‡; 181a-5p*‡; 221*‡; 486-5p; 548c-5p*; 638*; 874 4772-3p‡; 5787; 6869-5p*; 8075 |
| Response to treatment | 17-5p*‡; 18a/b‡; 19a/b*‡; 20a/b*‡; 21-5p*‡; 92a*‡; 96-5p; 100; 106a; 125b 196b-3p*‡; 199a/b-3p‡; 199a/b-5p‡; 200c*‡; 1229-5p*‡; 1246*‡ | let-7i; 16-5p*‡; 30e; 144-5p; 4772-3p‡ |

**Table 5.1** List of EV-miRNAs validated as biomarkers for CRC by studies included in systematic review. *Denotes miRNA identified in more than one study. ‡Denotes miRNA identified as biomarker in more than one outcome.

| miRNA | Outcome | Reference |
|---|---|---|
| hsa-let-7a-5p | Diagnostic | Maminezhad et al. (2020); Ogata-Kawata et al. (2014) |
| hsa-miR-16-5p | Diagnostic | Ostenfeld et al. (2016) |
| | Response to treatment | J. Han et al. (2020) |
| hsa-miR-17-5p | Diagnostic | Fu et al. (2018); H. Zhang et al. (2019a) |
| | Response to treatment | Kral et al. (2018) |
| hsa-miR-19a/b | Diagnostic | Eylem et al. (2020); Maminezhad et al. (2020); Zhu et al. (2017) |
| | Prognostic | Matsumura et al. (2015) |
| | Response to treatment | Kral et al. (2018) |
| hsa-miR-20a | Diagnostic | Maminezhad et al. (2020) |
| | Response to treatment | Kral et al. (2018) |
| hsa-miR-21 | Diagnostic | Eylem et al. (2020); Ogata-Kawata et al. (2014); L. Zhao et al. (2017b); Zhu et al. (2017) |
| | Prognostic | Perez et al. (2020); Tsukamoto et al. (2017) |
| | Response to treatment | Fuji et al. (2019); Jin et al. (2019); Kral et al. (2018) |
| hsa-miR-23a/b-3p | Diagnostic | Karimi et al. (2019); Ogata-Kawata et al. (2014); Ostenfeld et al. (2016) |
| hsa-miR-27a/b-3p | Diagnostic | X. X. Liu et al. (2018b); Ostenfeld et al. (2016) |
| | Prognostic | X. X. Liu et al. (2018b) |
| hsa-miR-92a-3p | Diagnostic | Eylem et al. (2020); Fu et al. (2018)<br>Min et al. (2019) |

| | | |
|---|---|---|
| | Prognostic<br>Response to treatment | Perez et al. (2020)<br>J. Han et al. (2020) |
| hsa-miR-141-3p | Diagnostic<br>Prognostic | Gasparello et al. (2020)<br>Meltzer et al. (2019); Santasusagna et al. (2018) |
| hsa-miR-150 | Diagnostic<br>Prognostic | Maminezhad et al. (2020); Y. J. Zhao et al. (2019)<br>Zou et al. (2019) |
| hsa-miR-181a-5p | Diagnostic<br>Prognostic | H. Zhang et al. (2019a)<br>Bjornetro et al. (2019) |
| hsa-miR-196b-5p | Diagnostic<br>Response to treatment | J. H. Wu et al. (2018)<br>Ren et al. (2017) |
| hsa-miR-200c | Prognostic<br>Response to treatment | Santasusagna et al. (2018)<br>Fuji et al. (2019) |
| hsa-miR-221-3p | Diagnostic<br>Prognostic | Gasparello et al. (2020)<br>L. Liu et al. (2018a) |
| hsa-miR-222-3p | Diagnostic<br>Prognostic | Gasparello et al. (2020); Ostenfeld et al. (2016)<br>Perez et al. (2020) |
| hsa-miR-320c/d | Diagnostic<br>Prognostic | J. Wang et al. (2017a)<br>Y. Y. Tang et al. (2019) |
| hsa-miR-548c-5p | Prognostic | Z. Y. Peng et al. (2019); Yan et al. (2017c) |
| hsa-miR-638 | Prognostic | Yan et al. (2017b); Yan et al. (2017c) |

| | | |
|---|---|---|
| hsa-miR-1229-5p | Diagnostic | Ogata-Kawata et al. (2014) |
| | Prognostic | H. Y. Hu et al. (2019a) |
| | Response to treatment | Jin et al. (2019) |
| hsa-miR-1246 | Diagnostic | Eylem et al. (2020); (Ogata-Kawata et al. 2014) |
| | Response to treatment | Jin et al. (2019) |
| hsa-miR-6869-5p | Prognostic | Yan et al. (2017c); Yan et al. (2018) |

**Table 5.2** List of miRNAs validated as a biomarker of CRC in more than one study.

Five of the miRNAs cited in more than one study (miR-17-5p, miR-19a, miR-19b, miR-20a and miR-92a-3p) are derived from a pro-tumorigenic cluster of six miRNAs known as oncomiR-1, which is amplified across a range of cancers (Mogilyansky and Rigoutsos 2013). OncomiR-1 can both promote and inhibit growth through differential expression of its constituent miRNAs in specific spatial and temporal patterns (Chakraborty and Krishnan 2017). Furthermore, individual oncomiR-1 miRNAs may exhibit both oncogenic and tumour suppressive activity. For example, miR-17-5p, which is the most prominent member of oncomiR-1, regulates both proliferative and apoptotic processes. Within gastrointestinal cancers, including CRC, it appears to act exclusively as an oncogene, whereas in hormone-driven cancers, including breast and prostate cancer it has tumour suppressive activity (Bobbili et al. 2017). miR-21 was cited in the most studies (nine) across all three investigated outcomes, and is possibly the most frequently upregulated miRNA across all cancer types (Bautista-Sanchez et al. 2020).

### 5.2.2 Comparative analysis of EV-miRNA cargo in non-switched and switched EVs from HCT116 and SW480 CRC cells

#### 5.2.2.1 Data calibration and quality assessment

The miRNA content of EVs is known to be influenced by microenvironmental stressors, whereby alterations in EV-miRNA cargo reconfigure metabolic pathways, remodel the ECM, and promote a range of other pro-tumorigenic behaviours (Harmati et al. 2019). Furthermore, a comparative proteomic analysis of non-switched and switched EVs from HCT116 cells undertaken by Dr Shih-Jung Fan (PDRA, Goberdhan Group) showed upregulation of a range of RNA binding proteins (RBPs) known to be involved in miRNA transport within Rab11a-exosomes. Therefore, a comparative analysis of the EV-miRNA cargo was undertaken in triplicate preparations of EVs isolated from HCT116 cells under glutamine-replete and -depleted conditions, and from control and Torin1 treated SW480 cells, which also showed hallmarks of the Rab11a-exosome switch (Figure 5.2A). HCT116 EVs contained a higher concentration of RNA than SW480 EVs (23.8 ng/µl vs. 9 ng/µl). In addition, switched EVs from HCT116 cells contained more RNA than non-switched EVs (34.8 ng/µl, switched vs. 23.8 ng/µl, non-switched), whereas RNA concentration was similar between EV subtypes in SW480 cells (10 ng/µl, switched vs. 9 ng/µl non-switched). RNA from both cells lines was enriched in short RNAs of between 20-30 bps, consistent with microRNA enrichment, and importantly, was devoid of rRNA contamination (Figure 5.2B). Samples were processed by UK Bioinformatics Ltd, whereby miRNA expression was measured using the Affymetrix GeneChip™ miRNA 4.0 array (ThermoFisher Scientific).

The bioinformatic analysis of the EV-miRNA data was undertaken in collaboration with Prof Francesca Buffa, Ryan Carter and Alessandro Barberis (Department of Oncology, University of Oxford). Following background adjustment for non-specific probe hybridisation, the data were normalised to enable comparison between different samples. Principle component analysis (PCA) of the calibrated data show that the differential expression of miRNAs between the two cell types is the dominant source of variation. While

PC1 also appeared to account for some of the differential expression between non-switched and switched EVs, there is also consistent variation according to PC2 (Figure. 5.2C). Clustering of samples was further explored by mapping the sample-to-sample Euclidean distance. The resultant heatmap showed that samples cluster most strongly according to cell type (Figure 5.2D), confirming the impression from the PCA plot.

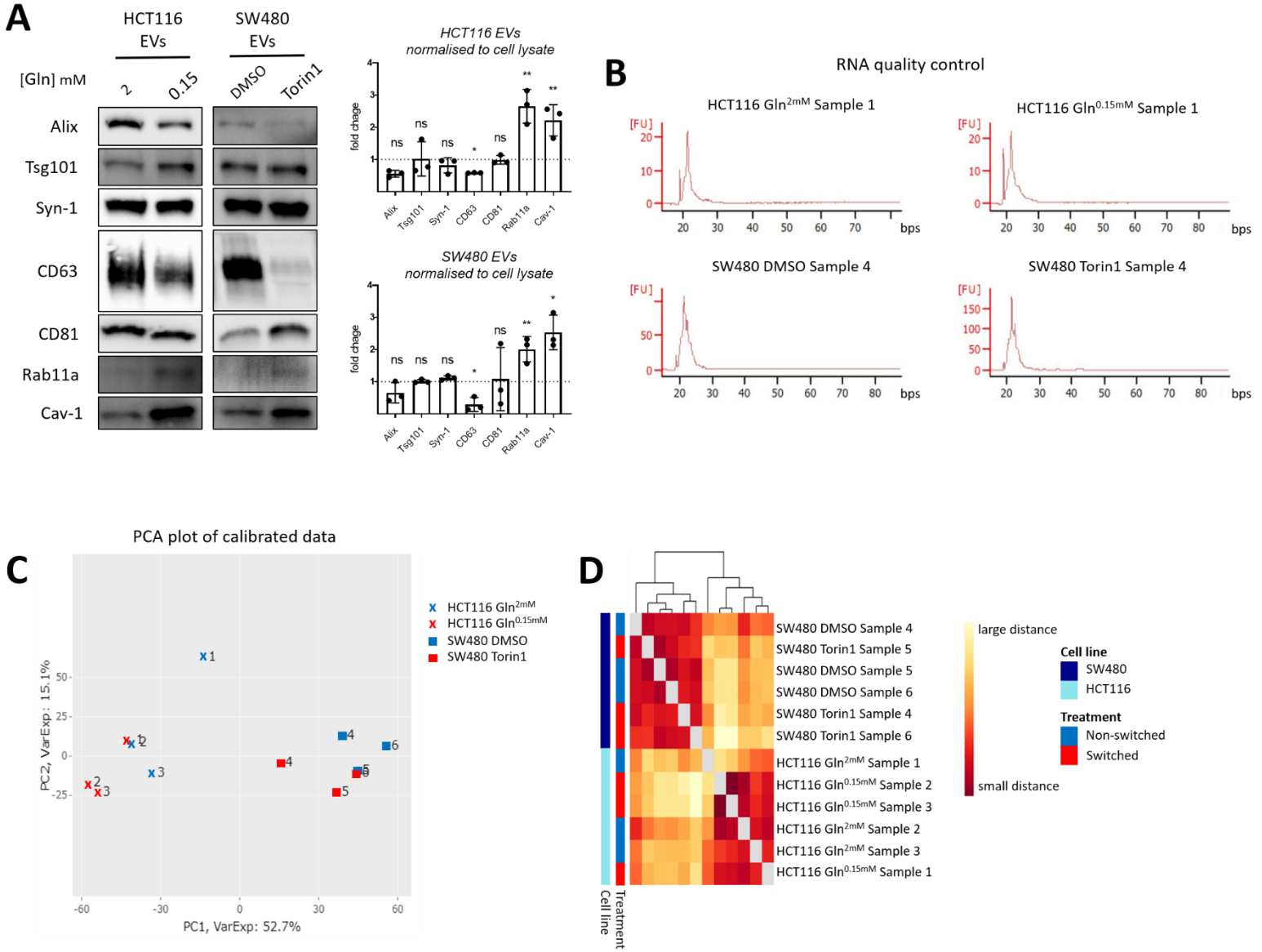
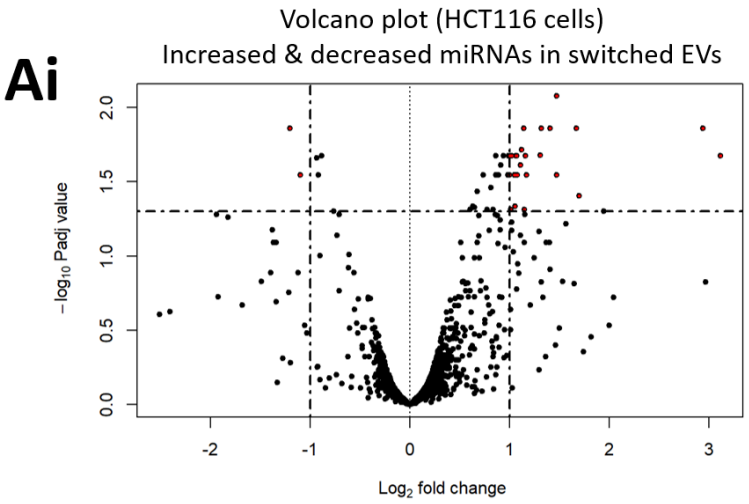

A
HCT116 EVs
SW480 EVs
[Gln] mM
2
0.15
DMSO
Torin1
Alix
Tsg101
Syn-1
CD63
CD81
Rab11a
Cav-1
HCT116 EVs normalised to cell lysate
SW480 EVs normalised to cell lysate
fold chage
ns
*
**
B
RNA quality control
HCT116 Gln2mM Sample 1
HCT116 Gln0.15mM Sample 1
SW480 DMSO Sample 4
SW480 Torin1 Sample 4
[FU]
bps
C
PCA plot of calibrated data
HCT116 Gln2mM
HCT116 Gln0.15mM
SW480 DMSO
SW480 Torin1
PC2, VarExp: 15.1%
PC1, VarExp: 52.7%
D
SW480 DMSO Sample 4
SW480 Torin1 Sample 5
SW480 DMSO Sample 5
SW480 DMSO Sample 6
SW480 Torin1 Sample 4
SW480 Torin1 Sample 6
HCT116 Gln2mM Sample 1
HCT116 Gln0.15mM Sample 2
HCT116 Gln0.15mM Sample 3
HCT116 Gln2mM Sample 2
HCT116 Gln2mM Sample 3
HCT116 Gln0.15mM Sample 1
large distance
small distance
Cell line
SW480
HCT116
Treatment
Non-switched
Switched
Cell line
Treatment

**Figure 5.2** Data calibration and quality assessment of EV-miRNAs isolated from HCT116 and SW480 CRC cells. (A) Triplicate preparations of non-switched and switched EVs from HCT116 (glutamine-replete, $Gln^{2mM}$ vs. glutamine-deplete, $Gln^{0.15mM}$) and SW480 (DMSO vs. Torin1) CRC cells were isolated using SEC. miRNA was isolated from these EVs and sent for microarray analysis, which was undertaken by UK Bioinformatics Ltd. (B) Isolated RNA was enriched in short RNAs of between 20-30 bps and devoid of rRNA contamination (graphs shown representative of all samples analysed). Following normalisation of the data, quality assessment was undertaken by principle component analysis (C) and heatmap clustering of each individual sample (D). The bioinformatic analysis was undertaken in collaboration with Ryan Carter and Alessandro Barberis (Buffa Group, Department of Oncology, University of Oxford).

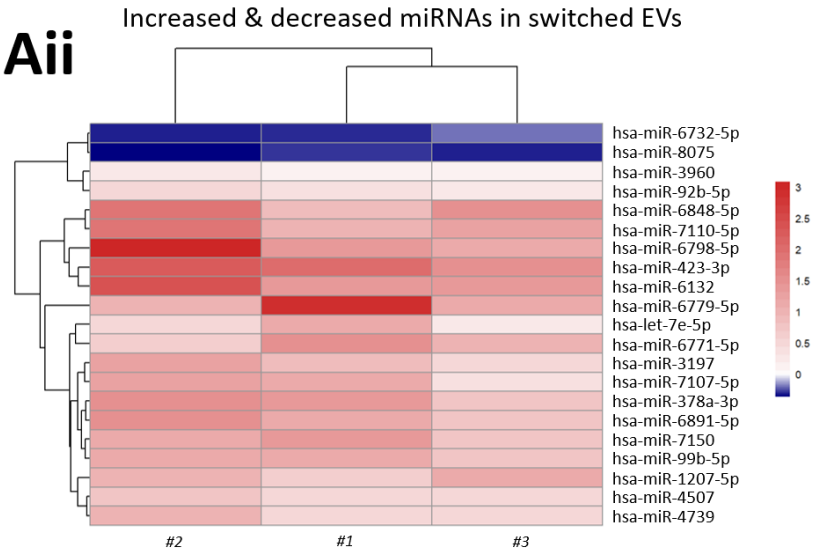
#### 5.2.2.2 HCT116 and SW480 CRC cells secrete EVs with distinct miRNA expression profiles

Differential miRNA expression was determined using paired linear modelling analysis. In order to account for type-1 errors a false discovery rate of 5% was used to produce adjusted p-values. Volcano plots of differently expressed miRNAs with a log fold change (LogFC) of greater than one or less than minus one, revealed 19 miRNAs that were increased and two miRNAs that were decreased in switched EVs from HCT116 cells (Figure 5.3Ai), and three increased and two decreased miRNAs in switched EVs from SW480 cells (Figure 5.3Bi). The identity and clustering of these EV-associated miRNAs are illustrated by heatmaps for each cell line (Figure 5.3Aii-Bii), which are also listed in Table 5.3 and Table 5.5 respectively. There was also a panel of miRNAs that had a lower overall LogFC but were significantly up or down-regulated in switched EVs. These are listed in Appendix C, which also provides a list of EV-associated miRNAs with a LogFC of greater than one or less than minus one, but for which these changes were not statistically significant.

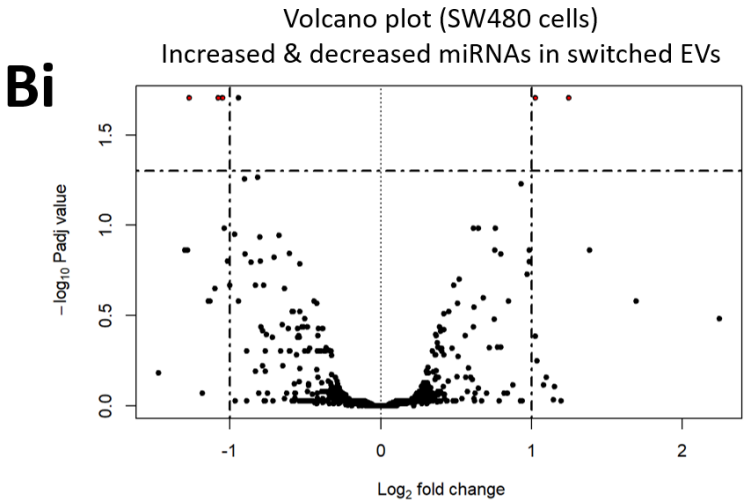
**Ai**


Volcano plot (HCT116 cells)
Increased & decreased miRNAs in switched EVs
−log10 Padj value
Log2 fold change

**Aii**


Increased & decreased miRNAs in switched EVs
hsa-miR-6732-5p
hsa-miR-8075
hsa-miR-3960
hsa-miR-92b-5p
hsa-miR-6848-5p
hsa-miR-7110-5p
hsa-miR-6798-5p
hsa-miR-423-3p
hsa-miR-6132
hsa-miR-6779-5p
hsa-let-7e-5p
hsa-miR-6771-5p
hsa-miR-3197
hsa-miR-7107-5p
hsa-miR-378a-3p
hsa-miR-6891-5p
hsa-miR-7150
hsa-miR-99b-5p
hsa-miR-1207-5p
hsa-miR-4507
hsa-miR-4739
#2
#1
#3

**Bi**


Volcano plot (SW480 cells)
Increased & decreased miRNAs in switched EVs
−log10 Padj value
Log2 fold change

**Bii**

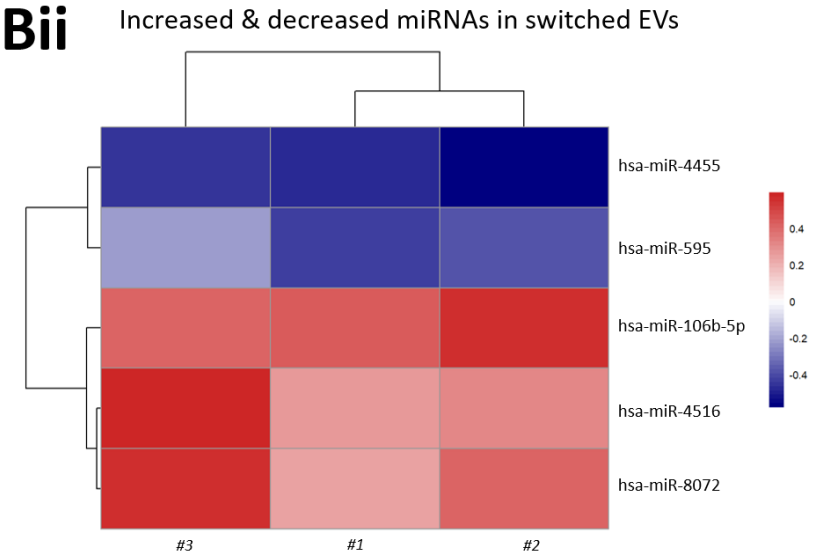

Increased & decreased miRNAs in switched EVs
hsa-miR-4455
hsa-miR-595
hsa-miR-106b-5p
hsa-miR-4516
hsa-miR-8072
#3
#1
#2

**Figure 5.3** HCT116 and SW480 CRC cells exhibit distinct miRNA expression profiles. (Ai-ii) Differential miRNA expression revealed 19 miRNAs that were increased, and two miRNAs that were decreased in triplicate preparations of switched EVs isolated from HCT116 CRC cells. (Bi-ii) Three miRNAs were increased and two were decreased in triplicate preparations of switched EVs isolated from SW480 CRC cells.

The EV-associated miRNAs that showed significant differential loading in non-switched and switched EVs from HCT116 cells are listed in Table 5.3. The miRDB database (Y. Chen and Wang 2020), does not contain any functional information or citations of EV or non-EV-mediated cancer-specific properties for the majority of these miRNAs. Of those miRNAs that have been previously studied, only miR-3197 has been reported in CRC, where it is up-regulated in tumour samples from patients with liver metastases, although this was not associated with EVs (Sayagues et al. 2016). With regards to the two miRNAs that were significantly downregulated in switched EVs, miR-8075 was also highlighted in the systematic review of plasma and serum-derived EVs in patients with CRC. The study by Yan et al. (2017a) also used microarray analysis to identify potential diagnostic biomarkers from serum-isolated EVs. Amongst the 39 aberrantly expressed miRNAs, downregulation of miR-8075 was validated using qRT-PCR in exosome-enriched samples from a cohort of 77 patients with CRC.

| miRNA | LogFC | P.value | P.adj | Reference(s) |
|---|---|---|---|---|
| hsa-miR-6779-5p | 1.70 | 0.0003 | 0.04 | |
| **hsa-miR-6132** | **1.67** | **0.00001** | **0.01** | **Sato et al. (2020)** |
| hsa-miR-7150 | 1.47 | 0.000002 | 0.008 | |
| hsa-miR-4739 | 1.41 | 0.00001 | 0.01 | |
| **hsa-miR-423-3p** | **1.32** | **0.0001** | **0.01** | **T. Guo et al. (2020); Shan et al. (2020)** |
| hsa-miR-7110-5p | 1.31 | 0.00004 | 0.02 | |
| hsa-miR-92b-5p | 1.17 | 0.0002 | 0.02 | |
| hsa-miR-6771-5p | 1.16 | 0.00008 | 0.02 | |
| hsa-miR-6798-5p | 1.15 | 0.0004 | 0.04 | |
| hsa-miR-4507 | 1.14 | 0.00002 | 0.01 | |
| hsa-miR-1207-5p | 1.12 | 0.00003 | 0.02 | |
| hsa-miR-3960 | 1.11 | 0.0001 | 0.02 | |
| hsa-miR-6848-5p | 1.08 | 0.0001 | 0.03 | |
| hsa-miR-6891-5p | 1.08 | 0.00004 | 0.02 | |
| hsa-miR-378a-3p | 1.07 | 0.00006 | 0.02 | |
| **hsa-miR-3197** | **1.05** | **0.0002** | **0.03** | **Sayagues et al. (2016)** |
| hsa-miR-7107-5p | 1.01 | 0.005 | 0.0005 | |
| hsa-miR-99b-5p | 1.01 | 0.00006 | 0.00006 | |
| hsa-let-7e-5p | 1.00 | 0.0002 | 0.0002 | |
| hsa-miR-6732-5p | -1.10 | 0.0001 | 0.01 | |
| ***hsa-miR-8075*** | ***-1.21*** | ***0.00002*** | ***0.02*** | ***Yan et al. (2017a)*** |

**Table 5.3** EV-associated miRNAs that showed differential loading in switched EVs isolated from HCT116 CRC cells. miRNAs in red italics were identified in a single study from the systematic review of EV-miRNAs as biomarkers for CRC. Green text highlights miRNAs with previously reported tumorigenic properties

Despite not fulfilling both the LogFC and statistical significance criteria, several of the HCT116 miRNAs listed in Appendix C are known to have interesting pro-tumorigenic properties. Of interest, miR-23a-3p was significantly increased in switched EVs (LogFC 0.65, P.adj. 0.04) and was highlighted in the systematic review by three studies that show it can be used to differentiate patients with CRC from healthy controls (Karimi et al. 2019; Ogata-Kawata et al. 2014; Ostenfeld et al. 2016). It is an important mediator of tumour cell

migration and invasion (N. Wang et al. 2018), and has also been shown to promote chemoresistance to 5'-fluorouracil by decreasing the expression of apoptosis-activating factors (Shang et al. 2014). Also up-regulated in HCT116-derived switched EVs was, miR-4741 (LogFC 0.99, P.adj. 0.02), which despite having an unknown function is a common miRNA detected in *KRAS* mutant CRC cell lines (Cha et al. 2015), and has been shown to be up-regulated in a range of solid tumours under hypoxic conditions (Zonneveld et al. 2019). miR-4492 (LogFC 20.4, P.adj. 0.20) and miR-5001 (LogFC 1.65, P.adj. 0.15) are also common miRNAs known to be up-regulated in KRAS mutant CRC cell lines (Cha et al. 2015). Finally, miR-7641 was non-significantly increased in HCT116 switched EVs (LogFC 3.00, P.adj. 0.15). Previous studies have shown that miR-7641 is enriched in EVs isolated from CRC organoids (Ji et al. 2014), as well as SW480 and SW620 cells (M. Chen et al. 2019a). Its expression in SW480-derived switched EVs was non-significantly decreased compared to control EVs (LogFC -0.8, P.adj. 0.85). While the function of miR-7641 is unclear, it may be involved in angiogenesis (Yoo et al. 2013), and correlates with advanced stage of diagnosis in breast cancer (Shen et al. 2021).

A proteomic analysis of EVs isolated from HCT116 cells showed increased expression of several RBPs, including hnRNPK, hnRNPA2B1 and hnRNPQ, in switched EVs. Of these, increased hnRNPA2B1 in Rab11a-exosomes was validated on western blot (Figure 5.4A), while glutamine-depletion did not alter its cellular expression (Figure 5.4B). hnRNPA2B1 is known to control the loading of specific miRNAs into exosomes (Cooks et al. 2018; Villarroya-Beltri et al. 2013). Consistent with this, of the six miRNAs known to possess hnRNPA2B1 binding motifs, five of these were increased, albeit not significantly, in switched EVs (Table 5.4). This included miR-1246, which was highlighted in three studies in the systematic review of EV-associated miRNAs in patients with CRC, which demonstrate its use as a potential diagnostic biomarker (Eylem et al. 2020; Ogata-Kawata et al. 2014), and as a predictive marker for resistance to 5-flourouracil and oxaliplatin therapy in advanced disease (Jin et al. 2019). Also known to interact with hnRNPA2B1 is

miR-125a-3p, which featured in the systematic review within a single study where it was shown to be a biomarker for early stage disease (J. Wang et al. 2017b).

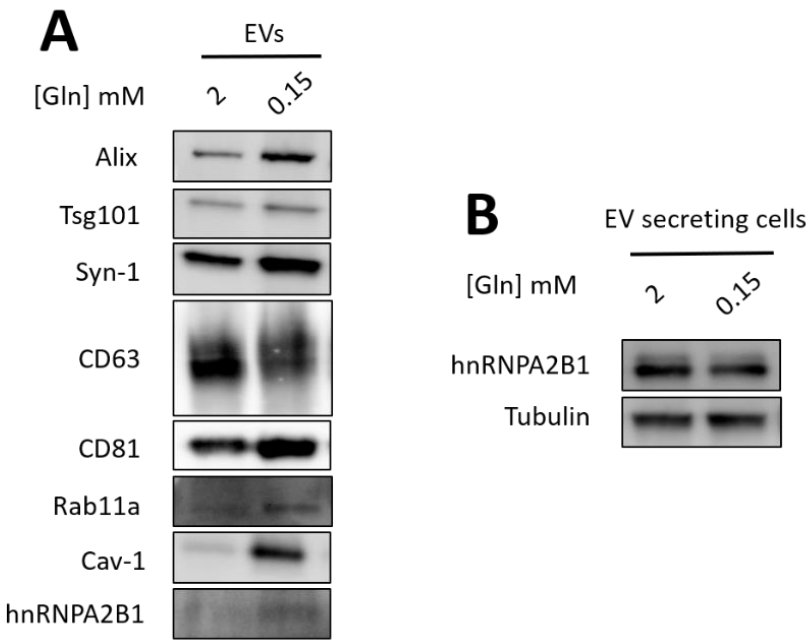



**Figure 5.4** The RNA-binding protein hnRNPA2B1 is increased in switched EVs secreted by HCT116 cells. (A) Western blot showing that glutamine-depletion ($Gln^{0.15mM}$) triggers HCT116 cells to secrete EVs containing increased levels of the the RNA-binding protein hnRNPA2B1. (B) The levels of intracellular hnRNPA2B1 are not affected by the availability of glutamine.

| miRNA | LogFC | P.value | P.adj | Reference(s) |
|---|---|---|---|---|
| hsa-miR-575 | 1.02 | 0.0007 | 0.06 | |
| **hsa-miR-1246** | **0.78** | **0.004** | **0.23** | **See Table 5.2** |
| ***hsa-miR-125a-3p*** | ***0.26*** | ***0.05*** | ***0.10*** | ***J. Wang et al. (2017b)*** |
| hsa-miR-198 | 0.12 | 0.28 | 0.84 | |
| hsa-887 | 0.03 | 0.77 | 0.96 | |
| hsa-601 | -0.23 | 0.06 | 0.63 | |

**Table 5.4** Differential expression of miRNAs isolated from HCT116 switched EVs that contain the hnRNPA2B1 binding motif. miRNAs in red text were identified in two or more studies (Table 5.2) from the systematic review of EV-miRNAs as biomarkers for CRC, while those in red italics were identified within a single study.

In contrast to the data for HCT116-derived EVs, fewer miRNAs showed significant differential expression in non-switched and switched EVs from SW480 cells (Table 5.5). miR-106b-5p is an oncomir that is up-regulated in a range of cancers (Sagar 2021), and is enriched in melanoma cell exosomes where it can trigger EMT in target cells (Luan et al. 2021). EV-derived miR-4516 is associated with increased tumour cell proliferation in triple-negative breast cancer (J. E. Kim et al. 2020b).

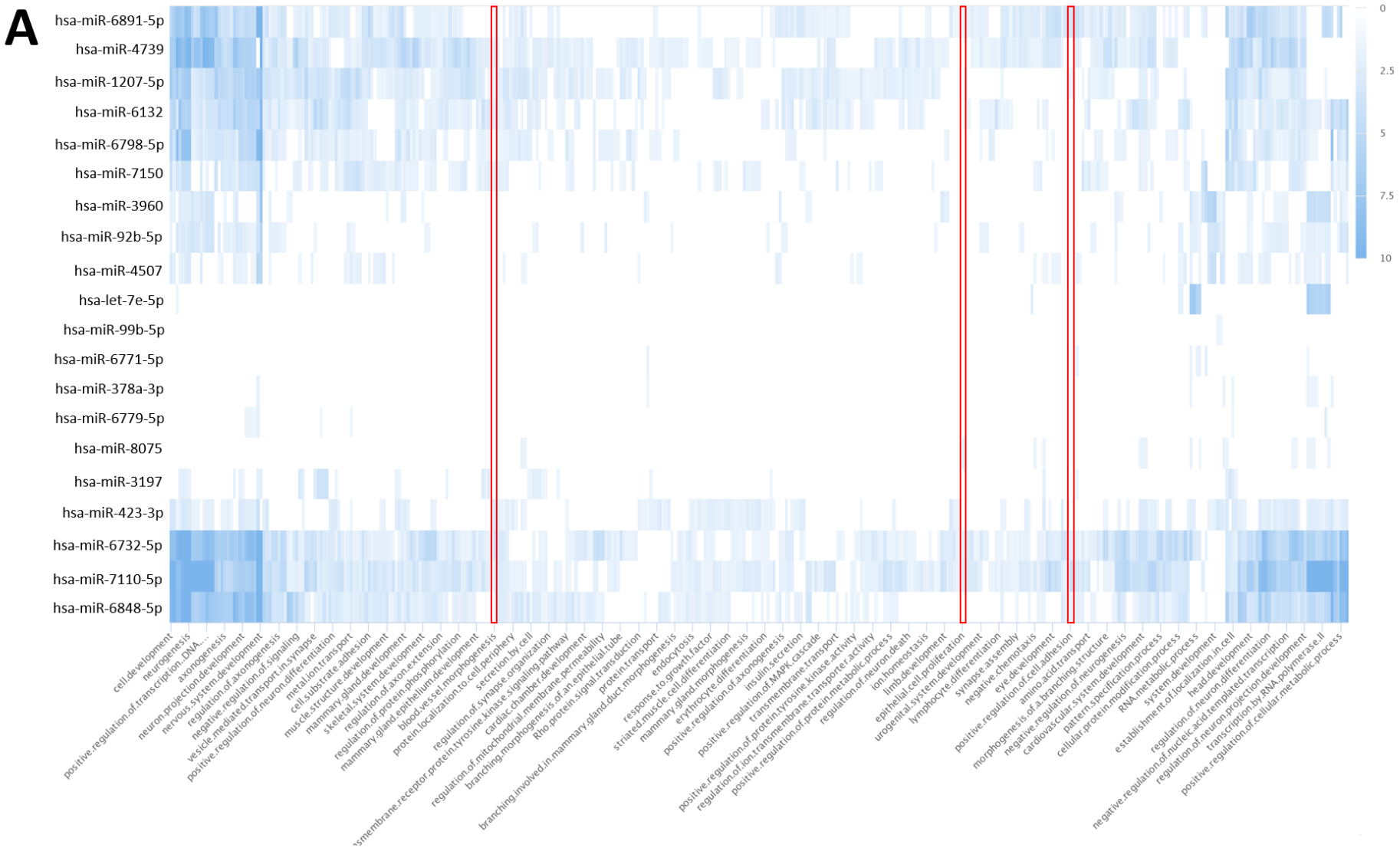
| miRNA | LogFC | P.value | P.adj | Reference(s) |
|---|---|---|---|---|
| hsa-miR-8072 | 1.28 | 0.00001 | 0.02 | |
| **hsa-miR-106b-5p** | **1.08** | **0.00001** | **0.02** | **Luan et al. (2021)** |
| **hsa-miR-4516** | **1.05** | **0.00001** | **0.02** | **J. E. Kim et al. (2020b)** |
| hsa-miR-4455 | -1.03 | 0.00001 | 0.02 | |
| hsa-miR-595 | -1.25 | 0.00001 | 0.02 | |

**Table 5.5** EV-associated miRNAs that showed differential loading in switched EVs isolated from SW80 CRC cells. Green text highlights miRNAs with previously reported tumorigenic properties.

While there was no overlap in the miRNAs that showed significant differential expression in switched EVs isolated from SW480 cells compared with HCT116 cells, data included in Appendix C does highlight five common EV-miRNAs between the two cell lines. These include, miR-25-3p, miR-182-5p and miR-4757-3p, which had a LogFC of greater than one in both cell lines, and, miR-1281 and miR-4668, which were decreased in both cell lines. Of note, miR-25-3p was included in the systematic review in a single study by Zeng et al. (2018), who showed that it drives pre-metastatic niche formation through promoting vascular permeability and angiogenesis, and has higher expression in patients with CRC metastases making it a potential biomarker for poor prognosis.

#### 5.2.2.3 Enrichment analysis of switched EV-miRNA cargoes

The majority of the EV-associated miRNAs highlighted in the differential analysis have not been previously studied, or have not been shown to have cancer-specific functions. Therefore, the miRPathDB online tool (Kehl et al. 2020) was used to search the gene ontology and KEGG pathway database in order to predict biological processes and signalling pathways that each of the miRNAs listed in Tables 5.3 and 5.4 may participate in (Figure 5.5 and 5.6).


A
hsa-miR-6891-5p
hsa-miR-4739
hsa-miR-1207-5p
hsa-miR-6132
hsa-miR-6798-5p
hsa-miR-7150
hsa-miR-3960
hsa-miR-92b-5p
hsa-miR-4507
hsa-let-7e-5p
hsa-miR-99b-5p
hsa-miR-6771-5p
hsa-miR-378a-3p
hsa-miR-6779-5p
hsa-miR-8075
hsa-miR-3197
hsa-miR-423-3p
hsa-miR-6732-5p
hsa-miR-7110-5p
hsa-miR-6848-5p
0
2.5
5
7.5
10
cell.development
neurogenesis
positive.regulation.of.transcription..DNA...
axonogenesis
neuron.projection.development
nervous.system.development
regulation.of.axonogenesis
regulation.of.signaling
negative.regulation.of.axonogenesis
vesicle.mediated.transport.in.synapse
positive.regulation.of.neuron.differentiation
metal.ion.transport
cell.substrate.adhesion
muscle.structure.development
mammary.gland.development
skeletal.system.development
regulation.of.axon.extension
regulation.of.protein.phosphorylation
mammary.gland.epithelium.development
blood.vessel.morphogenesis
protein.localization.to.cell.periphery
secretion.by.cell
regulation.of.synapse.organization
regulation.of.tyrosine.kinase.signaling.pathway
cardiac.chamber.development
regulation.of.mitochondrial.membrane.permeability
branching.morphogenesis.of.an.epithelial.tube
Rho.protein.signal.transduction
branching.involved.in.mammary.gland.duct.morphogenesis
protein.transport
response.to.growth.factor
endocytosis
striated.muscle.cell.differentiation
mammary.gland.morphogenesis
erythrocyte.differentiation
positive.regulation.of.axonogenesis
insulin.secretion
positive.regulation.of.MAPK.cascade
transmembrane.transport
positive.regulation.of.protein.tyrosine.kinase.activity
transmembrane.transporter.activity
regulation.of.ion.transmembrane.transport
positive.regulation.of.protein.metabolic.process
regulation.of.neuron.death
ion.homeostasis
limb.development
epithelial.cell.proliferation
urogenital.system.development
lymphocyte.differentiation
synapse.assembly
negative.chemotaxis
eye.development
regulation.of.cell.adhesion
amino.acid.transport
positive.regulation.of.neurogenesis
morphogenesis.of.a.branching.structure
negative.regulation.of.neurogenesis
cardiovascular.system.development
pattern.specification.process
cellular.protein.modification.process
RNA.metabolic.process
establishment.of.localization.in.cell
system.development
head.development
regulation.of.neuron.differentiation
negative.regulation.of.nucleic.acid.templated.transcription
regulation.of.neuron.projection.development
transcription.by.RNA.polymerase.II
positive.regulation.of.cellular.metabolic.process

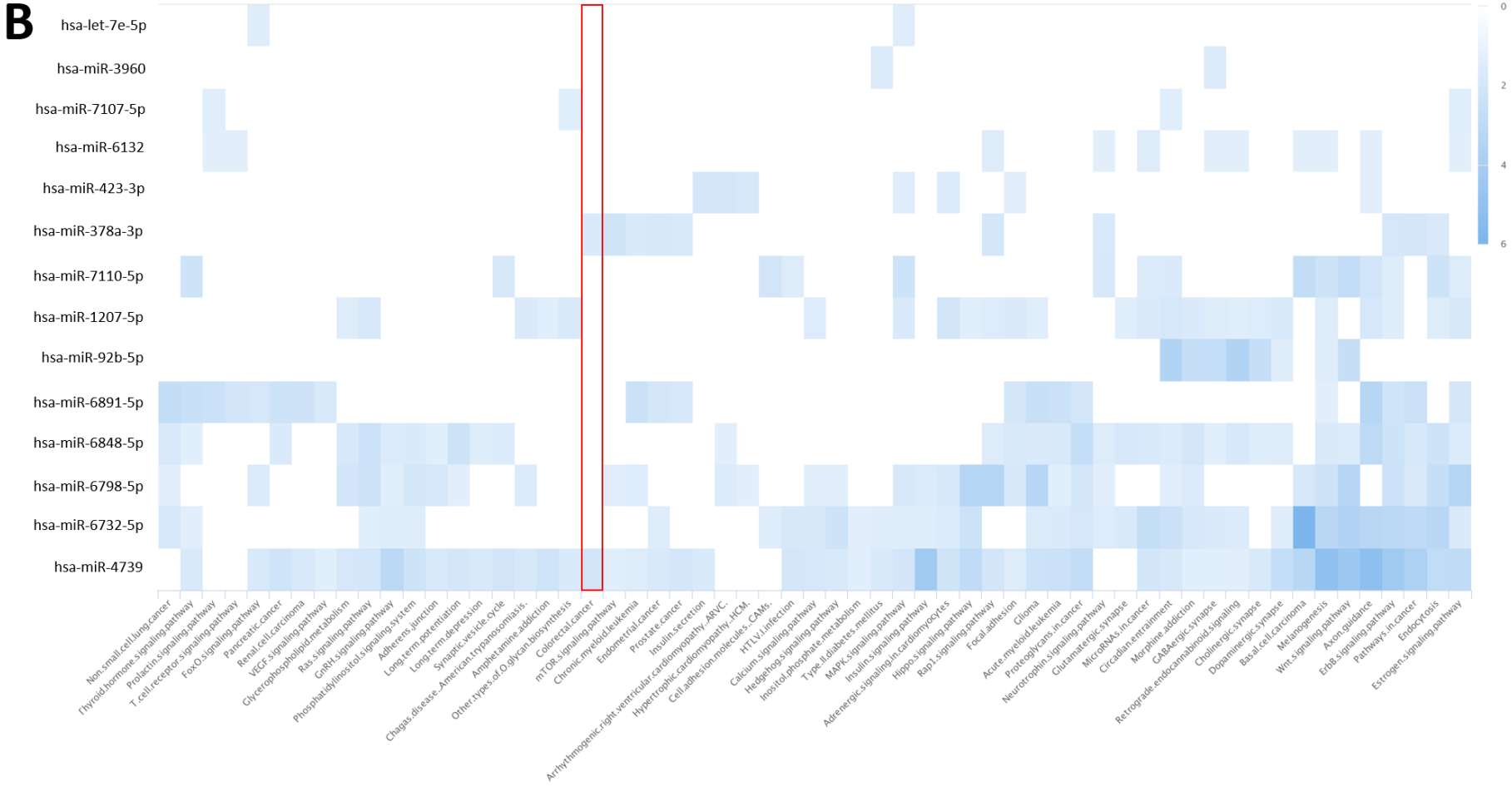

B
hsa-let-7e-5p
hsa-miR-3960
hsa-miR-7107-5p
hsa-miR-6132
hsa-miR-423-3p
hsa-miR-378a-3p
hsa-miR-7110-5p
hsa-miR-1207-5p
hsa-miR-92b-5p
hsa-miR-6891-5p
hsa-miR-6848-5p
hsa-miR-6798-5p
hsa-miR-6732-5p
hsa-miR-4739
0
2
4
6
Non-small cell lung cancer
Thyroid hormone signaling pathway
Prolactin signaling pathway
T cell receptor signaling pathway
FoxO signaling pathway
Pancreatic cancer
Renal cell carcinoma
VEGF signaling pathway
Glycerophospholipid metabolism
Ras signaling pathway
GnRH signaling pathway
Phosphatidylinositol signaling system
Adherens junction
Long-term potentiation
Long-term depression
Synaptic vesicle cycle
Chagas disease (American trypanosomiasis)
Amphetamine addiction
Other types of O-glycan biosynthesis
Colorectal cancer
mTOR signaling pathway
Chronic myeloid leukemia
Endometrial cancer
Prostate cancer
Insulin secretion
Arrhythmogenic right ventricular cardiomyopathy (ARVC)
Hypertrophic cardiomyopathy (HCM)
Cell adhesion molecules (CAMs)
HTLV-I infection
Calcium signaling pathway
Hedgehog signaling pathway
Inositol phosphate metabolism
Type II diabetes mellitus
MAPK signaling pathway
Insulin signaling pathway
Adrenergic signaling in cardiomyocytes
Hippo signaling pathway
Rap1 signaling pathway
Focal adhesion
Glioma
Acute myeloid leukemia
Proteoglycans in cancer
Neurotrophin signaling pathway
Glutamatergic synapse
MicroRNAs in cancer
Circadian entrainment
Morphine addiction
GABAergic synapse
Retrograde endocannabinoid signaling
Cholinergic synapse
Dopaminergic synapse
Basal cell carcinoma
Melanogenesis
Wnt signaling pathway
Axon guidance
ErbB signaling pathway
Pathways in cancer
Endocytosis
Estrogen signaling pathway

**Figure 5.5** EV-miRNAs that show differential expression in switched EVs isolated from HCT116 cells are predicted to participate in a range of biological functions and cancer-related signalling pathways. The online tool, miRPathDB, was used to undertake enrichment analysis in order to predict biological function (A) and signalling pathway activity (B) of the miRNAs found to be differentially expressed in switched EVs isolated from HCT116 CRC cells. Biological functions and pathways of interest are highlighted in red.

miRNAs that were differentially expressed in switched EVs isolated from HCT116 cells were predicted to participate in a wide range of biological processes (Figure 5.5A). The majority of these miRNAs were predicted to participate in a range of functions relating to neuronal development, including: neurogenesis, axonogenesis and neuron projection. Whether or not this prediction has any relevance to tumorigenesis is unclear. While neural growth and development primarily occurs during embryogenesis and early life, the regulatory networks that control these processes are also observed in cancer cells. In view of this, it has been argued that cancer cells more closely resemble embryonic neural cells rather than mesenchymal cells (Cao 2017). In addition, several pro-tumorigenic processes were also highlighted, including: epithelial cell proliferation (miR-6732-5p, miR6891-5p, miR-7110-5p and miR-8075), angiogenesis (miR-423-3p, 1207-5p, miR-4739, miR-6132, miR-6732-5p, miR-6798-5p, miR-7110-5p and miR-7150) and positive regulation of cell adhesion (miR-4739, miR-6732-5p, miR-6848-5p, miR-6891-5p and miR-7110-5p). Out of the 21 miRNAs that were differentially expressed in switched EVs isolated from HCT116 cells, 14 of these were predicted to participate in cell signalling pathways (Figure 5.5B). Two miRNAs, miR-378a-3p and miR-4739, were predicted to participate in known CRC signalling pathways, as well as in a range of other solid tumour cancers. Moreover, miR-4739 is also predicted to participate in a range of pathways that drive tumorigenesis in CRC, including the ERK, Wnt and VEGF pathways, as well as affecting adherins junctions, which may suggest it is implicated in driving EMT and, or, MET. Next, predicted gene targets within known CRC signalling pathways were searched for miR-378a-3p and miR-4739 (Table 5.6). This revealed a range of predicted targets within the Wnt pathway, as well as mediators of CIN

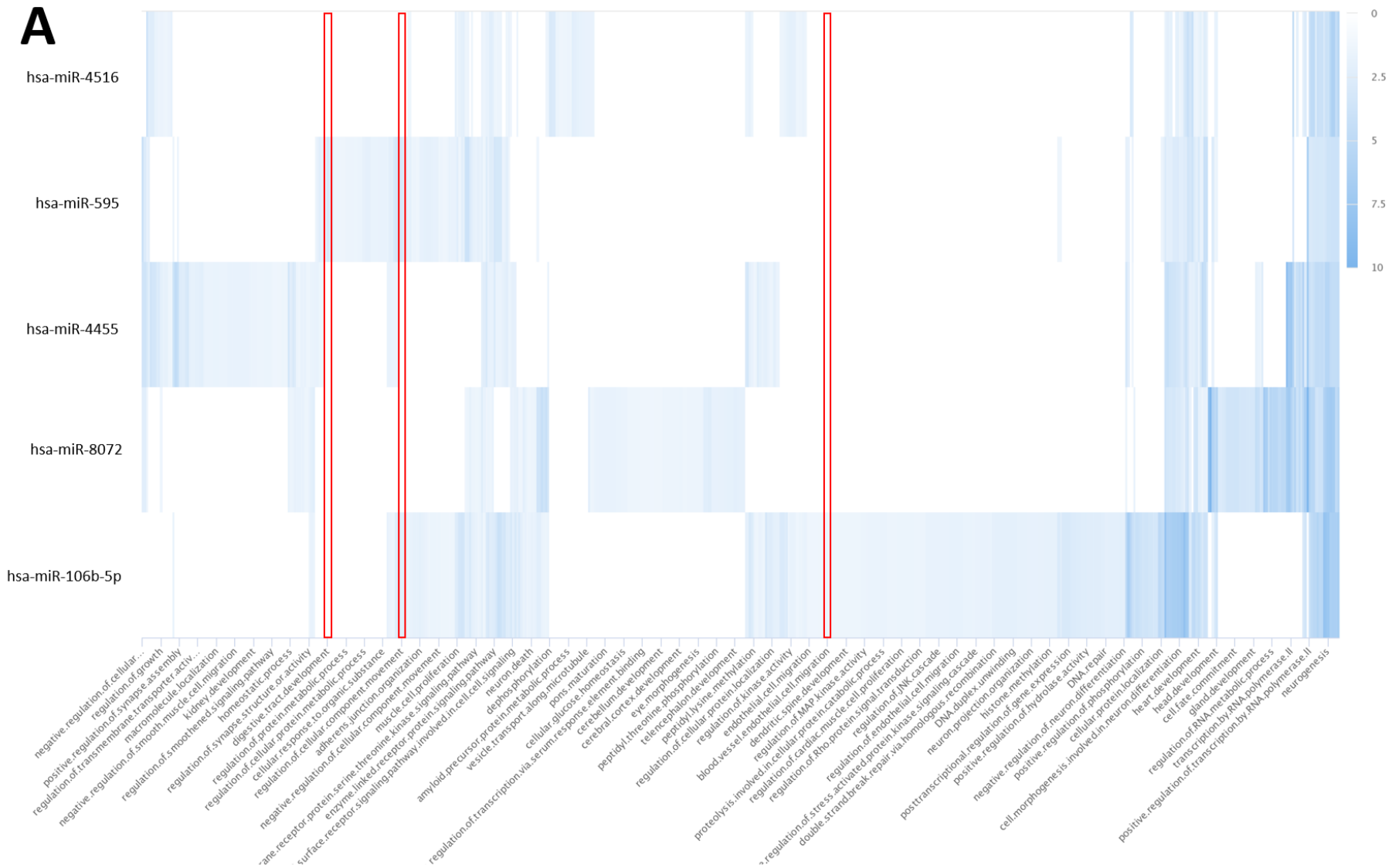
and MSI, which underpin the genetic instability of CRC. Interestingly, both miRNAs were also predicted to target genes that drive EMT.

| miRNA | Pathway | P-value | Targets |
|---|---|---|---|
| hsa-miR-378-3p | Canonical Wnt signalling in CRC | 0.006 | CCND2, CDK6, DVL1, KREMEN1, MYC, WNT10A |
| | EMT in CRC | 0.02 | AKT1, GRB2, ID2, MAPK1, TGFB2, WNT10A |
| | CIN and MSI in CRC | 0.02 | ALT1, MAPK1, MYC, TGFB2 |
| hsa-miR-4739 | Canonical Wnt signalling in CRC | 0.02 | APC2, AXIN1, CCND2, CCND3, CDK6, CHD8, CSNK1E, CTBP2, CTNNBIP1, CXXC4, DVL1, DVL3, FOSL1, FRAT1, FZD1, FZD10, FZD2, FZD3, FZD5, FZD7, FZD8, GSK3B, HNRNPU, JUN, KREMEN1, LEF1, NKD1, ROR2, RULBL1, SNEP2, SRFP1, SRFP5, TCF3, TCF7, TCF7L1, TCF7L2, TFAP2A, WNT1, WNT10A, WNT10B, WNT2, WNT2B, WNT3, WNT3A, WNT4, WNT7, WNT7A, WNT7B |
| | EMT in CRC | 0.02 | AKT2, CDH1, CDKL2, CLDN11, CLDN19, CLDN2, CLDN9, COL4A4 CRB3, CTDSP1, DLK1, DLL4, EIF5A2, FOXM1, FZD1, FZD10, FZD2, FZD3, FZD4, FZD5, FZD8, GSK3B, ITAGA5, JAG2, JUP, KRAS, MAP2K2, MAP2K3, MAP2K4, MAP2K6, MAPK1, MAPK13, MAPK14, MAPK3, MAPK8, MEF2D, MMP15, MMP2, NOTCH2, NOTCH3, NR2C2, OCLN, PIK3R2, PIK3R3, PKD1, PKP1, PROX1, RAF1, RBBP4, SHC1, SMAD2, SMAD3, TGFB1, TGFB2, TGFB3, TGFB3, TGFBR2, |

| | | | |
|---|---|---|---|
| | | | TMPRSS4, TP53, TRAF6, VTN, WNT1, WNT10A, WNT10B, WNT2, WNT2B, WNT3, WNT3A, WNT4, WNT6, WNT7A, WNT7B, WNT8B, WNT9A, WNT9B |
| | CIN and MSI in CRC | 0.03 | AKT2, APC1, APPL1, AXIN1, BAK1, BAX, BCL2L11, BIRC5, CASP9, DOCC, DDB2, EXOC2, GADD45G, GSK3B, JUN, KRAS, LEF1, MAPK1, MAPK10, MAPK3, MAPK8, MAPK9, MSH3, MSH6, NTN1, POLK, RAC2, RAF1, RALB, REL, SMAD2, SMAD3, TCF7, TCF7L1, TCF7L2, TGFB1, TGFB2, TGFB3, TGFBR2, TP53 |

**Table 5.6** Predicted gene targets within CRC pathways of miRNAs increased in switched EVs isolated from HCT116 CRC cells. Analysis undertaken using the miRPathDB online tool.

The same process was undertaken for EV-miRNAs that were differentially expressed in switched EVs from SW480 cells. Pro-tumorigenic biological processes that these miRNAs were predicted to participate in included: regulation of cell motility (miR-106b-5p and miR-595), blood vessel endothelial cell migration (miR-106b-5p) and digestive tract development (miR-595) (Figure 5.6A). Four out of the five miRNAs highlighted were predicted to participate in cell signalling pathways (Figure 5.6B). While none of these were specifically predicted to participate in CRC signalling, miR-106b-5p, miR-595 and miR-4516 were predicted to mediate signalling pathways in cancer. miR-4516 was also predicted to participate in Wnt signalling as well as modulating adherins junctions. Consistent with this, predicted gene targets of miR-4516 within CRC signalling pathways highlighted a range of genes known to promote EMT (Table 5.7). There were no predicted gene targets within CRC signalling pathways for miR-595.


A
hsa-miR-4516
hsa-miR-595
hsa-miR-4455
hsa-miR-8072
hsa-miR-106b-5p
0
2.5
5
7.5
10
negative.regulation.of.cellular...
regulation.of.growth
positive.regulation.of.synapse.assembly
regulation.of.transmembrane.transporter.activ...
negative.regulation.of.smooth.muscle.cell.migration
macromolecule.localization
kidney.development
homeostatic.process
regulation.of.smoothened.signaling.pathway
regulation.of.synapse.structure.or.activity
digestive.tract.development
regulation.of.protein.metabolic.process
regulation.of.cellular.protein.metabolic.process
cellular.response.to.organic.substance
regulation.of.cellular.component.movement
adherens.junction.organization
muscle.cell.proliferation
negative.regulation.of.cellular.component.movement
regulation.of.smoothened.signaling.pathway
neuron.death
dephosphorylation
pons.maturation
cellular.glucose.homeostasis
cerebellum.development
cerebral.cortex.development
eye.morphogenesis
peptidyl.threonine.phosphorylation
telencephalon.development
peptidyl.lysine.methylation
endothelial.cell.migration
regulation.of.kinase.activity
blood.vessel.endothelial.cell.migration
dendritic.spine.development
regulation.of.MAP.kinase.activity
regulation.of.cardiac.muscle.cell.proliferation
regulation.of.endothelial.cell.migration
regulation.of.JNK.cascade
regulation.of.stress.activated.protein.kinase.signaling.cascade
double.strand.break.repair.via.homologous.recombination
DNA.duplex.unwinding
histone.methylation
DNA.repair
regulation.of.gene.expression
regulation.of.hydrolase.activity
regulation.of.neuron.differentiation
regulation.of.phosphorylation
cellular.protein.localization
heart.development
head.development
cell.fate.commitment
gland.development
regulation.of.RNA.metabolic.process
transcription.by.RNA.polymerase.II
neurogenesis
positive.regulation.of.transcription.by.RNA.polymerase.II
cell.morphogenesis.involved.in.neuron.differentiation
positive.regulation.of.gene.expression
negative.regulation.of.gene.expression
posttranscriptional.regulation.of.gene.expression
neuron.projection.organization
regulation.of.Rho.protein.signal.transduction
proteolysis.involved.in.cellular.protein.catabolic.process
regulation.of.cellular.protein.catabolic.process
regulation.of.transcription.via.serum.response.element.binding
vesicle.transport.along.microtubule
amyloid.precursor.protein.metabolic.process
enzyme.linked.receptor.protein.signaling.pathway
negative.regulation.of.protein.serine.threonine.kinase.signaling.pathway
cellular.response.to.transforming.growth.factor.stimulus
regulation.of.transcription.by.RNA.polymerase.II
regulation.of.transcription.from.RNA.polymerase.II.promoter
regulation.of.cellular.response.to.transforming.growth.factor.stimulus
regulation.of.cell.cycle
regulation.of.cell.proliferation
regulation.of.cell.migration
regulation.of.cell.differentiation
regulation.of.cell.development
regulation.of.cell.communication
regulation.of.cell.cycle
regulation.of.cell.signaling
regulation.of.cellular.component.movement
regulation.of.cellular.component.organization
regulation.of.cellular.component.biogenesis
regulation.of.cellular.metabolic.process
regulation.of.cellular.process
regulation.of.biological.process
regulation.of.biological.quality
regulation.of.developmental.process
regulation.of.metabolic.process
regulation.of.multicellular.organism.development
regulation.of.multicellular.organism.process
regulation.of.nervous.system.development
regulation.of.neuron.differentiation
regulation.of.neuron.projection.development
regulation.of.organelle.organization
regulation.of.primary.metabolic.process
regulation.of.response.to.stimulus
regulation.of.signaling
regulation.of.signaling.pathway
regulation.of.system.process
regulation.of.transcription.by.RNA.polymerase.II
regulation.of.transcription.from.RNA.polymerase.II.promoter
regulation.of.transcription.from.RNA.polymerase.II.promoter.involved.in.cell.cycle.signaling
regulation.of.transcription.from.RNA.polymerase.II.promoter.involved.in.cell.cycle.signaling.pathway
regulation.of.transcription.from.RNA.polymerase.II.promoter.involved.in.cell.signaling
regulation.of.transcription.from.RNA.polymerase.II.promoter.involved.in.cell.signaling.pathway
regulation.of.transcription.from.RNA.polymerase.II.promoter.involved.in.signaling
regulation.of.transcription.from.RNA.polymerase.II.promoter.involved.in.signaling.pathway
regulation.of.transcription.from.RNA.polymerase.II.promoter.involved.in.transforming.growth.factor.stimulus
regulation.of.transcription.from.RNA.polymerase.II.promoter.involved.in.transforming.growth.factor.stimulus.signaling.pathway
regulation.of.transcription.from.RNA.polymerase.II.promoter.involved.in.transforming.growth.factor.stimulus.signaling.pathway.involved.in.cell.cell.signaling

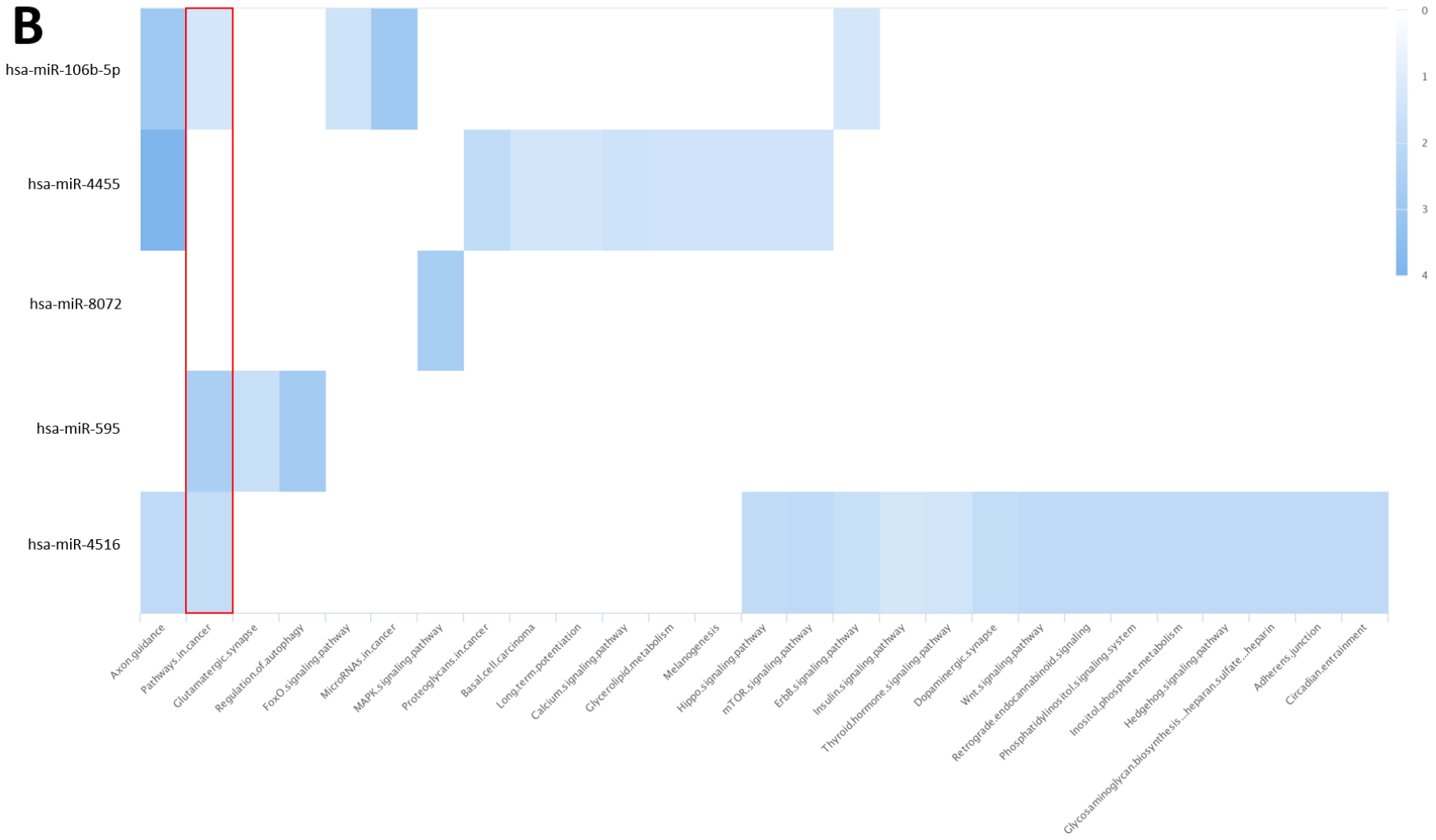

B
hsa-miR-106b-5p
hsa-miR-4455
hsa-miR-8072
hsa-miR-595
hsa-miR-4516
0
1
2
3
4
Axon.guidance
Pathways.in.cancer
Glutamatergic.synapse
Regulation.of.autophagy
FoxO.signaling.pathway
MicroRNAs.in.cancer
MAPK.signaling.pathway
Proteoglycans.in.cancer
Basal.cell.carcinoma
Long.term.potentiation
Calcium.signaling.pathway
Glycerolipid.metabolism
Melanogenesis
Hippo.signaling.pathway
mTOR.signaling.pathway
ErbB.signaling.pathway
Insulin.signaling.pathway
Thyroid.hormone.signaling.pathway
Dopaminergic.synapse
Wnt.signaling.pathway
Retrograde.endocannabinoid.signaling
Phosphatidylinositol.signaling.system
Inositol.phosphate.metabolism
Hedgehog.signaling.pathway
Glycosaminoglycan.biosynthesis...heparan.sulfate...heparin
Adherens.junction
Circadian.entrainment

**Figure 5.6** EV-miRNAs that show differential expression in switched EVs isolated from SW480 cells are predicted to participate in a range of biological functions and cancer-related signalling pathways. The online tool, miRPathDB, was used to undertake enrichment analysis in order to predict biological function (A) and signalling pathway activity (B) of the miRNAs found to be differentially expressed in switched EVs isolated from SW480 CRC cells. Biological functions and pathways of interest are highlighted in red.

| miRNA | Pathway | P-value | Targets |
|---|---|---|---|
| hsa-miR-106b-5p | CIN and MSI in CRC | 0.005 | APC, BCL2L11, CCND1, CDKN1A, CSNK1A1, CYCS, MAPK1, MSH3, MSH6, MYC, PMAIP1, SMAD4, TCF7L2, TGFBR2, TP53 |
| hsa-miR-4516 | EMT in CRC | 0.047 | AKT2, CDH1, CLDN11, CLDN14, CLDN19, CLDN5, CLDN8, CTDSP1, DLK1, FN1, FZD1, FZD2, FZD5, FZD8, MAP2K2, MAP2K3, MAP2K4, MAPK1, MAPK13, MAPK14, MAPK3, MEF2D, MMP14, MMP3, NOTHCH2, NR2CD, NRP2, OCLN, PAK1, PIK3CA, PIK3CB, PIK3R1, PKP1, PROX1, SMAD2, SPARC, TGFBR2, TJP1, TMPRSS4, TP53, TRAF6, WNT1, WNT10B, WNT2B, WNT3A, WNT4, WNT7B, WNT8B, WNT9A |

**Table 5.7** Predicted gene targets within CRC pathways of miRNAs increased in switched EVs isolated from SW480 CRC cells. Analysis undertaken using the miRPathDB online tool.

### 5.2.3 Isolating EVs using qEV size exclusion columns

#### 5.2.3.1 Isolating EVs from cell culture media using qEV columns

As only a limited amount of patient plasma was available, the qEV columns were initially optimised by isolating EVs from HCT116 CRC cells. Prepared media was added to the top of a qEV 35 nm size exclusion column and 500 µl fractions were collected. As per the manufacturer's instructions, the first six fractions corresponded to the void volume, with the

EVs being eluted in the following three fractions. Western blot analysis confirmed that detection of the EV markers within these fractions (7-9), and were particularly enriched within fraction eight (Figure 5.7Ai). This enrichment of EV markers was still observed once the fractions were combined, with only minimal detection of Tsg101 and Syn-1 within the adjacent combined fractions (Figure 5.7Aii). Consistent with the western blot analysis, NTA profiles showed that fraction eight was the most enriched in EVs (Figure 5.7Bi), although there was no significant difference between the size of particles detected in fractions 7-9. The NTA profile of the combined fractions had a concentration reflective of the sum of the individual EV fractions, with a mean particle size of 134.64 ± 70.08 nm (Figure 5.7Bii). Following elution of the EVs, the protein concentration increased substantially (Figure 5.7C), consistent with the standard chromatograms obtained during SEC. Finally, EVs isolated from glutamine-replete and -deplete HCT116 cells exhibited the classical EV switch signature (Figure 5.7D).

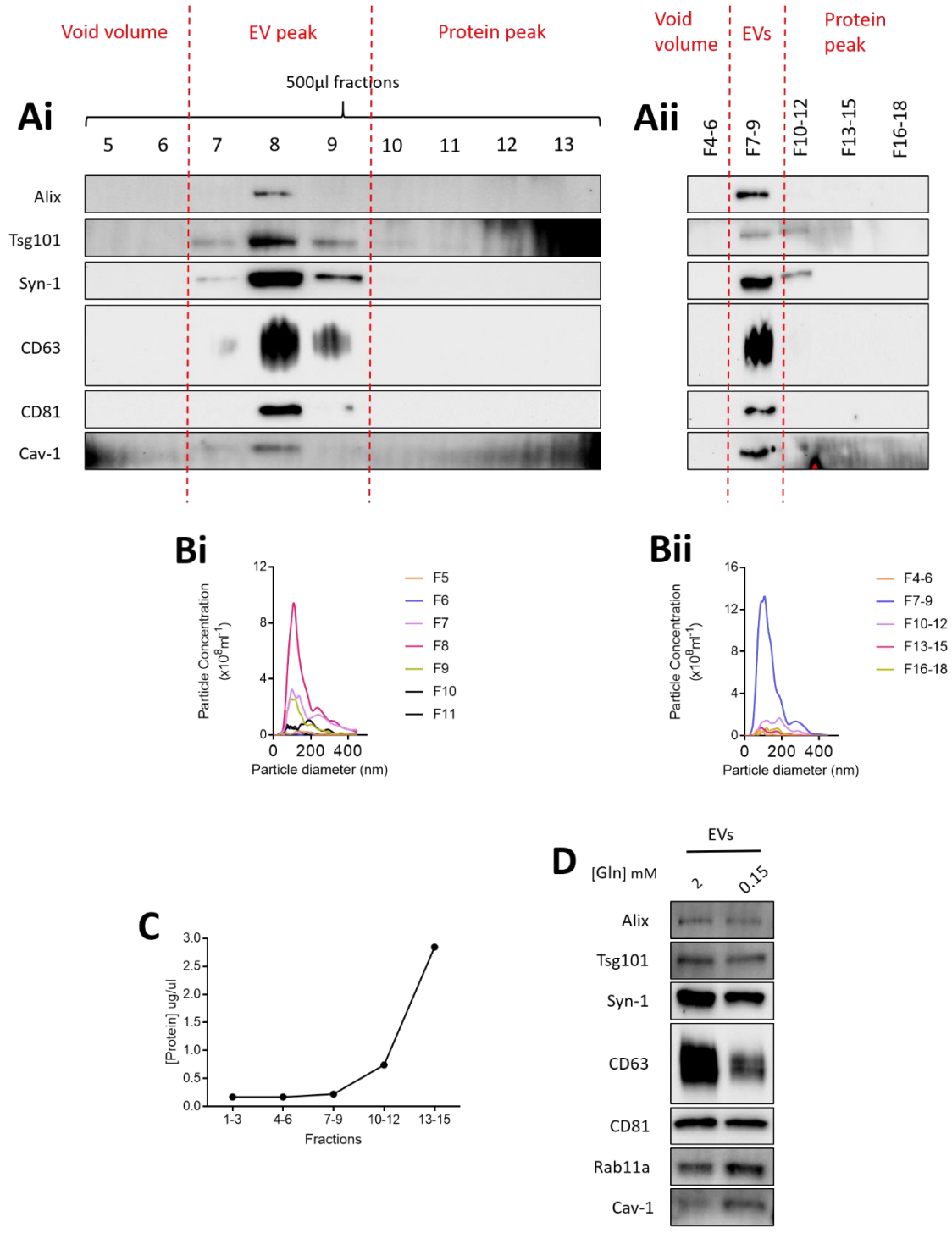



**Figure 5.7** qEV size exclusion columns can be used to isolate purified EV-preparations from HCT116 CRC cells. (Ai) Cell culture media (devoid of FBS and instead supplemented with ITS) was harvested from HCT116 CRC cells and added to the top of a qEV 35 nm size exclusion column. Immediately after this, 500 µl fractions were collected as per the manufacturers guidelines. Western blot analysis showed that the first six fractions (3 ml) were devoid of EV markers, while the following three fractions (7-9) were enriched in Alix, Tsg101, Syn-1 and the tetraspanins, CD63 and CD81. (Aii) The same pattern of enrichment was also observed when the fractions were combined, with some detection of Tsg101 and Syn-1 also occurring in the protein containing fractions, most likely representative of

ruptured vesicles. NTA profiles of individual (Bi) and combined (Bii) fractions. (C) Consistent with fraction 10 onwards corresponding to the classical protein peak observed during SEC, the protein concentration increased substantially following the elution of the EVs in fraction 7-9. (D) EVs isolated from HCT116 cells under glutamine-replete (2mM) and –deplete (0.15mM) conditions using the qEV 35 nm size exclusion columns exhibit the classical EV switch signature.

#### 5.2.3.2 Isolating EVs from patient plasma using qEV columns

Next, plasma isolated from a healthy control underwent centrifugation to remove any residual cells and larger particles before being added to the top of a qEV 35 nm size exclusion column. As shown during the EV isolations using cell culture media, EVs were eluted within fractions 7-9 (Figure 5.8). Unlike cell culture media, which undergoes a series of filtrations to reduce the amount of non-vesicular protein and other particles prior to SEC, this is not feasible in plasma due to the low volume of available sample. In addition, plasma is a complex fluid containing high concentrations of a wide range of particles and other constituents not present in cell culture media. This is reflected by the western blot analysis, which showed detection of the EV markers within fraction 7-9, followed by significant amounts of non-specific protein binding within the adjacent fractions, which corresponds to the protein peak (Figure 5.8A). Reassuringly, while a small amount of albumin, which is not associated with EVs, was detected within the EV-containing fractions, it was mainly confined to the protein peak. Furthermore, this relative amount of albumin detected within the EV containing fractions is consistent with the findings from other studies (Stranska et al. 2018). NTA demonstrated a typical EV profile for fraction 7-9, although the average particle size was slightly larger than that observed in EVs isolated from cell culture media (162.22 ± 71.38 nm) (Figure 5.8B). While TEM images of fraction 7-9 confirms the presence of EV-shaped particles, there is also clearly a higher concentration of smaller non-cup shaped particles (Figure 5.8C). These particles are most likely to represent chylomicrons or lipoproteins, which are highly abundant in plasma. Previous studies that have compared methods for isolating EVs from plasma or serum have shown that the EV containing fractions from qEV size exclusion columns do contain high amounts of lipoprotein

associated proteins, including APOB and APOE. It is felt that this arises due to a trade-off, whereby qEV columns are more efficient at separating EVs from protein than lipoproteins (Brennan et al. 2020).

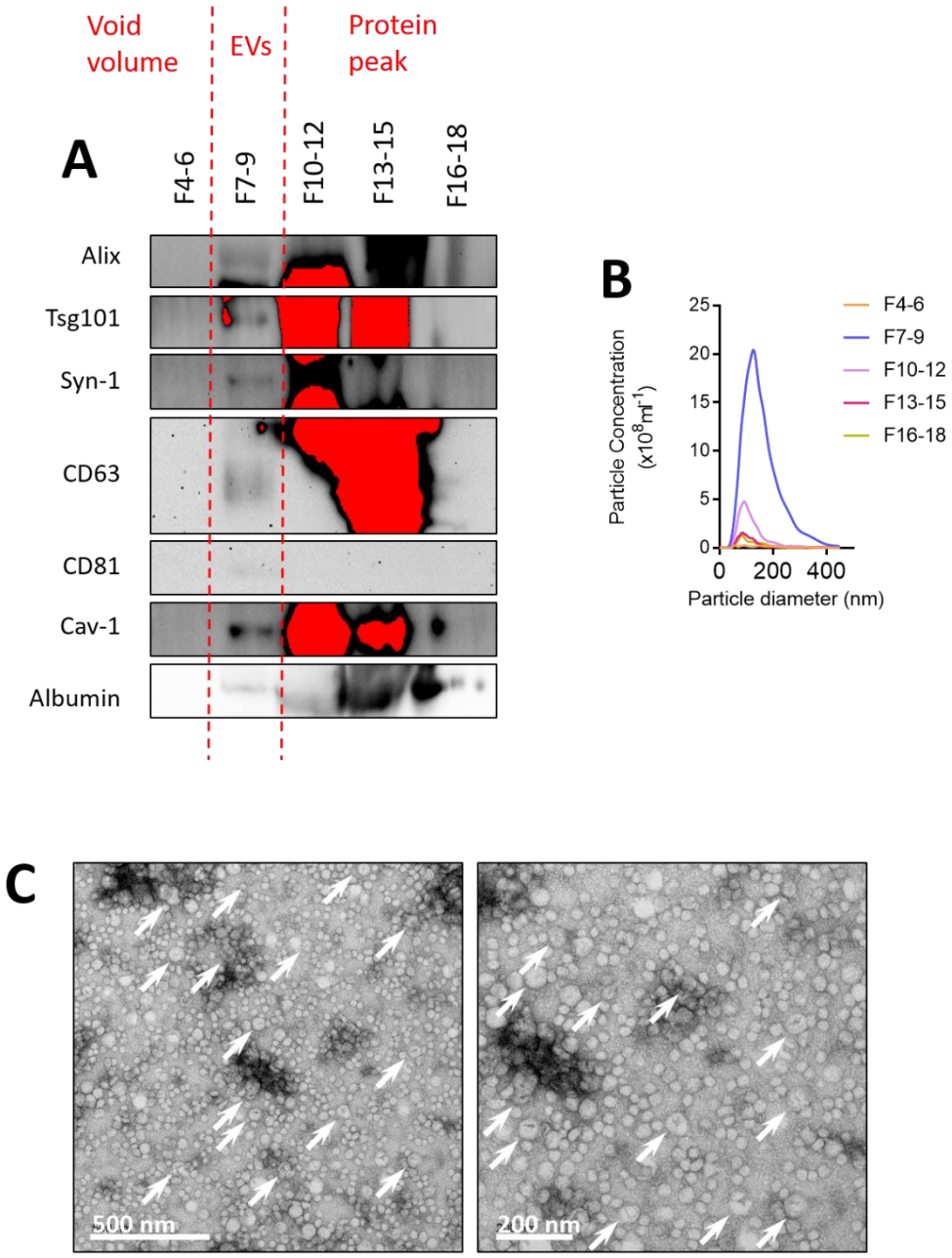



**Figure 5.8** qEV size exclusion columns can be used to isolate EVs from plasma. (A) Western blot analysis of EVs isolated from patient plasma using a qEV 35 nm size exclusion columns. As observed in EVs isolated from cell culture media, EV markers are absent within the void volume, and then enriched within fraction 7-9. Relative to the protein containing fractions (fraction 10 onwards) low levels of albumin are detected within the EV containing fractions. (B) NTA profile of the combined fractions. Fraction 7-9 is enriched in particles within the known size range of exosomes. (C) TEM images of isolated vesicles

demonstrating particles that exhibit the classic “cup” shape morphology of EVs, as well non-cup shaped particles, which are likely to represent lipoproteins.

The presence of lipoproteins within the EV fractions is relevant because they are also known to transport miRNAs (Vickers et al. 2011), which could confound any downstream analysis of EV-associated miRNA cargo. This has been investigated by Gaspar et al. (2020), who compared lipoprotein content within the EV containing fractions isolated using qEV size exclusion columns. They found that the lipoprotein content of the EV fractions is predominantly from low- (LDLs) and very low-density lipoproteins (VLDLs), and that the concentration of these is lowest within the initial EV containing fractions (corresponding to fraction 7-8 for the qEV columns used here). Moreover, LDLs and VLDLs transport less RNA compared to high density lipoproteins (HDLs), and have a miRNA signature that is broadly similar to EVs. Therefore, these findings suggest that LDL or VLDL contamination is less critical for downstream analysis of EV-associated miRNAs than that caused by potential HDL contamination. These findings coincide with the manufacturer’s recommendations for the qEV 35 nm size exclusion columns, which state that EV purity can be maximised by only harvesting the first two EV containing fractions (fraction 7-8). Therefore, subsequent EV isolations from patient samples utilised this approach.

### 5.2.4 Investigating plasma EV-miRNA cargoes in a cohort of patients with rectal cancer

#### 5.2.4.1 Patient cohort details

The cohort consisted of 10 patients with newly diagnosed rectal cancer who underwent initial treatment with nCRT (Table 5.8), as well as 10 healthy controls who were undergoing surveillance for either Barret’s oesophagus of colorectal polyps (Table 5.9). Plasma samples were provided by the Translational Gastroenterology Unit, NIHR Biomedical Research Centre, Oxford. Diagnostic, pre-treatment samples were acquired during the patients index investigation (endoscopy or CT-colonography) or initial clinical appointment, and post-treatment samples were obtained during their repeat endoscopy appointment

approximately six weeks after completing nCRT. The median age of patients was 64 years old (range 50 – 81) and controls 64.5 years old (range 51 – 88). Consistent with CRC being more common in men, nine out of the 10 patients were male, compared with seven of the controls. Observational studies show that approximately 20% of patients undergoing nCRT will show a complete response (van der Valk et al. 2018), although five out of 10 of the patients in this cohort demonstrated a complete response. In general, compared with non-responders, complete clinical response was associated with earlier stage of disease and a circumferential resection margin that was non-threatened on MRI. Of the five non-responders, four went onto have major surgical resection and one underwent endoscopic microsurgery (TEMS). Responders are likely to be over-represented within this cohort due to the research centres interest in these patients, meaning that they are more likely to be invited to provide clinical samples for research.

| Patient ID | Sex | Age‡ | Stage¥ | Complete nCRT response | Further treatment |
|---|---|---|---|---|---|
| P1 | M | 81 | I (T2 N0 M0) | Y | |
| P2 | M | 63 | I (T2 N0 M0*) | Y | |
| P3 | M | 66 | I (T2 N0 M0) | Y | |
| P4 | M | 56 | IIA (T3 N0 M0*) | N | LAR |
| P5 | M | 78 | IIIA (T3 N1 M0) | N | TEMS |
| P6 | M | 50 | IIIB (T3 N1 M0) | N | APER |
| P7 | M | 69 | I (T2 N0 M0*) | N | APER |
| P8 | M | 61 | IV (T3 N1 M1*) | N | APER |
| P9 | M | 65 | IV (T3 N2 M1) | Y | |
| P10 | F | 55 | IIA (T3 N0 M0) | Y | |

**Table 5.8** Patient demographics and clinical characteristics. ‡Age at time of index investigation (endoscopy or CT colonoscopy). ¥ UICC/AJCC stage. *Circumferential resection margin (CRM) threatened on MRI. LAR: low anterior resection; TEMS: transanal endoscopic microsurgery; APER: abdominoperineal resection of the rectum.

| Control ID | Sex | Age | Clinical background |
|---|---|---|---|
| C1 | M | 80 | Barrett's oesophagus |
| C2 | M | 57 | Barrett's oesophagus |
| C3 | F | 61 | Polyp (tubular adenoma, low grade dysplasia) |
| C4 | M | 82 | Barrett's oesophagus |
| C5 | M | 75 | Barrett's oesophagus |
| C6 | M | 59 | Polyp (sessile serrated, no dysplasia) |
| C7 | M | 63 | Barrett's oesophagus |
| C8 | M | 51 | Barrett's oesophagus |
| C9 | F | 66 | Barrett's oesophagus |
| C10 | F | 88 | Barrett's oesophagus |

**Table 5.9** Healthy control demographics and clinical background.

Comparison of EVs isolated from control and patient plasma, both pre- and post-nCRT demonstrated similar expression of the canonical EV markers (Figure 5.9A). Furthermore, the number and size of isolated EVs was similar (Figure 5.9B) and there was no difference in the protein or RNA concentration (Figure 5.9C).

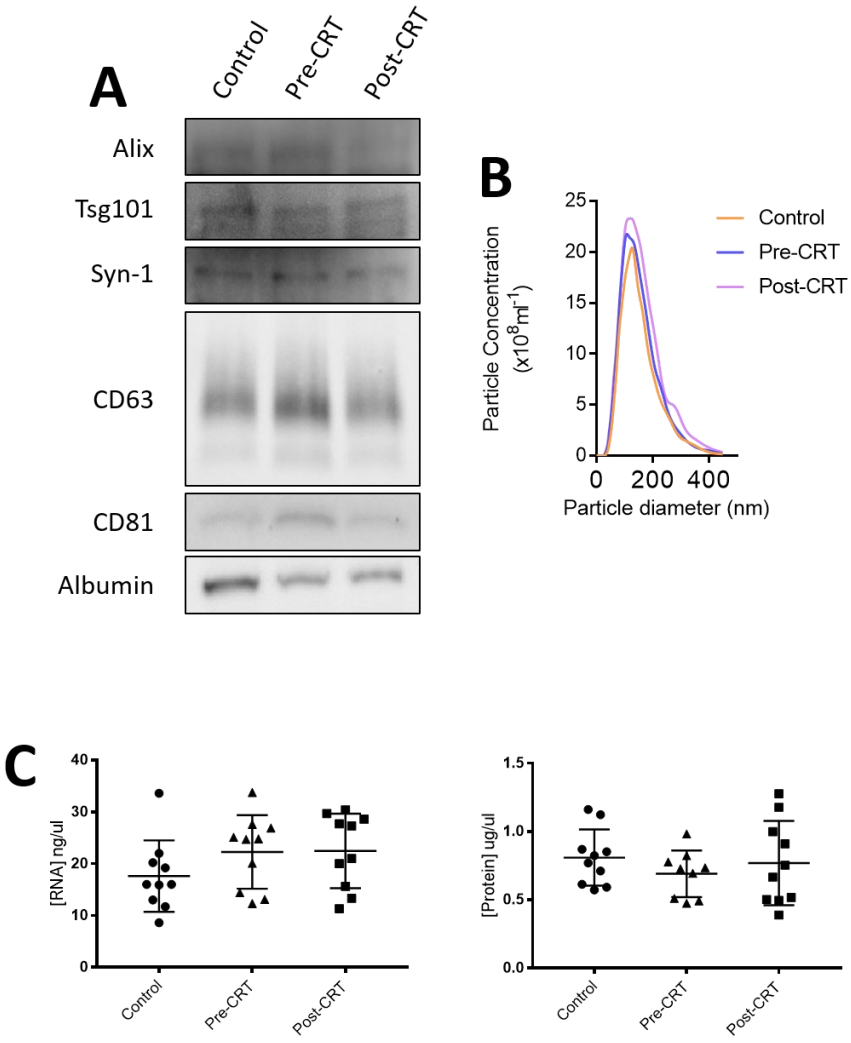
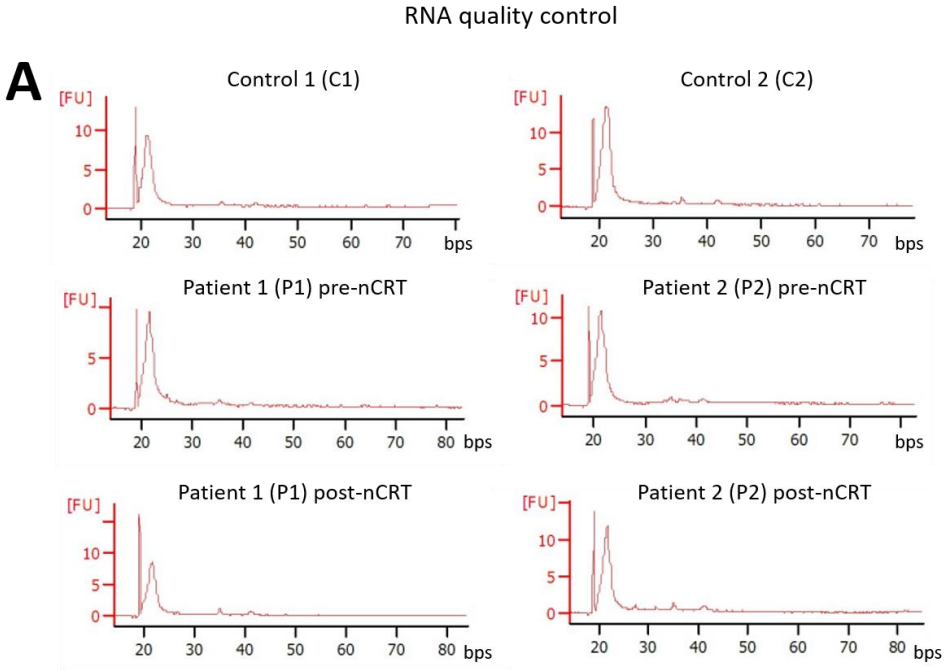


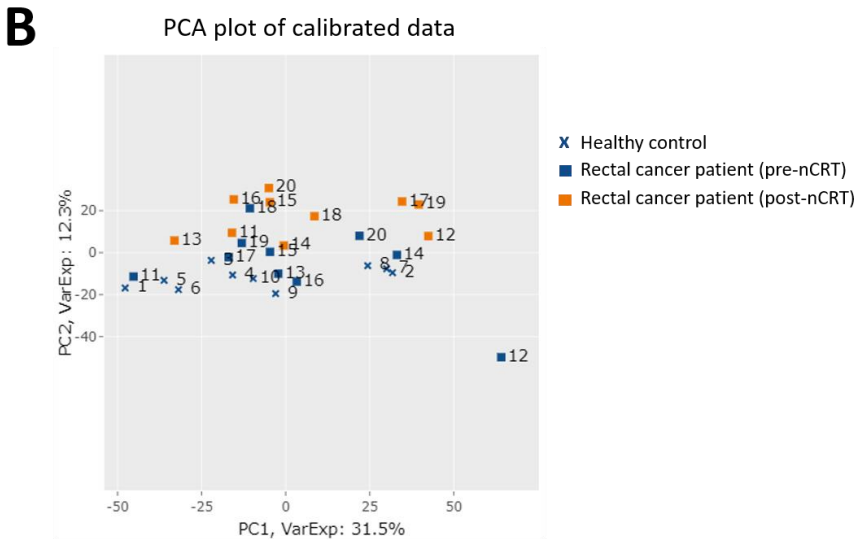

**Figure 5.9** Comparison of EVs isolated from healthy controls and patients pre- and post-nCRT. (A) Western blot analysis, (B) NTA profiles and (C) RNA and protein concentration of EVs isolated from the plasma of healthy controls and patients diagnosed with rectal cancer, pre- and post-neoadjuvant treatment. EV size and overall concentration of cargo does not appear to be affected by disease status or treatment.

### 5.2.4.2 Data calibration and quality assessment of plasma EV-miRNAs

As with the cell line work, samples were processed by UK Bioinformatics Ltd, whereby miRNA expression was measured using the Affymetrix GeneChip™ miRNA 4.0 array (ThermoFisher Scientific). RNA from all samples were enriched in short RNAs of between 20-30 bps, consistent with microRNA enrichment, and importantly, were devoid of rRNA contamination (Figure 5.10A). Following background adjustment and normalisation a PCA plot was generated to illustrate the variation of the data (Figure 5.10B). Within the PCA plot,

controls are labelled as 1 – 10, and patients as 11 – 20 (data point 11, corresponds to patient 1 (P1) within Table 5.8, point 12 to P2 and so on to point 20, which represents P10). When comparing controls with the rectal cancer cohort (pre-nCRT), PC2 appears to account for the variation between samples. PC2 also accounts for some the differential expression between pre- and post-nCRT samples, although there is also variation according to PC1. While the majority of samples appear to cluster closely to one another, pre-nCRT data point 12 appears to be an outlier. This is confirmed by mapping sample-to-sample Euclidean distance (Figure 5.10C), which shows a large distance of separation compared with the other 19 samples. Therefore, this sample was excluded from the downstream differential analysis.


A
RNA quality control
Control 1 (C1)
Control 2 (C2)
Patient 1 (P1) pre-nCRT
Patient 2 (P2) pre-nCRT
Patient 1 (P1) post-nCRT
Patient 2 (P2) post-nCRT
[FU]
bps


B
PCA plot of calibrated data
Healthy control
Rectal cancer patient (pre-nCRT)
Rectal cancer patient (post-nCRT)
PC2, VarExp: 12.3%
PC1, VarExp: 31.5%

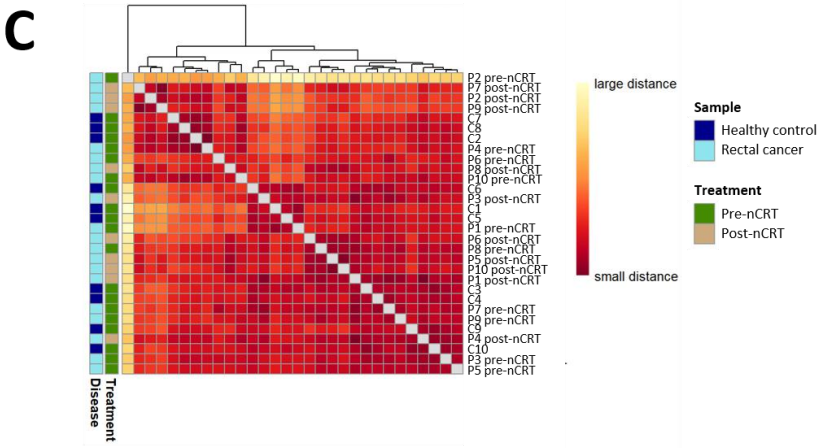

C
large distance
small distance
Sample
Healthy control
Rectal cancer
Treatment
Pre-nCRT
Post-nCRT
Disease
Treatment

**Figure 5.10** Data calibration and quality assessment of plasma EV-miRNAs. miRNA was isolated from EVs and sent for microarray analysis, which was undertaken by UK Bioinformatics Ltd. (A) Isolated RNA was enriched in short RNAs of between 20-30 bps and devoid of rRNA contamination (graphs shown representative of all samples analysed). Following normalisation of the data, quality assessment was undertaken by principle component analysis (B) and heatmap clustering of each individual sample (C). Sample 12 (corresponding to P2 pre-nCRT) was identified as an outlier and excluded from the downstream differential expression analysis. The bioinformatic analysis was undertaken in collaboration with Ryan Carter and Alessandro Barberis (Buffa Group, Department of Oncology, University of Oxford).

### 5.2.4.3 The plasma EV-miRNA profile of patients diagnosed with rectal cancer

To explore possible biomarkers of disease, differential miRNA expression between patients and controls was determined using non-paired linear modelling analysis assuming a false discovery rate of 5% (Table 5.10). Five miRNAs were found to be increased and one was decreased within patients with rectal cancer. Despite having a LogFC of greater than one or less than minus one, none of these changes reached statistical significance. Reasons for this include the small sample size and large degree of biological and environmental variation between individual patients and controls.

| miRNA | LogFC | P.value | P.adj | Reference(s) |
|---|---|---|---|---|
| **hsa-let-7a-5p** | **1.67** | **0.003** | **0.89** | **See Table 5.2** |
| **hsa-miR-126-3p** | **1.43** | **0.005** | **0.89** | **de Miguel Perez et al. (2020); C. Du et al. (2014)** |
| **hsa-miR-548a-3p** | **1.85** | **0.001** | **0.79** | **M. Wang et al. (2020b)** |
| **hsa-miR-638** | **1.11** | **0.002** | **0.89** | **See Table 5.2** |
| hsa-miR-3960 | 1.01 | 0.02 | 0.99 | |
| hsa-miR-6880-5p | -1.05 | 0.01 | 0.96 | |

**Table 5.10** EV-miRNAs that show differential expression in a cohort of patients with newly diagnosed rectal cancer. miRNAs in red text were identified in two or more studies (Table 5.2) from the systematic review of EV-miRNAs as biomarkers for CRC. Green text highlights miRNAs with previously reported tumorigenic properties.

Two of the miRNAs increased (let-7a-5p and miR-638) were included in more than one study within the systematic review of CRC plasma-derived EV-miRNAs. Previous studies have validated increased levels of EV-associated let-7a-5p within larger cohorts to diagnose CRC (Maminezhad et al. 2020; Ogata-Kawata et al. 2014), whereas decreased levels of miR-638 in serum exosomes is associated with increased risk of liver metastases and reduced overall and disease-free survival (Yan et al. 2017b; Yan et al. 2017a). EV-associated miR-126-3p is known to correlate positively with CEA levels in CRC, and was investigated as a possible biomarker for metastatic disease in CRC, but was not found to be significant (de Miguel Perez et al. 2020). Dysregulation of miR-126-3p has been investigated in hepatocellular carcinoma, where reduced tumour expression is associated with increased angiogenesis and metastases (C. Du et al. 2014). Similarly, miR-548-3p is an anti-proliferative, pro-apoptotic tumour-suppressor miRNA, and non-EV based studies have shown that its expression within tumours is decreased in breast and CRC (Shi et al. 2015; M. Wang et al. 2020b). Tumour cells are known to dispose of tumour-suppressive miRNAs in EVs (O'Brien et al. 2018), therefore, it is possible that increased EV-associated miR-126-3p and miR-548-3p represents an adaptive process to support continued tumour growth.

#### 5.2.4.4 nCRT for rectal cancer is associated with changes in plasma EV-miRNA cargo

Differential expression of EV-miRNA cargo was explored pre- and post-nCRT (Figure 5.11A). Treatment was associated with significant changes in the expression of two miRNAs: miR-6776 (LogFC 0.93, P.adj. 0.01) and miR-5189-3p (LogFC -1.02, P.adj. 0.01). In addition to these, a range of other miRNAs showed a LogFC of greater than one or less than minus one (Figure 5.11B, Table 5.11). In contrast to the cell line data, which mainly highlighted miRNAs that were increased in switched EVs, this data shows that roughly the same number of miRNAs are increased and decreased following nCRT. This may suggest that a significant proportion of the changes detected within this data were due to systemic

changes, and are not directly related to the tumour. The small sample size will also compound the ability to detect tumour-specific changes.

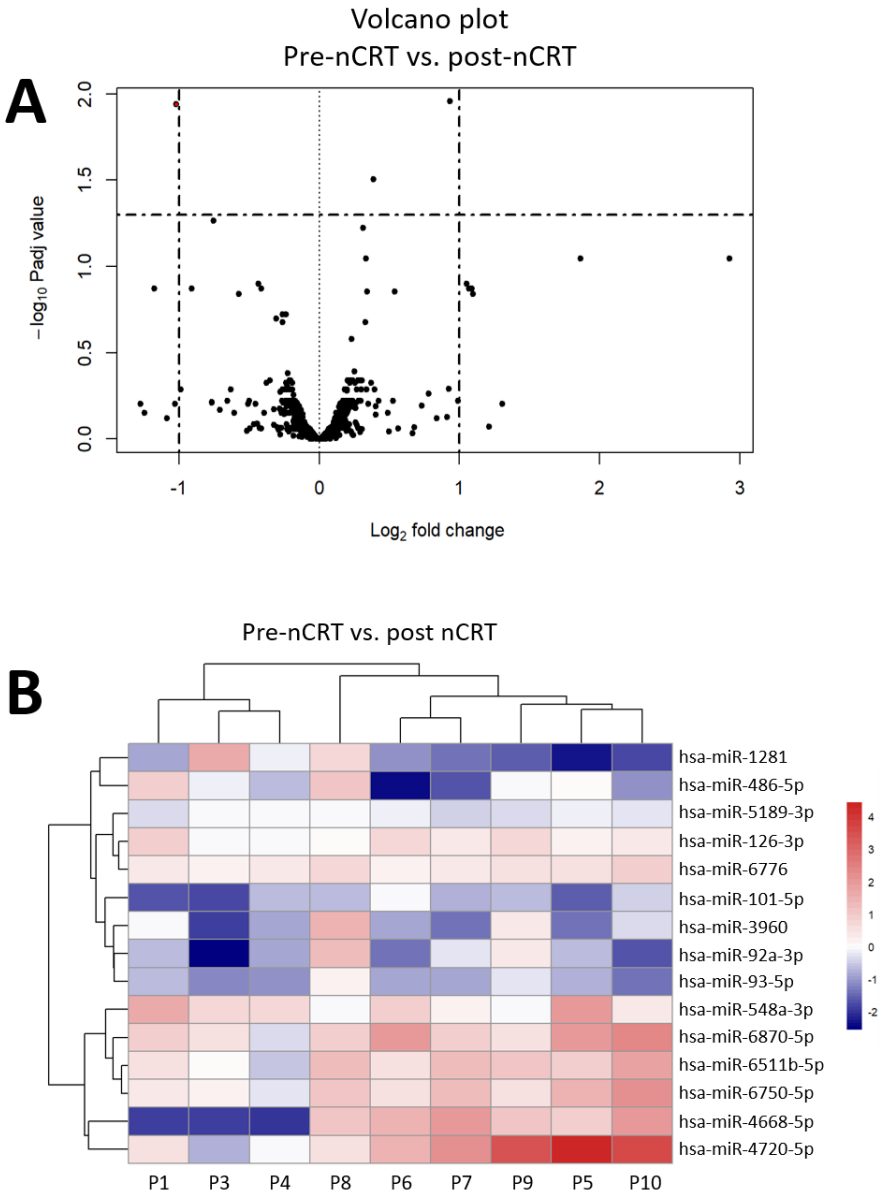



**Figure 5.11** nCRT is associated with changes in EV-miRNA cargo. (A) Differential miRNA expression revealed that treatment was associated with the significant changes in two miRNAs (miR-6776 was significantly upregulated post-nCRT, while miR-5189-3p was downregulated). (B) Heatmap of EV-miRNAs with a LogFC of greater than one or less than one following nCRT.

| miRNA | LogFC | P.value | P.adj | Reference(s) |
|---|---|---|---|---|
| hsa-miR-4720-5p | 2.92 | 0.00009 | 0.09 | |
| **hsa-miR-548a-3p** | **1.85** | **0.001** | **0.79** | **M. Wang et al. (2020b)** |
| hsa-miR-4668-5p | 1.21 | 0.11 | 0.85 | |
| hsa-miR-6750-5p | 1.10 | 0.0004 | 0.14 | |
| **hsa-miR-126-3p** | **1.09** | **0.0003** | **0.13** | **de Miguel Perez et al. (2020); C. Du et al. (2014)** |
| hsa-miR-6870-5p | 1.07 | 0.0002 | 0.13 | |
| hsa-miR-6511b-5p | 1.05 | 0.0002 | 0.13 | |
| hsa-miR-6776 | 0.93 | 0.000001 | 0.01 | |
| **hsa-miR-93-5p** | **-0.75** | **0.00003** | **0.05** | **Pellatt et al. (2016)** |
| hsa-miR-5189-3p | -1.02 | 0.000003 | 0.01 | |
| hsa-miR-3960 | -1.03 | 0.01 | 0.63 | |
| ***hsa-miR-486-5p*** | ***-1.09*** | ***0.05*** | ***0.76*** | ***Bjornetro et al. (2019)*** |
| hsa-miR-101-5p | -1.18 | 0.0003 | 0.13 | |
| hsa-miR-1281 | -1.25 | 0.04 | 0.71 | |
| **hsa-miR-92a-3p** | **-1.28** | **0.01** | **0.63** | **See Table 5.2** |

**Table 5.11** Changes in EV-miRNA cargo following nCRT. miRNAs in red text were identified in two or more studies (Table 5.2) from the systematic review of EV-miRNAs as biomarkers for CRC, while those in red italics were identified within a single study. Green text highlights miRNAs with previously reported tumorigenic properties.

Levels of EV-associated miR-92a-3p decreased the most following nCRT (LogFC -1.28, P.adj. 0.63). miR-92a-3p is derived from oncomiR-1, and in CRC it inactivates inhibitors of the Wnt pathway to promote tumour cell growth and angiogenesis. Furthermore, CRC cells are known to secrete abundant amounts of miR-92a-3p into the blood via EVs (N. O. Yamada and Senda 2021). Consistent with its well-established oncogenic properties, miR-92a-3p was highlighted in five studies in the systematic review, having been validated as a potential biomarker across all three outcomes assessed (diagnosis, prognosis and response to treatment). Decreased levels of miR-93-5p following nCRT almost reached statistical significance (LogFC -0.75, P.adj. 0.05). This forms part of the miR-106b-25

cluster of miRNAs, which is a paralog of oncomiR-1. Finally, miR-486-5p was also decreased following nCRT and was included in a single study in the systemic review, which showed that low levels within plasma exosomes was associated with lymph node metastases and poor prognosis in patients with rectal cancer (Bjornetro et al. 2019). As this analysis included both responders and non-responders to nCRT, the latter of whom were known to include a higher proportion of patients with lymph node metastases, it is possible that the decreased miR-486-5p detected here arises from this sub-set of patients. This is explored in the following section.

This pilot study has highlighted multiple miRNAs that appear to be altered in levels within plasma EVs following nCRT. Future work should focus on validating these changes within the patient samples using qRT-PCR. However, due to the small sample size the majority of these changes did not reach statistical significance. To determine the sample size required to confirm a significant change, power calculations were undertaken on a selection of miRNAs that showed a relatively large LogFC and lower adjusted p-values. The required level of significance was set at 0.00078, which was calculated by a paired t-test for the miRNA that showed the lowest adjusted p-value (miR-6776: LogFC 0.93, P.adj. 0.01). While traditionally the required level of significance is 0.05, the differential analysis in this patient study utilises empirical Bayes shrinkage, because of the large number of comparisons being made, which results in lower threshold p-values. Using this approach, the sample size required to demonstrate significance at a power of 0.8 are: miR-4720-5p (13 patients), miR-126-3p (18 patients), miR-93-5p (16 patients) and miR-101-5p (17 patients). This suggests that it should be feasible to verify several of the candidate miRNAs identified with only a modest scale-up of the patient analysis.

#### 5.2.4.5 Responders and non-responders to nCRT exhibit distinct EV-miRNA profiles

To further explore the relationship between EV-miRNA cargo and nCRT, pre and post-treatment paired analysis was undertaken for responders (Table 5.12) and non-responders (Table 5.13). With the exception of miR-4720-5p and miR-548-3p, which were increased following nCRT in both groups, responders and non-responders otherwise showed distinct EV-miRNA profiles. Given its known tumour suppressive activity the reason why miR-548-3p remains up-regulated in both groups post-treatment is unclear. The fact that it was also highlighted during the comparison with controls and the unpaired analysis pre- and post-treatment may indicate that it is a general marker of disease rather than a predictor of treatment outcome.

| miRNA | LogFC | P.value | P.adj | Reference(s) |
|---|---|---|---|---|
| hsa-miR-4720-5p | 2.63 | 0.008 | 0.93 | |
| **hsa-miR-548a-3p** | **1.85** | **0.001** | **0.79** | **M. Wang et al. (2020b)** |
| hsa-miR-3126-3p | 1.78 | 0.0008 | 0.79 | |
| **hsa-miR-126-3p** | **1.36** | **0.001** | **0.79** | **de Miguel Perez et al. (2020); C. Du et al. (2014)** |
| hsa-miR-26a-5p | 1.17 | 0.08 | 0.93 | |
| hsa-miR-6551b-5p | 1.11 | 0.004 | 0.93 | |
| **hsa-let-7a-5p** | **1.08** | **0.07** | **0.93** | **See Table 5.2** |
| hsa-miR-6750-5p | 1.08 | 0.02 | 0.93 | |
| hsa-let-7c-5p | 1.01 | 0.02 | 0.93 | |
| hsa-miR-7704 | -1.02 | 0.11 | 0.93 | |
| **hsa-miR-191-5p** | **-1.03** | **0.19** | **0.94** | **Ji et al. (2014)** |
| hsa-miR-5189-3p | -1.15 | 0.00004 | 0.27 | |
| hsa-miR-1281 | -1.16 | 0.19 | 0.94 | |
| hsa-miR-6808-3p | -1.16 | 0.002 | 0.79 | |
| hsa-miR-6089 | -1.21 | 0.00009 | 0.299 | |
| hsa-miR-101-5p | -1.51 | 0.002 | 0.79 | |
| **hsa-miR-92a-3p** | **-1.64** | **0.02** | **0.93** | **See Table 5.2** |

**Table 5.12** Changes in EV-miRNA cargo in patients that showed a complete clinical response to nCRT. miRNAs in red text were identified in two or more studies (Table 5.2) from the systematic review of EV-miRNAs as biomarkers for CRC. Green text highlights miRNAs with previously reported tumorigenic properties.

| miRNA | LogFC | P.value | P.adj | Reference(s) |
|---|---|---|---|---|
| hsa-miR-4720-5p | 3.16 | 0.0002 | 0.38 | |
| hsa-miR-4668-5p | 3.27 | 0.006 | 0.90 | |
| **hsa-miR-3613-3p** | **1.88** | **0.05** | **0.91** | **Y. Liu et al. (2020)** |
| **hsa-miR-548a-3p** | **1.87** | **0.006** | **0.71** | **M. Wang et al. (2020b)** |
| hsa-miR-6870-5p | 1.23 | 0.002 | 0.71 | |
| **hsa-miR-23a-3p** | **1.14** | **0.04** | **0.91** | **See Table 5.2** |
| hsa-miR-6750-5p | 1.11 | 0.0005 | 0.62 | |
| hsa-miR-6511b-5p | 1.00 | 0.001 | 0.71 | |
| hsa-miR-3665 | -1.15 | 0.03 | 0.90 | |
| hsa-miR-3960 | -1.24 | 0.03 | 0.90 | |
| hsa-miR-1281 | -1.32 | 0.03 | 0.90 | |
| ***hsa-miR-486-5p*** | ***-1.60*** | ***0.06*** | ***0.91*** | ***Bjornetro et al. (2019)*** |

**Table 5.13** Changes in EV-miRNA cargo in patients that did not show a complete clinical response to nCRT. miRNAs in red text were identified in two or more studies (Table 5.2) from the systematic review of EV-miRNAs as biomarkers for CRC, while those in red italics were identified within a single study. Green text highlights miRNAs with previously reported tumorigenic properties.

While the differential analysis of responders and non-responders did not reveal any significant changes following nCRT, the distinct EV-miRNA profiles provide several interesting insights into reasons why some individuals respond to nCRT while others do not. Responders to nCRT exhibited increased levels of EV-associated miR-126-3p, which is known to possess anti-tumorigenic properties (C. Du et al. 2014). EVs from non-responders had higher levels of miR-23a-3p following nCRT, which has previously been shown to promote chemotherapy resistance in CRC (H. L. Tang et al. 2012). Similarly, miR-3613-3p was also increased in non-responders. A study by Y. Liu et al. (2020) has

previously shown that exosomal miR-3613-3p promotes drug resistance in breast cancer. As discussed in the previous section, miR-92a-3p and miR-486-5p were both decreased following nCRT during the non-paired analysis. Interestingly, the decrease in these EV-miRNAs appears to distinguish nCRT responders from non-responders, whereby miR-92a-3p showed the largest decrease in responders (LogFC -1.64, P.adj. 0.93) and miR-486-5p showed the largest decrease in non-responders (LogFC -1.60, P.adj. 0.91). While the small sample size limits direct comparison, a non-paired analysis of responders and non-responders pre- and post-nCRT provided evidence that differences in miR-92a-3p and miR-486-5p expression can be detected before treatment. Therefore, these EV-miRNA changes may provide a novel method to predict response to nCRT.

## 5.3 Discussion

Due to their ability to promote and suppress gene expression, EV-associated miRNAs represent an important mechanism for intercellular communication during normal physiology, as well as disease. Cancer cells exhibit dysregulation of miRNA expression and the transfer of miRNAs via EVs between tumour cells and other cells within the tumour microenvironment is reported to promote primary tumorigenesis, as well as the development and growth of distant metastases (L. T. Vu et al. 2020). As EVs can be isolated from blood, the discovery of cancer specific EV-miRNA signatures could provide attractive candidates for biomarkers to be used in the diagnosis and management of CRC, independent of their functional activity. Therefore, the aim of this chapter was to investigate the EV-miRNA cargo both *in vitro*, within preparations of non-switched and switched EVs, and within plasma samples from a cohort of patients with newly diagnosed rectal cancer. Briefly, while HCT116 and SW480 cells were found to secrete EVs with distinct miRNA expression profiles, both secrete switched EVs that are enriched in miRNAs that are pro-tumorigenic. While the small sample size of the clinical study meant that it was underpowered to detect significant changes in plasma EV-miRNA expression, comparative

analysis between controls and patients with rectal cancer, as well as paired analysis pre- and post-neoadjuvant treatment highlighted a range of increased and decreased miRNAs that have previously been validated as CRC biomarkers. This was also the first known study to investigate the differences in EV-miRNA cargo between nCRT responders and non-responders, which highlighted a pattern of EV-miRNA expression as a potential biomarker to predict response to treatment.

### 5.3.1 Studies investigating EV-associated miRNAs in patients with CRC report highly heterogenous findings

As the profiling of EV-associated miRNAs from CRC cell lines and patient plasma was expected to produce large and complex data sets, a systematic review of previous studies investigating EV-miRNA cargo in patients with CRC was undertaken to assist with the interpretation of this data. The decision to focus on patient cohort studies was based on the absence of general EV-miRNA profiling studies for the CRC cell lines used in this thesis, as well as the aim to identify potential translational aspects of the EV switch for future investigation. This process highlighted the scientific interest within this field. Since 2014 there have been 53 studies, which collectively have identified 66 EV-associated miRNAs as biomarkers for CRC. Despite this, two thirds (44) of these miRNAs were only reported in a single study, making it difficult to assess the external validity of these findings. Reasons for this high degree of heterogeneity are likely to be multifactorial, as discussed below.

Forty of the included studies combined EV-miRNA data from patients with both colonic and rectal cancers. CRC is characterised by a high degree of molecular and genetic heterogeneity, which underlies observed clinical differences between cancers arising in the proximal, right-sided colon compared to those in the left colon and rectum. Coinciding with this, specific miRNA-mRNA associations characterise the different molecular subtypes of CRC (Perez-Villamil et al. 2017), and colonic tumours have been shown to exhibit differential miRNA expression based on their MMR status (Sarver et al. 2009). Therefore,

for these reasons it is probable that any combined analysis of colonic and rectal cancer samples will have a confounding effect on the reported results, and could account for some of the heterogeneity highlighted during this systematic review. The systematic review also included studies that isolated EVs from both plasma and serum. Serum is prepared following clotting, which is associated with the release of large quantities of EVs from platelets, which will contain miRNA. It has been estimated that the process of clot formation may account for over 50% of serum-derived EVs (Witwer et al. 2013). Furthermore, a study by K. Wang et al. (2012) has shown important quantitative and qualitative differences in the miRNA spectra isolated from plasma and serum from the same individuals, whereby the latter is enriched in high quantities of platelet-associated miRNAs. For these reasons, plasma is considered to be more representative of physiological levels of circulating EVs within the blood, and is recommended for use in studies investigating EVs in patient samples (Witwer et al. 2013). Despite this, the majority of studies included in the systematic review (35 out of 53) isolated EVs from serum. Of the 18 studies that isolated EVs from plasma, 11 of these were studies that reported EV-associated miRNAs that were identified in more than one study, suggesting that a large proportion of the heterogeneity is associated with studies that used serum samples.

The systematic review also included studies that isolated EVs using a range of different methods, including: dUC, various precipitation-based techniques and SEC. This will also explain some of the heterogeneity of validated EV-associated miRNAs, as the different methods used to isolate EVs from plasma and serum are known to result in distinct EV preparations, including varying levels of non-EV, miRNA-associated contaminants (Brennan et al. 2020; Buschmann et al. 2018; Lobb et al. 2015). When compared with dUC and SEC, commercial precipitation-based results produce the least purified preparations of EVs, with high levels of other plasma components, including lipoproteins and other extracellular proteins also known to transport miRNA (Konoshenko et al. 2018). Despite this, 35 of the studies (66%) included in the systematic review isolated EVs using one of

these precipitation-based methods, and these were evenly distributed amongst miRNAs that were validated in a single study, and miRNAs that were validated in multiple studies.

While different isolation methods result in different EV preparations, all studies should provide proof of adherence to the MISEV guidelines, which can add evidence to support any downstream findings that are thought to be EV-related. Ogata-Kawata et al. (2014) conducted the first study investigating EV-associated miRNAs as biomarkers for CRC. This study predates the publication of even the first edition of the MISEV guidelines (Lotvall et al. 2014), and apart from demonstrating the presence of CD81 in UC pellets, does not provide any further evidence to confirm the identity of isolated vesicles. However, there was variable adherence to the MISEV guidelines in a significant proportion of other studies included in the systematic review, including in studies published after the second edition of the guidelines in 2018, at which point adherence was recommended as a condition of publication (Thery et al. 2018). For example, a study by H. Zhang et al. (2019a) that validated a seven-miRNA signature (including miR-17-5p and miR-181a-5p that were validated in more than one study) in plasma EVs for the diagnosis of CRC did not provide any quantitative or qualitative data for the EV preparations. An included study that validated EV-associated miR-125b as a biomarker for FOLFOX resistance only provided a single TEM image of vesicular-like structures alongside a quantitative analysis of CD9-positive structures (Yagi et al. 2019). While the studies by Fu et al. (2018) and (Wei et al. 2020) included western blot analysis, NTA profiles and TEM images, these did not include any negative EV markers so an assessment of EV purity cannot be made. No study included in the systematic review provided complete adherence to all of the MISEV recommendations, which may account for the lack of reproducibility in studies that were investigating the same outcomes.

Of the 22 EV-associated miRNAs that were reported in more than one study, this included a range of candidates with known pro-tumorigenic activity in CRC. Nine studies highlighted

miRNAs that are derived from oncomir-1 across all three outcomes (diagnosis, prognosis and response to treatment). This is perhaps unsurprising as the oncomir-1 miRNAs exert a broad range of pro-tumorigenic effects through dysregulation of multiple cellular processes, including: proliferation (targeting TGF-β and SMAD), cell cycle regulation (targeting p21 and E2F1) and cell death (targeting PTEN) (Mogilyansky and Rigoutsos 2013). In particular, expression of four oncomiR-1 miRNAs (miR-17-5p, miR-19a, miR-19b and miR-20a) were found to negatively correlate to treatment response in rectal cancer in a study that also examined EV-associated miRNAs in plasma using a microarray-based detection method, which is similar to the method used for the patient-based miRNA analysis undertaken in this chapter (Kral et al. 2018). miR-21 was the most cited miRNA, in nine studies across all three outcomes. In CRC, exosomal-miR-21-mediated downregulation of PTEN and PDCD4 is associated with increased proliferation, invasion and therapy resistance (Sun et al. 2020). It was one of five miRNAs validated in the first study of circulating exosomal miRNAs as biomarkers for the diagnosis of CRC (Ogata-Kawata et al. 2014). Subsequent studies have shown that it can be used to diagnose early stage disease (L. Zhao et al. 2017b), and its expression correlates with increasing stage of disease, where it can also be used to accurately predict recurrence and overall survival (Tsukamoto et al. 2017). Similarly, high circulating levels of EV-associated miR-21 are associated with poor response to chemotherapy (Fuji et al. 2019; Jin et al. 2019; Kral et al. 2018).

### 5.3.2 EV-miRNA data from CRC cell lines reveals differential loading of EV cargo under microenvironmental stress

HCT116 and SW480 cells secrete switched EVs with distinct miRNA expression profiles. The tumour microenvironment is well known to modulate EV secretion and cargo, including EV-associated miRNAs (Kucharzewska and Belting 2013). In breast cancer cells, hypoxia induces the secretion of EVs with increased levels of miR-210, which is a potent stimulator of angiogenesis (King et al. 2012). In another study, melanoma cells subjected to a range of stress conditions were shown to secrete EVs with distinct miRNA spectra involved in

specific adaptive functions, including: upregulation of glycolysis, gluconeogenesis, proliferation and cellular migration (Harmati et al. 2019). A similar range of functions was predicted for the EV-associated miRNAs detected in switched EVs from HCT116 and SW480 cells. Therefore, while previous studies have highlighted the association between microenvironmental stress and selective loading of specific miRNAs into EVs, the results presented here demonstrate that this is accompanied by the secretion of switched EVs. It is important to note that for some of the EV-miRNAs that show altered levels, their cellular expression levels may also respond to mTORC1 inhibition, which should be investigated following the validate of specific EV-miRNAs by qRT-PCR.

Interestingly, in contrast to the patient cohort analysis, very few of the EV-associated miRNAs highlighted in the systematic review were found to be significantly increased or decreased within the cell line data. Whereas cell culture is performed under tightly controlled experimental conditions, a range of biological and environmental factors also contribute to the differences observed in patient EV-miRNA cargo. Furthermore, it is likely that a proportion of miRNAs highlighted in patient studies represent a systemic response to an underlying cancer and originate from non-tumour cells both within and outside of the tumour microenvironment.

While the majority of miRNAs that are increased or decreased in switched EVs have not been previously implicated in tumorigenesis, or currently have unknown function, this is not uncommon in this type of study. Despite this, enrichment analysis of these miRNAs showed that HCT116 and SW480 cells both secrete switched EVs that contain miRNAs that regulate a range of tumorigenic processes, including EMT, migration and angiogenesis, as well as modulating Wnt signalling, which is a canonical CRC signalling pathway. Interestingly, four miRNAs increased in switched EVs from HCT116 cells were predicted to positively regulate cellular adhesion (miR-4739, miR-6848-5p, miR-6891-5p and miR-7110-5p). This is of relevance to the findings reported in Chapter 4, which showed that the

switched EV-induced reduction in recipient cell migration and invasion coincided with an increase in E-cadherin expression. In contrast to the effects on tumour growth, the underlying mechanisms responsible for this MET-type behaviour are currently unknown, but based on the findings presented here, could involve EV-miRNAs.

HCT116 cells were shown to secrete switched EVs containing increased levels of miR-23a-3p, although this increase was not statistically significant. Increased levels of EV-miR-23a-3p has previously been highlighted as a potential EV-based biomarker for diagnosing CRC (Karimi et al. 2019; Ogata-Kawata et al. 2014; Ostenfeld et al. 2016). Dysregulation of miR-23a-3p expression is observed in a range of cancers, often being down-regulated in haematological and genitourinary cancers and overexpressed in head and neck and gastrointestinal malignancies (N. Wang et al. 2018). Consistent with its overexpression in switched EVs, microenvironmental stress, including hypoxia has been shown to increase transcription of a cluster of miRNAs that includes miR-23a-3p (Khan et al. 2016). While there are no studies that have investigated the biological role of EV-associated miR-23a-3p in CRC, non-EV based studies in other cancers have demonstrated its role as a promoter and repressor of tumour cell migration and invasion. In breast cancer cells, Ma et al. (2017) showed that miR-23a promotes EMT and tumour cell invasion by directly targeting the CDH1 gene leading to reduced expression of E-cadherin and activation of Wnt signalling. Conversely, it has also been shown to promote MET and reduce tumour cell migration and invasion in endometrial cancer through down-regulation of SMAD3, which is associated with increased E-cadherin and reduced vimentin expression (P. Liu et al. 2016). It is possible that increased miR-23a-3p in switched EVs mediates the reduction in recipient cell migration and invasion that was shown in the previous chapter. This can be investigated in future studies by validating the increased levels of miR-23a-3p in switched EVs using qRT-PCR and then co-treating EVs with an anti-miR-23a to see whether this reverses the effects on migration, invasion and the coinciding MET-like phenotype.

Despite showing that switched EVs contain increased and decreased levels of EV-associated miRNAs when compared to non-switched EVs, there was no overlap in those miRNAs that were differentially expressed between the two CRC cell lines studied. This is consistent with the data calibration, whereby principle component analysis and clustering of samples by Euclidean distance showed that the main source of variation in the data was between the two cell lines. While this may be explained by the different treatments used to trigger the EV switch (glutamine-depletion in HCT116 cells and Torin1 treatment in SW480 cells), it is also consistent with previous studies in CRC that have shown EV-miRNA cargo varies according to the genetic and molecular properties of the tumour cells (Perez-Villamil et al. 2017; Sarver et al. 2009). This is also evident when comparing exosomes and microvesicles isolated from SW480 and SW620 cells, which exhibit distinct miRNA expression profiles despite originating from the same patient (M. Chen et al. 2019a). It is also supported by the findings reported in the previous chapter, whereby EVs isolated from SW480 cells were shown to be devoid of AREG, which is increased in Rab11a-exosomes from HCT116 cells. Caco-2 cells also secrete switched EVs containing increased levels of AREG, so future work should characterise the EV-miRNA cargo of these EVs to see whether there is any overlap with the findings reported for HCT116 cells.

The fold changes reported for each of the EV-associated miRNAs under stress conditions, including the non-significant candidates listed in Appendix C, were all relatively small. The study by M. Chen et al. (2019a) that examined the different EV-miRNA profiles of SW480 and SW620 cells reported log fold changes of up to ± 11, which presumably primarily reflects the underlying molecular and cellular differences between the two cell types. In contrast to this, the much subtler differences reported here are explained by the fact that EV preparations contain a mixture of different EV subtypes, including non-switched and switched EVs. The balance of these two EV populations changes under stress conditions, but only by a few fold. As only triplicate sets of EVs from each cell line were compared, the resulting fold change between some EV-associated miRNAs is unlikely accurately

represent the actual ration and it will certainly not match changes observed in studies comparing EV-miRNA cargoes from different cell lines. Increasing the number of EV preparations from each cell line would have led to more significant fold changes being measured. This was the case in the proteomic analysis of non-switched and switched EVs isolated from HCT116 cells undertaken by Dr Shih-Jung Fan (PDRA Goberdhan Group), which was based on five sets of EV preparations.

An additional factor contributing to the relatively small fold changes detected during this analysis, including the subsequent patient analysis is related to the microarray-based method that was used to profile the EV-associated miRNAs. Despite being the most popular method for transcript profiling, microarrays are limited by relatively high levels of background hybridisation. This reduces the accuracy of measurements for transcripts present at low levels, which is particularly relevant when studying EV-miRNAs. RNA sequencing (RNA-seq) overcomes this main limitation as it does not rely on species- or transcript-specific probes. While there have been no studies comparing microarrays with RNA-seq for EV-miRNA profiling, studies comparing the methods for mRNA detection in T-cells and MSCs have shown that RNA-seq was superior in detecting low abundance transcripts, including different isoforms as well as allowing for the detection of more differentially expressed genes with higher fold changes (J. Li et al. 2016a; S. Zhao et al. 2014).

### 5.3.3 Altered miRNA loading in switched EVs from HCT116 cells may be due to increased levels of specific RNA loading proteins

EVs are known to contain RBPs along with their RNA substrates. Switched EVs were shown to contain increased levels of the RBP, hnRNPA2B1, which validated a finding from a previous proteomic analysis of EVs isolated from HCT116 CRC cells. Overexpression of cellular hnRNPA2B1 has been associated with drug resistance in breast cancer (Klinge et al. 2019), and the regulation of KRAS-dependent growth in pancreatic adenocarcinoma

(Barcelo et al. 2014). Furthermore, hnRNPA2B1 is increased in CRC, where its expression correlates with preoperative CEA levels, advanced TNM stage and poorer prognosis following treatment (Zhou et al. 2019).

hnRNPA2B1 has emerged as a key RBP in the sorting of specific miRNAs into exosomes and microvesicles through direct interaction with GGAG motif located at the 3'-end of certain miRNAs (Fabbiano et al. 2020). Five miRNAs that possess this motif were found to be increased at non-significant levels in switched EVs (miR-575, miR-1246, miR-125a-3p, miR-198 and miR-887). Interestingly, trafficking of hnRNPA2B1 into microvesicles requires Cav-1, increased levels of which characterise the EV switch signature on Western blot (H. Lee et al. 2019). In exosomes, post-translational sumoylation controls the hnRNPA2B1-dependent sorting of miRNAs (Villarroya-Beltri et al. 2013). Sumoylated-hnRNPA2B1 controls the loading of miR-1246 into exosomes, which trigger the reprogramming of macrophages into immunosuppressive tumour-associated macrophages, which correlates with poor survival in patients with colonic tumours (Cooks et al. 2018). Therefore, future work should investigate the sumoylation status of hnRNPA2B1 in switched EVs to determine whether this is a unique feature of the recycling endosomal pathway of EV biogenesis. The functional link between miR-1246 and cancer has been demonstrated in a range of cancers, where it has been shown to promote invasiveness and stemness (Neerincx et al. 2015), and has been proposed as a biomarker for the early detection of disease. Indeed, the systematic review performed here highlighted EV-associated miR-1246 as a potential diagnostic and treatment response biomarker in CRC (Eylem et al. 2020; Jin et al. 2019; Ogata-Kawata et al. 2014).

#### 5.3.4 Changes in EV-miRNA cargo following nCRT may predict response to treatment

The initial treatment of rectal cancer is nCRT, which is administered in order to downsize tumours and to increase the subsequent rate of curative surgical resection (Feeney et al. 2019). Interestingly, up to 20% of patients who receive nCRT exhibit a complete clinical

response, and pending regular endoscopic surveillance, may avoid major pelvic surgery that often involves a permanent stoma (van der Valk et al. 2018). Identifying the underlying pathophysiological mechanisms that underpin why certain individuals respond to nCRT, while others do not, may reveal novel biomarkers that could be utilised to personalise treatment. EV-miRNAs have been shown to predict response to neoadjuvant treatment in breast cancer and prostate cancer (Labbe et al. 2020; Rodriguez-Martinez et al. 2019). In rectal cancer, Bjørnetrø et al. (2017) found that EV-associated miR-663a is decreased in CRC cell lines exposed to hypoxic conditions, and that low levels of this miRNA were associated with poor tumour response to radiotherapy.

This pilot study was the first to investigate the EV-miRNA profile in patients undergoing nCRT for rectal cancer and to compare responders with non-responders. The small sample size alongside biological and environmental variation between patients will account for the limited number of significant miRNA changes detected, although subsequent power calculations showed that only a small increase in sample size is required to detect statistical significance for miRNAs that showed a large fold change and lower adjusted p-value. In addition, as discussed above for the cell line data, the microarray method used to measure EV-miRNA levels may also account for the relatively low fold changes detected in this study. In comparison to the cell line data, the accuracy of microarray detection is likely to be even lower for whole plasma, which will contain a much wider range of EV-miRNAs that are representative of an individual's systemic physiology, many of which will be present at low abundance. For these reasons, RNA-seq may be a more appropriate method to investigate EV-miRNA content in plasma and serum. A study by Srinivasan et al. (2019) used RNA-seq to profile the miRNA content of EVs isolated from the serum of healthy controls. They found large biological variation (detected as large fold changes) between individuals, with extremely low levels of technical variation between repeat samples from the same individual. These findings highlight the strengths of RNA-seq to support EV-miRNA biomarker development. Throughout this study a large proportion of the EV-miRNAs

highlighted do not have proven tumorigenic properties or do not yet have a known function. Possible reasons for this include the microarray detection method, which is known to involve a degree of background hybridisation, and, or the presence of lipoprotein contaminants within the isolated EV preparations. Together these explanations may also account for why there was minimal overlap of EV-miRNAs highlighted in this study compared with those reported in the systematic review.

nCRT for rectal cancer resulted in decreased levels of miR-92a-3p and miR-93-5p, both of which are derived from well-known oncogenic miRNA clusters. miR-92a-3p was highlighted in fives studies in the systematic review. Higher levels of miR-92a-3p combined with increased miR-222, which was also highlighted in the systematic review, are associated with lower overall survival in patients with metastatic CRC (Perez et al. 2020). The decrease in EV-associated miR-93-5p was particularly interesting as this almost reached statistical significance, and a power calculation showed that only a small increase in the sample size would be required to confirm this (16 patients). Increased cellular expression of miR-93-5p has been shown to distinguish colonic and rectal tumours from normal mucosa (Pellatt et al. 2016). As a component of the miR-106b-25 cluster of miRNAs, which is a paralog of oncomiR-1, miR-93-5p has similar pro-tumorigenic functions to the miR-17-92a cluster, whereby its overexpression is association with increased tumour growth and angiogenesis (Liang et al. 2017). In CRC cells, overexpression of miR-93a-5p promotes cell G1/S cell cycle transition and increases the expression of efflux transporters that mediate resistance of chemotherapy (S. J. Wang et al. 2017c).

A comparison of nCRT responders and non-responders revealed several interesting insights into why some individuals respond to treatment while others do not. Responders exhibited increased levels of EV-associated miR-126-3p after treatment, which is known to possess anti-tumorigenic properties and may therefore denote less aggressive disease. Alternatively, it is possible that tumour cells selectively export miR-126-3p in exosomes due

to its anti-tumorigenic properties. Reduced cellular expression of miR-126-3p is associated with increased tumour angiogenesis (C. Du et al. 2014), which would make the tumour more radiosensitive and more likely to respond to nCRT. EV-associated miR-92a-3p and miR-486-5p were both decreased following nCRT during the paired analysis. Interestingly the decrease in these EV-miRNAs appears to distinguish nCRT responders from non-responders. EV-associated miR-92a-3p showed the largest decrease in responders, and is consistent with a study included within the systematic review, which showed high expression of EV-associated miR-92a-3p is associated with chemotherapy resistance in CRC, and forms part of a miRNA panel to predict response to treatment (J. Han et al. 2020). In contrast, miR-486-5p showed the largest decrease in non-responders. As already discussed, low plasma levels of EV-associated miR-486-5p can predict poor prognosis in CRC (Bjornetro et al. 2019), which is consistent with it being reduced in patients who did not respond to nCRT and who tended to have more advanced stage of disease, including a threatened CRM and lymph node metastases. Future work should validate these changes in matched samples using qRT-PCR and to investigate whether responders and non-responders showed corresponding increased or decreased levels of these candidate miRNAs in their pre-treatment samples, as was suggested by a non-paired analysis. If confirmed this would justify further study in a larger cohort of patients, which would enable threshold levels of EV-miRNA expression to be set that could be used for predicting treatment response.

# CHAPTER 6

## SUMMARY & CONCLUSIONS

# 6. Research summary and future implications

## 6.1 Summary of research aims

Each year 1.9-million people globally are diagnosed with CRC, which is predicted to rise to over 2.5-million within the next 15 years (Globocan 2020). Despite advances in early detection and treatment, the incidence is rising quickest in those under 40-years of age, and five-year survival from metastatic disease remains below 15% (Siegel et al. 2020). While surgery represents the cornerstone of curative treatment, there are limited options available for advanced disease, and acquired drug resistance is common. Therefore, there is an urgent need for research to unravel the biological and molecular mechanisms that drive CRC tumorigenesis in order to identify novel therapeutic targets as well as biomarkers to enable early diagnosis and to predict treatment response.

The persistent proliferation of tumour cells leads to a hypoxic and nutrient-depleted microenvironment. Adaptation to these microenvironmental stresses is a key mechanism driving tumour progression and promotes the proliferation of aggressive tumour cell clones (Chouaib et al. 2017). Cancer cells secrete large quantities of biologically active EVs into the tumour microenvironment, which are important mediators in promoting adaptation in response to microenvironmental stress (E. Yang et al. 2020). Furthermore, tumour cell-derived EVs are released into the bloodstream where they promote metastatic spread by priming the pre-metastatic niche (Wei et al. 2020). Indeed, EV-mediated signalling is now known to be involved in each of the hallmarks of cancer growth and survival (Becker et al. 2016). The Goberdhan Group recently reported a novel EV-biogenesis pathway that is activated in CRC cells in response to glutamine-depletion, which is an important cancer cell metabolite (Fan et al. 2020). Reduced glutamine leads to a reduction in signalling via mTORC1, a canonical signalling hub involved in controlling cellular adaptation, which triggers an intracellular switch in the biogenesis and profile of secreted of EVs. This EV switch is characterised by an increase in the biogenesis and secretion of Rab11a-labelled

exosomes from the recycling endosomal pathway, alongside a reduction in EV biogenesis and secretion from the classical late endosomal pathway.

As the EV switch is triggered by microenvironmental stressors known to be experienced by tumour cells and which are known to select for more aggressive tumour cells, it was hypothesised that these would have important tumorigenic functions. Therefore, the central aim of this thesis was to investigate the cargo and function of these switched EVs in CRC. In order to do this a robust and reliable method of isolating switched EVs from cultured CRC cells was required. This was undertaken in Chapter 3, where the specific aim was: *to validate size exclusion chromatography to isolate purified samples of non-switched and switched EVs, and to use this to investigate EV switching in other CRC cell lines*. Following this, the tumorigenic roles of non-switched and switched EVs were explored in Chapter 4, which aimed to: *investigate the functional properties of switched EVs on CRC cell proliferation, migration and invasion, including the underlying mechanisms driving these behaviours.* Finally, EV-associated miRNAs were investigated *in vitro* and within a patient cohort, where the specific aim was: *to explore the differences in miRNA cargo between non-switched and switched EVs from different CRC cell lines, and to investigate whether this corresponds to miRNA changes following a diagnosis of CRC and, or, treatment with nCRT.* The important findings of each chapter will now be summarised alongside a discussion of the potential future clinical implications.

## 6.2 Aim (i) Validating SEC to isolate and study EV switching in CRC cell lines

### 6.2.1 SEC can be used to isolate highly purified preparations of EVs

The initial work that led to the discovery and characterisation of the EV switch involved isolating EVs using UC. The limitations of UC, which include: particle aggregation, EV rupture and poor experimental reproducibility (Linares et al. 2015; Sidhom et al. 2020;

Torres Crigna et al. 2021), prevented the reliable functional analysis of switched EVs, which is dependent on purified samples of intact vesicles. In contrast to UC, SEC is associated with less non-vesicular contamination and good reproducibility (Boing et al. 2014; Gardiner et al. 2016). In addition, by combining SEC with pre-injection UF, highly purified EV preparations can be isolated at high yields with intact functional properties (Nordin et al. 2015). In Chapter 3, SEC was shown to be an effective and valid method to isolate highly purified preparations of EVs, including Rab11a-exosomes, that could be modulated according to the exogenous glutamine status levels that the secreting cells are exposed to. Validation was assessed according to the internationally recognised MISEV 2018 guidelines (Thery et al. 2018), with isolated EVs demonstrating the biophysical and morphological properties, as well as the protein cargoes that are characteristic of exosomes. This led to the discovery that Rab11a-exosomes are distinct from EVs labelled with Cav-1, which is also upregulated by glutamine-depletion.

### 6.2.2 Reduced mTORC1 signalling triggers the release of Rab11a-exosomes in a panel of CRC cell lines

Using SEC, hypoxia was also shown to stimulate the release of Rab11a-exosomes in HCT116 cells. In addition, treatment with the mTOR inhibitor, Torin-1 triggered EV switching in a panel of other CRC cell lines (Caco-2, SW480 and SW620), which are representative of CRC genetic heterogeneity. Collectively, these findings provide further evidence that mTORC1 is involved in the biogenesis and secretion of different EV subpopulations in response to changes within the tumour microenvironment, and is consistent with the findings from the Goberdhan Group reported in breast, cervical and prostate cancer cell lines. In contrast to HCT116 cells, none of the other investigated CRC cell lines underwent EV switching in response to short-term glutamine-depletion. It is unclear whether this represents differences in cellular glutamine metabolism or sensitivity, but future work should investigate whether longer term glutamine withdrawal is associated with the EV switch.

### 6.2.3 Clinical implications

The validation of SEC as a method to isolate highly purified preparations of EVs in a consistent manner from cell lines in different physiological or pharmacological conditions enabled the functional roles of switched EVs to be investigated in Chapter 4, as well as an exploration of EV-miRNA cargo in Chapter 5. These investigations could collectively lead to novel CRC biomarkers or future CRC therapeutic targets. In particular, the use of EVs as cancer biomarkers has considerable potential, and could have applications spanning diagnosis, predicting response to treatment and post-treatment surveillance (Dai et al. 2020). In Chapter 3 HLA-C and TfR were shown to be increased in switched EVs, and through Co-IP it was possible to immunocapture specific switched EV subtypes. While further methodological work is required to improve pull-down efficiency, it may be possible to apply these techniques to complex biological fluids, such as plasma or serum, to determine whether switched EVs can be detected in patients with CRC. The secretion of switched EVs containing TfR is particularly interesting as previous studies have identified serum EV-associated TfR as a biomarker of early stage CRC (Shiromizu et al. 2017).

Despite the potential value of EV-based biomarkers, their routine clinical use is currently limited by the lack of a validated method for isolating blood-borne EVs that meets the required international standards for accuracy and precision. Furthermore, methods such as Co-IP are unlikely to be practical for high through-put processing. Microfluidic-based technologies have been promoted as a possible solution that addresses the drawbacks of employing traditional EV isolation methods with complex biological fluids (Su et al. 2019; M. Wu et al. 2017). This technology engineers specific EV-binding antibodies to immobilised magnetic nanoparticles, which enables targeted EV extraction as plasma or serum undergoes repeated circulation through the microfluidics circuit. Sancho-Albero et al. (2020) recently validated a microfluidics device to isolate exosomes from whole blood, which was used in the diagnosis and monitoring of pancreatic cancer. Therefore, it may be

possible to adapt this method to target TfR or HLA-C to study EV heterogeneity, and to develop biomarker co-detection strategies in the analysis of patient samples.

## 6.3 Aim (ii) Investigating the functional role of switched EVs in CRC pathogenesis

### 6.3.1 Switched EVs promote AREG-dependent growth and drug resistance

Cancer cell-derived EVs have been widely reported to increase tumour growth through autocrine and paracrine signalling (L. Han et al. 2019; Xavier et al. 2020). Consistent with this, switched EVs were shown to promote the dose-dependent growth of recipient cells cultured in reduced-serum conditions. This effect was lost following selective knockdown of *CHMP5*, which was identified through parallel work undertaken by Dr Shih-Jung Fan (PDRA, Goberdhan Group) as being essential for the biogenesis and secretion of switched EVs. Switched EVs secreted by HCT116 and Caco-2 cells were shown to contain increased levels of the EGFR-ligand, AREG, which validated the findings of a previous proteomic analysis undertaken by the Goberdhan Group Based on this finding, switched EVs were also shown to increase EGFR-ERK signalling in recipient cells, consistent with an AREG-dependent mechanism for promoting growth. This was further validated by selective neutralisation of AREG, which blocked the growth promoting property of switched EVs and coincided with reduced ERK signalling. This data was included in the EV switch study by Fan et al. (2020) (Appendix A). This AREG-dependent growth was further demonstrated *in vivo* using a chick-embryo model. Despite containing a very low dose of AREG, switched EVs had a growth promoting effect 20,000 – 200,000 times greater than rAREG, which is consistent with previous studies that have demonstrated the high potency of EV-associated AREG (Higginbotham et al. 2011; Q. Zhang et al. 2019b). Interestingly, EVs secreted by SW480 and SW620 cells did not contain AREG, and did not exhibit any growth promoting effect in recipient cells, providing further evidence that this effect is AREG-dependent.

Switched EVs isolated from HCT116 cells were able to promote the AREG-dependent growth of Caco-2 recipient cells, consistent with paracrine EV-signalling between different cancer cell clones. Cetuximab is an anti-EGFR antibody used in the treatment of *KRAS* wild-type metastatic CRC, although acquired drug resistance develops in virtually all patients (B. Zhao et al. 2017a). While understanding of resistance pathways is limited, recent studies have shown that *KRAS* mutant, cetuximab-resistant CRC cells secrete exosomes that promote resistance in *KRAS* wild-type, cetuximab-sensitive cells (S. Zhang et al. 2017b). Consistent with this finding, switched EVs isolated from HCT116 (*KRAS* mutant) cells were able to induce AREG-dependent cetuximab resistance in Caco-2 (*KRAS* wild-type) cells. As Caco-2 cells also secrete switched EVs that contain increased levels of AREG and EGFR inhibition may reduce mTORC1 signalling in Cetuximab-treated cells, it is possible that autocrine EV signalling may also trigger cetuximab resistance in the absence of *KRAS* mutant clones.

### 6.3.2 Switched EVs reduce recipient cell migration, invasion and mesenchymal protein expression

EVs are known to participate in a range of inter and intracellular signalling pathways to promote the phenotypic changes required for tumour metastasis, particularly EMT (H. Zhao et al. 2018). Moreover, previous studies have shown that AREG-containing EVs increase the invasiveness of recipient cells *in vitro* and *in vivo* (Higginbotham et al. 2011; Q. Zhang et al. 2019b). Therefore, it was a surprise to find that switched EVs from HCT116 cells reduced recipient cell migration and invasion by up to 50%. Subsequent assays found that this response was AREG-independent, indicating that an alternative, and as yet unidentified mechanism drives this effect. The significance of these findings are currently unclear, particularly as *in vivo* data from the chick embryo model suggested that switched EVs may promote an AREG-dependent reduction in tumour cell intravasation. Consistent with an EV-mediated reduction in migration and invasion, switched EVs also led to an increase in the expression of the epithelial marker, E-cadherin, and a reduction in N-cadherin and vimentin

expression. The reduction in N-cadherin and vimentin was also detected within metastatic deposits within the chick embryo model. This change in protein expression denotes MET, which is the morphological transition circulating tumour cells undergo once they arrive at a metastatic site. This is the first report of EV-mediated MET in CRC, and provides evidence that switched EVs may also promote CRC metastasis. While the tumorigenic properties of non-switched EVs were not specifically investigated, *in vitro* and *in vivo* evidence generated in this chapter suggest that they may also drive other aspects of tumorigenesis by promoting opposing effects to those triggered by Rab11a-exosomes.

### 6.3.3 Clinical implications

The functional data presented in Chapter 4 presents several translational opportunities. Further understanding of the mTORC1 pathway and the associated intracellular mechanisms that control the biogenesis and secretion of Rab11a-exosomes, as well as their subsequent uptake by recipient cells, may reveal therapeutic targets that can be targeted to suppress these EV-mediated adaptation mechanisms, which ultimately drive tumorigenesis. Conversely, the possible angiogenic promoting properties of switched EVs could be utilised to increase tumour sensitivity to radiotherapy, which is used in the neoadjuvant treatment of CRC. Poor tumour oxygenation is associated with resistance to radiotherapy (Koukourakis 2001). Therefore, perhaps the therapeutic stimulation of EV switching could overcome this, which could be achieved using Akt/mTORC1 inhibitors. Indeed, the therapeutic use of the rapalog everolimus, has been associated with radiosensitising effects in a range of cancers, including: breast, prostate and renal cell cancer (J. J. Lee et al. 2015; Narayan et al. 2017).

One potential application whereby switched EVs may serve as valuable biomarkers could be in monitoring patients treated with cetuximab, where treatment failure is common and difficult to predict. The nature of this test could include isolating EVs from plasma or serum and then measuring Rab11a or AREG content. As AREG is located within the EV

membrane, it may be feasible to use microfluidics to isolate these vesicles. If feasible, this would enable a potential correlation between EV-associated AREG and cetuximab resistance to be investigated, and if proven, could help predict treatment failure. This information could be used to tailor treatment, possibly to select patients likely to benefit from additional EGFR-targeted therapies. There is early phase I/II data demonstrating the potential benefits of dual EGFR blockade with cetuximab and the EGFR small molecular inhibitor, erlotinib, in overcoming cetuximab resistance in non-small cell lung cancer (Wheler et al. 2013). It is possible that this dual approach to EGFR inhibition could overcome the potent activity of AREG-containing EVs, and may prevent or delay the onset of resistance.

An alternative biomarker-based application could focus on the potential EMT-MET promoting properties of CRC EVs, which could be used as a proxy measurement to predict metastasis, or even recurrence following curative surgery. Once secreted, tumour-derived EVs can enter the vascular and lymphatic circulation and promote pre-metastatic niche formation at secondary tumour sites. These processes are likely to persist even after the primary tumour has been resected, and may be insensitive to adjuvant chemotherapy. Therefore, EV-mediated metastasis may help explain why between 30-40% of patients who undergo curative resection for CRC will develop locoregional, and, or, systemic metastases within five years, despite the use of adjuvant chemotherapy (Chapuis et al. 2019). Therefore, future work should focus on identifying EV cargoes that drive these metastatic processes so that their clinical use as biomarkers can be investigated.

## 6.4 Aim (iii) Investigating EV-miRNA cargo in non-switched and switched EVs, and within a rectal cancer cohort

### 6.4.1 Microenvironmental stress modulates the miRNA content of EVs *in vitro*

To investigate other potential translational aspects of the EV switch, an analysis of the EV-miRNA profile of non-switched and switched EVs from HCT116 and SW480 cells was undertaken. This showed that the two CRC cell lines secreted EVs with unique miRNA cargoes, consistent with the findings in Chapter 4, which showed that SW480-derived EVs do not contain AREG, an important pro-tumorigenic cargo detected in switched EVs isolated from HCT116 cells. Moreover, quantitative differences in a range of miRNAs were highlighted in switched EVs, suggesting that microenvironmental stress is an important stimulus controlling EV-miRNA loading. While, many of the EV-miRNAs highlighted do not have known tumorigenic properties, increased levels of miR-23a-3p and decreased levels of miR-8075 are consistent with changes detected in clinical studies, which can be used to diagnose early stage CRC (Karimi et al. 2019; Ogata-Kawata et al. 2014; Ostenfeld et al. 2016; Yan et al. 2017a). Enrichment analysis showed that many of the EV-miRNAs highlighted are predicted to participate in a range of pro-tumorigenic biological processes and signalling pathways. Of note, four miRNAs that were increased in switched EVs from HCT116 cells are predicted to positively regulate cell adhesion (miR-4739, miR-6848-5p, miR-6891-5p and miR-7110-5p). This is relevant to the findings from Chapter 4, which showed that switched EVs increase E-cadherin expression in recipient cells. Therefore, these miRNAs should be investigated to determine whether they are responsible for the AREG-independent reduction in migration and invasion that is mediated by switched EVs. Finally, HCT116-derived switched EVs were shown to contain increased levels of the RBP, hnRNPA2B1, which coincided with increased levels of its known miRNA substrates. This included miR-1246, which has known immunosuppressive tumorigenic properties (Cooks et al. 2018), and has been validated as a diagnostic and treatment response biomarker in clinical studies (Eylem et al. 2020; Jin et al. 2019; Ogata-Kawata et al. 2014)

### 6.4.2 nCRT for rectal cancer is associated with changes in EV-miRNA profile and may differentiate responders from non-responders

Tumorigenesis is associated with altered EV-miRNA cargo, which can be detected in bodily fluids, including plasma and serum. This has led to growing interest in the use of circulating EV-associated miRNAs as cancer biomarkers (Alves Dos Santos et al. 2020; Thind and Wilson 2016), and was demonstrated by the range of EV-miRNAs highlighted in the systematic review of clinical studies investigating their use as biomarkers for CRC. In Chapter 5, a SEC-based method was used to isolate EVs from 10 patients with rectal cancer, who underwent initial treatment with nCRT. This pilot study was the first to compare responders to treatment with non-responders. Interestingly, there was no overlap in the EV-miRNAs highlighted in this analysis compared with the *in vitro* analysis of non-switched and switched EVs isolated from the CRC cell lines. This suggests that a significant proportion of EV-miRNA changes that are detected within the blood of patients with cancer represent a systemic response to an underlying cancer.

nCRT was associated with decreased levels of EV-miRNAs that are derived from well-known oncogenic miRNA clusters, including: miR-92a-3p and miR-93-5p. The use of miR-92a-3p has been validated in numerous clinical studies as biomarker for CRC diagnosis (Eylem et al. 2020; Fu et al. 2018; Min et al. 2019), and for predicting poor prognosis (Perez et al. 2020) and resistance to platinum-based chemotherapy (J. Han et al. 2020). Interesting EV-miRNA differences were detected between nCRT responders and non-responders. EVs from responders contained increased levels of anti-tumorigenic miR-126-3p and decreased levels of miR-92a-3p. Non-responders showed decreased levels of miR-486-5p, which is consistent with previous studies that have shown low circulating levels of this miRNA are associated with poor prognosis in CRC (Bjornetro et al. 2019). Therefore, this pilot study has highlighted a novel pattern of EV-miRNA changes that may have translational uses in predicting outcome from nCRT.

### 6.4.3 Clinical implications

The EV-miRNA data from the *in vitro* analysis and the pilot clinical study undertaken in Chapter 5 may have important translational benefits. Switched EVs can contain increased levels of hnRNPA2B1, an RBP known to selectively load pro-tumorigenic miR-1246 into EVs. Due to its involvement in multiple cancers, hnRNPA2B1 has been investigated as a potential therapeutic target. Epirubicin is an anthracycline chemotherapy agent already in clinical use for the adjuvant treatment of breast cancer, and phase II trials are underway in metastatic CRC (Tarpgaard et al. 2016). Perez-Boza et al. (2020) showed that epirubicin can disrupt hnRNPA2B1-miRNA interactions, leading to its relocation to the nucleus and changes in the miRNA profile of secreted exosomes. As observed in CRC, EV-associated miR-1246 has known pro-tumorigenic effects in breast cancer (X. J. Li et al. 2017b). Therefore, the plasma EV-miRNA profile of patients treated with epirubicin should be analysed to determine whether they contain reduced levels of known RBP-associated miRNAs, including miR-1246. In addition to this, Soung et al. (2019) have developed a small molecular inhibitor, MO-460, which prevents the hnRNPA2B1-induced translation of HIF-1α, even under hypoxic conditions. HIF-1α increases the expression of Rabs that drive increased EV secretion under hypoxic conditions (Bister et al. 2020; C. Shao et al. 2018a), which may include the secretion of pro-tumorigenic switched EVs. Therefore, it is possible that inhibition of hnRNPA2B1 could also block the secretion of switched EVs.

Approximately one in five patients with rectal cancer will have a complete clinical response to nCRT, meaning that through regular surveillance they can potentially avoid surgery. The remaining 80% of patients will require major life-changing pelvic surgery, often requiring a permanent colostomy to cure their cancer (van der Valk et al. 2018). It is possible that a proportion of those patients who eventually undergo surgery had tumours that were resistant to nCRT, but there is currently no investigation available to identify these individuals. The analysis of patient samples before and after nCRT has identified EV-miRNA changes that appear to distinguish responders from non-responders. These should

be validated in matched samples, and then investigated in a larger cohort of patients treated with nCRT. This approach may enable the initial treatment of rectal cancer to be personalised, which may involve recommending an alternative to nCRT, or progressing straight t o surgery in patients who are predicted to respond poorly to nCRT. Furthermore, by undertaking surgery earlier in predicted non-responders, it may be possible to excise the tumour through minimally invasive methods, such as TEMS or TAMIS, leaving the rectum in place and avoiding the consequences of major surgery.

## 6.5 Conclusions

There have been many studies of EV biology in CRC, including extensive work in cell lines and in patients. However, one of the central challenges with these studies to date has been that they reveal remarkable complexity in EV secretion and functions, reflecting both patient variability and the fact that EV isolation methods produce complex mixtures of EV subtypes.

This thesis has built on a recent body of work highlighting the effect of microenvironmental stress on the production of different exosome subtypes and in particular the secretion of increased numbers of pro-tumorigenic Rab11a-exosomes. It has highlighted the functional differences of Rab11a-exosome-enriched preparations in colorectal cancer versus exosome preparations made in non-stressed conditions, including the fact that the former vesicle preparations can induce more tumour growth, MET transition and resistance to the drug cetuximab. AREG has been highlighted as a key protein cargo involved in this process and a series of miRNA cargos that may also have important roles have also been identified.

Therefore, separation of EVs into different subtypes and particularly the identification of Rab11a-exosomes has permitted the roles of specific EVs to be better characterised. This has enabled the development of a series of hypotheses that now need to be tested in cell lines and in patients. These experiments may ultimately suggest new therapies to block the

production or activities of specific EV subtypes involved in stress-induced tumour progression. Furthermore, this work suggests that by separating specific subtypes of CRC EVs from patient plasma in the future, it may be possible to identify more robust biomarkers, not only for early stage detection, but also for prediction of patient response to treatment, addressing two of the most pressing deficiencies in current CRC care. Finally, the fundamental findings and approaches used here can be easily employed in the study of other cancer types. It will, therefore, be interesting in the coming years to determine whether all cancers use similar EV signalling mechanisms to adapt to microenvironmental stress and whether this provides a new generic target to block tumour progression.

# Appendix A – Fan *et al* (2020) EV switch study

*Article*

SOURCE DATA | TRANSPARENT PROCESS | OPEN ACCESS

THE EMBO JOURNAL

# Glutamine deprivation alters the origin and function of cancer cell exosomes

Shih-Jung Fan[1,†], Benjamin Kroeger[1,†], Pauline P Marie[1], Esther M Bridges[2], John D Mason[1], Kristie McCormick[1], Christos E Zois[2], Helen Sheldon[2], Nasullah Khalid Alham[3,4], Errin Johnson[5], Matthew Ellis[1], Maria Irina Stefana[1], Cláudia C Mendes[1], Stephen Mark Wainwright[1], Christopher Cunningham[6], Freddie C Hamdy[6], John F Morris[1], Adrian L Harris[2], Clive Wilson[1] & Deborah CI Goberdhan[1,*]

## Abstract

**Exosomes are secreted extracellular vesicles carrying diverse molecular cargos, which can modulate recipient cell behaviour. They are thought to derive from intraluminal vesicles formed in late endosomal multivesicular bodies (MVBs). An alternate exosome formation mechanism, which is conserved from fly to human, is described here, with exosomes carrying unique cargos, including the GTPase Rab11, generated in Rab11-positive recycling endosomal MVBs. Release of Rab11-positive exosomes from cancer cells is increased relative to late endosomal exosomes by reducing growth regulatory Akt/mechanistic Target of Rapamycin Complex 1 (mTORC1) signalling or depleting the key metabolic substrate glutamine, which diverts membrane flux through recycling endosomes. Vesicles produced under these conditions promote tumour cell proliferation and turnover and modulate blood vessel networks in xenograft mouse models *in vivo*. Their growth-promoting activity, which is also observed *in vitro*, is Rab11a-dependent, involves ERK-MAPK-signalling and is inhibited by antibodies against amphiregulin, an EGFR ligand concentrated on these vesicles. Therefore, glutamine depletion or mTORC1 inhibition stimulates release from Rab11a compartments of exosomes with pro-tumorigenic functions, which we propose promote stress-induced tumour adaptation.**

**Keywords** exosome; extracellular vesicle; mechanistic Target of Rapamycin; multivesicular body; Rab11(a)

**Subject Categories** Cancer; Membranes & Trafficking; Metabolism

**DOI** 10.15252/embj.2019103009 | Received 21 July 2019 | Revised 9 February 2020 | Accepted 10 February 2020

**The EMBO Journal (2020) e103009**

## Introduction

Extracellular vesicles (EVs), produced in intracellular compartments or by plasma membrane shedding events, have emerged as critical players in cell–cell communication (Tkach & Théry, 2016; Maas *et al*, 2017). They deliver specific combinations of proteins, nucleic acids and lipids to recipient cells. EVs function in normal physiological processes, such as reproduction (Corrigan *et al*, 2014), immune responses (Bruno *et al*, 2015), neural development and maintenance (Krämer-Albers & Hill, 2016), and metabolism (Thomou *et al*, 2017). They also have roles in pathological events (Huang-Doran *et al*, 2017; Maas *et al*, 2017; Veerman *et al*, 2019) with much focus on the role of EVs in promoting tumour growth, survival and metastasis (Becker *et al*, 2016). These effects involve interactions of tumour cells with each other and surrounding stromal cells (Wendler *et al*, 2017). EVs can alter the tumour microenvironment, for example, by promoting endothelial network formation (Sheldon *et al*, 2010). In turn, microenvironmental stresses, such as hypoxia (Kucharzewska *et al*, 2013), can affect this signalling by driving changes in the tumour EV profile. The functional relevance of stress-induced EV signalling has, however, not been extensively characterised. This is of particular interest in cancer, where depletion of oxygen and key metabolites, such as glutamine (Zhang *et al*, 2017), is an inevitable outcome of rapid tumour growth.

Preparations of secreted EVs from cell lines and primary cell cultures include microvesicles derived from the plasma membrane and exosomes made inside cells (Théry *et al*, 2018). Exosomes are EVs of about 30–150 nm in diameter, formed by the inward budding of the limiting membrane of intracellular compartments, widely thought to be late endosomes. Exosome secretion results from fusion of the resulting multivesicular bodies (MVBs) with the plasma membrane (Maas *et al*, 2017). The transmembrane tetraspanins CD63 and CD81 are often used to identify exosomes (Kowal

1 Department of Physiology, Anatomy and Genetics, University of Oxford, Oxford, UK
2 Department of Oncology, Weatherall Institute of Molecular Medicine, University of Oxford, Oxford, UK
3 Institute of Biomedical Engineering, Department of Engineering Science, University of Oxford, Oxford, UK
4 Nuffield Department of Surgical Sciences, Oxford NIHR Biomedical Research Centre (BRC), John Radcliffe Hospital, University of Oxford, Oxford, UK
5 Sir William Dunn School of Pathology, University of Oxford, Oxford, UK
6 Nuffield Department of Surgical Sciences, John Radcliffe Hospital, University of Oxford, Oxford, UK
*Corresponding author (lead contact). Tel: +44 1865 282836; E-mail: deborah.goberdhan@dpag.ox.ac.uk
†These authors contributed equally to this work

© 2020 The Authors. Published under the terms of the CC BY 4.0 license

*et al*, 2016; Mateescu *et al*, 2017). Members of the Endosomal Sorting Complexes Required for Transport (ESCRT) family (Colombo *et al*, 2013) and ceramides (Trajkovic *et al*, 2008) regulate two proposed exosome biogenesis pathways. Several endosomal Rab GTPases, which promote trafficking between specific intracellular compartments, also play important roles (Ostrowski *et al*, 2010). Whether these mechanisms contribute to the heterogeneity observed in exosome preparations (Zhang *et al*, 2018) remains largely undetermined.

We have developed a *Drosophila* model to investigate exosome biogenesis *in vivo* (Corrigan *et al*, 2014; reviewed in Wilson *et al*, 2017). This uses the prostate-like secondary cells (SCs) of the fly male accessory glands (AGs), which secrete exosomes in to the AG lumen and have unusually large intracellular membrane-bound compartments (Fig 1A), including Rab11-positive endosomes and Rab7-positive lysosomes.

Here, we present evidence that specific exosome subtypes are made in SC and human cancer cell recycling endosomal MVBs labelled by Rab11 family members. Furthermore, preferential release of Rab11a-marked exosomes from these compartments is triggered by depleting cancer cells of exogenous glutamine. This Rab11a-secretory switch is reproduced by reducing growth factor-regulated Akt and amino acid-sensitive mechanistic (formerly mammalian) Target of Rapamycin Complex 1 (mTORC1; Dibble & Cantley, 2015) signalling. We show that these exosomes have distinct cargos and unique *in vitro* activities. Since they also alter tumour cell growth and vessel formation in a human tumour xenograft mouse model, we propose that they contribute to adaptive responses to metabolic stress.

## Results

### Rab11-labelled multivesicular bodies make exosomes via an ESCRT-dependent mechanism in *Drosophila* secondary cells

To study exosome biogenesis in *Drosophila* SCs, we overexpressed the human exosome marker CD63-GFP. It labels the limiting membranes of large Rab7-positive acidic late endosomes and lysosomes (LELs) in SCs and of approximately 10 non-acidic compartments, containing a central, protein-rich, dense-core granule (DCG; Fig 1A–C), which are Rab11-positive (Redhai *et al*, 2016; Prince *et al*, 2019). Using super-resolution 3D-SIM, a few fluorescent intraluminal vesicles (ILVs) were observed inside LELs, although most GFP fluorescence is quenched by the acidic microenvironment (Redhai *et al*, 2016). Clusters of CD63-GFP-positive ILVs were also observed within the Rab11-positive compartments (Fig 1C and Movie EV1), the majority of which were of typical exosome size (Fig EV1A). ILVs were also seen in EM micrographs of the non-acidic and acidic compartments in non-transgenic flies (Fig EV1E).

To analyse ILV formation in these Rab11 compartments further, we studied SCs from flies expressing YFP-Rab11 from the endogenous *Rab11* locus, a so-called "gene trap" (Dunst *et al*, 2015). YFP-Rab11's fluorescence intensity was much lower than CD63-GFP and so not amenable to super-resolution imaging. Therefore, we imaged this marker using wide-field deconvolution fluorescence microscopy, which resolves membrane-bound ILVs as puncta (Fig 1D). The compartmental organisation of SCs expressing *YFP-Rab11* is not significantly perturbed, in contrast to SCs expressing CD63-GFP, which appear to increase trafficking to acidic compartments (Corrigan *et al*, 2014; Redhai *et al*, 2016). For example, the numbers of large non-acidic compartments are unaffected compared to wild-type flies, whereas CD63-GFP expression roughly doubles their number and produces enlarged acidic compartments (Fig EV1B–D; Redhai *et al*, 2016). Fluorescent puncta were seen inside YFP-Rab11-positive SC compartments (Fig 1D), but fewer than with CD63-GFP (Fig 1C). On rare occasions (< 0.5% of cells), YFP-Rab11-labelled structures were sufficiently large that they could be resolved as ILVs (Fig EV1F). Unlike CD63-GFP (Fig EV1G), the Rab11 fusion protein did not traffic to the plasma membrane (Fig EV1H; Movie EV2). Sporadic YFP-Rab11-positive puncta were observed in the AG lumen, both in the gene trap line (Fig EV1H) and when YFP-Rab11 was specifically overexpressed in SCs (Fig EV1I). In contrast, a YFP-Rab7 gene trap fusion protein (Dunst *et al*, 2015) primarily trafficked to acidic LELs, which were abnormally enlarged (Fig 1E), and marked very few puncta in the AG lumen. To further investigate whether Rab11 is inside ILVs in Rab11 compartments, we co-expressed the YFP-Rab11 gene trap with a CD63-mCherry construct. CD63-mCherry trafficked to the limiting membrane of a subset of large non-acidic, DCG-containing compartments, which often excluded YFP-Rab11 at their surface (Fig EV1J). Inside these compartments, however, the two markers partially co-localised. This suggests that Rab11 is intravesicular, but it is not always associated with tetraspanin-labelled ILVs, perhaps because these molecules must co-localise at the endosomal limiting membrane to permit this. Taken together, we conclude that Rab11-labelled exosomes are formed at low levels in Rab11 SC compartments and secreted.

In searching for other markers of these alternative exosomes, we found using 3D-SIM that an overexpressed GFP-tagged form of Breathless (Btl; a fly homologue of the human transmembrane FGF receptor), which is normally expressed in SCs (Fig EV1K), trafficked on to ILVs in DCG-containing, Rab11 compartments (Fig 1F). Its expression did not affect the large non-acidic compartments in SCs and had only a minor effect on acidic compartment number (Fig EV1B–D). In some SCs, Btl-GFP, like YFP-Rab11, was found in the lumen of an LEL, but, unlike CD63-GFP, these markers were rarely, if ever, observed on the LEL limiting membrane (Appendix Fig S1), presumably because they reach this destination by sporadic fusion of LELs with Rab11 compartments (Corrigan *et al*, 2014) and not by endocytic trafficking. As with YFP-Rab11, transmembrane Btl-GFP protein was secreted in puncta into the AG lumen (Fig 2A). We, therefore, conclude that Rab11 and Btl are selective membrane-associated markers for at least some of the exosomes generated in Rab11 compartments of SCs, which we collectively term "Rab11-exosomes".

To test whether biogenesis of these exosomes is ESCRT-dependent, the temperature-inducible GAL4/GAL80$^{ts}$/UAS system was used to knock down three *ESCRT*s implicated in mammalian and *Drosophila* exosome secretion (McCullough *et al*, 2013; Matusek *et al*, 2014), namely *Stam* (an ESCRT-0 subunit), *Vps28* (an ESCRT-I subunit) and *shrub* (*shrb*; the fly orthologue of mammalian *Chmp4a-c*, encoding an ESCRT-III subunit) in adult SCs. All treatments affected the number and size of large non-acidic compartments in SCs expressing Btl-GFP (Fig 2), YFP-Rab11 (Fig EV2A–F) and CD63-GFP (Appendix Fig S2). In Btl-GFP- and

 © 2020 The Authors

CD63-GFP-expressing SCs, the number of non-acidic compartments increased in all three knockdowns (Fig 2A–E; Appendix Fig S2A–E), but analysis of *Rab11* gene trap males indicated that although drastically reduced in size, many of these non-acidic compartments retained Rab11 identity (Fig EV2A–E). For all three *ESCRT* knockdowns, the proportion of these compartments containing

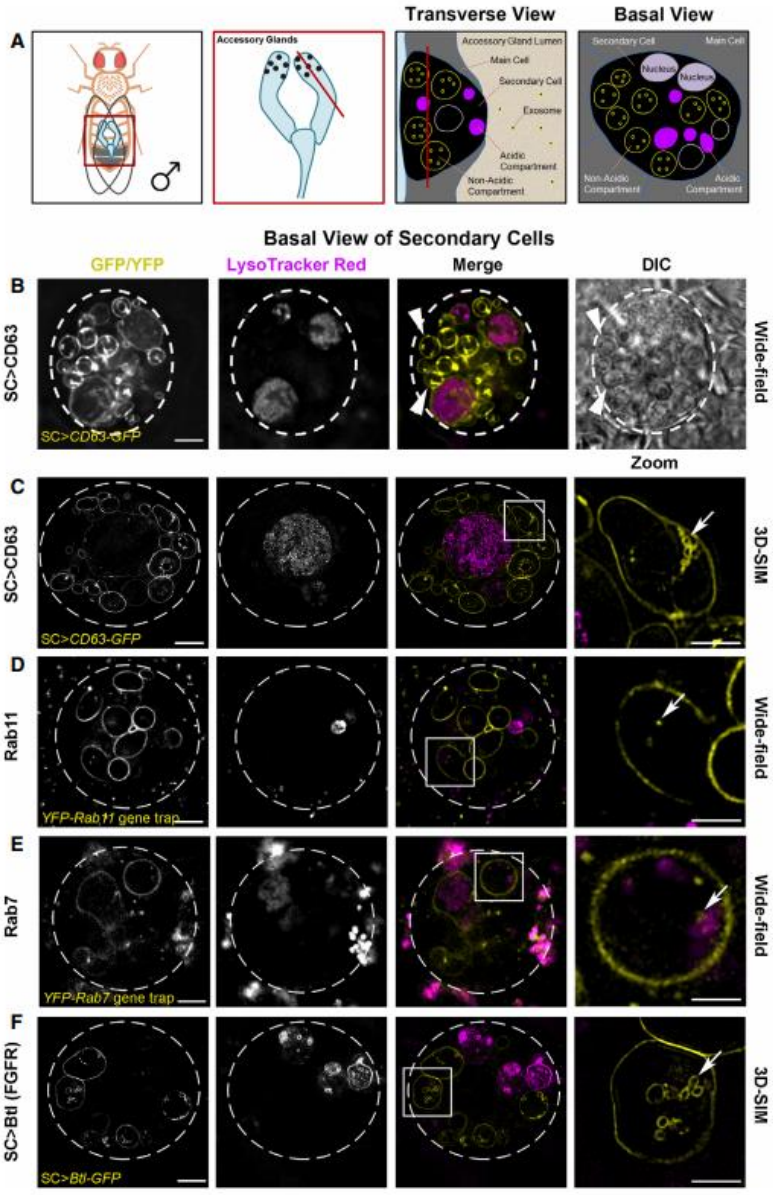



**Figure 1.**

© 2020 The Authors

**Figure 1. Rab11 compartments of *Drosophila* secondary cells contain intraluminal vesicles with specific cargos.**

A Schematics illustrate the fly accessory glands and associated secondary cells, highlighting their acidic and non-acidic exosome-forming compartments. First panel shows male fruit fly and its accessory glands. Boxed region is enlarged in second panel, revealing secondary cells (SCs; black dots), with red line indicating the plane of section through the AG lumen, which is used to generate the transverse view through a SC and surrounding main cells within the epithelial layer in the third panel. The unusually large, acidic late endosomes and lysosomes (Rab7-positive; magenta) and non-acidic compartments, characteristic of SCs, which we demonstrate here contain intraluminal vesicles (ILVs, some of which are Rab11-positive, yellow), are labelled. The red line in the third panel shows the basal SC plane of section in the fourth panel and images in this figure.

B–F Basal views through living SCs, with dashed white circles approximating the outline of a single SC, and acidic compartments marked by the vital dye LysoTracker® Red (magenta). In merge images, a single non-acidic (C, D and F) and acidic (E) compartment containing intraluminal vesicles (ILVs) is boxed and magnified in the right panel (Zoom). ILVs appear as membrane-delineated vesicles, using super-resolution 3D-structured illumination (3D-SIM) microscopy for the brighter overexpressed GFP-tagged constructs (yellow; C and F). However, ILVs appear only as puncta, using lower resolution wide-field microscopy for the fainter endogenously expressed YFP-tagged Rab GTPases (yellow; D and E). (B) Wide-field fluorescence image, including differential interference contrast (DIC), of SC expressing a GFP-tagged version of human CD63 (CD63-GFP). CD63-GFP expression is apparent on the limiting membranes of non-acidic compartments and their ILVs and also on the limiting membranes of the enlarged acidic compartments. Most large non-acidic compartments are Rab11-positive (D) and contain dense-core granules, which have a "fried egg" appearance with DIC (arrowheads) (Corrigan *et al*, 2014; Redhai *et al*, 2016). (C) 3D-SIM image of CD63-GFP-expressing SC. Arrow highlights CD63-GFP-marked ILVs (Zoom). Many more ILVs are apparent in non-acidic compartments in a complete Z-stack of a non-acidic compartment (Movie EV1). (D) Wide-field fluorescence image of an SC expressing a *YFP-Rab11* gene trap. YFP-Rab11 marks the limiting membranes of most non-acidic compartments and internal puncta (arrow in Zoom), but not the surface of acidic compartments (Appendix Fig S1B). (E) Wide-field fluorescence image of SC expressing a *YFP-Rab7* gene trap. YFP-Rab7 marks the limiting membranes of acidic compartments and internal puncta (arrow in Zoom). Enlarged acidic compartments are also present in adjacent main cells. (F) 3D-SIM image of SC expressing a GFP-tagged version of Breathless (Btl-GFP). Btl-GFP marks the limiting membranes of non-acidic compartments and their ILVs (arrow in Zoom), but not the surface of acidic compartments (Appendix Fig S1C). Images from 6-day-old male flies shifted to 29°C at eclosion. This induces GAL4/UAS-dependent SC transgene expression in (B, C and F). The genotypes of flies carrying multiple transgenes are as follows: *w; P[ω+, UAS-CD63-GFP] P[ω+, tub-GAL80$^{ts}$]/+; dsx-GAL4/+* (B and C); *w; P[ω+, tub-GAL80$^{ts}$]/+; dsx-GAL4/P[ω+, UAS-btl-GFP]* (F).

Data information: Scale bar in B–F (5 μm) and in C–F, Zoom (2 μm).

fluorescent puncta was significantly decreased (Figs 2F and EV2F; Appendix Fig S2F) and the number of secreted fluorescent puncta in the AG lumen was also greatly reduced (Fig 2G; Appendix Fig S2G). To test whether ESCRT proteins associate with Rab11 compartments, a Shrb-GFP fusion protein (Sweeney *et al*, 2006) was transiently expressed in SCs. It accumulated in subdomains and puncta at the surface of large non-acidic and acidic compartments (Fig EV2G; Movie EV3), consistent with our finding that *shrb* plays a role in generating ILVs in both Rab11 and LEL compartments. We conclude that the ESCRTs, including the ESCRT-0 Stam, which unlike other classes of ESCRT, is not thought to be involved in microvesicle biogenesis (McCullough *et al*, 2013), are required for ILV formation in Rab11 compartments *in vivo*. Furthermore, these ILVs are secreted as exosomes loaded with specific cargos.

### Rab11a-labelled multivesicular bodies also generate intraluminal vesicles in HCT116 colorectal cancer cells

To investigate whether human Rab11-labelled compartments also generate exosomes, we initially analysed HCT116 colorectal cancer (CRC) cells, which have clusters of perinuclear endosomal and Golgi compartments (Fan *et al*, 2016). In human cells, Rab11a, one of the two Rab11 isoforms, which primarily associates with recycling endosomes, has been reported to be associated with EVs (Keerthikumar *et al*, 2016) and to regulate exosome secretion (Savina *et al*, 2002). Using pan-Rab11, Rab11a- and Rab11b-specific antibodies, we found that Rab11a is the predominant Rab11 isoform in HCT116 cells (Appendix Fig S3A). In contrast to CD63, which co-localises with the LEL marker, LAMP1, Rab11a compartments are distinct from LELs, marked with LAMP2 (Fig 3A and B), and have very limited overlap with CD63 (Fig 3C). This differs from overexpression of fluorescent CD63 in SCs, where some CD63 enters Rab11 compartments (Fig 1B).

By overexpressing GFP-Rab11a in HCT116 cells, which induces clustering of Rab11a-positive compartments, we were able to use super-resolution 3D-SIM microscopy to detect internalised GFP in these compartments (Fig 3E), suggesting that Rab11a is incorporated into ILVs. To enlarge endosomal compartments, a GFP-tagged, constitutively active form of early endosomal Rab5 was expressed, which inhibits maturation of recycling and late endosomes, leading to the formation of enlarged immature endosomal compartments (Fig 3F). The endosomal Rab GTPases, Rab11a and Rab7, were both observed in subdomains at the surface of these Rab5-positive compartments and also on spatially distinct internal puncta (Fig 3F), demonstrating that the endosomal system can generate ILVs carrying either of these Rab signatures. We conclude that HCT116 cells contain both late and recycling endosomal MVBs and, as apparent in *Drosophila* SCs, the ILVs produced within them carry different cargos, including specific Rab GTPases.

### Glutamine depletion of HCT116 Cells induces a switch to secretion of Rab11a-exosomes with distinct cargos

To explore whether HCT116 CRC cells secrete Rab11a-positive exosomes, we collected small EVs for 24 h from cells cultured in serum-free conditions, but supplemented with insulin. This maintained growth factor signalling, as assessed by phosphorylation of mTORC1 downstream readouts, 4E-Binding Protein 1 (4E-BP1) and S6 (Appendix Fig S4A; 2.00 mM glutamine in Fig 4A). EVs isolated by ultracentrifugation were enriched for proteins that preferentially associate with exosomes (Figs 4B and EV3D), namely, the cytosolic adaptor protein Syntenin-1 (Syn-1), the ESCRT-I component Tsg101 and the tetraspanins CD81 and CD63 (Kowal *et al*, 2016). Low levels of Rab11a were also present, but not ER, Golgi or early endosome markers.

Glutamine is a major metabolic substrate in HCT116 cells (Jiang *et al*, 2013). We have previously shown that nutrient stress induced

 © 2020 The Authors

by glutamine depletion inhibits a rapamycin-resistant form of nutrient-sensitive mTORC1, without complete suppression of S6 phosphorylation (Fan *et al*, 2016). We investigated whether cells respond to such treatment by altering their EV secretion, as they do in hypoxic stress (Kucharzewska *et al*, 2013). As expected, glutamine depletion reduced cellular levels of hyper-phosphorylated 4E-

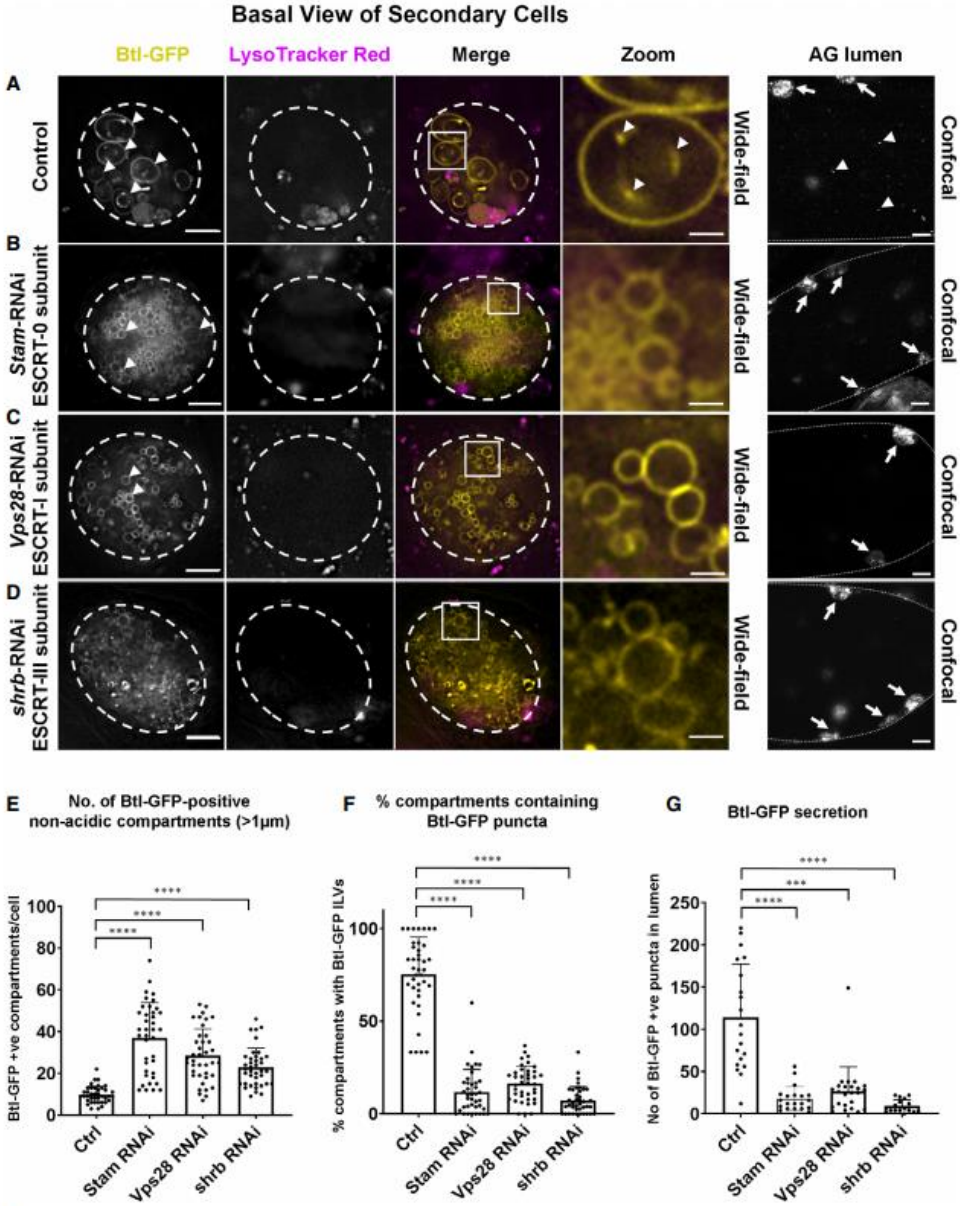



Figure 2.

© 2020 The Authors

**Figure 2. Exosome biogenesis in Rab11 compartments of *Drosophila* secondary cells is ESCRT-dependent.**

A–D Wide-field fluorescence images of basal views through living SCs expressing a GFP-tagged form of Btl-GFP (yellow) in non-acidic compartments, with SC outline approximated by dashed white circles. Acidic compartments are marked by LysoTracker Red® (magenta). Boxed non-acidic compartments in merge images are magnified in A–D, Zoom. On the right, lower magnification confocal transverse images of fixed accessory gland (AG) lumens are shown with dotted lines indicating the basal side of the AG epithelial layer, which contains several fluorescent SCs (highlighted by arrows). (A) SC with no RNAi construct expressed (control) and AG lumen from same genotype. Btl-GFP-positive compartments containing fluorescent ILVs (in Btl-GFP panel), ILV membranes inside compartments (in Zoom panel) and secreted fluorescent puncta (AG lumen panel) are marked by arrowheads. (B) SC also expressing RNAi construct targeting ESCRT-0 subunit, *Stam*, and AG lumen from same genotype. Btl-GFP-positive ILVs (Zoom) and secreted puncta (AG lumen) are strongly reduced. (C) SC also expressing RNAi construct targeting ESCRT-I subunit, *Vps28*, and AG lumen from same genotype. Btl-GFP-positive ILVs (Zoom) and secreted puncta (AG lumen) are strongly reduced. (D) SC also expressing RNAi construct targeting ESCRT-III subunit, *shrb*, and AG lumen from same genotype. Btl-GFP-positive ILVs (Zoom) and secreted puncta are strongly reduced.

E Bar chart showing the number of large (diameter greater than one micrometre) non-acidic Btl-GFP-positive compartments per SC. Data from 39 SCs (three per gland) are shown.

F Bar chart showing percentage of these large Btl-GFP compartments containing Btl-GFP-positive ILVs in control and *ESCRT* knockdown SCs. Data from 39 SCs (three per gland) are shown.

G Bar chart showing the total number of Btl-GFP fluorescent puncta in 10 Z-planes from the AG lumen following *ESCRT* knockdown in SCs, compared to controls without knockdown. Data from at least 17 AG lumens per condition are shown.

Data information: All data are from 6-day-old male flies shifted to 29°C at eclosion to induce expression of transgenes. Genotypes are as follows: *w*; *P[ω+, tub-GAL80$^{ts}$]/+; dsx-GAL4/P[ω+, UAS-btl-GFP]* with no knockdown construct (A), UAS-*Stam*-RNAi (HMS01429; B), UAS-*Vps28*-RNAi (v31894; C) or UAS-*shrb*-RNAi (v106823; D). Scale bars in A-D (5 μm); in A–D Zoom (1 μm); in A–D, AG lumen (20 μm). Data were analysed by one-way ANOVA. ****$P < 0.0001$, ***$P < 0.001$ relative to control. Bars and error bars in E–G denote mean ± SD.
Source data are available online for this figure.

BP1 and phosphorylated S6 (Figs 4A, EV3A and EV4E) over the 24-h EV collection period. Cellular expression of all exosome proteins was unaffected by glutamine depletion, except for CD63, which was reduced (Fig 4A). Blocking lysosomal function by buffering lysosomal protons with chloroquine over 24 h strongly increased CD63 levels under both conditions and suppressed the difference between conditions (Appendix Fig S4B), suggesting that slightly more CD63 is degraded when glutamine levels are depleted. There were comparably low levels of cell death in secreting cells under both glutamine-depleted (10.2 ± 1.5%) and glutamine-replete (11.5 ± 2.5%; $n = 3$) conditions, as measured by Trypan blue staining.

Nanoparticle Tracking Analysis (NTA) of EV preparations (Dragovic *et al*, 2011) revealed that EV numbers (when normalised to cell lysate protein levels) were not significantly changed compared to control values after glutamine depletion, and EV size distribution was unaltered (Figs 4B, EV3B and EV4E), a finding supported by transmission electron microscopic analysis (Fig EV3C).

However, by analysing EVs generated by the same protein mass of cells under these two conditions (a proxy for cell number; Baietti *et al*, 2012), we observed that glutamine depletion of HCT116 cells altered the secretion of specific exosome markers (Fig 4B). While exosome-associated Syn-1, Tsg101 and CD81 were only slightly decreased after glutamine depletion, when normalised to cell lysate protein levels, secretion of late endosomal CD63, which is reported to mark only a subset of exosomes in small EV preparations (Kowal *et al*, 2016), was more strongly reduced (Figs 4B and 5G). By contrast, Rab11a was increased by several fold (Figs 4B and 5G). Hypoxic stress increases levels of cytosolic lipid raft-associated caveolin-1 (Cav-1; Kucharzewska *et al*, 2013) in EVs. This protein was detected in EV preparations from HCT116 cells and its secretion was also enhanced by glutamine depletion (Figs 4B and 5G).

No marker is known to distribute evenly across all exosome or EV subtypes, so it was not possible to use a specific protein on the Western to reliably normalise signals on EV Western blots. We therefore analysed our data using a number of different variables for normalisation to confirm our findings (Fig EV3E). EV preparations contain mixtures of exosomes, microvesicles and protein aggregates (Jeppesen *et al*, 2019); we found particle number measured by NTA to vary considerably relative to secreting cell mass. However, by including more biological replicates, we confirmed that levels of CD63 per EV fell more than other exosome markers following glutamine depletion, which may be partly explained by the reduction in cellular CD63 (Fig 4A), and Rab11a and Cav-1 levels were strongly increased (Fig EV3E). The same pattern was observed when CD81, Tsg101 or Syn-1 was employed to normalise Western blots of EVs (Fig EV3E).

To standardise our analysis in different cells and conditions in this study, we loaded EV preparations from cells of an equivalent protein mass under different conditions and directly compared the Western blot signals. However, normalising signals to the levels of CD81, which is thought to mark a broad subset of tetraspanin-labelled exosomes (Kowal *et al*, 2016; Jeppesen *et al*, 2019), led to the same conclusions (Appendix Fig S5). Furthermore, increased Rab11a and Cav-1 and decreased CD63 were also observed when Western signals were normalised to the change in mean particle number across three or more biological repeats, as measured by NTA (Fig EV4E).

Importantly, a similar switch in Rab11a secretion was demonstrated in EVs isolated by size-exclusion chromatography (SEC; Fig EV3F and F′), an alternative method for EV isolation based on particle size, which we found more consistent in comparative EV isolation experiments. We employed this method for most of our subsequent studies, but confirmed key findings, such as intravesicular localisation of Rab11a and functional activity using both approaches. Since we also observed that Rab11a and CD63 remain in separate compartments in HCT116 cells after glutamine depletion (Fig 3D), our data suggest that the endosomal origin of exosomes secreted from CRC cells is altered under these conditions, so that more exosomes are released from Rab11a compartments.

One alternative explanation is that Rab11a is secreted in microvesicles shed from the surface of HCT116 cells under stress. Although Rab11a-positive recycling endosomal compartments are observed below the plasma membrane, very little, if any, Rab11a is trafficked to the surface in either glutamine-replete or

 © 2020 The Authors

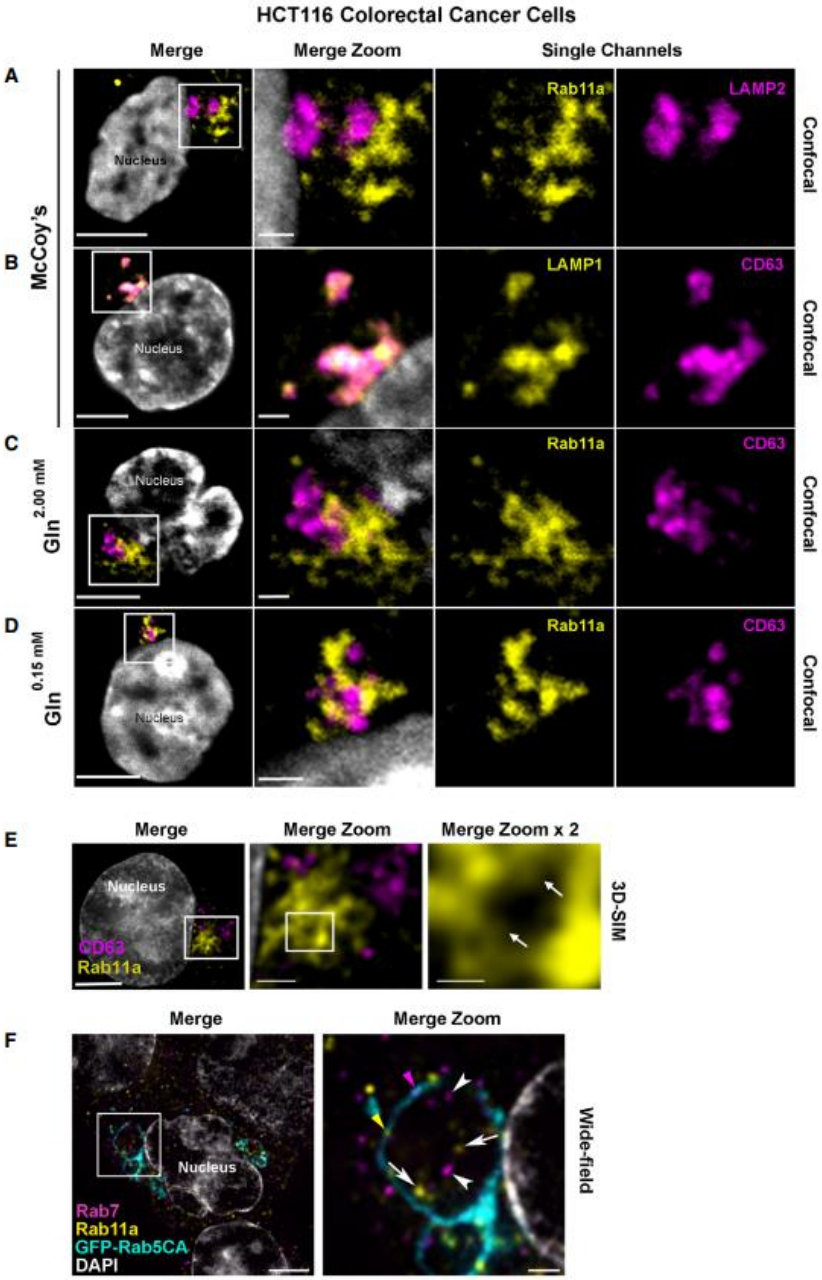



Figure 3.

© 2020 The Authors

**Figure 3. Rab11a labels a distinct subset of multivesicular bodies and their intraluminal vesicles in HCT116 colorectal cancer cells.**

A–D Confocal images of fixed HCT116 cells, with boxed regions enlarged to the right. DAPI (grey) marks nucleus. Rab11a antibody is isoform-specific except in (F). (A) Rab11a (yellow) is located in compartments distinct from the late endosomal and lysosomal marker, LAMP2 (magenta). (B) CD63 (magenta) predominantly co-localises with the late endosomal and lysosomal marker, LAMP1 (yellow). (C) Rab11a (yellow) is located in compartments distinct from CD63 (magenta) under glutamine-replete conditions. (D) Rab11a (yellow) is located in compartments distinct from CD63 (magenta) under glutamine-depleted conditions.

E Super-resolution 3D-SIM image of fixed HCT116 cell expressing GFP-Rab11a (yellow), and stained with CD63 (magenta). DAPI (grey) marks nucleus. Boxed Rab11a-positive compartments, which frequently cluster, are magnified in Merge Zoom. This panel is further magnified in Merge Zoom × 2, revealing GFP-Rab11a (arrows in right panel) inside compartments.

F Wide-field fluorescence image of fixed HCT116 cells, stained with Rab11a (yellow) and Rab7 (magenta), expressing constitutively active GFP-tagged Rab5 (GFP-Rab5CA; cyan), which stalls endosomal maturation and produces enlarged Rab5-positive endosomes. One of these is boxed in the Merge and magnified in Merge Zoom, revealing internal puncta marked by Rab11a (arrows) and Rab7 (arrowheads) and limiting membrane subdomains of Rab11a (yellow arrowhead) and Rab7 (magenta arrowhead). DAPI (grey) marks nuclei.

Data information: Scale bars in A–F (5 μm), in Merge Zoom (1 μm) and in Merge Zoom × 2 (0.5 μm).

glutamine-depleted conditions (Appendix Fig S4C and D). This is in sharp contrast to CD81, which concentrates at the plasma membrane. To further demonstrate that Rab11a is associated with exosomes, we separated EV preparations using high-resolution iodixanol-PBS density gradients, on which exosomes, microvesicles and protein aggregates fractionate differently, though not entirely separately (Jeppesen *et al*, 2019). Although Rab11a levels were too low in EVs from glutamine-replete cells to draw firm conclusions (Appendix Fig S6A), Rab11a was distributed in the same way as exosomal CD63 and CD81 in EVs from glutamine-depleted cells, but did not fully overlap with the microvesicle marker, Annexin A1 (AnxA1; Fig 4C).

To demonstrate that endosomal Rab11a is a *bona fide* internal exosome marker and not an associated contaminant in the isolation procedure, EVs induced by glutamine depletion were subjected to proteinase K digestion in the absence and presence of the detergent Triton X-100. While most proteins partially exposed on the exosome surface like CD81 were destroyed by both treatments, Rab11a behaved like other internal markers, such as Syn-1, and was only fully digested in the presence of detergent, either in EV preparations isolated by ultracentrifugation (Fig 4D) or by SEC (Appendix Fig S6C). CD63 was not digested even in the presence of Triton X-100, but it was degraded in the presence of a more potent detergent, lithium dodecyl sulphate (Appendix Fig S6B), suggesting that Triton either does not fully disrupt the CD63/lipid interactions or allow sufficient unfolding of exosomal CD63 to permit digestion.

To confirm that CD63 and Rab11a mark different exosome subtypes, CD63-positive vesicles were immunocaptured and analysed by Western blot. Both in glutamine-replete and in glutamine-depleted conditions, while CD81 and other standard exosome markers were pulled down in roughly equivalent proportions, little, if any, specific Rab11a binding was observed (Fig 4E, Appendix Fig S6D). In fact, under glutamine-depleted conditions, only a small fraction of Rab11a was immunocaptured by CD81 pull-down (Fig 4F), consistent with the finding that these markers are largely separated inside cells (Appendix Fig S4C and D), and supporting our conclusion that Rab11a marks an alternative exosome subtype.

### Glutamine depletion and inhibition of Akt/mTORC1 signalling induces an "exosome switch" in cancer cell lines of different origins

We tested the effect of glutamine depletion on EV secretion by other cancer cell lines, selecting a glutamine concentration that suppressed, but did not completely block S6 phosphorylation. Culturing HeLa cervical cancer cells in glutamine-depleted medium, which reduced phosphorylation of S6 and 4E-BP1, slightly increased EV number (Appendix Fig S7A, A′, and A‴, Fig EV4E) and increased Rab11a secretion relative to other exosome markers (Fig 5A and G, Appendix Figs S3B, S5B and C, and S7A″), while cellular levels of Rab11a were unaffected (Appendix Fig S7A). In the prostate cancer cell line, LNCaP, depletion of extracellular glutamine, which also reduced S6 and 4E-BP1 phosphorylation (Appendix Fig S7B, Fig EV4E), led to an increase in EV levels of Rab11a relative to CD81 (Appendix Figs S5D and H), while EV number and CD63 remained unchanged, but this increase was not significant relative to cell lysate protein mass (Figs 5B and G, and EV4E, Appendix Fig S7B′). Cav-1 was not detectable in this cell line. We conclude that HeLa and LNCaP cells, like HCT116 cells, respond to glutamine depletion by increasing secretion of exosome-associated Rab11a (though in LNCaP cells, only relative to other exosome markers), presumably by releasing more Rab11a-exosomes.

Since glutamine depletion reduces mTORC1 activity, we tested whether blocking mTORC1 with the mTOR-specific inhibitor Torin 1 (Thoreen *et al*, 2009) could also induce an exosome switch. In LNCaP cells, Torin 1 treatment slightly elevated the number of EVs produced, but reduced CD63 and strongly increased Rab11a in EVs relative to cell lysate protein and CD81 (Figs 5C and G, Appendix Figs S5E and H), without affecting cellular levels of these proteins (Appendix Fig S7C and C′, Fig EV4E). However, in other cell lines like HCT116, the mTORC1 inhibitors, Torin 1 and rapamycin, had a much stronger inhibitory effect on mTORC1 activity and particularly S6 phosphorylation when compared to glutamine depletion (Fig EV4A, B and E), and this was associated with an approximately 50% reduction in EV particle numbers (Fig EV4A″, B″ and E). Secretion of all exosome markers, and particularly CD63, was significantly reduced (Fig EV4A′ and B′), suggesting a more general suppression of exosome release. For rapamycin, we found that a very similar result was obtained using SEC for EV isolation, confirming that these findings are independent of EV isolation technique (Appendix Fig S7E).

A more modest mTORC1 inhibition in HCT116 cells was induced by knocking down *raptor*, which encodes a core mTORC1 component. EVs were collected for 24 h after 3 days of knockdown. Under these conditions, cellular levels of Syn-1, Tsg101 and CD63 were all decreased (Fig EV4C) and EV number was also reduced (Fig EV4C′ and E), but residual phosphorylation of S6 was more variably maintained (Fig EV4C and E). This treatment induced a reduction in most standard secreted exosome

 © 2020 The Authors

proteins, with a stronger decrease in CD63 (Fig 5D). However, Rab11a and Cav-1 secretion per unit cell protein mass was maintained, and indeed, it was increased relative to CD81 and EV number (Fig 5D, Appendix Figs S5F and H). These findings are again consistent with induction of an mTORC1-regulated switch in the balance of exosome secretion from late endosomal to Rab11a compartments.

Since mTORC1 activity is controlled by growth factor signalling, we also tested the effect of the Akt inhibitor AZD5363 on exosome secretion by HCT116 cells, which carry an activating mutation in upstream PI3KCA (Ahmed *et al*, 2013). A switch in exosome secretion was again observed (Fig 5E and G, Appendix Fig S5G), most notably involving an increase in Rab11a and Cav-1 in EVs relative to cell lysate protein or CD81, in the absence of similar changes in cellular levels of these proteins or EV number (Fig EV4D, D′ and E). In addition to blocking phosphorylation of the Akt target PRAS40, this treatment partially inhibited phosphorylation of mTORC1 targets, S6 and 4E-BP1 (Fig EV4D and E), which might account for the switch. HCT116 cells also harbour a mutation in KRAS, which activates the ERK MAP kinase signalling cascade downstream of

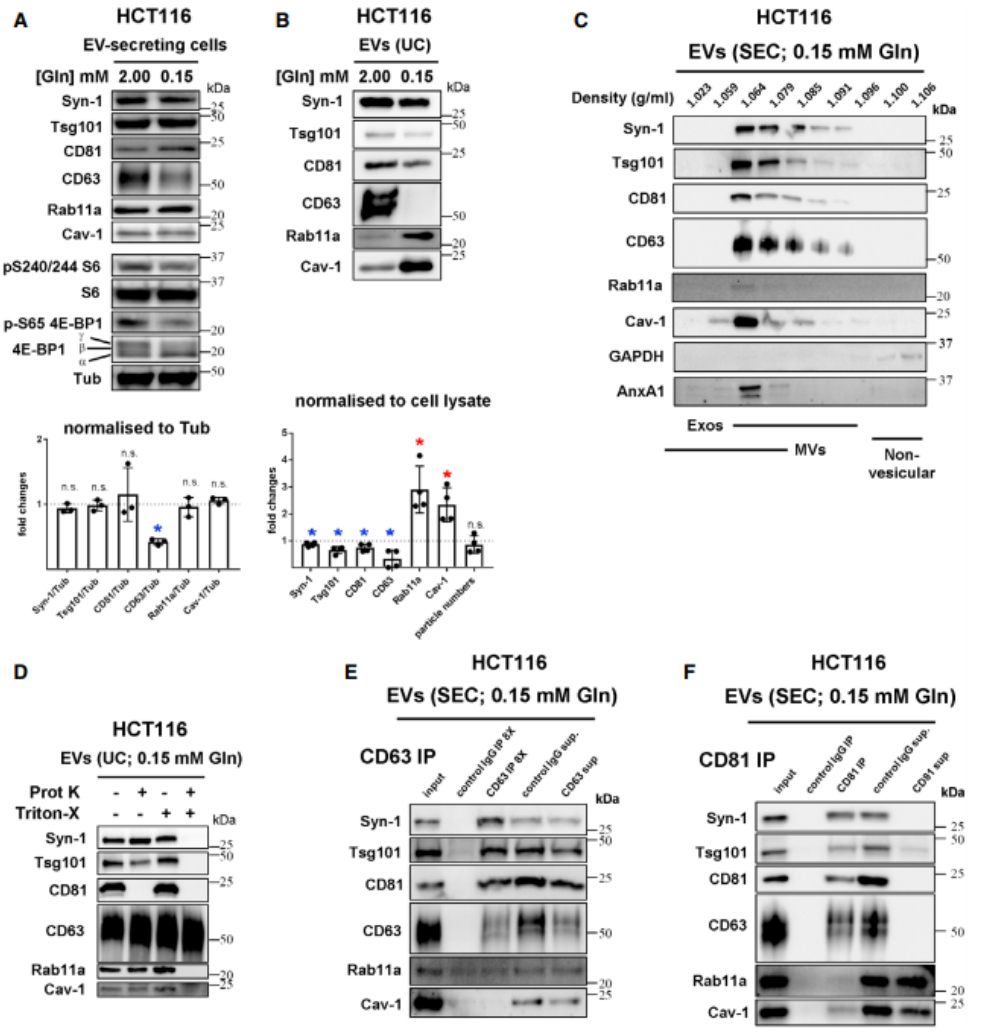



**Figure 4.**

© 2020 The Authors

**Figure 4. Reduction in extracellular glutamine induces a switch to Rab11a-positive exosome secretion in HCT116 colorectal cancer cells.**

A Western blot analysis of putative exosome markers in lysates from HCT116 cells cultured in glutamine-replete (2.00 mM) and glutamine-depleted (0.15 mM) medium for 24 h. Gel was loaded with equal amounts of protein (total cell lysate protein was reduced by 19 ± 4% after glutamine depletion). The activity of mTORC1 was assessed via phosphorylation of S6 and 4E-BP1, using phospho-specific antibodies and a pan-4E-BP1 antibody, where the hyper-phosphorylated form of 4E-BP1 produced by mTORC1 gives the slowest migrating γ band. Bar chart shows the abundance of putative exosome proteins relative to tubulin in these lysates.

B–F Western blot analyses of EV preparations. (B) EVs isolated by ultracentrifugation (UC) of medium from HCT116 cells cultured in glutamine-replete and glutamine-depleted conditions for 24 h and loaded according to cell lysate protein levels to compare secretion on a per cell basis, as shown in bar chart from four biological replicates. (C) EV preparation isolated by size-exclusion chromatography (SEC) from glutamine-depleted HCT116 cells and then separated by high-resolution iodixanol-PBS density centrifugation. Note that exosomes (exos) and microvesicles (MVs) are found in only partially overlapping fractions and the pattern of Rab11a separation mirrors that of exosome markers (primarily 1.064–1.085 g/ml). (D) EVs isolated by UC under glutamine-depleted conditions as in (B) and then subjected to proteinase K (Prot K) digestion in the presence or absence of Triton® X-100 (Triton X). Only membrane-associated CD81 is digested in the absence of Triton® X-100, while CD63 is resistant to digestion, even in the presence of Triton® X-100. SEC-isolated EVs also behave similarly (Appendix Fig S6C). (E) EVs isolated under glutamine-depleted conditions were immunocaptured with anti-CD63 antibodies coupled to magnetic beads. This method only pulls down a fraction of CD63, so the protein from pull-down of eight times the input is loaded for comparison. Approximately the same low levels of Rab11a are captured by control IgG and anti-CD63 beads. (F) EVs isolated under glutamine-depleted conditions were immunocaptured with anti-CD81 antibodies coupled to magnetic beads. All or most CD63 and CD81 appears to be pulled down, but < 10% of Rab11a and Cav-1 is captured. NTA analysis suggests about 10% of all particles are pulled down with this approach.

Data information: Bar charts derived from at least three independent experiments and analysed by the Kruskal–Wallis test: $*P < 0.05$; n.s. = not significant. Bars and error bars denote mean ± SD. Significantly decreased levels are in blue and increased levels are in red.
Source data are available online for this figure.

growth factor receptors and has been implicated in regulating the proteome of CRC cell exosomes (Demory Beckler *et al*, 2013). Cells treated with a specific inhibitor that can block activated KRAS, BI-2852 (Kessler *et al*, 2019), did not show significant changes in mTORC1 activity (Appendix Fig S7D) and did not alter their EV secretion (Fig 5F, Appendix Fig S7D′), suggesting that the effect of KRAS on exosomes does not involve a switch to Rab11a-exosome secretion. Overall, our data from CRC, cervical and prostate cancer cell lines lead us to conclude that glutamine depletion or inhibition of Akt/mTORC1 signalling induces a switch in the balance of exosome secretion towards vesicles from recycling endosomal compartments, increasing exosome levels of Rab11a, as well as Cav-1, by several fold. Stronger mTORC1 blockade suppresses general exosome secretion, so although the balance of exosome secretion may still be shifted towards recycling endosomes, total Rab11a secretion is not increased.

### Glutamine depletion-induced extracellular vesicles have altered activities that are dependent on Rab11a

Since EVs secreted by glutamine-depleted HCT116 cells have altered cargos, we tested whether this affected their bioactivity. When EVs from glutamine-replete and glutamine-depleted cells were prepared by ultracentrifugation, then mixed with naïve recipient HCT116 cells, 30 min prior to plating, the stress-induced EVs selectively stimulated cell growth under low serum conditions (Fig 6A). Cell proliferation was enhanced by this treatment (Fig EV5A), but rates of apoptosis were unaffected (Fig EV5B). The same activity was reproduced with EVs isolated by SEC and shown to be dose-dependent (Figs 6A and EV5C), so both of these methods were employed in subsequent functional assays.

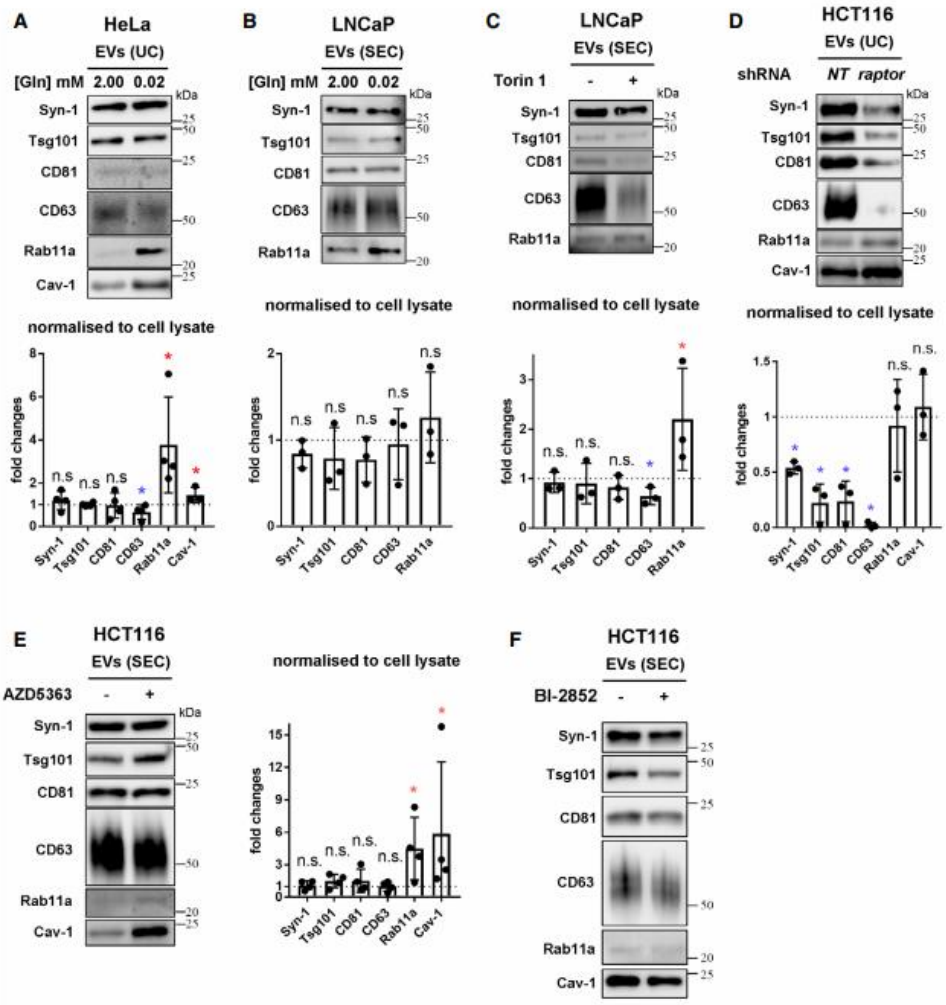
To test for effects of glutamine depletion-induced EVs on stromal cells, EV preparations were also added to human umbilical vein endothelial cells (HUVECs), which were then plated in Matrigel® to assess their ability to form and maintain a tubular network. EVs isolated under glutamine-replete and glutamine-depleted conditions increased network formation compared to PBS-treated controls (Fig 6B). Network maintenance was, however, enhanced by EVs from glutamine-depleted cells, suggesting that these EVs are better at supporting a stable capillary network. Therefore, following glutamine depletion, HCT116 cells secrete EVs enriched in exosomes from Rab11a-positive endosomes that display novel or enhanced activities.

To test whether trafficking through the Rab11a-dependent recycling endosomal pathway was essential for the increased growth induced by EVs from glutamine-depleted cells, *Rab11a* was knocked down in secreting cells. This suppressed Rab11a levels in cells (Fig EV5D) and EVs (Fig 6C), reduced the number of EVs secreted by approximately 40% (Fig EV5D′), but had no effect on mTORC1 activity or cellular levels of exosome proteins (Fig EV5D). Exosome markers Syn-1, Tsg101 and CD63 were not significantly altered in EVs compared to controls and Cav-1 secretion was increased (Fig 6C), suggesting that Rab11a compartments are not the only route for secretion of these molecules. Knockdown did, however, strongly suppress the enhanced growth-promoting activity of EVs produced by glutamine-depleted cells (Fig 6C′). We conclude that this activity is likely to involve Rab11a-dependent exosome secretion.

### Altered endosomal pathway trafficking induces an exosome switch

We reasoned that changes in endosomal trafficking might be involved in switching the balance of exosome secretion to favour Rab11a-exosomes following glutamine depletion. To test this, the internalisation of molecules that specifically traffic from the plasma membrane either to LELs or to Rab11a compartments was assessed under both glutamine-replete and glutamine-depleted conditions. While CD63 accumulates in LEL compartments (Fig 3B), transferrin (Tfn) is returned to the plasma membrane after endocytosis, via the rapid recycling pathway and Rab11a-positive recycling endosomes (Mayle *et al*, 2012). Consistent with this, internalised Alexa-488-conjugated Tfn partly co-localised with Rab11a in HCT116 cells (Appendix Fig S8A), but not with the LEL marker LAMP2 (Appendix Fig S8B). When HCT116 cells were depleted of

 © 2020 The Authors




G

| | HCT116 | | | HeLa | LNCaP | |
|---|---|---|---|---|---|---|
| EV Proteins | [Gln]↓ | *raptor* shRNA | AZD5363 | [Gln]↓ | [Gln]↓ | Torin 1 |
| Syn-1 | 0.87±0.07 * | 0.54±0.06 * | 1.11±0.42 | 1.20±0.43 | 0.84±0.16 | 0.92±0.20 |
| Tsg101 | 0.66±0.13 * | 0.22±0.17 * | 1.50±0.62 | 1.01±0.09 | 0.79±0.36 | 0.90±0.41 |
| CD81 | 0.74±0.14 * | 0.24±0.18 * | 1.53±1.07 | 0.97±0.59 | 0.77±0.26 | 0.82±0.24 |
| CD63 | 0.33±0.33 * | 0.02±0.03 * | 1.01±0.44 | 0.66±0.33 * | 0.95±0.41 | 0.64±0.18 * |
| Rab11a | 2.90±0.87 * | 0.92±0.42 | 4.52±2.89 * | 3.78±2.21 * | 1.26±0.52 | 2.20±1.04 * |
| Cav-1 | 2.34±0.63 * | 1.09±0.30 | 5.88±6.64 * | 1.45±0.36 * | n.a. | n.a. |

Figure 5.

© 2020 The Authors

**Figure 5. Reduction in extracellular glutamine or Akt/mTORC1 signalling induces a switch to Rab11a-positive exosome secretion in three different cancer cell lines.**

Western blot analyses of EV preparations. Gel loading is normalised to cell lysate protein levels. Bar charts present changes in levels of putative exosome proteins relative to cell lysate protein.

A EVs isolated by UC of medium from HeLa cells cultured in glutamine-replete (2.00 mM) and -depleted (0.02 mM) conditions for 24 h (see Appendix Fig S7A" for analysis of SEC-isolated EVs).

B EVs isolated by size-exclusion chromatography (SEC; fractions two to seven) from LNCaP cells cultured in glutamine-replete (2.00 mM) and -depleted (0.02 mM) conditions for 24 h.

C EVs isolated by SEC from LNCaP cells cultured in the presence or absence of 120 nM Torin 1 for 24 h.

D EVs isolated by UC from HCT116 cells cultured for 24 h following 3 days of *raptor* or non-targeting (*NT*) shRNA knockdown.

E EVs isolated by SEC from HCT116 cells cultured in the presence or absence of 3 μM Akt inhibitor AZD5363 for 24 h.

F EVs isolated by SEC from HCT116 cells cultured under glutamine-replete conditions in the presence or absence of 10 μM KRAS inhibitor BI-2852 (or control compound BI2853) for 24 h.

G Table summarising the EV protein analyses in Figs 4 and 5 (normalised to cell lysate protein levels). Data analysed by the Kruskal–Wallis test: $*P < 0.05$. Significantly decreased levels are in blue and increased levels are in red.

Data information: Bar charts derived from at least three independent experiments and analysed by the Kruskal–Wallis test: $*P < 0.05$; n.s. = not significant. Bars and error bars denote mean ± SD. Significantly decreased levels are in blue and increased levels are in red.
Source data are available online for this figure.

glutamine, uptake of an anti-CD63 antibody, assessed by confocal imaging and Western analysis, was significantly reduced (Fig 6D and E), consistent with the reduced levels and increased degradation of CD63 in these cells (Appendix Fig S4B). By contrast, uptake of fluorescent (Fig 6D) and biotin-conjugated (Fig 6E) Tfn were significantly elevated, demonstrating that flux through the recycling endosomal pathway is increased in response to glutamine depletion.

Since altered endosomal trafficking is associated with a glutamine-regulated switch in exosome secretion, we hypothesised that a similar switch might be induced in HCT116 cells by inhibiting traffic through the late endosomal pathway. Knockdown of *Rab7* substantially reduced EV secretion, decreased CD63 in EV preparations under glutamine-replete conditions, but increased Rab11a levels, without having a major effect on marker expression levels in cells (Figs 6F and EV5E and E′; cellular levels of Rab11a were in fact slightly reduced). The resulting EVs stimulated growth of serum-depleted HCT116 cells (Fig 6F′), demonstrating that altering the balance of late and recycling endosomal trafficking can induce changes analogous to the switch in exosome secretion caused by reducing glutamine.

### EVs secreted from glutamine-depleted cells induce ERK-dependent growth in HCT116 recipient cells and are blocked by an anti-amphiregulin antibody

Since EVs from glutamine-depleted HCT116 cells induce growth in recipient cells, we investigated whether growth factor signalling might be involved. Phosphorylation of the MAPK ERK was enhanced when serum-starved HCT116 cells were incubated for 30 min with EV preparations from glutamine-depleted cells (Fig 7A). Indeed, treating recipient HCT116 cells with the ERK inhibitor SCH772984 for the first 24 h of culture after EV addition completely blocked the extra growth induced by these vesicles (Fig 7B, Appendix Fig S8C), demonstrating that elevated ERK signalling is critically involved in growth stimulation.

Since epidermal growth factor receptor (EGFR) signalling plays a key role in CRC growth and the EGF ligand amphiregulin (AREG) is expressed by HCT116 cells (Nagathihall *et al*, 2014) and known to be packaged into CRC-derived exosomes (Higginbotham *et al*, 2011), we tested whether AREG was present on EVs from glutamine-depleted HCT116 cells. Glutamine depletion increased levels of a ~ 26 kDa membrane-associated form of AREG (Brown *et al*, 1998) in cell lysates and in EVs produced by SEC and UC under these conditions (Figs 7C and EV5F, Appendix Fig S8D). Treating EV preparations from glutamine-depleted and control cells with a neutralising antibody to AREG (Raimondo *et al*, 2019) partially suppressed ERK activation in target cells (Fig 7C″) and blocked the growth-promoting effect of glutamine depletion-induced EVs (Fig 7C′), suggesting that AREG-positive vesicles play a critical role in this process. Consistent with previous studies (Zhang *et al*, 2019), ELISA measurements of AREG in EV preparations from glutamine-depleted cells revealed that the minimum concentration of AREG required to promote proliferation is extremely low (1.4 pg AREG/ml; Fig EV5C). Glutamine depletion therefore induces the secretion of Rab11a-exosomes in HCT116 cells, and low levels of AREG on the EVs produced by these cells play an important role in the enhanced growth-promoting activity of these vesicles.

### Glutamine depletion-induced extracellular vesicles promote tumour cell turnover *in vivo*

To test whether the enhanced activities of EV preparations from glutamine-depleted HCT116 cells could be replicated *in vivo*, we established HCT116 xenografts in exponential growth phase and then directly injected them every 3 days over 9 days with EVs, isolated from HCT116 cells under glutamine-replete and glutamine-depleted conditions. Xenografts were analysed 24 h following the last injection of EVs. There was no change in overall tumour growth over this short time period following exposure to either type of EV preparation (Appendix Fig S9). However, there were significant histological differences within the xenografts for different treatments. As previously reported (Sheldon *et al*, 2010), injecting EVs into xenografts led to increased overall vessel number (Fig 8A); however, the effect of the two EV preparations was different, with vessel lumen size significantly increased in xenografts exposed to EVs from glutamine-depleted cells. The increased number of blood vessels for both EV treatments correlated with elevated tumour cell proliferation (Fig 8B). Again, consistent with observations *in vitro*, exposure to EV preparations from glutamine-depleted cells led to the highest levels of proliferating cells in the viable regions of the

 © 2020 The Authors

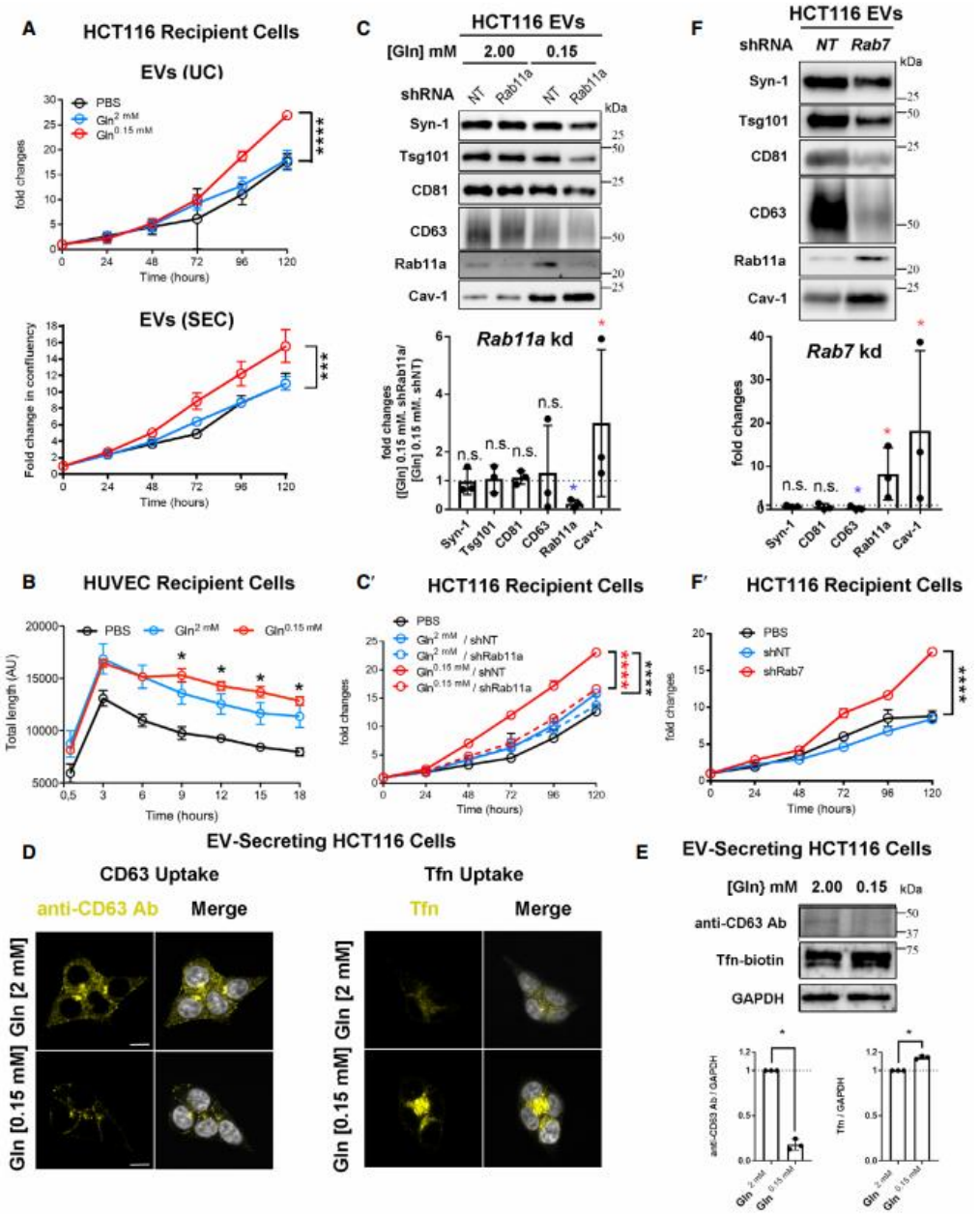

A
HCT116 Recipient Cells
EVs (UC)
PBS
Gln2 mM
Gln0.15 mM
fold changes
Time (hours)
****
EVs (SEC)
Fold change in confluency
Time (hours)
***
C
HCT116 EVs
[Gln] mM 2.00 0.15
shRNA NT Rab11a NT Rab11a
kDa
Syn-1
Tsg101
CD81
CD63
Rab11a
Cav-1
Rab11a kd
fold changes ([Gln] 0.15 mM. shRab11a/ [Gln] 0.15 mM. shNT)
n.s.
*
F
HCT116 EVs
shRNA NT Rab7
Rab7 kd
fold changes
B
HUVEC Recipient Cells
Total length (AU)
Time (hours)
C'
HCT116 Recipient Cells
PBS
Gln2 mM / shNT
Gln2 mM / shRab11a
Gln0.15 mM / shNT
Gln0.15 mM / shRab11a
fold changes
Time (hours)
F'
HCT116 Recipient Cells
PBS
shNT
shRab7
fold changes
Time (hours)
D
EV-Secreting HCT116 Cells
CD63 Uptake
anti-CD63 Ab
Merge
Tfn Uptake
Tfn
Merge
Gln [2 mM]
Gln [0.15 mM]
E
EV-Secreting HCT116 Cells
[Gln} mM 2.00 0.15 kDa
anti-CD63 Ab
Tfn-biotin
GAPDH
anti-CD63 Ab / GAPDH
Tfn / GAPDH

Figure 6.

**Figure 6. Rab11a-dependent exosome secretion is induced by altered endosomal trafficking and promotes recipient tumour cell growth.**

A Growth curves for HCT116 recipient cells in reduced (1%) serum conditions following 30-min pre-incubation with EVs isolated by UC ($10^4$ per cell; top) or by SEC ($4 \times 10^3$ per cell; bottom) from glutamine-replete and glutamine-depleted HCT116 cells or with vehicle (PBS). Fold change in confluency is a measure of cell area occupying well relative to zero time, as measured by IncuCyte software.

B Cumulative tube length for HUVEC recipient cells following treatment with $10^4$ EVs isolated by UC from glutamine-replete and glutamine-depleted HCT116 cells or with vehicle (PBS). Both EV preparations promote tubulation, but the network is more stable with EVs from glutamine-depleted HCT116 cells.

C Western blot analysis of EVs isolated by UC from HCT116 cells cultured in glutamine-replete and glutamine-depleted medium for 24 h, following transduction with a *Rab11a* or control non-targeting (NT) shRNA knockdown construct over previous 2 days. Bar chart shows change in putative exosome proteins in EVs secreted from *Rab11a* knockdown cells relative to NT-treated cells in glutamine-depleted conditions, following initial normalisation to cell lysate protein. (C') Growth curves are for HCT116 recipient cells pre-treated with EVs isolated as in (C) or with vehicle (PBS). ****$P$ colour denotes significant increase relative to EVs from glutamine-replete cells (black) and *Rab11a* knockdown cells (red).

D Left-hand group of four images shows cells grown in glutamine-replete (2.00 mM) and glutamine-depleted (0.15 mM) conditions for 24 h, then incubated with an anti-CD63 antibody (yellow) for 30 min at 4°C, washed with PBS, chased at 37°C for 30 min, then fixed, immunostained and imaged. Right-hand group of four images shows cells grown in glutamine-replete and glutamine-depleted conditions for 24 h, incubated with Tfn-Alexa Fluor® 488 (yellow) for 30 min at 4°C, shifted to 37°C for 30 min, then washed, immediately fixed and imaged.

E Western blot showing levels of anti-CD63 heavy-chain and biotin-conjugated Tfn in HCT116 cells cultured for 24 h in glutamine-replete or glutamine-depleted conditions, incubated for 30 min in medium containing these molecules at 4°C, then chased at 37°C for 15 min (the chase step was not performed for Tfn in D, to reduce loss due to rapid recycling of Tfn).

F Western blot analysis of EVs isolated by UC from HCT116 cells in glutamine-replete medium, transduced with a *Rab7* or non-targeting (NT) control shRNA knockdown construct. Bar charts show changes in putative exosome proteins in EVs isolated by ultracentrifugation, following normalisation to cell lysate protein. (F') Growth curves are for HCT116 recipient cells pre-treated with EVs isolated as in (F) or with vehicle (PBS).

Data information: Scale bars in D (5 μm) apply to all panels. Growth curves were reproduced in three independent experiments and analysed by two-way ANOVA. Bar charts derived from three independent experiments and analysed by the Kruskal–Wallis test: ****$P < 0.0001$, ***$P < 0.001$, *$P < 0.05$. Bars and error bars denote mean ± SD. Significantly decreased levels are in blue and increased levels are in red in panels C and F.
Source data are available online for this figure.

tumour (Fig 8B). However, an overall increase in necrosis (Fig 8C) and in hypoxia, as indicated by expression of carbonic anhydrase (CA9) as a downstream hypoxia marker (Fig 8D; McIntyre *et al*, 2016), was also induced by EV treatment and particularly by EV preparations from glutamine-depleted cells. Overall, we conclude that changes in EV production driven by glutamine depletion induce increased cell turnover *in vivo*, which may contribute to adaptive changes under these metabolic stress conditions.

## Discussion

Exosomes are important mediators of signalling between cells, particularly in cancer, but the mechanisms by which exosome signals might change in response to microenvironmental stress have remained largely unexplored. Here, using human CRC, cervical and prostate cancer cell lines, and supported by a fly *in vivo* exosome biogenesis model, we provide evidence that exosomes are not only formed in late endosomal MVBs, but also in Rab11/11a-positive recycling endosomal MVBs. These latter exosomes carry distinct cargos, including Rab11/11a, providing a diagnostic signature for their compartment of origin. Furthermore, they appear to be preferentially released by cancer cells following glutamine depletion or Akt/mTORC1 inhibition, generating unique biological effects *in vitro* and *in vivo* (shown schematically in Fig 8E). We propose that this previously undescribed exosome subtype plays a unique role in tumour adaptation to metabolic stresses.

### Rab11/11a-positive compartments are novel sites of exosome biogenesis

Knockdown studies in human cells and *Drosophila* have highlighted a role for Rab11 family members in exosome secretion (Savina *et al*, 2002; Koles *et al*, 2012; Beckett *et al*, 2013; Messenger *et al*, 2018). In fact, one report previously identified Rab11a-positive MVBs in human cells (Savina *et al*, 2005). These experiments were, however, taken as evidence for Rab11a facilitating MVB trafficking to the cell surface and/or docking MVBs there. Our *in vivo* analysis in *Drosophila*, together with imaging studies and EV analysis in human cell lines, indicates that Rab11 compartments are conserved sites of exosome biogenesis. Rab11 family members are classically associated with recycling endosomes, but are also implicated in regulating secretory traffic from the Golgi (Welz *et al*, 2014). Human Rab11a-positive exosomes, however, appear to be generated in recycling endosomes, because their secretion is upregulated when traffic through the recycling pathway is increased, and Rab11a-positive ILVs can form in enlarged Rab5CA-induced endosomes. High-resolution imaging in the fly system has allowed us to demonstrate that production of these vesicles is ESCRT-dependent, suggesting parallels with late endosomal exosomes in their biogenesis mechanisms. Regulators include the ESCRT-0 Stam, which, unlike other classes of ESCRT, is not thought to be involved in microvesicle biogenesis (McCullough *et al*, 2013), providing further support that vesicles secreted into the AG lumen are an alternative form of exosomes.

Glutamine depletion induces a switch in the balance of exosome marker secretion in cancer cells from CD63 to Rab11a, a result observed with two very different EV isolation methods. Using density gradient separation, we have shown that most of Rab11a in EV preparations from glutamine-depleted cells co-fractionates with exosome markers. However, immunocapture experiments reveal that CD63- and Rab11a-containing exosomes are essentially distinct. A small proportion of Rab11a is carried on exosomes marked by CD81, which is one of the best-established markers for "classical" exosomes. Currently, we cannot determine whether significant numbers of Rab11a-negative, CD81-positive exosomes are made in Rab11a compartments, or whether they are primarily formed in other endosomal compartments (Fig 8E). Interestingly, in *Drosophila* SCs, human CD63 can be incorporated into ILVs in Rab11

 © 2020 The Authors

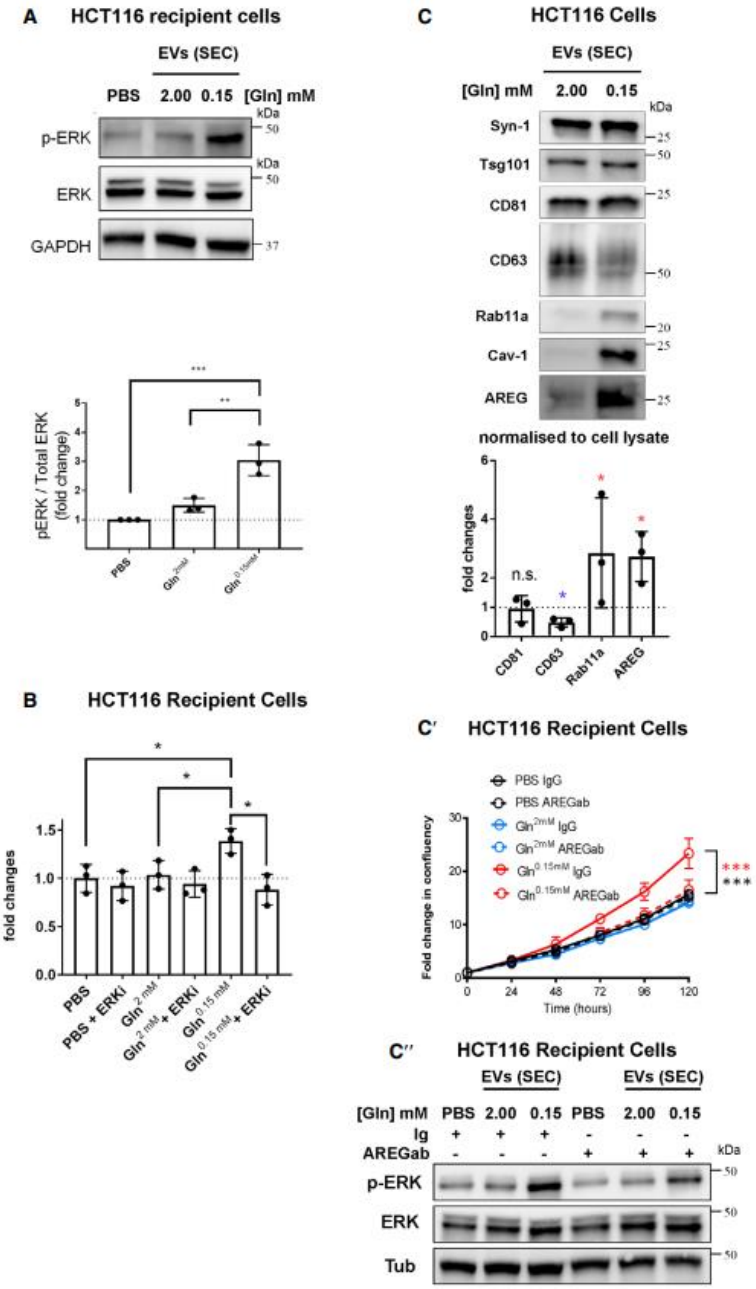

A
HCT116 recipient cells
EVs (SEC)
PBS 2.00 0.15 [Gln] mM
kDa
p-ERK
ERK
GAPDH
pERK / Total ERK (fold change)
PBS
Gln2mM
Gln0.15mM
B
HCT116 Recipient Cells
fold changes
PBS
PBS + ERKi
Gln 2 mM
Gln 2 mM + ERKi
Gln 0.15 mM
Gln 0.15 mM + ERKi
C
HCT116 Cells
EVs (SEC)
[Gln] mM 2.00 0.15
Syn-1
Tsg101
CD81
CD63
Rab11a
Cav-1
AREG
normalised to cell lysate
fold changes
n.s.
CD81
CD63
Rab11a
AREG
C′
HCT116 Recipient Cells
PBS IgG
PBS AREGab
Gln2mM IgG
Gln2mM AREGab
Gln0.15mM IgG
Gln0.15mM AREGab
Fold change in confluency
Time (hours)
C″
HCT116 Recipient Cells
EVs (SEC)
EVs (SEC)
[Gln] mM PBS 2.00 0.15 PBS 2.00 0.15
Ig
AREGab
p-ERK
ERK
Tub

Figure 7.

**Figure 7. EVs induced by glutamine depletion promote amphiregulin- and ERK-dependent growth in HCT116 recipient cells.**

A Western blot analysis of ERK phosphorylation (p-ERK) in recipient serum-deprived HCT116 cells pre-treated with EVs isolated by SEC from glutamine-replete or glutamine-depleted HCT116 cells or vehicle (PBS). Bar chart shows ratio of p-ERK to ERK levels from triplicate independent experiments.

B Bar chart shows HCT116 recipient cell growth over 120 h, after pre-treatment with EV preparations isolated as in (A) or with PBS, and then incubation for the first 24 h of culture in the presence or absence of the ERK inhibitor SCH772984 (1.00 μM). Growth curves are shown in Appendix Fig S8C.

C Western blot analysis showing levels of the EGFR ligand, amphiregulin (AREG) in EVs isolated by SEC of medium from HCT116 cells cultured in glutamine-replete (2.00 mM) or glutamine-depleted (0.15 mM) conditions for 24 h. Gel loading was normalised to cell lysate protein levels. AREG's molecular weight (approximately 26–28 kDa) suggests it is in its membrane-associated form (see Appendix Fig S8D). In the bar chart, the levels of putative exosome proteins were normalised to cell lysate protein levels. Significantly decreased levels are in blue and increased levels are in red. (C') Growth curves in low (1%) serum are for HCT116 recipient cells pre-treated with the EV preparations [isolated as in (C)], which had themselves been pre-treated with and without anti-AREG neutralising antibody or with a control IgG. Solid red line shows growth-promoting effect of EVs isolated under glutamine depletion, which is blocked by anti-AREG antibody (red dashed line). ***P colour denotes significant increase relative to EVs from glutamine-replete cells (black) and after anti-AREG treatment of EVs (red). (C") Western blot analysis of ERK phosphorylation (p-ERK) in recipient serum-deprived HCT116 cells pre-treated with EVs isolated by SEC from glutamine-replete (2.00 mM) or glutamine-depleted (0.15 mM) HCT116 cells or vehicle (PBS), which were pre-treated with anti-AREG (AREGab) or a control immunoglobulin (Ig). Note increase in ERK phosphorylation using EVs from glutamine-depleted cells, which is blunted by the addition of the anti-AREG antibody.

Data information: Growth curves were reproduced in three independent experiments and analysed by two-way ANOVA. Bar charts derived from three independent experiments and analysed by ANOVA or the Kruskal–Wallis test: ***$P < 0.001$, **$P < 0.01$, *$P < 0.05$. Bars and error bars denote mean ± SD.
Source data are available online for this figure.

compartments, and some of these exosomes appear to contain Rab11 (Fig EV1J). However, even in this system, the vast majority of CD63 traffics to LEL compartments, suggesting that co-localisation is likely to be the result of high-level expression in these cells leading to co-trafficking of these markers to recycling endosomal compartments.

Since we do not currently have a method to isolate Rab11a-labelled exosomes, we cannot exclude the possibility that increased Rab11a secretion under stress conditions is explained by loading more Rab11a into a similar number of exosomes. However, this seems unlikely, because we have shown that these stress conditions increase secretory traffic through the recycling endosomal pathway, and that diverting traffic through this pathway by *Rab7* knockdown is sufficient to both increase Rab11a secretion and induce growth effects that mirror those seen after glutamine depletion.

Both in *Drosophila* (Corrigan *et al*, 2014) and in glutamine-depleted human cells, blocking Rab11/11a activity inhibits the biological activities of secreted EVs, suggesting a key role for exosomes generated in Rab11/11a compartments. This manipulation could have other indirect effects on secretion; for example, it has been implicated in CD63-marked exosome secretion (Messenger *et al*, 2018; van Niel *et al*, 2018). However, at least in HCT116 cells, *Rab11a* knockdown leads to only modest or no reduction in several other exosome markers in EV preparations and increases Cav-1 secretion. The treatment therefore appears to have relatively specific effects on Rab11a-exosome secretion in this cell type and suggests these exosomes have important disease-relevant activities.

The continued release of Cav-1, which partially co-fractionates with exosome markers, following *Rab11a* knockdown in HCT116 cells suggests that its secretion under stress conditions involves another EV biogenesis pathway, within unidentified intracellular compartments and/or from the cell surface. Secretion of Cav-1-containing small EVs of unknown subcellular origin has also recently been shown to be under metabolic (Crewe *et al*, 2018), as well as hypoxic (Kucharzewska *et al*, 2013) control. In the latter case, this may involve reduced constitutive endocytosis (Bourseau-Guilmain *et al*, 2016), but a role for different endosomal pathways has not been investigated. Distinguishing the different classes of tumour EV that are produced under metabolic stress should assist in determining what cancer-relevant functions are associated with each specific EV subtype, as we have done for Rab11a-exosomes.

Although not major constituents of exosomes, the identification of Rab11/11a and potentially Rab7 (Fig 3F) as signatures for exosome origin suggests a new approach for distinguishing different exosome subtypes in EV preparations. In flies, the selective labelling by Rab11 of smaller numbers of vesicles in Rab11 compartments than CD63-GFP or Btl-GFP suggests the existence of subpopulations of vesicles in a single compartment, which we may have partly distinguished by co-expressing YFP-Rab11 with CD63-mCherry (Fig EV1J). Unlike transmembrane proteins present on the limiting membrane of secretory compartments, Rabs are thought to disengage from the lipid bilayer before or during plasma membrane fusion, as evidenced by our fly (Fig EV1G and H) and human (Appendix Fig S4C and D) cell data, so they are unlikely to be incorporated into microvesicles shed from the cell surface. Multiple Rabs have been reported to be present in EV preparations (Keerthikumar *et al*, 2016) and several are only partially pulled down by anti-tetraspanin EV immunocapture (Kowal *et al*, 2016), suggesting that other exosome subtypes are yet to be identified. Of particular interest are Rab35 and Rab27 family members, which, like Rab11, have been implicated in exosome release (Hsu *et al*, 2010; Ostrowski *et al*, 2010). Whether they mark additional exosome biogenesis pathways or primarily promote trafficking from other pathways remains to be determined.

### Tumour exosome signalling is regulated by metabolic stress and Akt/mTORC1 signalling

Our finding that several cancer cell types alter their exosome secretion and signalling following glutamine depletion highlights a novel function for the recycling endosomal exosome biogenesis pathway in a tumour's response to its microenvironment. In contrast to cancer cells, the highly secretory SCs of the fly AG release exosomes from Rab11-positive compartments containing DCGs in a regulated fashion under normal physiological conditions (Corrigan *et al*, 2014; Redhai *et al*, 2016). Consequently, we have not been able to assess whether there is a switch in exosome secretion by these cells under nutrient stress. Rab11 family members have also been implicated in granule secretion from pancreatic beta cells (Sugawara *et al*, 2009) and *Drosophila* salivary glands (Farkaš *et al*, 2015), although to date, ILVs have not

 © 2020 The Authors

been reported in the much smaller compartments involved. It will be interesting to investigate whether highly secretory cells use an entirely different mechanism to control Rab11-exosome secretion or whether there is an unappreciated link to cellular stress, perhaps involving the ER stress that is likely to be induced in these cells.

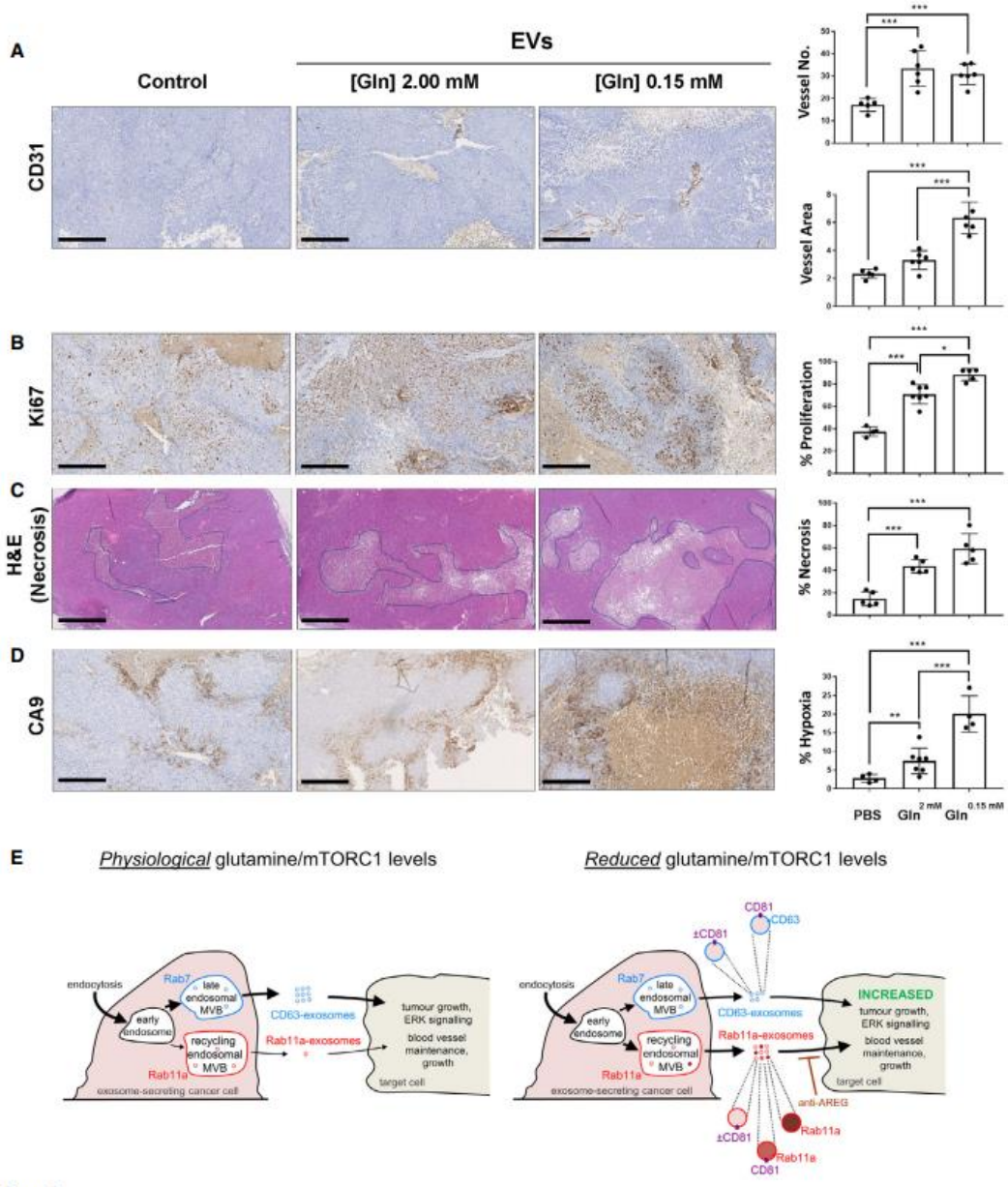



**Figure 8.**

© 2020 The Authors

**Figure 8. EVs from glutamine-depleted HCT116 cells increase tumour cell turnover and vessel growth in mouse HCT116 xenografts.**

HCT116 flank tumours produced by subcutaneous injection were established for 20 days before injection at 3-day intervals with vehicle (PBS), or EVs isolated by UC from glutamine-replete or glutamine-depleted HCT116 cells. Tumours were excised 24 h after last of four injections for analysis. Panels show representative immunostained histological sections of tumour tissue quantified using the Visiopharm Integrator System.

A Sections immunostained for CD31, which labels endothelial cells and blood vessels, with blood vessel number (upper) and total area (lower) represented in bar charts.

B Sections immunostained for Ki67, which stains proliferative cells. Proportion of tumour cells with Ki69 staining is represented in bar chart.

C Sections stained with haematoxylin and eosin, which highlights necrotic regions (pale staining). Proportion of tumour area that is necrotic is represented in bar chart.

D Sections immunostained for CA9, which is expressed in hypoxic regions. Proportion of tumour cells with CA9 staining is represented in bar chart.

E Schematic model showing how in cancer cells, regulation of endosomal trafficking by depletion of exogenous glutamine or reduced Akt/mTORC1 signalling can induce a change in the balance of exosome production. Relative levels of a mixed population of exosomes from the established Rab7-late endosomal multivesicular bodies (MVBs), termed "CD63-exosomes", are reduced relative to the mixed exosome population from Rab11a-labelled recycling endosomal MVBs, termed "Rab11a-exosomes", a subset of which appear to be marked with Rab11a. Although CD63 does not appear to be trafficked through these latter compartments, the "classical" exosome marker CD81 appears to be present at undefined levels and marks some Rab11a-containing exosomes. The resulting vesicles can increase ERK signalling and cell growth in recipient tumour cells and enhance growth and stability of network formation in endothelial cells. The growth effects are Rab11a-dependent and can be blocked by anti-AREG antibodies. Thickness of arrows indicates relative levels of membrane flux through the two exosome-generating endosomal routes.

Data information: Scale bar is 250 μm, except for (C), which is 500 μm. Data were analysed by one-way ANOVA; $n \geq 4$; $^{*}P < 0.05$, $^{**}P < 0.01$, $^{***}P < 0.001$. Bars and error bars denote mean ± SD.
Source data are available online for this figure.

Growth factor- and nutrient-dependent regulation of many cellular functions, including proliferation, apoptosis, autophagy and metabolism, involves mTORC1 (Goberdhan *et al*, 2016). The roles of mTORC1 in secretion, particularly exosome release, have been less extensively studied. A recent report suggested that exosome secretion is increased after mTORC1 inhibition in mouse embryonic fibroblasts, but markers like Rab11a and Cav-1 were not analysed in this study (Zou *et al*, 2018). Our findings suggest that therapeutic blockade of PI3K/Akt or mTORC1, but not KRAS, signalling in cancer can induce a switch in secreted exosome subtype, although in some cells, complete mTORC1 inhibition appears to strongly reduce all exosome secretion. In addition to highlighting a new role for growth factor signalling and glutamine in exosome regulation, and its potential role in adaptation mechanisms, our data indicate the importance of monitoring mTORC1 activity during EV isolation procedures.

### Exosome signalling in tumour adaptation

We were initially surprised to find that the release of recycling endosomal exosomes from glutamine-depleted HCT116 cells enhances tumour cell growth, in addition to promoting blood vessel maintenance *in vitro*. Our subsequent xenograft analysis has allowed us to detect similar activities *in vivo* and develop a model that may explain these findings.

Consistent with previous reports (Sheldon *et al*, 2010), we observed that injecting EVs from glutamine-replete or glutamine-depleted cells increased the number of blood vessels within tumours. However, EVs from glutamine-depleted cells also preferentially increased proliferation in the tumour, which likely contributed to the elevated hypoxia and necrosis within the xenografts, despite the increased number of blood vessels. Tumour cells under nutrient and hypoxic stress are known to adapt to such metabolic stress conditions to survive and grow. For example, cancer cells can become "glutamine addicted", whereby glutamine metabolism is able to sustain proliferation (Tardito *et al*, 2015). These cells often upregulate their growth regulatory pathways to achieve this. For instance, oncogenic KRAS drives glutamine metabolism in lung adenocarcinoma (Romero *et al*, 2017), while in lung squamous cell carcinoma, where mTORC1 is frequently hyper-activated, it has been observed that tumours that are highly resistant to conventional chemotherapy respond to inhibitors targeting the glutamine pathway (Lukey *et al*, 2018). Therefore, although we show an important role for amphiregulin in glutamine depletion-induced, EV-mediated growth, the HCT116 cell line already has activating PI3KCA and KRAS mutations, which may allow it to respond differently to the exosomes generated under such circumstances.

Release of Rab11a-exosomes under metabolic stress provides a mechanism for generating the heterogeneity in tumours that might drive adaptive changes. The secretion of growth-promoting molecules associated with Rab11a-exosomes from cells might promote their quiescence or even apoptosis. However, it could also stimulate a subpopulation of target cells that are more resistant to metabolic stress to activate ERK and other growth factor cascades, proliferate, alter their metabolism and potentially outcompete their neighbours.

Our *in vitro* studies suggest that low levels of membrane-associated AREG and the ERK signalling it induces may be involved in this process, although we cannot eliminate the possibility that binding of the anti-AREG antibody to AREG-containing exosomes also indirectly interferes with other functions of growth-promoting exosomes.

Since glutamine is now recognised as a key metabolite in several cancers (Zhang *et al*, 2017), glutamine depletion is likely to be a common event in growing tumours, which would trigger a switch to Rab11a-exosome secretion. Reducing growth factor and associated mTORC1 signalling could have similar effects. Therefore, blocking this form of Rab11a-exosome communication may have therapeutic value in suppressing adaptation and/or resistance mechanisms, a concept that needs to be explored with further *in vivo* experiments. In addition, the use of exosomes as biomarkers for cancer and other diseases has considerable clinical potential (Barile & Vassalli, 2017; Shah *et al*, 2018). Our data suggest that the tumour exosome profile can indicate the response of cancer cells to microenvironmental stresses, anti-angiogenic drugs and inhibitors of Akt/mTORC1 signalling. A better understanding of metabolically regulated exosome secretion should therefore lead to exosome profiling being applied with increasing precision in future diagnosis and in prognostic applications involving such treatments.


© 2020 The Authors

## Materials and Methods

### *Drosophila* stocks and genetics

The following fly stocks, acquired from the Bloomington *Drosophila* Stock Centre, unless otherwise stated, were used: *UAS-CD63-GFP* (Panáková *et al*, 2005; a gift from S. Eaton, Max Planck Institute of Molecular Cell Biology and Genetics, Dresden, Germany), *dsx-GAL4* (Rideout *et al*, 2010; a gift from S. Goodwin, University of Oxford, UK), *tubulin-GAL80$^{ts}$*; *UAS-Btl-GFP* (Sato & Kornberg, 2002), *YFP$^{MYC}$-Rab11* and *YFP$^{MYC}$-Rab7* (Dunst *et al*, 2015, a gift from F. Karch and E. Prince, Department of Genetics and Evolution, University of Geneva, Switzerland), *UAS-Stam-RNAi* (TRiP.HMS01429: Ni *et al*, 2011), *UAS-shrb-RNAi* (v106823: Dietzl *et al*, 2007; Matusek *et al*, 2014; Vienna *Drosophila* Resource Centre [VDRC]); *UAS-Vps28-RNAi* (v31894; Dietzl *et al*, 2007; Matusek *et al*, 2014; VDRC), *btl-Gal4* (*btl$^{NP6593}$*; Hayashi *et al*, 2002; Kyoto *Drosophila* Stock Centre); *UAS-GFP$^{NLS}$*; *UAS-YFP-Rab11* (Zhang *et al*, 2007), *UAS-shrb-GFP* (Sweeney *et al*, 2006); and *w$^{1118}$* (a gift from L. Partridge, UCL, UK). The C-terminal end of the human CD63 coding sequence was fused in frame to mCherry, and the resulting gene cloned downstream of UAS sequences in the vector pUAST (Brand & Perrimon, 1993), which was then used to generate transgenic lines.

Flies were reared at 18°C in vials with standard cornmeal agar medium containing, per litre, 12.5 g agar, 75 g cornmeal, 93 g glucose, 31.5 g inactivated yeast, 8.6 g potassium sodium tartrate, 0.7 g calcium and 2.5 g nipagen (dissolved in 12 ml ethanol). They were transferred onto fresh food every 3–4 days. No additional dried yeast was added to the vials.

Temperature-controlled, SC-specific expression of *UAS-CD63-GFP*, *UAS-Btl-GFP* and *UAS-Rab11-YFP* was achieved by combining these transgenes with the specific driver, *dsx-GAL4* and the temperature-sensitive, ubiquitously expressed repressor *tubulin-GAL80$^{ts}$*. Newly eclosed virgin adult males were transferred to 28.5°C to induce post-developmental SC-specific expression. For knockdown experiments, the same strategy was employed, but in the presence of a UAS-RNAi transgene. Six-day-old adult virgin males were used throughout this study to ensure that age- and mating-dependent effects on SC biology were mitigated (Leiblich *et al*, 2012; Redhai *et al*, 2016).

To produce a pulse of Shrb-GFP expression, newly eclosed virgin males were kept at 25°C (permissive for GAL80$^{ts}$ activity) for 6 days, before being transferred to 28.5°C for a 4 h "pulse" of transgene expression under *dsx-GAL4* control, then returned to 25°C for a further 4 h before imaging.

### Preparation of accessory glands for live imaging

Adult male flies were anaesthetised using $CO_2$. The anaesthetised flies were submerged in ice-cold PBS (Gibco®) during the microdissection procedure. The whole male reproductive tract was carefully pulled out of the body cavity. The testes were then removed by scission close to the seminal vesicles, as they often folded over the AGs, obscuring imaging. Care was taken to keep the seminal vesicles and vas deferens intact in order to prevent damage to the papilla of the anterior ejaculatory duct. The AG epithelium can be stressed by damage to this valve-like papilla, through which the spermatozoa and AG contents are transferred during mating. Finally, the remaining reproductive tissues, including the AGs, were isolated by separation of the ejaculatory bulb from the external genitalia, fat tissues and gut.

The isolated AGs were kept in PBS on ice until sufficient numbers had been obtained (typically for approximately 15 min). They were then stained with ice-cold 500 nM LysoTracker® Red DND-99 (Invitrogen®) in 1 × PBS for 5 min. Finally, the glands were washed in ice-cold PBS for 1 min before being mounted onto High Precision microscope cover glasses (thickness No. 1.5H, Marienfeld-Superior). A custom-built holder secured the cover glasses in place during imaging with both the super-resolution 3D-SIM and wide-field systems. To avoid dehydration and hypoxia, the glands were carefully maintained in a small drop of PBS, surrounded by 10S Voltalef® (VWR Chemicals), an oxygen-diffusible hydrocarbon oil (Parton *et al*, 2010) and kept stably in place by the application of a small cover glass (VWR).

### Imaging

#### *Confocal imaging*

Confocal images of cultured cells and AGs were acquired either by using a Zeiss LSM 510 Meta [Axioplan 2], an Olympus FV1000 microscope set-up with 100× NA1.4 oil objective or an LSM 880 laser scanning confocal microscope equipped with a 63×, NA 1.4 Plan APO oil DIC objective (Carl Zeiss). RI 1.514 objective immersion oil (Carl Zeiss) was employed.

#### *Super-resolution 3D-SIM microscopy*

For super-resolution 3D-SIM, fixed human cells or freshly prepared living *Drosophila* AGs were imaged on a DeltaVision OMX V3 system (GE Healthcare Life Sciences) equipped with a 60×, NA 1.42 Plan Apo oil objective (Olympus), sCMOS cameras (PCO), and 405, 488, 593 and 633 nm lasers. Objective immersion oil of RI 1.516 (Cargille Labs) was used to produce optimal reconstruction for a few μm along the *z*-axis of the sample.

The microscope was kept at approximately 20°C throughout experiments. Images were acquired in sequential imaging mode, with Z-stacks, typically spanning 8–12 μm, being acquired with 15 images per plane (five phases, three angles) and a *z*-distance of 0.125 μm. The raw data were computationally reconstructed in the softWoRx 6.0 software package (GE Healthcare Life Sciences), using a Weiner filter of 0.002 and wavelength-specific optical transfer functions (OTFs) to generate super-resolution images with twofold improved resolution in all three axes. The ImageJ2 plugin "SIMcheck" (Ball *et al*, 2015) was used to analyse the quality of the reconstructed images. As the OMX system uses separate cameras for each colour, the originally produced images required careful re-alignment. To make the appropriate adjustments, reference Z-stacks of 200 nm TetraSpeck Microspheres (Invitrogen®, T7280) were aligned using custom-automated software (OMX Editor) that corrected for X, Y and Z shifts, magnification and rotation differences between channels. The resulting transformations were then applied to align the images of the test samples.

#### *Wide-field microscopy*

For wide-field imaging, living SCs were imaged using a DeltaVision Elite wide-field fluorescence deconvolution microscope (GE Healthcare Life Sciences) equipped with both a 100×, NA 1.4 UPlanSApo oil objective (Olympus) and a 60×, NA 1.42

© 2020 The Authors

UPlanSApo oil objective (Olympus), as well as a CoolSNAP HQ2 CCD camera (Photometrics®) and a seven-colour illumination system (SPECTRA light engine®, Lumencor). A 1.6× auxiliary magnification lens and objective immersion oil with RI 1.514 (Cargille Labs) were used throughout. The microscope room was temperature-controlled at ~ 18°C. The images acquired were typically Z-stacks spanning 8–12 μm depth with a *z*-distance of 0.2 μm. Images were subsequently deconvolved using the Resolve 3D-constrained iterative deconvolution algorithm within the softWoRx 5.5 software package (GE Healthcare Life Sciences).

#### *Electron microscopy*

To image isolated EVs, 10 μl of a purified EV suspension was incubated on a glow discharged 300 mesh copper grid coated with a carbon film for 2 min, blotted with filter paper and stained for 10 s with 2% uranyl acetate. The grid was then blotted and air-dried. Grids were imaged in a Tecnai FEI T12 transmission electron microscope (TEM) operated at 120 kV with a Gatan Oneview digital camera.

For SC studies, a high-pressure freezing (HPF) and freeze substitution method was employed. AGs from 6-day-old virgin $w^{1118}$ males were carefully dissected in ice-cold PBS under a dissection microscope. The glands were then removed from the PBS and coated in yeast paste (dry baker's yeast mixed with 10% methanol), which acts as a cryo-protectant. Four or five glands were transferred using forceps into the well of a membrane carrier (1.5 mm diameter, 100 μm deep, Leica). The carriers were then loaded into bayonet pods (Leica) and transferred using a manual loading device to the high-pressure freezer (EM PACT2, Leica). Samples were frozen immediately at 2,000 bar.

The carriers were carefully moved into pre-cooled 2-ml screw-top cryotubes containing pre-cooled freeze substitution medium (0.1% uranyl acetate and 1% osmium tetroxide in dry acetone) within the sample chamber of an automatic freeze substitution unit (EM AFS2, Leica) held at −130°C. Over the following 40 h, the samples were gradually brought up to room temperature to avoid formation of ice crystals.

Following freeze substitution, the glands were then moved using a plastic Pasteur pipette into fresh 2-ml tubes of 100% acetone. Samples were then gradually infiltrated with Agar 100 Hard resin (Agar Scientific) at room temperature over several days. Samples were first incubated with a 3:1 mix of 100% dry acetone:resin (without accelerator) for 2 h, then a 1:1 mix for 3 h, then a 1:3 mix for 2 h. The samples were left overnight in 100% resin (with accelerator from then on), which was replaced with fresh 100% resin four times over 32 h. The glands were carefully transferred to and positioned in embedding capsules, and the resin was polymerised at 60°C in an oven over 40 h. Ultrathin (90 nm) sections were taken with a Diatome diamond knife on a Leica UC7 ultramicrotome and transferred to 200 mesh copper grids, which were then post-stained for 5 min in uranyl acetate, washed 8 times in water and then stained for 5 min in lead citrate. The grids were washed seven times in water, and allowed to dry. Samples were imaged as described for EV preparations above.

#### *Drosophila* exosome secretion assay

Control virgin 6-day-old SC>CD63-GFP- or SC>Btl-GFP-expressing males and virgin CD63-GFP/Btl-GFP males also expressing an RNAi against ESCRT components *Stam*, *shrb* or *Vps28* in SCs were dissected in 4% paraformaldehyde (Sigma-Aldrich) dissolved in PBS. The glands were left in 4% paraformaldehyde for 20 min to preserve the luminal contents before being washed in PBS for 5 min. Glands were then mounted onto SuperFrost® Plus glass slides (VWR), removing excess liquid using a tissue and finally immersed in a drop of Vectashield® with DAPI (Vector Laboratories) for imaging by confocal microscopy.

Exosome secretion was measured using a modification of a previously described approach (Corrigan *et al*, 2014), in which multiple areas of luminal fluorescent puncta (exosomes or exosome aggregates) were sampled within the central third of each gland. Identical microscope settings and equipment were used throughout. At each sampling location, three different Z-planes were analysed, spaced by 5 μm for CD63-GFP, and 10 different Z-planes were analysed, spaced by 1 μm for Btl-GFP, with the first image in the Z-stack located exactly 5 μm apical to the main cell nuclei for both markers. This helped to ensure similar fluorescence levels between glands of the same genotype.

The automated analysis of exosome secretions by SCs was performed using ImageJ2 (Schindelin *et al*, 2015), distributed by Fiji. The raw data from each lumenal area were thresholded using the Kapur–Sahoo–Wong (Maximum Entropy) method (Kapur *et al*, 1985) to determine the outlines of fluorescent particles. The "Analyse Particles" function was then used to determine the total number of fluorescent puncta.

#### Analysis of ILV content in large non-acidic compartments

Living SCs from 6-day-old SC>Btl-GFP-, SC>CD63-GFP-, or SC>YFP-Rab11-expressing flies (with or without RNAi expression) were imaged using identical settings by wide-field microscopy. The total number of fluorescently labelled non-acidic compartments and the total number of these compartments that contained fluorescently labelled puncta was counted in each cell, using a full Z-stack of the epithelium. Three individual SCs were analysed from each of 13 glands.

#### SC compartment analysis

Secondary cell compartment numbers were manually analysed in ImageJ2 using the "Cell Counter" plugin. Complete Z-stacks of individual cells were scored for the number of large non-acidic compartments (LysoTracker Red®-negative) and the number of large acidic late endosomal and lysosomal (LEL) compartments (LysoTracker Red®-positive). The diameter of the largest LEL was measured manually at the Z-plane where the diameter was at its greatest using the line tool (see Corrigan *et al*, 2014; Redhai *et al*, 2016). Both fluorescently labelled and non-transgenic $w^{1118}$ flies were analysed using a combination of fluorescence and DIC microscopy on the wide-field microscope. Three individual SCs per gland from each of 10 glands were used to calculate the mean compartment number in each genotype.

#### Measurement of ILV diameter

Super-resolution 3D-SIM images of living SCs expressing CD63-GFP were used to determine the diameter of individual ILVs within non-

 © 2020 The Authors

acidic compartments. Careful manual measurements were taken of the diameters of ILVs within individual compartments using the line tool in ImageJ2. Many ILVs were smaller than the resolution limits of super-resolution 3D-SIM and were visualised as individual bright puncta (< 100 nm diameter). The three largest compartments per SC were analysed by this method, and the mean was calculated from three separate SCs in each of three glands.

#### Cell culture

HCT116, HeLa and LNCaP cells were purchased from ATCC to ensure authenticity and tested regularly for mycoplasma. Cells were grown in McCoy's 5A modified medium (Life Technologies; HCT116), DMEM (Life Technologies; HeLa) or RPMI-1640 medium (Life Technologies; LNCaP), supplemented with 10% heat-inactivated foetal calf serum (FBS), 100 U/ml penicillin–streptomycin (Life Technologies) and incubated in 5% $CO_2$ at 37°C prior to EV collection.

#### Extracellular vesicle isolation

During EV isolation, HCT116 and HeLa cells were maintained in serum-free basal medium (DMEM/F12) supplemented with 1% ITS (insulin–transferrin–selenium; #41400045 Life Technologies) (Tauro *et al*, 2013) for 24 h. LNCaP cells were cultured in RPMI-1640 supplemented with 1% ITS for 24 h. For glutamine depletion experiments, cells were grown for 24 h in DMEM/F12 medium without L-glutamine (#21331046; Life Technologies) supplemented with 1% ITS and 2.00 mM or low glutamine (0.15 mM for HCT116; 0.02 mM for HeLa and LNCaP; Life Technologies). For each cell line, a dose–response curve with different glutamine concentrations was produced, and a glutamine concentration that significantly decreased 4E-BP1 phosphorylation without strongly inhibiting S6 phosphorylation was selected. Torin 1 was added at 100 nM (HCT116) or 120 nM (LNCaP), rapamycin at 10 nM, and AZD5363 at 3 μM. Generally, about 8–9 × $10^6$ HCT116 cells, 4 × $10^6$ HeLa cells, or 12 × $10^6$ LNCaP cells were seeded per 15-cm cell culture plate (typically 10–15 plates used per condition) and allowed to settle for 16–24 h in complete medium before a 24-h EV collection. Cells were typically 80–90% confluent at the end of the collection period. The culture medium was pre-cleared by centrifuging at 500 *g* for 10 min at 4°C and 2,000 *g* for another 10 min at 4°C to remove cells, debris and large vesicles. The supernatant was filtered using 0.22-μm filters (Milex®).

For EV isolation by differential ultracentrifugation (UC), large volumes of the EV-containing filtrate were concentrated using a tangential flow filter (TFF) set-up with a 100-kDa membrane (Vivaflow 50R, Sartorius) using a 230V pump (Masterflex). The EV suspension was typically centrifuged at 100,000–108,000 *g* for 70–120 min in a Beckman 55.2 Ti or 70 Ti rotor at 4°C (Beckman Coulter). For activity assays and some experiments involving Western analysis, the EV pellet was resuspended in 25 ml PBS and the ultracentrifugation step repeated to minimise soluble protein contaminants. Finally, the EV pellet was resuspended in 70–100 μl PBS for subsequent experiments. For activity, proteinase K and most NTA assays, EVs were used within 24 h, but for other analyses, including EVs used for xenograft injections, they were stored at −80°C prior to thawing and use on the day of the injection experiment.

To isolate EVs by SEC, EV-containing filtrate from a 2,000 *g* centrifugation was concentrated using a 100-kDa TFF filter to a volume of approximately 30 ml and then further concentrated in 100 kDa Amicon filters by sequential centrifugation at 4,000 *g* for 10 min at 4°C to a final volume of 1 ml. This was injected into a size-exclusion column (column size 24 cm × 1 cm containing Sepharose 4B, 84 nm pore size) set-up in an AKTA start system (GE Healthcare Life Science) and eluted with PBS, collecting 30 × 1 ml fractions. Fractions corresponding to the initial "EV peak" (fractions two to five for HCT116 and HeLa cells and fractions two to seven for LNCaP cells, which appeared before the large protein peak) were pooled in 100-kDa Amicon tubes to a final volume of approximately 100 μl for analysis.

Initially, EV preparations for Western and functional analysis were assessed after normalisation based on the mass of protein in EV-secreting cells and on EV number, determined by NTA. To determine the mass of protein in EV-secreting cells, cells were washed in PBS twice and then lysed on ice in cold RIPA buffer supplemented with protease and phosphatase inhibitors (Sigma). Cell debris was pelleted by centrifugation at 13,000 *g* for 10 min at 4°C. Protein concentration in the supernatant was measured by bicinchoninic acid (BCA) assay (Pierce, Thermo Scientific).

To test whether EV proteins were located inside vesicles, EV samples were resuspended in Dulbecco's PBS (DPBS; Gibco®, #14040-083), then incubated with or without proteinase K at 25 μg/ml (Roche, #03115828001), and with or without 0.1% Triton X (Sigma, #T8787) or with 1.1% LDS (lithium dodecyl sulphate) at 37°C for 30 min. Proteinase K digestion was terminated using 5 mM PMSF (Cell Signaling Technology, #8553S), and the samples were subjected to Western blot analysis.

For EV immunocapture, EV samples were isolated from fifty 15-cm cell culture plates using SEC and then resuspended in 500 μl PBS supplemented with protease inhibitors (Sigma; P8340). For pull-down, 150 μl of each sample was incubated at 4°C overnight with 150 μl of magnetic beads conjugated with CD63 or CD81 antibodies (ThermoFisher; 10606D and 10616D, respectively) or with the equivalent amount of Protein G beads (ThermoFisher; 10612D), which were covalently linked with mouse control IgGs (Cell Signaling Technology; 5415S). To reduce non-specific binding, the beads were pre-washed three times with PBS containing 0.5% BSA. The captured proteins were removed from the beads by incubating with 2× Laemmli buffer at 37°C for 60 min and then at 95°C for 10 min, before analysing by Western blot.

#### Nanoparticle tracker analysis (NanoSight®)

The NS500 NanoSight® was used. Thirty-second videos were captured between three and five times per EV sample at known dilution (normalised to protein mass of secreting cells). Particle concentrations were measured within the linear range of the NS500 between about 2–10 × $10^8$ particles per ml. Particle movement was analysed by NTA software 2.3 (NanoSight Ltd.) to obtain particle size and concentration.

#### EV separation by high-resolution iodixanol-PBS density gradients

Extracellular vesicles were isolated using SEC from conditioned medium produced by fifty plates of HCT116 cells grown in either

© 2020 The Authors

glutamine-replete or glutamine-depleted conditions for 24 h and concentrated using ultrafiltration at 4,000 *g* for 8 min at 4°C with 100 kDa Amicon Ultra-15 filter units (Milex®) to a final volume of 750 µl. Iodixanol (Optiprep™, Sigma-Aldrich) density medium was prepared with PBS to generate discontinuous gradients (12–36%). A bottom loading method for EV analysis was utilised (Jeppesen *et al*, 2019), whereby EVs were mixed with the 36% iodixanol step and pipetted at the bottom of an ultracentrifuge tube, with subsequent decreasing concentrations of iodixanol carefully layered in four steps (30, 24, 18, 12%) to complete the gradient. The tubes were then ultracentrifuged at 120,000 *g* for 15 h at 4°C using a SW41 Ti swinging-bucket rotor (Beckman Coulter). Twelve 1 ml fractions were then collected from the top of the gradient and weighed to calculate each fraction density. Each fraction then underwent ultrafiltration using 100 kDa Amicon Ultra-4 filter units (4,000 *g* at 4°C for 4–10 min) to give a final volume of approximately 70 µl. The samples were analysed by Western blotting.

#### Genetic manipulation of cultured cells

For shRNA knockdown, the following conditions were used. For *Rab11a*, cells were cultured for 2 days following transfection with *Rab11a* shRNA lentivirus (GTTGTCCTTATTGGAGATTC; TRCN0000381243; Sigma) before EV collection. For *raptor*, cells were cultured for 3 days following transfection with *raptor* shRNA lentivirus (Addgene #1858; Sarbassov *et al*, 2005) before EV collection. For *Rab7a*, cells were cultured for 3 days following transfection with *Rab7* shRNA lentivirus (GGCTAGTCACAATGCA-GATAT; in pHR-U6 vector) before EV collection. For NT shRNA, the shRNA sequence was CAACAAGATGAAGAGCACCAA (SHC 202, Sigma).

Transient transfections of fusion protein constructs were carried out when the cells reached 80% confluency with the transfection reagent Lipofectamine® 2000 in serum-reduced OptiMEM® medium (Gibco®, Life Technologies), and following manufacturers' instructions to obtain maximum transfection rates. Constructs were GFP-Rab5CA (Q79L; Addgene #35140) and GFP-Rab11 WT (Addgene #12674).

#### Western analysis

Both cell lysates and EV preparations were electrophoretically separated using 10% mini-PROTEAN® precast gels (Bio-Rad). We loaded gels for Western analysis with EV lysates extracted from the same protein mass of secreting cells, so that changes in band intensity on the blots with glutamine depletion reflected a net change in secretion of the marker on a per cell basis. Glutamine depletion did not significantly affect EV number. Furthermore, the normalisation method for analysing EV proteins on Western blots did not affect the overall conclusions from our analysis (Figs 4B and EV4E, Appendix Fig S5). However, after some drug and knockdown treatments, EV production was reduced by up to 50% (Fig EV4E). We continued to load EV protein gels for Westerns based on EV-secreting cell protein mass to ensure that any changes in protein levels did not result from testing EVs produced by different numbers of cells.

Extracellular vesicle preparations were lysed in RIPA or 1× sample buffer. Protein preparations were ultimately dissolved in either reducing (containing 5% β-mercaptoethanol) or non-reducing (for CD63 and CD81 detection) sample buffer and were heated to 90–100°C for 10 min before loading with a pre-stained protein ladder (Bio-Rad). Proteins were wet-transferred to polyvinylidene difluoride (PVDF) membranes at 100 V for 1 h using a Mini Trans-Blot Cell (Bio-Rad). The membranes were then blocked with either 5% milk (optimal for CD63 detection) or 5% BSA in TBS buffer with Tween-20 (TBST) for 30 min and probed overnight at 4°C with primary antibody diluted in blocking buffer. After 3 × 10 min washing steps with TBST, the membranes were probed with the relevant secondary antibodies for 1 h at 22°C. Following 3 × 10 min wash steps, the signals were detected using the enhanced chemiluminescent detection reagent (Clarity®, Bio-Rad) and the Touch Imaging System (Bio-Rad). Relative band intensities were quantified by ChemiDoc® software (Bio-Rad) or ImageJ. Signals were normalised to tubulin (cell lysates), or cell lysate protein or CD81 (HCT116, HeLa and LNCaP EVs). Note, as shown in Figs 4B and EV3E, that if EV protein signals are normalised to cell lysate levels, EV particle number, CD81, Syn-1 or Tsg101, relative levels of Rab11a (and Cav-1) are generally increased after glutamine depletion or partial blockade of mTORC1 signalling, while CD63 is typically reduced.

Antibody suppliers, catalogue numbers and concentrations used were as follows: rabbit anti-4E-BP1 (Cell Signaling Technology #9644, 1:1,000), rabbit anti-p-4E-BP1-Ser65 (Cell Signaling Technology #9456, 1:1,000), rabbit anti-S6 (Cell Signaling Technology #2217, 1:4,000), rabbit anti-p-S6-Ser240/244 S6 (Cell Signaling Technology #5364, 1:4,000), rabbit anti-Raptor (Cell Signaling Technology #2280, 1:1,000), rabbit anti-caveolin-1 (Cell Signaling Technology #3238, 1:500), goat anti-AREG (R&D Systems #AF262, 1:200), mouse anti-Tubulin (Sigma #T8328, 1:4,000), rabbit anti-GAPDH (Cell Signaling Technology #2118, 1:2,000), mouse anti-CD81 (Santa Cruz #23962, 1:500), mouse anti-CD63 (BD Biosciences # 556019, 1:500), rabbit anti-Syntenin-1 antibody (Abcam ab133267, 1:500), rabbit anti-Tsg101 (Abcam ab125011, 1:500), mouse anti-Rab11 (BD Biosciences #610657, 1:500), rabbit anti-Rab11a (Cell Signaling Technology; 2413S, 1:500), rabbit anti-Rab11b (Cell Signaling Technology; 2414S, 1:500), rabbit anti-p44/42 MAPK (ERK; Cell Signaling Technology #4695, 1:1,000), rabbit anti-p-p44/42 MAPK (Cell Signaling Technology #4370, 1:1,000), rabbit anti-PRAS40 (Cell Signaling Technology #2691, 1:1,000), rabbit anti-p-PRAS40-Thr246 (Cell Signaling Technology #2997, 1:1,000), rabbit anti-Rab7 (Cell Signaling Technology #9367, 1:1,000), rabbit anti-calnexin (Abcam #ab213243, 1:1,000), sheep anti-TGN46 (Bio-Rad; AHP500G, 1:1,000), rabbit anti-Annexin A1 (Cell Signaling Technology; 32934, 1:500), anti-mouse IgG (H+L) HRP conjugate (Promega #W4021, 1:10,000), anti-rabbit IgG (H+L) HRP conjugate (Promega #W4011, 1:10,000), anti-goat IgG (H+L) HRP conjugate (R&D Systems #HAF109, 1:100).

#### Measurement of AREG concentration by ELISA

Extracellular vesicle samples were lysed in Cell Lysis Buffer 2 (R&D SYSTEMS; 895347) supplemented with protease inhibitors (Sigma; P8340) at room temperature for 30 min. The amount of AREG protein in the EV samples was measured using Quantikine ELISA—Human amphiregulin Immunoassay (R&D SYSTEMS; DAR00) according to the manufacturer's instructions.


© 2020 The Authors

### Immmunostaining of cultured human cells

For immunofluorescence studies, cultured cells on coverslips were fixed in 4% paraformaldehyde for 15 min at ~ 23°C, washed 3 × 10 min in PBS, and permeabilised with 0.05% Triton X-100/PBS for 30 s. After three PBS washes, cells were incubated with the primary antibody prepared in 5% donkey serum/PBS in a humid chamber at 4°C overnight. The coverslips were washed 4 × 10 min in PBS and then incubated with the appropriate secondary antibodies diluted in 5% donkey serum/PBS for 1 h at ~ 23°C. Following 4 × 10 min PBS washes, the coverslip was mounted on a glass slide with DAPI-containing mounting medium (VectorShield; Vector Laboratories) and sealed with nail polish. Antibody concentrations were as follows: mouse anti-Rab11 (detects both isoforms; BD Biosciences #610657, 1:50), mouse anti-CD63 (BD Biosciences #556019, 1:100), rabbit anti-Rab7 (Cell Signaling Technology #9367, 1:50), mouse anti-CD81 (Santa Cruz; SC-23962, 1:100), rabbit anti-Rab11a (Cell Signaling Technology; 2413S, 1:50), rabbit anti-Lamp1 (Cell Signaling Technology; 9091S, 1:100); mouse anti-Lamp2 (Abcam; ab25631, 1:100), GFP-Booster ATTO 488 (Chromotek gba488-100, 1:500), donkey anti-rabbit IgG (H+L) (DyLight® 550; Abcam ab96892, 1:500), donkey anti-mouse IgG (H+L) (Alexa Fluor® 488 AffiniPure; Jackson ImmunoResearch #715-545-151, 1:500).

Cell viability was measured by Trypan Blue staining. HCT116 cells were trypsinised and then resuspended in McCoy's 5A medium (Gibco®, #26600080). The cell suspension was mixed with Trypan blue solution (Sigma, #T8154) at 1:1 ratio and the number of blue staining (non-viable) cells and total cell number were assessed using a haemocytometer.

### Growth, proliferation, apoptosis and neutralising antibody assays

For growth assays, $2 \times 10^3$ HCT116 cells per well were seeded in a 96-well plate in 100 µl of medium, following pre-treatment with freshly prepared EVs for 30 min in PBS at 37°C (up to $10^4$ EVs [isolated by UC or SEC] per cell for controls, which is roughly the number of EVs secreted by each HCT116 cell in 24 h). The cells were maintained in McCoy's 5A medium in reduced serum (1% FBS) conditions. Growth was followed over a period of 5 days by live image acquisition using the IncuCyte ZOOM® analysis system (10× magnification; Essen Bioscience) to automatically detect cell edges and to generate a confluence mask for cell coverage area calculation, which was normalised to confluence at zero time (giving fold change in confluency). Each biological replicate is represented as mean of at least eight technical replicates.

For ERK inhibition experiments, SCH772984 (S7101; Selleck-Chem) was added to the cell suspension along with the exosomes to a final concentration of 1 µM. The medium was changed 24 h after cell plating.

To assess cell proliferation, cells were fixed with methanol and stained with DAPI. The number of nuclei/field for three fields per well was counted manually from fluorescence microscope images. To measure levels of apoptosis, caspase-3 and caspase-7 activities were assayed using 1 µM of Cell Player® caspase-3/7 reagent (Essen Bioscience), monitored with the IncuCyte ZOOM® system.

AREG-neutralising antibody experiments were performed in a 96-well plate using $2 \times 10^3$ HCT116 cells per well treated with 4,000 SEC-isolated EVs per recipient cell, using goat anti-AREG (R&D Systems #AF262, 1:200), and goat IgG (R&D Systems, AB-108-C) as a control antibody treatment. Prior to mixing with recipient cells, EVs were pre-incubated with 4 µg/ml anti-AREG or control antibody in McCoy's 5A medium with 1% FBS for 2 h at 37°C. The mixture was then added to the recipient cells (also in reduced serum media) and allowed to incubate for a further 30 min before plating. Growth was monitored using the IncuCyte ZOOM® analysis system in the same fashion as standard growth assays described above.

All assays were repeated on at least three independent occasions.

### Tubulation assay with HUVEC cells

Human umbilical vein endothelial cells were suspended in LONZA medium (endothelial basal medium-2—EBM2) containing freshly prepared exosomes ($10^4$ UC-isolated EVs per cell). After 10-min incubation, $6 \times 10^3$ cells were seeded onto a solidified thin layer of BD phenol red-free Matrigel (BD Bioscience) in a 96-well plate and incubated at 37°C. Images of vessel growth were captured at 3-h intervals for 18 h by live image acquisition using the IncuCyte ZOOM® microscope (10× lens). Quantification of tubule length was performed using ImageJ. Each biological replicate is represented as mean of at least eight technical replicates.

### Assessment of EV-induced ERK activation

To assess ERK activation upon EV treatment, HCT116 cells were plated in six-well plates. After 24 h, the cells were serum-starved for an additional 18 h. At this point, freshly prepared exosomes ($10^4$ UC-isolated EVs per cell) were added and the mixture incubated for 1 h at room temperature. Cell lysates were generated and analysed by Western blot.

### Cellular uptake assays

For confocal analysis of Tfn uptake, $5 \times 10^4$ HCT116 cells were plated on a coverslip in McCoy's 5A medium supplemented with 10% FBS and cultured overnight, followed by a 24-h incubation in DMEM/F-12, 1% ITS, with 2.00 mM or 0.15 mM glutamine at 37°C. The cells were then washed using cold PBS and cultured in DMEM/F-12, 1% ITS, containing transferrin-Alexa Fluor® 488 (ThermoFisher Scientific #T13342, 1:200) with the appropriate glutamine concentration at 4°C for 30 min, followed by a 30-min incubation at 37°C. The cells were fixed for confocal imaging. For the anti-CD63 antibody uptake experiments, cells washed with cold PBS were cultured in DMEM/F-12, 1% ITS, containing mouse anti-CD63 antibodies (BD Biosciences # 556019, 1:50) and the appropriate glutamine concentration at 4°C for 30 min. The cells were then washed with PBS, prior to 30-min incubation at 37°C and a subsequent 30-min chase in DMEM/F-12, 1% ITS with the appropriate glutamine concentration. The cells were fixed, incubated with secondary antibody for the anti-CD63 uptake experiments and then imaged by confocal microscopy.

For Western analysis, $2 \times 10^5$ HCT116 cells were plated in each well of a six-well plate in serum-supplemented McCoy's 5A medium. After 20 h, the culture medium was replaced by DMEM/F-12, 1% ITS containing 2.00 mM or 0.15 mM glutamine. After 24 h, the cells were shifted to 4°C for 10 min to stop intracellular vesicular trafficking and then incubated in DMEM/F-12, 1% ITS, containing

© 2020 The Authors

mouse anti-CD63 antibodies (1:50) and 50 μg/ml transferrin-biotin (Sigma #T3915) with appropriate glutamine concentration (2.00 or 0.15 mM) at 4°C for 30 min. After washing with cold PBS, the cells were incubated in DMEM/F-12, 1% ITS, with appropriate glutamine concentration at 37°C for 15 min and then lysed using RIPA buffer.

#### Generation and histological analysis of HCT116 tumours in xenograft mouse models

All procedures were carried out in accordance with Home Office licence 30/3197. HCT116 xenografts were established by subcutaneous injection of $2.5 \times 10^6$ cells into the flank of seven female CD1 nude mice (aged 5–6 weeks; Charles River) per group. When tumours had grown to an average group tumour volume of 100 $mm^3$, then mice were treated with four intratumoral injections ($1 \times 10^8$ EVs/100 μl exosome suspension in PBS or PBS vehicle) at 3-day intervals in a semi-blind study, as previously described (Sheldon *et al*, 2010). Tumour growth was measured three times a week using callipers and volume calculated using the formula 1/6 π × length × width × height. Twenty-four hours after the last injection, tumours were excised and half of the tumour fixed in 4% formalin overnight at 4°C before being processed and embedded in paraffin wax and sectioned for histological evaluation.

A standard haematoxylin and eosin protocol was followed to assess the morphology and the amount of necrosis in xenografts. For immunohistochemistry staining, slides were dewaxed and antigen retrieval performed at pH 6. Slides were stained using the FLEX staining kit (Agilent). Endogenous peroxidase activity was blocked before slides were stained with antibodies diluted 1:100, namely rabbit anti-Ki67 (M7240; Dako, Glostrup, Denmark), rabbit anti-CA9 (M75; BD Biosciences), and mouse anti-CD31 (JC70, Dako) for 1 h at 22°C. Slides were incubated with the appropriate anti-rabbit/anti-mouse HRP-coupled secondary antibody (Dako) for 30 min at room temperature and washed in Flex buffer and 3,3′-diaminobenzidine (Flex-DAB; Dako) was applied to the sections for 10 min. The slides were counterstained by immersing in Flex-haematoxylin solution (Dako) for 5 min, washed and air-dried before mounting with mounting medium (Sigma). Secondary-only control staining was done routinely, but was consistently negative.

Expression of CA9 and Ki67, as well as vessel number and size, and viable/necrotic areas were quantified on whole sections using the Visiopharm Integrator System. The HDAB-DAB colour deconvolution band was used to detect positively stained cells. Threshold classification was employed to identify necrotic and living regions and then identify number of positive-staining cells within the latter regions. Threshold levels were checked against control xenograft staining before being set and the xenografts from all groups were then analysed in the same way. Vessel number and size were determined as part of a post-processing step, where areas surrounded by CD31-positive endothelial cells were automatically filled in and the areas generated were counted and quantified.

#### Statistical analysis

Before parametric tests were employed, the Shapiro–Wilk test was used to confirm normality of the datasets. For larger datasets, Levene's test was used to evaluate equality of variances. For Western blots, relative signal intensities were analysed using the Kruskal–Wallis test. For the growth and tubulation assays, data were analysed by two-way ANOVA. For SC analysis, a one-way ANOVA test was employed for normally distributed data, with *post hoc* Dunnett's two-tailed *t*-tests used to directly compare individual control and experimental datasets. Non-parametric data were analysed using a Kruskal–Wallis test. We employed power calculations based on previous experiments to ensure the appropriate numbers of animals were used. In order to provide a statistical power of at least 80% to detect a twofold difference in the mean tumour volume between groups, with tumour volume variation of up to 50% within groups, and a statistical difference level of $\alpha = 0.05$, a sample size of seven mice per group is required.

**Expanded View** for this article is available online.


### Acknowledgements

We thank C. P. Alves for his contributions to the work presented. We are grateful to I. Dobbie and to A. Pielach for technical expertise and support with microscopy, which was undertaken in the Wellcome Trust-funded MICRON Oxford Advanced Bioimaging Unit and Dunn School EM Facility. We thank S. Eaton, S. Goodwin, E. Prince and F. Karch, as well as the Bloomington, Vienna and Kyoto Stock Centres for *Drosophila* stocks; J. Whitburn for cells; and the Developmental Studies Hybridoma Bank (Iowa) for antibodies. We are particularly grateful to K. E. Carr for comments on the manuscript. We acknowledge the support of Cancer Research UK (C19591/A19076, C602/A18974), the Cancer Research UK Oxford Centre Development Fund (C38302/A12278), the BBSRC (BB/K017462/1, BB/L007096/1, BB/N016300/1, BB/R004862/1), the Breast Cancer Research Foundation (ANR 00162), the Wellcome Trust (Strategic Awards #091911, #107457 and 102347/Z/13/Z), the National Institute for Health Research (NIHR) Oxford Biomedical Research Centre (BRC) and the John Fell Fund, Oxford (141/063).


### Author contributions

Experimental design conceptualisation, S-JF, BK, PPM, EMB, JDM, KM, CEZ, HS, NKA, EJ, ME, MIS, CCM, SMW, CC, FCH, JFM, ALH, CW, DCIG; experimental work, S-JF, BK, PPM, EMB, JDM, KM, CEZ, EJ, JFM; data analysis, S-JF, BK, PPM, EMB, JDM, KM, CEZ, HS, NKA, EJ, ME, MIS, JFM; writing and editing manuscript, CW, DCIG; reviewing and editing manuscript, S-JF, BK, PPM, EMB, JDM, KM, CEZ, HS, NKA, EJ, ME, MIS, CCM, SMW, CC, FCH, JFM, ALH; and funding acquisition, ALH, CW, DCIG.

### Conflict of interest

The authors declare that they have no conflict of interest.

## References


Ahmed D, Eide PW, Eilertsen IA, Danielsen SA, Eknæs M, Hektoen M, Lind GE, Lothe RA (2013) Epigenetic and genetic features of 24 colon cancer cell lines. *Oncogenesis* 2: e71

Baietti MF, Zhang Z, Mortier E, Melchior A, Degeest G, Geeraerts A, Ivarsson Y, Depoortere F, Coomans C, Vermeiren E *et al* (2012) Syndecan-syntenin-ALIX regulates the biogenesis of exosomes. *Nat Cell Biol* 14: 677–685

Ball G, Demmerle J, Kaufmann R, Davis I, Dobbie I, Schermelleh L (2015) SIMcheck: a toolbox for successful super-resolution structured illumination microscopy. *Sci Rep* 5: 15915

Barile L, Vassalli G (2017) Exosomes: therapy delivery tools and biomarkers of diseases. *Pharmacol Ther* 174: 63–78



© 2020 The Authors

Becker A, Thakur BK, Weiss JM, Kim HS, Peinado H, Lyden D (2016) Extracellular vesicles in cancer: cell-to-cell mediators of metastasis. *Cancer Cell* 30: 836 – 848

Beckett K, Monier S, Palmer L, Alexandre C, Green H, Bonneil E, Raposo G, Thibault P, Le Borgne R, Vincent JP (2013) *Drosophila* S2 cells secrete wingless on exosome-like vesicles but the wingless gradient forms independently of exosomes. *Traffic* 14: 82 – 96

Bourseau-Guilmain E, Menard JA, Lindqvist E, Indira Chandran V, Christianson HC, Cerezo Magaña M, Lidfeldt J, Marko-Varga G, Welinder C, Belting M (2016) Hypoxia regulates global membrane protein endocytosis through caveolin-1 in cancer cells. *Nat Commun* 7: 11371

Brand AH, Perrimon N (1993) Targeted gene expression as a means of altering cell fates and generating dominant phenotypes. *Development* 118: 401 – 415

Brown CL, Meise KS, Plowman GD, Coffey RJ, Dempsey PJ (1998) Cell surface ectodomain cleavage of human amphiregulin precursor is sensitive to a metalloprotease inhibitor. Release of a predominant N-glycosylated 43-kDa soluble form. *J Biol Chem* 273: 17258 – 17268

Bruno S, Deregibus MC, Camussi G (2015) The secretome of mesenchymal stromal cells: role of extracellular vesicles in immunomodulation. *Immunol Lett* 168: 154 – 158

Colombo M, Moita C, van Niel G, Kowal J, Vigneron J, Benaroch P, Manel N, Moita LF, Théry C, Raposo G (2013) Analysis of ESCRT functions in exosome biogenesis, composition and secretion highlights the heterogeneity of extracellular vesicles. *J Cell Sci* 126: 5553 – 5565

Corrigan L, Redhai S, Leiblich A, Fan S-J, Perera SM, Patel R, Gandy C, Wainwright SM, Morris JF, Hamdy F *et al* (2014) BMP-regulated exosomes from *Drosophila* male reproductive glands reprogram female behavior. *J Cell Biol* 206: 671 – 688

Crewe C, Joffin N, Rutkowski JM, Kim M, Zhang F, Towler DA, Gordillo R, Scherer PE (2018) An endothelial-to-adipocyte extracellular vesicle axis governed by metabolic state. *Cell* 175: 695 – 708

Demory Beckler M, Higginbotham JN, Franklin JL, Ham AJ, Halvey PJ, Imasuen IE, Whitwell C, Li M, Liebler DC, Coffey RJ (2013) Proteomic analysis of exosomes from mutant KRAS colon cancer cells identifies intercellular transfer of mutant KRAS. *Mol Cell Proteomics* 12: 343 – 355

Dibble CC, Cantley LC (2015) Regulation of mTORC1 by PI3K signaling. *Trends Cell Biol* 25: 545 – 555

Dietzl G, Chen D, Schnorrer F, Su KC, Barinova Y, Fellner M, Gasser B, Kinsey K, Oppel S, Scheiblauer S *et al* (2007) A genome-wide transgenic RNAi library for conditional gene inactivation in *Drosophila*. *Nature* 448: 151 – 156

Dragovic RA, Gardiner C, Brooks AS, Tannetta DS, Ferguson DJ, Hole P, Carr B, Redman CW, Harris AL, Dobson PJ *et al* (2011) Sizing and phenotyping of cellular vesicles using nanoparticle tracking analysis. *Nanomedicine* 7: 780 – 788

Dunst S, Kazimiers T, von Zadow F, Jambor H, Sagner A, Brankatschk B, Mahmoud A, Spannl S, Tomancak P, Eaton S *et al* (2015) Endogenously tagged rab proteins: a resource to study membrane trafficking in *Drosophila*. *Dev Cell* 33: 3513 – 3565

Fan S-J, Snell C, Turley H, Li J-L, McCormick R, Perera SMW, Heublein S, Kazi S, Azad A, Wilson C *et al* (2016) PAT4 levels control amino-acid sensitivity of rapamycin-resistant mTORC1 from the Golgi and affect clinical outcome in colorectal cancer. *Oncogene* 35: 3004 – 3015

Farkas R, Beňová-Liszeková D, Mentelová L, Mahmood S, Ďatková Z, Beňo M, Pečeňová L, Raška O, Šmigová J, Chase BA *et al* (2015) Vacuole dynamics in the salivary glands of *Drosophila melanogaster* during prepupal development. *Dev Growth Differ* 57: 74 – 96

Goberdhan DCI, Wilson C, Harris AL (2016) Amino acid sensing by mTORC1: intracellular transporters mark the spot. *Cell Metab* 23: 580 – 589

Hayashi S, Ito K, Sado Y, Taniguchi M, Akimoto A, Takeuchi H, Aigaki T, Matsuzaki F, Nakagoshi H, Tanimura T *et al* (2002) GETDB, a database compiling expression patterns and molecular locations of a collection of Gal4 enhancer traps. *Genesis* 34: 58 – 61

Higginbotham JN, Demory Beckler M, Gephart JD, Franklin JL, Bogatcheva G, Kremers GJ, Piston DW, Ayers GD, McConnell RE, Tyska MJ *et al* (2011) Amphiregulin exosomes increase cancer cell invasion. *Curr Biol* 21: 779 – 786

Hsu C, Morohashi Y, Yoshimura S, Manrique-Hoyos N, Jung S, Lauterbach MA, Bakhti M, Grønborg M, Möbius W, Rhee J *et al* (2010) Regulation of exosome secretion by Rab35 and its GTPase-activating proteins TBC1D10A-C. *J Cell Biol* 189: 223 – 232

Huang-Doran I, Zhang CY, Vidal-Puig A (2017) Extracellular vesicles: novel mediators of cell communication in metabolic disease. *Trends Endocrinol Metab* 28: 3 – 18

Jeppesen DK, Fenix AM, Franklin JL, Higginbotham JN, Zhang Q, Zimmerman LJ, Liebler DC, Ping J, Liu Q, Evans R *et al* (2019) Reassessment of exosome composition. *Cell* 177: 428 – 445

Jiang P, Du W, Mancuso A, Wellen KE, Yang X (2013) Reciprocal regulation of p53 and malic enzymes modulates metabolism and senescence. *Nature* 493: 689 – 693

Kapur JN, Sahoo PK, Wong ACK (1985) A new method for gray-level picture thresholding using the entropy of the histogram. *Comput Vis Graph Image Process* 29: 273 – 285

Keerthikumar S, Chisanga D, Ariyaratne D, Al Saffar H, Anand S, Zhao K, Samuel M, Pathan M, Jois M, Chilamkurti N *et al* (2016) ExoCarta: a web-based compendium of exosomal cargo. *J Mol Biol* 428: 688 – 692

Kessler D, Gmachl M, Mantoulidis A, Martin LJ, Zoephel A, Mayer M, Gollner A, Covini D, Fischer S, Gerstberger T *et al* (2019) Drugging an undruggable pocket on KRAS. *Proc Natl Acad Sci USA* 116: 15823 – 15829

Koles K, Nunnari J, Korkut C, Barria R, Brewer C, Li Y, Leszyk J, Zhang B, Budnik V (2012) Mechanism of evenness interrupted (Evi)-exosome release at synaptic boutons. *J Biol Chem* 287: 16820 – 16834

Kowal J, Arras G, Colombo M, Jouve M, Morath JP, Primdal-Bengtson B, Dingli F, Loew D, Tkach M, Théry C (2016) Proteomic comparison defines novel markers to characterize heterogeneous populations of extracellular vesicle subtypes. *Proc Natl Acad Sci USA* 113: E968 – E977

Krämer-Albers EM, Hill AF (2016) Extracellular vesicles: interneural shuttles of complex messages. *Curr Opin Neurobiol* 39: 101 – 107

Kucharzewska P, Christianson HC, Welch JE, Svensson KJ, Fredlund E, Ringnér M, Mörgelin M, Bourseau-Guilmain E, Bengzon J, Belting M (2013) Exosomes reflect the hypoxic status of glioma cells and mediate hypoxia-dependent activation of vascular cells during tumor development. *Proc Natl Acad Sci USA* 110: 7312 – 7317

Leiblich A, Marsden L, Gandy C, Corrigan L, Jenkins R, Hamdy F, Wilson C (2012) Bone morphogenetic protein- and mating-dependent secretory cell growth and migration in the Drosophila accessory gland. *Proc Natl Acad Sci USA* 109: 19292 – 19297

Lukey MJ, Katt WP, Cerione RA (2018) Targeting therapy resistance: when glutamine catabolism becomes essential. *Cancer Cell* 33: 795 – 797

Maas SL, Breakefield XO, Weaver AM (2017) Extracellular vesicles: unique intercellular delivery vehicles. *Trends Cell Biol* 27: 172 – 188

Mateescu B, Kowal EJ, van Balkom BW, Bartel S, Bhattacharyya SN, Buzás EI, Buck AH, de Candia P, Chow FW, Das S *et al* (2017) Obstacles and opportunities in the functional analysis of extracellular vesicle RNA - an ISEV position paper. *J Extracell Vesicles* 6: 1286095

© 2020 The Authors

Matusek T, Wendler F, Polès S, Pizette S, D'Angelo G, Fürthauer M, Thérond PP (2014) The ESCRT machinery regulates the secretion and long-range activity of Hedgehog. *Nature* 516: 99 – 103

Mayle KM, Le AM, Kamei DT (2012) The intracellular trafficking pathway of transferrin. *Biochim Biophys Acta* 1820: 264 – 281

McCullough J, Colf LA, Sundquist W (2013) Membrane fission reactions of the mammalian ESCRT pathway. *Annu Rev Biochem* 82: 663 – 692

McIntyre A, Hulikova A, Ledaki I, Snell C, Singleton D, Steers G, Seden P, Jones D, Bridges E, Wigfield S *et al* (2016) Disrupting hypoxia-induced bicarbonate transport acidifies tumor cells and suppresses tumor growth. *Cancer Res* 76: 3744 – 3755

Messenger SW, Woo SS, Sun Z, Martin TFJ (2018) A $Ca^{2+}$-stimulated exosome release pathway in cancer cells is regulated by Munc13-4. *J Cell Biol* 217: 2877 – 2890

Nagathihall N, Beesetty Y, Lee W, Washington MK, Chen X, Lockhart AC, Merchant NB (2014) Novel mechanistic insights into ectodomain shedding of EGFR Ligands Amphiregulin and TGF-α: impact on gastrointestinal cancers driven by secondary bile acids. *Cancer Res* 74: 2062 – 2072

Ni JQ, Zhou R, Czech B, Liu LP, Holderbaum L, Yang-Zhou D, Shim HS, Tao R, Handler D, Karpowicz P *et al* (2011) A genome-scale shRNA resource for transgenic RNAi in *Drosophila*. *Nat Methods* 8: 405 – 407

van Niel G, D'Angelo G, Raposo G (2018) Shedding light on the cell biology of extracellular vesicles. *Nat Rev Mol Cell Biol* 19: 213 – 228

Ostrowski M, Carmo NB, Krumeich S, Fanget I, Raposo G, Savina A, Moita CF, Schauer K, Hume AN, Freitas RP *et al* (2010) Rab27a and Rab27b control different steps of the exosome secretion pathway. *Nat Cell Biol* 12: 19 – 30

Panáková D, Sprong H, Marois E, Thiele C, Eaton S (2005) Lipoprotein particles are required for hedgehog and wingless signalling. *Nature* 435: 58 – 65

Parton RM, Vallés AM, Dobbie IM, Davis JJ (2010) Live cell imaging in *Drosophila melanogaster*. *Cold Spring Harb Protoc* 2010: pdb.top75

Prince E, Kroeger B, Gligorov D, Wilson C, Eaton S, Karch F, Brankatschk M, Maeda R (2019) Rab-mediated trafficking in the secondary cells of *Drosophila* male accessory glands and its role in fecundity. *Traffic* 20: 137 – 151

Raimondo S, Saieva L, Vicario E, Pucci M, Toscani D, Manno M, Raccosta S, Giuliani N, Alessandro R (2019) Multiple myeloma-derived exosomes are enriched of amphiregulin (AREG) and activate the epidermal growth factor pathway in the bone microenvironment leading to osteoclastogenesis. *J Hematol Oncol* 12: 2

Redhai S, Hellberg JE, Wainwright M, Perera SW, Castellanos F, Kroeger B, Gandy C, Leiblich A, Corrigan L, Hilton T *et al* (2016) Regulation of dense-core granule replenishment by autocrine BMP signalling in *Drosophila* secondary cells. *PLoS Genet* 12: e1006366

Rideout EJ, Dornan AJ, Neville MC, Eadie S, Goodwin SF (2010) Control of sexual differentiation and behavior by the doublesex gene in *Drosophila melanogaster*. *Nat Neurosci* 13: 458 – 466

Romero R, Sayin VI, Davidson SM, Bauer MR, Singh SX, LeBoeuf SE, Karakousi TR, Ellis DC, Bhutkar A, Sánchez-Rivera FJ *et al* (2017) Keap1 loss promotes Kras-driven lung cancer and results in dependence on glutaminolysis. *Nat Med* 23: 1362 – 1368

Sarbassov DD, Guertin DA, Ali SM, Sabatini DM (2005) Phosphorylation and regulation of Akt/PKB by the rictor-mTOR complex. *Science* 307: 1098 – 1101

Sato M, Kornberg TB (2002) FGF is an essential mitogen and chemoattractant for the air sacs of the *Drosophila* tracheal system. *Dev Cell* 3: 195 – 207

Savina A, Vidal M, Colombo MI (2002) The exosome pathway in K562 cells is regulated by Rab11. *J Cell Sci* 115: 2505 – 2515

Savina A, Fader CM, Damiani MT, Colombo MI (2005) Rab11 promotes docking and fusion of multivesicular bodies in a calcium-dependent manner. *Traffic* 6: 131 – 143

Schindelin J, Rueden CT, Hiner MC, Eliceiri KW (2015) The ImageJ ecosystem: an open platform for biomedical image analysis. *Mol Reprod Dev* 82: 518 – 529

Shah R, Patel T, Freedman JE (2018) Circulating extracellular vesicles in human disease. *N Engl J Med* 379: 958 – 966

Sheldon H, Heikamp E, Turley H, Dragovic R, Thomas P, Oon CE, Leek R, Edelmann M, Kessler B, Sainson RC *et al* (2010) New mechanism for Notch signaling to endothelium at a distance by Delta-like 4 incorporation into exosomes. *Blood* 116: 2385 – 2394

Sugawara K, Shibasaki T, Mizoguchi A, Saito T, Seino S (2009) Rab11 and its effector Rip11 participate in regulation of insulin granule exocytosis. *Genes Cells* 14: 445 – 456

Sweeney NT, Brenman JE, Jan YN, Gao FB (2006) The coiled-coil protein shrub controls neuronal morphogenesis in *Drosophila*. *Curr Biol* 16: 1006 – 1011

Tardito S, Oudin A, Ahmed SU, Fack F, Keunen O, Zheng L, Miletic H, Sakariassen PØ, Weinstock A, Wagner A *et al* (2015) Glutamine synthetase activity fuels nucleotide biosynthesis and supports growth of glutamine-restricted glioblastoma. *Nat Cell Biol* 17: 1556 – 1568

Tauro BJ, Greening DW, Mathias RA, Mathivanan S, Ji H, Simpson RJ (2013) Two distinct populations of exosomes are released from LIM1863 colon carcinoma cell-derived organoids. *Mol Cell Proteomics* 12: 587 – 598

Théry C, Witwer KW, Aikawa E, Alcaraz MJ, Anderson JD, Andriantsitohaina R, Antoniou A, Arab T, Archer F, Atkin-Smith GK *et al* (2018) Minimal information for studies of extracellular vesicles 2018 (MISEV2018): a position statement of the International Society for Extracellular Vesicles and update of the MISEV2014 guidelines. *J Extracell Vesicles* 7: 1535750

Thomou T, Mori MA, Dreyfuss JM, Konishi M, Sakaguchi M, Wolfrum C, Rao TN, Winnay JN, Garcia-Martin R, Grinspoon SK *et al* (2017) Adipose-derived circulating miRNAs regulate gene expression in other tissues. *Nature* 542: 450 – 455

Thoreen CC, Kang SA, Chang JW, Liu Q, Zhang J, Gao Y, Reichling LJ, Sim T, Sabatini DM, Gray NS (2009) An ATP-competitive mammalian target of rapamycin inhibitor reveals rapamycin-resistant functions of mTORC1. *J Biol Chem* 284: 8023 – 8032

Tkach M, Théry C (2016) Communication by extracellular vesicles: where we are and where we need to go. *Cell* 164: 1226 – 1232

Trajkovic K, Hsu C, Chiantia S, Rajendran L, Wenzel D, Wieland F, Schwille P, Brügger B, Simons M (2008) Ceramide triggers budding of exosome vesicles into multivesicular endosomes. *Science* 319: 1244 – 1247

Veerman RE, Güçlüler Akpinar G, Eldh M, Gabrielsson S (2019) Immune cell-derived extracellular vesicles - functions and therapeutic applications. *Trends Mol Med* 25: 382 – 394

Welz T, Wellbourne-Wood J, Kerkhoff E (2014) Orchestration of cell surface proteins by Rab11. *Trends Cell Biol* 24: 407 – 415

Wendler F, Favicchio R, Simon T, Alifrangis C, Stebbing J, Giamas G (2017) Extracellular vesicles swarm the cancer microenvironment: from tumor-stroma communication to drug intervention. *Oncogene* 36: 877 – 884

Wilson C, Leiblich A, Goberdhan DC, Hamdy F (2017) The *Drosophila* accessory gland as a model for prostate cancer and other pathologies. *Curr Top Dev Biol* 121: 339 – 375

Zhang J, Schulze KL, Hiesinger PR, Suyama K, Wang S, Fish M, Acar M, Hoskins RA, Bellen HJ, Scott MP (2007) Thirty-one flavors of *Drosophila* Rab proteins. *Genetics* 176: 1307 – 1322

 © 2020 The Authors

Zhang J, Pavlova NN, Thompson CB (2017) Cancer cell metabolism: the essential role of the nonessential amino acid, glutamine. *EMBO J* 36: 1302 – 1315

Zhang H, Freitas D, Kim HS, Fabijanic K, Li Z, Chen H, Mark MT, Molina H, Martin AB, Bojmar L *et al* (2018) Identification of distinct nanoparticles and subsets of extracellular vesicles by asymmetric flow field-flow fractionation. *Nat Cell Biol* 20: 332 – 343

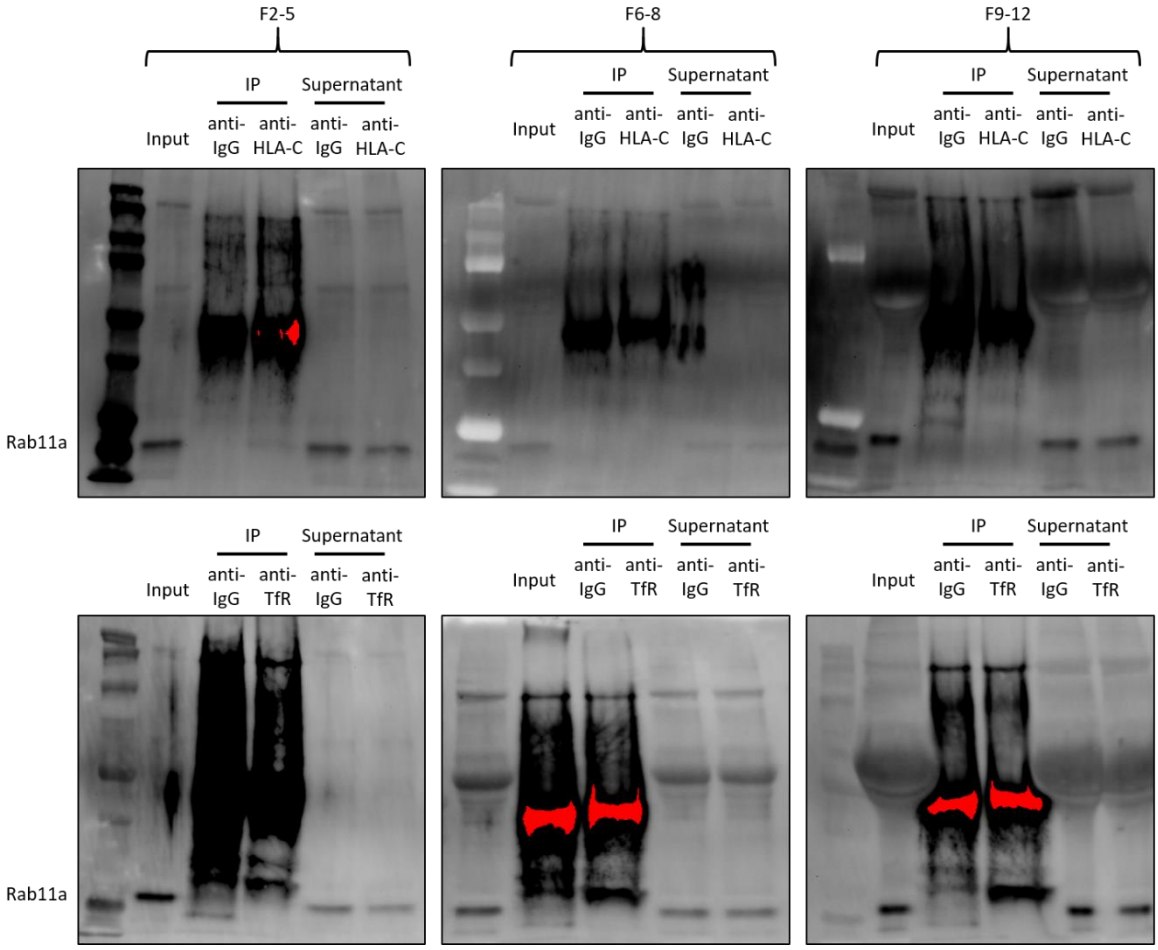
Zhang Q, Higginbotham JN, Jeppesen DK, Yang YP, Li W, McKinley ET, Graves-Deal R, Ping J, Britain CM, Dorsett KA *et al* (2019) Transfer of functional cargo in exomeres. *Cell Rep* 27: 940 – 954.e6

Zou W, Lai M, Zhang Y, Zheng L, Xing Z, Li T, Zou Z, Song Q, Zhao X, Xia L *et al* (2018) Exosome release is regulated by mTORC1. *Adv Sci (Weinh)* 6: 1801313

**License:** This is an open access article under the terms of the Creative Commons Attribution 4.0 License, which permits use, distribution and reproduction in any medium, provided the original work is properly cited.

# Appendix B – Uncropped western blot images

Uncropped western blots of Rab11a corresponding to Figure 3.8 (page 100). A combination of non-specific binding and strong signal intensity caused by the Ig heavy and light chains (despite use of a conformation-specific secondary antibody) necessitated a tight crop to highlight the correct band.



# Appendix C – Additional EV-miRNA data

## HCT116 cells

EV-associated miRNAs that showed differential loading in switched EVs isolated from HCT116 cells with a non-significant LogFC >1.0 or < -1.0. miRNAs in red text were identified in two or more studies (Table 5.2) from the systematic review of EV-miRNAs as biomarkers for CRC, while those in red italics were identified in a single study. Green text highlights miRNAs with previously reported tumorigenic properties.

| miRNA | LogFC | P.value | P.adj | Reference(s) |
|---|---|---|---|---|
| **hsa-miR-7641** | **3.00** | **0.003** | **0.15** | **M. Chen et al. (2019a); Ji et al. (2014)** |
| **hsa-miR-4492** | **2.04** | **0.005** | **0.20** | **Cha et al. (2015)** |
| **hsa-miR-222-3p** | **2.00** | **0.01** | **0.29** | **See Table 5.2** |
| hsa-miR-744-5p | 1.95 | 0.0005 | 0.05 | |
| hsa-miR-4467 | 1.82 | 0.01 | 0.35 | |
| **hsa-miR-4505** | **1.74** | **0.02** | **0.44** | **Raimondo et al. (2020)** |
| **hsa-miR-5001** | **1.65** | **0.003** | **0.15** | **Cha et al. (2015)** |
| hsa-miR-2411 | 1.57 | 0.0008 | 0.06 | |
| hsa-miR-151a-5p | 1.50 | 0.01 | 0.32 | |
| **hsa-miR-125b-5p** | **1.46** | **0.02** | **0.40** | **Gerloff et al. (2020); M. Wu et al. (2020b)** |
| hsa-miR-4532 | 1.41 | 0.001 | 0.08 | |
| hsa-miR-3135b | 1.37 | 0.001 | 0.08 | |
| **hsa-miR-365b-5p** | **1.37** | **0.03** | **0.48** | **Coon et al. (2020)** |
| hsa-miR-1275 | 1.33 | 0.005 | 0.19 | |
| ***hsa-miR-25-3p*** | ***1.32*** | ***0.003*** | ***0.15*** | ***Zeng et al. (2018)*** |
| hsa-miR-4757-3p | 1.30 | 0.05 | 0.58 | |
| hsa-miR-1343-5p | 1.25 | 0.002 | 0.10 | |
| **hsa-miR-221-3p** | **1.16** | **0.0006** | **0.05** | **See Table 5.2** |
| hsa-miR-30c-5p | 1.11 | 0.001 | 0.07 | |
| hsa-miR-937-5p | 1.10 | 0.003 | 0.13 | |
| hsa-miR-1273g-3p | 1.07 | 0.004 | 0.17 | |

| | | | | |
|---|---|---|---|---|
| hsa-miR-31-5p | 1.04 | 0.002 | 0.09 | |
| hsa-miR-182-5p | 1.03 | 0.17 | 0.78 | |
| hsa-miR-575 | 1.03 | 0.0008 | 0.06 | |
| hsa-let-7i-5p | 1.01 | 0.006 | 0.23 | |
| hsa-miR-6775-5p | 1.01 | 0.01 | 0.31 | |
| hsa-miR-6722-3p | -1.03 | 0.01 | 0.33 | |
| hsa-miR-3064-5p | -1.10 | 0.01 | 0.29 | |
| hsa-miR-6782-5p | -1.12 | 0.002 | 0.13 | |
| **hsa-miR-3613-3p** | **-1.20** | **0.04** | **0.52** | **Y. Liu et al. (2020)** |
| hsa-miR-548a-3p | -1.27 | 0.004 | 0.18 | |
| hsa-miR-4668-5p | -1.27 | 0.03 | 0.49 | |
| hsa-miR-5189-3p | -1.33 | 0.10 | 0.71 | |
| hsa-miR-3621 | -1.34 | 0.001 | 0.08 | |
| hsa-miR-4701 | -1.34 | 0.005 | 0.20 | |
| hsa-miR-6806-3p | -1.40 | 0.001 | 0.08 | |
| hsa-miR-1281 | -1.92 | 0.005 | 0.05 | |
| **hsa-miR-455-3p** | **-2.51** | **0.007** | **0.25** | **Xin et al. (2020)** |

EV-associated miRNAs that showed significant differential loading in switched EVs isolated from HCT116 cells but with lower LogFC. miRNAs in red text were identified in two or more studies (Table 5.2) from the systematic review of EV-miRNAs as biomarkers for CRC. Green text highlights miRNAs with previously reported tumorigenic properties.

| miRNA | LogFC | P.value | P.adj | Reference(s) |
|---|---|---|---|---|
| **hsa-miR-4741** | **0.99** | **0.00006** | **0.02** | **Cha et al. (2015); Zonneveld et al. (2019)** |
| hsa-miR-151a-3p | 0.99 | 0.001 | 0.03 | |
| hsa-miR-877-5p | 0.94 | 0.00007 | 0.02 | |
| hsa-miR-4508 | 0.91 | 0.0001 | 0.02 | |
| hsa-miR-4270 | 0.86 | 0.00008 | 0.02 | |
| hsa-miR-6087 | 0.86 | 0.0002 | 0.03 | |
| hsa-miR-5095 | 0.82 | 0.003 | 0.03 | |
| hsa-miR-4640-5p | 0.74 | 0.001 | 0.02 | |
| **hsa-miR-23a-3p** | **0.65** | **0.0004** | **0.04** | **See Table 5.2** |

| | | | |
|---|---|---|---|
| hsa-miR-320e | -0.88 | 0.00005 | 0.02 |
| hsa-miR-6808-3p | -0.91 | 0.0002 | 0.03 |
| hsa-miR-6880 | -0.93 | 0.00009 | 0.02 |

## SW480 cells

EV-associated miRNAs that showed differential loading in switched EVs isolated from SW480 cells with a non-significant LogFC >1.0 or < -1.0. miRNAs in red italics were identified in a single study from the systematic review of EV-miRNAs as biomarkers for CRC. Green text highlights miRNAs with previously reported tumorigenic properties.

| miRNA | LogFC | P.value | P.adj | Reference(s) |
|---|---|---|---|---|
| **hsa-miR-3651** | **1.47** | **0.01** | **0.66** | **C. Li et al. (2020a)** |
| hsa-miR-107 | 1.30 | 0.0004 | 0.14 | |
| hsa-miR-27b-3p | 1.28 | 0.0004 | 0.14 | |
| hsa-miR-182-5p | 1.18 | 0.03 | 0.85 | |
| hsa-miR-103a-3p | 1.14 | 0.001 | 0.26 | |
| hsa-miR-3940 | 1.13 | 0.001 | 0.26 | |
| hsa-miR-361-5p | 1.04 | 0.0001 | 0.10 | |
| ***hsa-miR-25-3p*** | ***1.02*** | ***0.0006*** | ***0.16*** | ***Zeng et al. (2018)*** |
| hsa-miR-4757-3p | 1.00 | 0.001 | 0.21 | |
| hsa-miR-4484 | -1.02 | 0.005 | 0.41 | |
| hsa-miR-101-5p | -1.04 | 0.01 | 0.56 | |
| hsa-miR-1281 | -1.08 | 0.02 | 0.77 | |
| hsa-miR-3616 | -1.15 | 0.02 | 0.78 | |
| hsa-miR-7844-5p | -1.20 | 0.07 | 0.94 | |
| hsa-miR-3149 | -1.38 | 0.003 | 0.14 | |
| hsa-miR-1306-3p | -1.69 | 0.002 | 0.26 | |
| hsa-miR-4668-5p | -2.24 | 0.003 | 0.33 | |

# References


Ahmed, D., et al. (2013), 'Epigenetic and genetic features of 24 colon cancer cell lines', *Oncogenesis,* 2, e71.

Alvarez, M. L., et al. (2012), 'Comparison of protein, microRNA, and mRNA yields using different methods of urinary exosome isolation for the discovery of kidney disease biomarkers', *Kidney Int,* 82 (9), 1024-32.

Alves Dos Santos, K., et al. (2020), 'Circulating Exosomal miRNAs as Biomarkers for the Diagnosis and Prognosis of Colorectal Cancer', *Int J Mol Sci,* 22 (1).

Amin, M.B., et al. (2017), *AJCC Cancer Staging Manua* (8th Edition edn.: Springer).

Andre, T., et al. (2015), 'Adjuvant Fluorouracil, Leucovorin, and Oxaliplatin in Stage II to III Colon Cancer: Updated 10-Year Survival and Outcomes According to BRAF Mutation and Mismatch Repair Status of the MOSAIC Study', *J Clin Oncol,* 33 (35), 4176-87.

Andreu, Z., et al. (2016), 'Comparative analysis of EV isolation procedures for miRNAs detection in serum samples', *J Extracell Vesicles,* 5, 31655.

Aoki, K., et al. (2003), 'Colonic polyposis caused by mTOR-mediated chromosomal instability in Apc+/Delta716 Cdx2+/- compound mutant mice', *Nat Genet,* 35 (4), 323-30.

Arnold, M., et al. (2017), 'Global patterns and trends in colorectal cancer incidence and mortality', *Gut,* 66 (4), 683-91.

Ashar, Y. V., et al. (2020), 'BMS-599626, a Highly Selective Pan-HER Kinase Inhibitor, Antagonizes ABCG2-Mediated Drug Resistance', *Cancers (Basel),* 12 (9).

Atay, S., et al. (2011), 'Morphologic and proteomic characterization of exosomes released by cultured extravillous trophoblast cells', *Exp Cell Res,* 317 (8), 1192-202.

Atkin, W., et al. (2013), 'Computed tomographic colonography versus colonoscopy for investigation of patients with symptoms suggestive of colorectal cancer (SIGGAR): a multicentre randomised trial', *Lancet,* 381 (9873), 1194-202.

Bachurski, D., et al. (2019), 'Extracellular vesicle measurements with nanoparticle tracking analysis - An accuracy and repeatability comparison between NanoSight NS300 and ZetaView', *J Extracell Vesicles,* 8 (1), 1596016.

Baietti, M. F., et al. (2012), 'Syndecan-syntenin-ALIX regulates the biogenesis of exosomes', *Nat Cell Biol,* 14 (7), 677-85.

Baranyai, T., et al. (2015), 'Isolation of Exosomes from Blood Plasma: Qualitative and Quantitative Comparison of Ultracentrifugation and Size Exclusion Chromatography Methods', *PLoS One,* 10 (12), e0145686.

Barcelo, C., et al. (2014), 'Ribonucleoprotein HNRNPA2B1 interacts with and regulates oncogenic KRAS in pancreatic ductal adenocarcinoma cells', *Gastroenterology,* 147 (4), 882-92 e8.

Bautista-Sanchez, D., et al. (2020), 'The Promising Role of miR-21 as a Cancer Biomarker and Its Importance in RNA-Based Therapeutics', *Mol Ther Nucleic Acids,* 20, 409-20.

Bebelman, M. P., et al. (2020), 'Real-time imaging of multivesicular body-plasma membrane fusion to quantify exosome release from single cells', *Nat Protoc,* 15 (1), 102-21.

Becker, A., et al. (2016), 'Extracellular Vesicles in Cancer: Cell-to-Cell Mediators of Metastasis', *Cancer Cell,* 30 (6), 836-48.

Bertagnolli, M. M., et al. (2009), 'Microsatellite instability predicts improved response to adjuvant therapy with irinotecan, fluorouracil, and leucovorin in stage III colon cancer: Cancer and Leukemia Group B Protocol 89803', *J Clin Oncol,* 27 (11), 1814-21.

Bhurwal, A., et al. (2016), 'Endoscopic mucosal resection: learning curve for large nonpolypoid colorectal neoplasia', *Gastrointest Endosc,* 84 (6), 959-68 e7.

Bigagli, E., et al. (2016), 'Exosomes secreted from human colon cancer cells influence the adhesion of neighboring metastatic cells: Role of microRNA-210', *Cancer Biol Ther,* 17 (10), 1062-69.

Biondi, A., et al. (2013), 'Laparoscopic-assisted versus open surgery for colorectal cancer: short- and long-term outcomes comparison', *J Laparoendosc Adv Surg Tech A,* 23 (1), 1-7.

Bisschop, C., et al. (2017), 'Short-Course Radiotherapy Followed by Neoadjuvant Bevacizumab, Capecitabine, and Oxaliplatin and Subsequent Radical Treatment in Primary Stage IV Rectal Cancer: Long-Term Results of a Phase II Study', *Ann Surg Oncol,* 24 (9), 2632-38.

Bister, N., et al. (2020), 'Hypoxia and extracellular vesicles: A review on methods, vesicular cargo and functions', *J Extracell Vesicles,* 10 (1), e12002.

Bjornetro, T., et al. (2019), 'An experimental strategy unveiling exosomal microRNAs 486-5p, 181a-5p and 30d-5p from hypoxic tumour cells as circulating indicators of high-risk rectal cancer', *Journal of Extracellular Vesicles,* 8 (1).

Bjørnetrø, Tonje, et al. (2017), 'Abstract 4514: Low release of exosomal miR-663a from hypoxic tumor cells and poor tumor response to neoadjuvant radiotherapy in rectal cancer patients', *Molecular and Cellular Biology, Genetics*, 4514-14.

Blaser, B., et al. (2012), 'Antitumor activities of ATP-competitive inhibitors of mTOR in colon cancer cells', *BMC Cancer,* 12, 86.

Bobbili, M. R., et al. (2017), 'OncomiR-17-5p: alarm signal in cancer?', *Oncotarget,* 8 (41), 71206-22.

Boing, A. N., et al. (2014), 'Single-step isolation of extracellular vesicles by size-exclusion chromatography', *J Extracell Vesicles,* 3.

Bormann, F., et al. (2019), 'Epigenetic regulation of Amphiregulin and Epiregulin in colorectal cancer', *Int J Cancer,* 144 (3), 569-81.

Botteri, E., et al. (2008), 'Smoking and colorectal cancer: a meta-analysis', *JAMA,* 300 (23), 2765-78.

Bradbury, K. E., Murphy, N., and Key, T. J. (2020), 'Diet and colorectal cancer in UK Biobank: a prospective study', *Int J Epidemiol,* 49 (1), 246-58.

Brennan, K., et al. (2020), 'A comparison of methods for the isolation and separation of extracellular vesicles from protein and lipid particles in human serum', *Sci Rep,* 10 (1), 1039.

Brenner, Hermann, Kloor, Matthias, and Pox, Christian Peter (2014), 'Colorectal cancer', *The Lancet,* 383 (9927), 1490-502.

Burton, S., et al. (2006), 'MRI directed multidisciplinary team preoperative treatment strategy: the way to eliminate positive circumferential margins?', *Br J Cancer,* 94 (3), 351-7.

Busatto, S., et al. (2018), 'Tangential Flow Filtration for Highly Efficient Concentration of Extracellular Vesicles from Large Volumes of Fluid', *Cells,* 7 (12).

Buschmann, D., et al. (2018), 'Evaluation of serum extracellular vesicle isolation methods for profiling miRNAs by next-generation sequencing', *J Extracell Vesicles,* 7 (1), 1481321.

Cai, S., et al. (2014), 'Alcohol drinking and the risk of colorectal cancer death: a meta-analysis', *Eur J Cancer Prev,* 23 (6), 532-9.

Cam, H., et al. (2010), 'mTORC1 signaling under hypoxic conditions is controlled by ATM-dependent phosphorylation of HIF-1alpha', *Mol Cell,* 40 (4), 509-20.

Campos, A., et al. (2019), 'Cell Intrinsic and Extrinsic Mechanisms of Caveolin-1-Enhanced Metastasis', *Biomolecules,* 9 (8).

Campos, A., et al. (2018), 'Caveolin-1-containing extracellular vesicles transport adhesion proteins and promote malignancy in breast cancer cell lines', *Nanomedicine (Lond),* 13 (20), 2597-609.

Cao, Y. (2017), 'Tumorigenesis as a process of gradual loss of original cell identity and gain of properties of neural precursor/progenitor cells', *Cell and Bioscience,* 7.

Cha, D. J., et al. (2015), 'KRAS-dependent sorting of miRNA to exosomes', *Elife,* 4, e07197.

Chakraborty, S. and Krishnan, Y. (2017), 'A structural map of oncomiR-1 at single-nucleotide resolution', *Nucleic Acids Res,* 45 (16), 9694-705.

Chapuis, P. H., et al. (2019), 'Recurrence and cancer-specific death after adjuvant chemotherapy for Stage III colon cancer', *Colorectal Dis,* 21 (2), 164-73.

Chen, H. C. (2005), 'Boyden chamber assay', *Methods Mol Biol,* 294, 15-22.

Chen, M., et al. (2019a), 'Distinct shed microvesicle and exosome microRNA signatures reveal diagnostic markers for colorectal cancer', *PLoS One,* 14 (1), e0210003.

Chen, S. H., et al. (2019b), 'Emergence of RAS mutations in patients with metastatic colorectal cancer receiving cetuximab-based treatment: a study protocol', *BMC Cancer,* 19 (1), 640.

Chen, Y. and Wang, X. (2020), 'miRDB: an online database for prediction of functional microRNA targets', *Nucleic Acids Res,* 48 (D1), D127-D31.

Chittleborough, T. J., et al. (2020), 'Increasing Incidence of Young-Onset Colorectal Carcinoma A 3-Country Population Analysis', *Dis Colon Rectum,* 63 (7), 903-10.

Chouaib, S., et al. (2017), 'Hypoxic stress: obstacles and opportunities for innovative immunotherapy of cancer', *Oncogene,* 36 (4), 439-45.

Chow, F. C. and Chok, K. S. (2019), 'Colorectal liver metastases: An update on multidisciplinary approach', *World J Hepatol,* 11 (2), 150-72.

Christ, L., et al. (2017), 'Cellular Functions and Molecular Mechanisms of the ESCRT Membrane-Scission Machinery', *Trends Biochem Sci,* 42 (1), 42-56.

Chuo, S. T., Chien, J. C., and Lai, C. P. (2018), 'Imaging extracellular vesicles: current and emerging methods', *J Biomed Sci,* 25 (1), 91.

Condon, K. J. and Sabatini, D. M. (2019), 'Nutrient regulation of mTORC1 at a glance', *J Cell Sci,* 132 (21).

Cooks, T., et al. (2018), 'Mutant p53 cancers reprogram macrophages to tumor supporting macrophages via exosomal miR-1246', *Nat Commun,* 9 (1), 771.

Coon, J., Kingsley, K., and Howard, K. M. (2020), 'miR-365 (microRNA): Potential Biomarker in Oral Squamous Cell Carcinoma Exosomes and Extracellular Vesicles', *Int J Mol Sci,* 21 (15).

Coumans, F. A. W., et al. (2017), 'Methodological Guidelines to Study Extracellular Vesicles', *Circ Res,* 120 (10), 1632-48.

Crespo, Piero and Casar, Berta (2016), 'The Chick Embryo Chorioallantoic Membrane as an in vivo Model to Study Metastasis', *Bio-Protocol,* 6 (20).

Crewe, C., et al. (2018), 'An Endothelial-to-Adipocyte Extracellular Vesicle Axis Governed by Metabolic State', *Cell,* 175 (3), 695-708 e13.

CRUK 'Bowel cancer statistics', <https://www.cancerresearchuk.org/health-professional/cancer-statistics/statistics-by-cancer-type/bowel-cancer#heading-One>, accessed 02/02/2021.

Cruz, L., et al. (2018), 'Extracellular Vesicles: Decoding a New Language for Cellular Communication in Early Embryonic Development', *Front Cell Dev Biol,* 6, 94.

D'Souza-Schorey, C. and Schorey, J. S. (2018), 'Regulation and mechanisms of extracellular vesicle biogenesis and secretion', *Essays Biochem,* 62 (2), 125-33.

Dai, J., et al. (2020), 'Exosomes: key players in cancer and potential therapeutic strategy', *Signal Transduct Target Ther,* 5 (1), 145.

de Miguel Perez, D., et al. (2020), 'Extracellular vesicle-miRNAs as liquid biopsy biomarkers for disease identification and prognosis in metastatic colorectal cancer patients', *Sci Rep,* 10 (1), 3974.

De Palma, F. D. E., et al. (2019), 'The Molecular Hallmarks of the Serrated Pathway in Colorectal Cancer', *Cancers (Basel),* 11 (7).

De Roock, W., et al. (2011), 'KRAS, BRAF, PIK3CA, and PTEN mutations: implications for targeted therapies in metastatic colorectal cancer', *Lancet Oncol,* 12 (6), 594-603.

De Sousa E Melo, F., et al. (2013), 'Poor-prognosis colon cancer is defined by a molecularly distinct subtype and develops from serrated precursor lesions', *Nature Medicine,* 19 (5), 614-18.

Dekker, Evelien, et al. (2019), 'Colorectal cancer', *The Lancet,* 394 (10207), 1467-80.

Demory Beckler, M., et al. (2013), 'Proteomic analysis of exosomes from mutant KRAS colon cancer cells identifies intercellular transfer of mutant KRAS', *Mol Cell Proteomics,* 12 (2), 343-55.

Dibble, C. C. and Manning, B. D. (2013), 'Signal integration by mTORC1 coordinates nutrient input with biosynthetic output', *Nat Cell Biol,* 15 (6), 555-64.

Dickhout, A. and Koenen, R. R. (2018), 'Extracellular Vesicles as Biomarkers in Cardiovascular Disease; Chances and Risks', *Front Cardiovasc Med,* 5, 113.

Dolcetti, Riccardo, et al. (1999), 'High Prevalence of Activated Intraepithelial Cytotoxic T Lymphocytes and Increased Neoplastic Cell Apoptosis in Colorectal Carcinomas with Microsatellite Instability', *The American Journal of Pathology,* 154 (6), 1805-13.

Dossou, A. S. and Basu, A. (2019), 'The Emerging Roles of mTORC1 in Macromanaging Autophagy', *Cancers (Basel),* 11 (10).

Doyle, L. M. and Wang, M. Z. (2019), 'Overview of Extracellular Vesicles, Their Origin, Composition, Purpose, and Methods for Exosome Isolation and Analysis', *Cells,* 8 (7).

Du, C., et al. (2014), 'MiR-126-3p suppresses tumor metastasis and angiogenesis of hepatocellular carcinoma by targeting LRP6 and PIK3R2', *J Transl Med,* 12, 259.

Du, D., et al. (2018), 'Optimal Interval to Surgery After Neoadjuvant Chemoradiotherapy in Rectal Cancer: A Systematic Review and Meta-analysis', *Clin Colorectal Cancer,* 17 (1), 13-24.

Elmunzer, B. J., et al. (2012), 'Effect of flexible sigmoidoscopy-based screening on incidence and mortality of colorectal cancer: a systematic review and meta-analysis of randomized controlled trials', *PLoS Med,* 9 (12), e1001352.

Endzelins, E., et al. (2018), 'Extracellular Vesicles Derived from Hypoxic Colorectal Cancer Cells Confer Metastatic Phenotype to Non-metastatic Cancer Cells', *Anticancer Res,* 38 (9), 5139-47.

Eylem, C. C., et al. (2020), 'Untargeted multi-omic analysis of colorectal cancer-specific exosomes reveals joint pathways of colorectal cancer in both clinical samples and cell culture', *Cancer Letters,* 469, 186-94.

Fabbiano, F., et al. (2020), 'RNA packaging into extracellular vesicles: An orchestra of RNA-binding proteins?', *J Extracell Vesicles,* 10 (2), e12043.

Fan, S. J. and Goberdhan, D. C. I. (2018), 'PATs and SNATs: Amino Acid Sensors in Disguise', *Front Pharmacol,* 9, 640.

Fan, S. J., et al. (2016), 'PAT4 levels control amino-acid sensitivity of rapamycin-resistant mTORC1 from the Golgi and affect clinical outcome in colorectal cancer', *Oncogene,* 35 (23), 3004-15.

Fan, S. J., et al. (2020), 'Glutamine deprivation alters the origin and function of cancer cell exosomes', *EMBO J,* 39 (16), e103009.

Fares, J., et al. (2020), 'Molecular principles of metastasis: a hallmark of cancer revisited', *Signal Transduct Target Ther,* 5 (1), 28.

Fearon, Eric R. and Vogelstein, Bert (1990), 'A genetic model for colorectal tumorigenesis', *Cell,* 61 (5), 759-67.

Feeney, G., et al. (2019), 'Neoadjuvant radiotherapy for rectal cancer management', *World J Gastroenterol,* 25 (33), 4850-69.

Feng, Z., et al. (2005), 'The coordinate regulation of the p53 and mTOR pathways in cells', *Proc Natl Acad Sci U S A,* 102 (23), 8204-9.

Fotheringham, S., et al. (2019), 'Challenges and solutions in patient treatment strategies for stage II colon cancer', *Gastroenterol Rep (Oxf),* 7 (3), 151-61.

Francipane, M. G. and Lagasse, E. (2014), 'mTOR pathway in colorectal cancer: an update', *Oncotarget,* 5 (1), 49-66.

Fu, F., et al. (2018), 'Circulating Exosomal miR-17-5p and miR-92a-3p Predict Pathologic Stage and Grade of Colorectal Cancer', *Transl Oncol,* 11 (2), 221-32.

Fuji, T., et al. (2019), 'Detection of circulating microRNAs with Ago2 complexes to monitor the tumor dynamics of colorectal cancer patients during chemotherapy', *Int J Cancer,* 144 (9), 2169-80.

Gallaher, J. A., Brown, J. S., and Anderson, A. R. A. (2019), 'The impact of proliferation-migration tradeoffs on phenotypic evolution in cancer', *Sci Rep,* 9 (1), 2425.

Galon, J., et al. (2006), 'Type, density, and location of immune cells within human colorectal tumors predict clinical outcome', *Science,* 313 (5795), 1960-4.

Garcia-Albeniz, X. and Chan, A. T. (2011), 'Aspirin for the prevention of colorectal cancer', *Best Pract Res Clin Gastroenterol,* 25 (4-5), 461-72.

Garcia-Contreras, M., et al. (2017), 'Exosomes as biomarkers and therapeutic tools for type 1 diabetes mellitus', *European Review for Medical and Pharmacological Sciences,* 21 (12), 2940-56.

Gardiner, C., et al. (2016), 'Techniques used for the isolation and characterization of extracellular vesicles: results of a worldwide survey', *J Extracell Vesicles,* 5, 32945.

Gaspar, L. S., et al. (2020), 'Simple and Fast SEC-Based Protocol to Isolate Human Plasma-Derived Extracellular Vesicles for Transcriptional Research', *Mol Ther Methods Clin Dev,* 18, 723-37.

Gasparello, J., et al. (2020), 'A Distinctive microRNA (miRNA) Signature in the Blood of Colorectal Cancer (CRC) Patients at Surgery', *Cancers,* 12 (9).

Gerloff, D., et al. (2020), 'Melanoma-Derived Exosomal miR-125b-5p Educates Tumor Associated Macrophages (TAMs) by Targeting Lysosomal Acid Lipase A (LIPA)', *Cancers (Basel),* 12 (2).

Giallombardo, M., et al. (2016), 'Exosome-mediated drug resistance in cancer: the near future is here', *Ther Adv Med Oncol,* 8 (5), 320-2.

Globocan 'Global Cancer Observatory: Global colorectal cancer statistics 2020', <https://gco.iarc.fr/today/data/factsheets/cancers/10_8_9-Colorectum-fact-sheet.pdf>, accessed 02/02/2021.

Goberdhan, D. C., Wilson, C., and Harris, A. L. (2016), 'Amino Acid Sensing by mTORC1: Intracellular Transporters Mark the Spot', *Cell Metab,* 23 (4), 580-9.

Goda, N., et al. (2003), 'Hypoxia-inducible factor 1alpha is essential for cell cycle arrest during hypoxia', *Mol Cell Biol,* 23 (1), 359-69.

Grady, W. M. and Markowitz, S. D. (2015), 'The molecular pathogenesis of colorectal cancer and its potential application to colorectal cancer screening', *Dig Dis Sci,* 60 (3), 762-72.

Grant, B. D. and Donaldson, J. G. (2009), 'Pathways and mechanisms of endocytic recycling', *Nat Rev Mol Cell Biol,* 10 (9), 597-608.

Gu, Y. Y., et al. (2019), 'Suppressing the secretion of exosomal miR-19b by gw4869 could regulate oxaliplatin sensitivity in colorectal cancer', *Neoplasma,* 66 (1), 39-45.

Guerreiro, E. M., et al. (2018), 'Efficient extracellular vesicle isolation by combining cell media modifications, ultrafiltration, and size-exclusion chromatography', *PLoS One,* 13 (9), e0204276.

Gulhati, P., et al. (2011), 'mTORC1 and mTORC2 regulate EMT, motility, and metastasis of colorectal cancer via RhoA and Rac1 signaling pathways', *Cancer Res,* 71 (9), 3246-56.

Guo, F., et al. (2014), 'MiR-101 suppresses the epithelial-to-mesenchymal transition by targeting ZEB1 and ZEB2 in ovarian carcinoma', *Oncol Rep,* 31 (5), 2021-8.

Guo, T., et al. (2020), 'The Identification of Plasma Exosomal miR-423-3p as a Potential Predictive Biomarker for Prostate Cancer Castration-Resistance Development by Plasma Exosomal miRNA Sequencing', *Front Cell Dev Biol,* 8, 602493.

Guo, Y., et al. (2019), 'Effects of exosomes on pre-metastatic niche formation in tumors', *Mol Cancer,* 18 (1), 39.

Half, E., Bercovich, D., and Rozen, P. (2009), 'Familial adenomatous polyposis', *Orphanet J Rare Dis,* 4, 22.

Hampel, H. (2018), 'Population Screening for Hereditary Colorectal Cancer', *Surg Oncol Clin N Am,* 27 (2), 319-25.

Han, J., et al. (2020), 'Plasma Exosomal miRNA Expression Profile as Oxaliplatin-Based Chemoresistant Biomarkers in Colorectal Adenocarcinoma', *Front Oncol,* 10, 1495.

Han, L., Lam, E. W., and Sun, Y. (2019), 'Extracellular vesicles in the tumor microenvironment: old stories, but new tales', *Mol Cancer,* 18 (1), 59.

Hanahan, D. and Weinberg, R. A. (2011), 'Hallmarks of cancer: the next generation', *Cell,* 144 (5), 646-74.

Hanson, P. I. and Cashikar, A. (2012), 'Multivesicular body morphogenesis', *Annu Rev Cell Dev Biol,* 28, 337-62.

Hao, Y., et al. (2016), 'Oncogenic PIK3CA mutations reprogram glutamine metabolism in colorectal cancer', *Nat Commun,* 7, 11971.

Harmati, M., et al. (2019), 'Small extracellular vesicles convey the stress-induced adaptive responses of melanoma cells', *Sci Rep,* 9 (1), 15329.

Hausser, J. and Alon, U. (2020), 'Tumour heterogeneity and the evolutionary trade-offs of cancer', *Nat Rev Cancer,* 20 (4), 247-57.

Hebron, K. E., et al. (2018), 'Alternative splicing of ALCAM enables tunable regulation of cell-cell adhesion through differential proteolysis', *Scientific Reports,* 8.

Heerboth, S., et al. (2015), 'EMT and tumor metastasis', *Clin Transl Med,* 4, 6.

Heitman, J., Movva, N. R., and Hall, M. N. (1991), 'Targets for cell cycle arrest by the immunosuppressant rapamycin in yeast', *Science,* 253 (5022), 905-9.

Henrikson, N. B., et al. (2015), 'Family history and the natural history of colorectal cancer: systematic review', *Genet Med,* 17 (9), 702-12.

Hewitson, P., et al. (2008), 'Cochrane systematic review of colorectal cancer screening using the fecal occult blood test (hemoccult): an update', *Am J Gastroenterol,* 103 (6), 1541-9.

Higginbotham, J. N., et al. (2011), 'Amphiregulin exosomes increase cancer cell invasion', *Curr Biol,* 21 (9), 779-86.

Hol, L., et al. (2010), 'Screening for colorectal cancer: randomised trial comparing guaiac-based and immunochemical faecal occult blood testing and flexible sigmoidoscopy', *Gut,* 59 (1), 62-8.

Hong, C. S., et al. (2016), 'Isolation of biologically active and morphologically intact exosomes from plasma of patients with cancer', *J Extracell Vesicles,* 5, 29289.

Hornick, N. I., et al. (2015), 'Serum Exosome MicroRNA as a Minimally-Invasive Early Biomarker of AML', *Scientific Reports,* 5.

Hoshino, A., et al. (2015), 'Tumour exosome integrins determine organotropic metastasis', *Nature,* 527 (7578), 329-35.

Hu, H. Y., et al. (2019a), 'Exosomal miR-1229 derived from colorectal cancer cells promotes angiogenesis by targeting HIPK2', *Int J Biol Macromol,* 132, 470-77.

Hu, J. L., et al. (2019b), 'CAFs secreted exosomes promote metastasis and chemotherapy resistance by enhancing cell stemness and epithelial-mesenchymal transition in colorectal cancer', *Mol Cancer,* 18 (1), 91.

Hu, X., et al. (2020), 'Exosomes Derived from Hypoxic Colorectal Cancer Cells Transfer miR-410-3p to Regulate Tumor Progression', *J Cancer,* 11 (16), 4724-35.

Hu, Y., et al. (2015), 'Fibroblast-Derived Exosomes Contribute to Chemoresistance through Priming Cancer Stem Cells in Colorectal Cancer', *PLoS One,* 10 (5), e0125625.

Huang, Y. M., et al. (2020), 'Comparison of clinical outcomes between laparoscopic and open surgery for left-sided colon cancer: a nationwide population-based study', *Scientific Reports,* 10 (1).

Huang, Z. and Feng, Y. (2017), 'Exosomes Derived From Hypoxic Colorectal Cancer Cells Promote Angiogenesis Through Wnt4-Induced beta-Catenin Signaling in Endothelial Cells', *Oncol Res,* 25 (5), 651-61.

Huang, Z., et al. (2018), 'Exosomes Derived from Hypoxic Colorectal Cancer Cells Transfer Wnt4 to Normoxic Cells to Elicit a Prometastatic Phenotype', *Int J Biol Sci,* 14 (14), 2094-102.

Huber, V., et al. (2005), 'Human colorectal cancer cells induce T-cell death through release of proapoptotic microvesicles: role in immune escape', *Gastroenterology,* 128 (7), 1796-804.

Hurwitz, S. N., et al. (2016), 'Proteomic profiling of NCI-60 extracellular vesicles uncovers common protein cargo and cancer type-specific biomarkers', *Oncotarget,* 7 (52), 86999-7015.

Jacobs, B., et al. (2009), 'Amphiregulin and epiregulin mRNA expression in primary tumors predicts outcome in metastatic colorectal cancer treated with cetuximab', *J Clin Oncol,* 27 (30), 5068-74.

Jeppesen, D. K., et al. (2019), 'Reassessment of Exosome Composition', *Cell,* 177 (2), 428-45 e18.

Jess, T., Rungoe, C., and Peyrin-Biroulet, L. (2012), 'Risk of colorectal cancer in patients with ulcerative colitis: a meta-analysis of population-based cohort studies', *Clin Gastroenterol Hepatol,* 10 (6), 639-45.

Ji, H., et al. (2014), 'Deep sequencing of RNA from three different extracellular vesicle (EV) subtypes released from the human LIM1863 colon cancer cell line uncovers distinct miRNA-enrichment signatures', *PLoS One,* 9 (10), e110314.

Jin, G. Y., et al. (2019), 'A panel of serum exosomal microRNAs as predictive markers for chemoresistance in advanced colorectal cancer', *Cancer Chemotherapy and Pharmacology,* 84 (2), 315-25.

Johnstone, R. M., et al. (1987), 'Vesicle formation during reticulocyte maturation. Association of plasma membrane activities with released vesicles (exosomes)', *J Biol Chem,* 262 (19), 9412-20.

Jonker, D. J., et al. (2007), 'Cetuximab for the treatment of colorectal cancer', *N Engl J Med,* 357 (20), 2040-8.

Juan, T. and Furthauer, M. (2018), 'Biogenesis and function of ESCRT-dependent extracellular vesicles', *Semin Cell Dev Biol,* 74, 66-77.

Kang, Hyejin, Kim, Jiyoon, and Park, Jaesung (2017), 'Methods to isolate extracellular vesicles for diagnosis', *Micro and Nano Systems Letters,* 5 (1).

Kannarkatt, J., et al. (2017), 'Adjuvant Chemotherapy for Stage II Colon Cancer: A Clinical Dilemma', *J Oncol Pract,* 13 (4), 233-41.

Karimi, N., et al. (2019), 'Serum overexpression of miR-301a and miR-23a in patients with colorectal cancer', *J Chin Med Assoc,* 82 (3), 215-20.

Katsuno, H., et al. (2020), 'Robotic Surgery for Rectal Cancer: Operative Technique and Review of the Literature', *J Anus Rectum Colon,* 4 (1), 14-24.

Kehl, T., et al. (2020), 'miRPathDB 2.0: a novel release of the miRNA Pathway Dictionary Database', *Nucleic Acids Res,* 48 (D1), D142-D47.

Khambata-Ford, S., et al. (2007), 'Expression of epiregulin and amphiregulin and K-ras mutation status predict disease control in metastatic colorectal cancer patients treated with cetuximab', *J Clin Oncol,* 25 (22), 3230-7.

Khan, A. U. H., et al. (2016), 'Human Leukemic Cells performing Oxidative Phosphorylation (OXPHOS) Generate an Antioxidant Response Independently of Reactive Oxygen species (ROS) Production', *EBioMedicine,* 3, 43-53.

Kim, H., et al. (2020a), 'The Emerging Roles of Exosomes as EMT Regulators in Cancer', *Cells,* 9 (4).

Kim, J. and Guan, K. L. (2019), 'mTOR as a central hub of nutrient signalling and cell growth', *Nature Cell Biology,* 21 (1), 63-71.

Kim, J., et al. (2015), 'Isolation of High-Purity Extracellular Vesicles by Extracting Proteins Using Aqueous Two-Phase System', *PLoS One,* 10 (6), e0129760.

Kim, J. E., et al. (2020b), 'The stromal loss of miR-4516 promotes the FOSL1-dependent proliferation and malignancy of triple negative breast cancer', *Cancer Lett,* 469, 256-65.

King, H. W., Michael, M. Z., and Gleadle, J. M. (2012), 'Hypoxic enhancement of exosome release by breast cancer cells', *BMC Cancer,* 12, 421.

Klaus, B. and Reisenauer, S. (2016), 'An end to end workflow for differential gene expression using Affymetrix microarrays', *F1000Res,* 5, 1384.

Klinge, C. M., et al. (2019), 'HNRNPA2/B1 is upregulated in endocrine-resistant LCC9 breast cancer cells and alters the miRNA transcriptome when overexpressed in MCF-7 cells', *Sci Rep,* 9 (1), 9430.

Ko, S. Y., et al. (2019), 'Cancer-derived small extracellular vesicles promote angiogenesis by heparin-bound, bevacizumab-insensitive VEGF, independent of vesicle uptake', *Commun Biol,* 2, 386.

Konoshenko, M. Y., et al. (2018), 'Isolation of Extracellular Vesicles: General Methodologies and Latest Trends', *Biomed Res Int,* 2018, 8545347.

Kornilov, R., et al. (2018), 'Efficient ultrafiltration-based protocol to deplete extracellular vesicles from fetal bovine serum', *J Extracell Vesicles,* 7 (1), 1422674.

Kosaka, N., et al. (2019), 'Exploiting the message from cancer: the diagnostic value of extracellular vesicles for clinical applications', *Exp Mol Med,* 51 (3), 1-9.

Koukourakis, M. I. (2001), 'Tumour angiogenesis and response to radiotherapy', *Anticancer Res,* 21 (6B), 4285-300.

Kowal, J., et al. (2016), 'Proteomic comparison defines novel markers to characterize heterogeneous populations of extracellular vesicle subtypes', *Proc Natl Acad Sci U S A,* 113 (8), E968-77.

Kral, J., et al. (2018), 'Expression profile of miR-17/92 cluster is predictive of treatment response in rectal cancer', *Carcinogenesis,* 39 (11), 1359-67.

Kramer-Albers, E. M., et al. (2007), 'Oligodendrocytes secrete exosomes containing major myelin and stress-protective proteins: Trophic support for axons?', *Proteomics Clin Appl,* 1 (11), 1446-61.

Kreimer, S. and Ivanov, A. R. (2017), 'Rapid Isolation of Extracellular Vesicles from Blood Plasma with Size-Exclusion Chromatography Followed by Mass Spectrometry-Based Proteomic Profiling', *Methods Mol Biol,* 1660, 295-302.

Kucharzewska, P. and Belting, M. (2013), 'Emerging roles of extracellular vesicles in the adaptive response of tumour cells to microenvironmental stress', *J Extracell Vesicles,* 2.

Kucharzewska, P., et al. (2013), 'Exosomes reflect the hypoxic status of glioma cells and mediate hypoxia-dependent activation of vascular cells during tumor development', *Proc Natl Acad Sci U S A,* 110 (18), 7312-7.

Labbe, M., et al. (2020), 'microRNAs identified in prostate cancer: Correlative studies on response to ionizing radiation', *Mol Cancer,* 19 (1), 63.

Lane, R. E., et al. (2018), 'Extracellular vesicles as circulating cancer biomarkers: opportunities and challenges', *Clin Transl Med,* 7 (1), 14.

Lanspa, S.J. and Lynch, H.T. (2010), 'Quality Indicators for Colonoscopy and the Risk of Interval Cancer', *New England Journal of Medicine,* 363 (14), 1371-73.

Lee, H., et al. (2019), 'Caveolin-1 selectively regulates microRNA sorting into microvesicles after noxious stimuli', *J Exp Med,* 216 (9), 2202-20.

Lee, J., et al. (2017), 'Prevalence and characteristics of hereditary non-polyposis colorectal cancer (HNPCC) syndrome in immigrant Asian colorectal cancer patients', *BMC Cancer,* 17 (1), 843.

Lee, J. J., Loh, K., and Yap, Y. S. (2015), 'PI3K/Akt/mTOR inhibitors in breast cancer', *Cancer Biol Med,* 12 (4), 342-54.

Li, C., et al. (2020a), 'MicroRNA3651 promotes colorectal cancer cell proliferation through directly repressing Tbox transcription factor 1', *Int J Mol Med,* 45 (3), 956-66.

Li Destri, G., et al. (2015), 'Preoperative carcinoembryonic antigen and prognosis of colorectal cancer. An independent prognostic factor still reliable', *Int Surg,* 100 (4), 617-25.

Li, J., et al. (2016a), 'Comparison of microarray and RNA-Seq analysis of mRNA expression in dermal mesenchymal stem cells', *Biotechnol Lett,* 38 (1), 33-41.

Li, L., et al. (2016b), 'Exosomes Derived from Hypoxic Oral Squamous Cell Carcinoma Cells Deliver miR-21 to Normoxic Cells to Elicit a Prometastatic Phenotype', *Cancer Res,* 76 (7), 1770-80.

Li, P., et al. (2017a), 'Progress in Exosome Isolation Techniques', *Theranostics,* 7 (3), 789-804.

Li, S., et al. (2020b), 'The roles of exosomes in cancer drug resistance and its therapeutic application', *Clin Transl Med,* 10 (8), e257.

Li, X. J., et al. (2017b), 'Exosomal MicroRNA MiR-1246 Promotes Cell Proliferation, Invasion and Drug Resistance by Targeting CCNG2 in Breast Cancer', *Cell Physiol Biochem,* 44 (5), 1741-48.

Liang, L., et al. (2017), 'MiR-93-5p enhances growth and angiogenesis capacity of HUVECs by down-regulating EPLIN', *Oncotarget,* 8 (63), 107033-43.

Liangsupree, T., Multia, E., and Riekkola, M. L. (2021), 'Modern isolation and separation techniques for extracellular vesicles', *J Chromatogr A,* 1636, 461773.

Lichtenstein, P., et al. (2000), 'Environmental and heritable factors in the causation of cancer--analyses of cohorts of twins from Sweden, Denmark, and Finland', *N Engl J Med,* 343 (2), 78-85.

Lin, K. J., et al. (2012), 'The effect of estrogen vs. combined estrogen-progestogen therapy on the risk of colorectal cancer', *Int J Cancer,* 130 (2), 419-30.

Linares, R., et al. (2015), 'High-speed centrifugation induces aggregation of extracellular vesicles', *J Extracell Vesicles,* 4, 29509.

Liu, L., et al. (2018a), 'Prognostic and predictive value of long non-coding RNA GAS5 and mircoRNA-221 in colorectal cancer and their effects on colorectal cancer cell proliferation, migration and invasion', *Cancer Biomarkers,* 22 (2), 283-99.

Liu, P., et al. (2016), 'MicroRNA-23a regulates epithelial-to-mesenchymal transition in endometrial endometrioid adenocarcinoma by targeting SMAD3', *Cancer Cell Int,* 16 (1), 67.

Liu, P. H., et al. (2019), 'Association of Obesity With Risk of Early-Onset Colorectal Cancer Among Women', *JAMA Oncol,* 5 (1), 37-44.

Liu, X. X., et al. (2018b), 'Circulating Exosomal miR-27a and miR-130a Act as Novel Diagnostic and Prognostic Biomarkers of Colorectal Cancer', *Cancer Epidemiology Biomarkers & Prevention,* 27 (7), 746-54.

Liu, Y., et al. (2020), 'MiR-3613-3p from carcinoma-associated fibroblasts exosomes promoted breast cancer cell proliferation and metastasis by regulating SOCS2 expression', *IUBMB Life,* 72 (8), 1705-14.

Lobb, R. J., et al. (2015), 'Optimized exosome isolation protocol for cell culture supernatant and human plasma', *J Extracell Vesicles,* 4, 27031.

Lopez-Campos, F., et al. (2020), 'Watch and wait approach in rectal cancer: Current controversies and future directions', *World J Gastroenterol,* 26 (29), 4218-39.

Lotvall, J., et al. (2014), 'Minimal experimental requirements for definition of extracellular vesicles and their functions: a position statement from the International Society for Extracellular Vesicles', *J Extracell Vesicles,* 3, 26913.

Lu, C., et al. (2017), 'MicroRNA-92a promotes epithelial-mesenchymal transition through activation of PTEN/PI3K/AKT signaling pathway in non-small cell lung cancer metastasis', *Int J Oncol,* 51 (1), 235-44.

Lu, P., et al. (2019), 'Anatomic Distribution of Colorectal Adenocarcinoma in Young Patients', *Dis Colon Rectum,* 62 (8), 920-24.

Luan, W. K., et al. (2021), 'Exosomal miR-106b-5p derived from melanoma cell promotes primary melanocytes epithelial-mesenchymal transition through targeting EphA4', *Journal of Experimental & Clinical Cancer Research,* 40 (1).

Luo, Z. W., et al. (2019), 'Increased expression of Ki-67 is a poor prognostic marker for colorectal cancer patients: a meta analysis', *Bmc Cancer,* 19.

Ma, F., et al. (2017), 'MiR-23a promotes TGF-beta1-induced EMT and tumor metastasis in breast cancer cells by directly targeting CDH1 and activating Wnt/beta-catenin signaling', *Oncotarget,* 8 (41), 69538-50.

MacDermid, E., et al. (2009), 'Improving patient survival with the colorectal cancer multi-disciplinary team', *Colorectal Dis,* 11 (3), 291-5.

Maia, J., et al. (2018), 'Exosome-Based Cell-Cell Communication in the Tumor Microenvironment', *Front Cell Dev Biol,* 6, 18.

Mallegol, J., et al. (2007), 'T84-intestinal epithelial exosomes bear MHC class II/peptide complexes potentiating antigen presentation by dendritic cells', *Gastroenterology,* 132 (5), 1866-76.

Maminezhad, H., et al. (2020), 'A panel of six-circulating miRNA signature in serum and its potential diagnostic value in colorectal cancer', *Life Sci,* 258, 118226.

Mani, S. A., et al. (2008), 'The epithelial-mesenchymal transition generates cells with properties of stem cells', *Cell,* 133 (4), 704-15.

Mannavola, F., et al. (2019), 'Revisiting the Role of Exosomes in Colorectal Cancer: Where Are We Now?', *Front Oncol,* 9, 521.

Matsumoto, N., et al. (2004), 'Increased level of oxidized LDL-dependent monocyte-derived microparticles in acute coronary syndrome', *Thromb Haemost,* 91 (1), 146-54.

Matsumura, T., et al. (2015), 'Exosomal microRNA in serum is a novel biomarker of recurrence in human colorectal cancer', *British Journal of Cancer,* 113 (2), 275-81.

McBride, J. D., Rodriguez-Menocal, L., and Badiavas, E. V. (2017), 'Extracellular Vesicles as Biomarkers and Therapeutics in Dermatology: A Focus on Exosomes', *J Invest Dermatol,* 137 (8), 1622-29.

McCormick, K (2018), 'Intercellular signalling in the prostate cancer tumour microenvironment: implications for disease progression [DPhil thesis]', (University of Oxford).

McCormick, K, et al. (2020), 'Anti-androgens induce Rab11a-exosome secretion in prostate cancer by suppressing amino acid-sensitive PAT4-mTORC1 signalling', *bioRxiv preprint: https://www.biorxiv.org/content/10.1101/2020.09.18.300137v1*.

Melick, C. H. and Jewell, J. L. (2020), 'Regulation of mTORC1 by Upstream Stimuli', *Genes (Basel),* 11 (9).

Meltzer, S., et al. (2019), 'Circulating Exosomal miR-141-3p and miR-375 in Metastatic Progression of Rectal Cancer', *Translational Oncology,* 12 (8), 1038-44.

Miller, I., et al. (2018), 'Ki67 is a Graded Rather than a Binary Marker of Proliferation versus Quiescence', *Cell Rep,* 24 (5), 1105-12 e5.

Min, L., et al. (2019), 'Loss of Circulating Exosomal miR-92b is a Novel Biomarker of Colorectal Cancer at Early Stage', *International Journal of Medical Sciences,* 16 (9), 1231-37.

Mogilyansky, E. and Rigoutsos, I. (2013), 'The miR-17/92 cluster: a comprehensive update on its genomics, genetics, functions and increasingly important and numerous roles in health and disease', *Cell Death Differ,* 20 (12), 1603-14.

Moher, D., et al. (2009), 'Preferred reporting items for systematic reviews and meta-analyses: the PRISMA statement', *PLoS Med,* 6 (7), e1000097.

Mol, E. A., et al. (2017), 'Higher functionality of extracellular vesicles isolated using size-exclusion chromatography compared to ultracentrifugation', *Nanomedicine,* 13 (6), 2061-65.

Monahan, K. J., et al. (2020), 'Guidelines for the management of hereditary colorectal cancer from the British Society of Gastroenterology (BSG)/Association of Coloproctology of Great Britain and Ireland (ACPGBI)/United Kingdom Cancer Genetics Group (UKCGG)', *Gut,* 69 (3), 411-44.

Montazeri, Z., et al. (2020), 'Systematic meta-analyses, field synopsis and global assessment of the evidence of genetic association studies in colorectal cancer', *Gut,* 69 (8), 1460-71.

Morotti, M., et al. (2019), 'Hypoxia-induced switch in SNAT2/SLC38A2 regulation generates endocrine resistance in breast cancer', *Proc Natl Acad Sci U S A,* 116 (25), 12452-61.

Munro, A., et al. (2015), 'Do Multidisciplinary Team (MDT) processes influence survival in patients with colorectal cancer? A population-based experience', *BMC Cancer,* 15, 686.

Muralidharan-Chari, V., et al. (2010), 'Microvesicles: mediators of extracellular communication during cancer progression', *J Cell Sci,* 123 (Pt 10), 1603-11.

Nagathihalli, N. S., et al. (2014), 'Novel mechanistic insights into ectodomain shedding of EGFR Ligands Amphiregulin and TGF-alpha: impact on gastrointestinal cancers driven by secondary bile acids', *Cancer Res,* 74 (7), 2062-72.

Nam, R. K., et al. (2016), 'MiR-301a regulates E-cadherin expression and is predictive of prostate cancer recurrence', *Prostate,* 76 (10), 869-84.

Narayan, V., et al. (2017), 'Phase 1 Trial of Everolimus and Radiation Therapy for Salvage Treatment of Biochemical Recurrence in Prostate Cancer Patients Following Prostatectomy', *Int J Radiat Oncol Biol Phys,* 97 (2), 355-61.

Neerincx, M., et al. (2015), 'MiR expression profiles of paired primary colorectal cancer and metastases by next-generation sequencing', *Oncogenesis,* 4, e170.

Ng, Y. H., et al. (2013), 'Endometrial exosomes/microvesicles in the uterine microenvironment: a new paradigm for embryo-endometrial cross talk at implantation', *PLoS One,* 8 (3), e58502.

Nguyen, H. T. and Duong, H. Q. (2018), 'The molecular characteristics of colorectal cancer: Implications for diagnosis and therapy', *Oncol Lett,* 16 (1), 9-18.

Ni, K., et al. (2020), 'The Evolving Role of Caveolin-1: A Critical Regulator of Extracellular Vesicles', *Med Sci (Basel),* 8 (4).

Nordin, J. Z., et al. (2015), 'Ultrafiltration with size-exclusion liquid chromatography for high yield isolation of extracellular vesicles preserving intact biophysical and functional properties', *Nanomedicine,* 11 (4), 879-83.

O'Brien, J., et al. (2018), 'Overview of MicroRNA Biogenesis, Mechanisms of Actions, and Circulation', *Front Endocrinol (Lausanne),* 9, 402.

Ogata-Kawata, H., et al. (2014), 'Circulating Exosomal microRNAs as Biomarkers of Colon Cancer', *Plos One,* 9 (4).

Oliveira, A. F., Bretes, L., and Furtado, I. (2019), 'Review of PD-1/PD-L1 Inhibitors in Metastatic dMMR/MSI-H Colorectal Cancer', *Front Oncol,* 9, 396.

Onodi, Z., et al. (2018), 'Isolation of High-Purity Extracellular Vesicles by the Combination of Iodixanol Density Gradient Ultracentrifugation and Bind-Elute Chromatography From Blood Plasma', *Front Physiol,* 9, 1479.

Ostenfeld, M. S., et al. (2016), 'miRNA profiling of circulating EpCAM(+) extracellular vesicles: promising biomarkers of colorectal cancer', *J Extracell Vesicles,* 5, 31488.

Ostrowski, M., et al. (2010), 'Rab27a and Rab27b control different steps of the exosome secretion pathway', *Nat Cell Biol,* 12 (1), 19-30; sup pp 1-13.

Oszvald, A., et al. (2020), 'Fibroblast-Derived Extracellular Vesicles Induce Colorectal Cancer Progression by Transmitting Amphiregulin', *Front Cell Dev Biol,* 8, 558.

Palm, W., et al. (2015), 'The Utilization of Extracellular Proteins as Nutrients Is Suppressed by mTORC1', *Cell,* 162 (2), 259-70.

Palmer, C. K., et al. (2014), 'Reasons for non-uptake and subsequent participation in the NHS Bowel Cancer Screening Programme: a qualitative study', *Br J Cancer,* 110 (7), 1705-11.

Peeters, P. J., et al. (2015), 'The risk of colorectal cancer in patients with type 2 diabetes: associations with treatment stage and obesity', *Diabetes Care,* 38 (3), 495-502.

Pellatt, D. F., et al. (2016), 'Expression Profiles of miRNA Subsets Distinguish Human Colorectal Carcinoma and Normal Colonic Mucosa', *Clin Transl Gastroenterol,* 7, e152.

Peng, Y. and Croce, C. M. (2016), 'The role of MicroRNAs in human cancer', *Signal Transduct Target Ther,* 1, 15004.

Peng, Z. Y., Gu, R. H., and Yan, B. (2019), 'Downregulation of exosome-encapsulated miR-548c-5p is associated with poor prognosis in colorectal cancer', *Journal of Cellular Biochemistry,* 120 (2), 1457-63.

Perez-Boza, J., et al. (2020), 'hnRNPA2B1 inhibits the exosomal export of miR-503 in endothelial cells', *Cell Mol Life Sci,* 77 (21), 4413-28.

Perez-Villamil, B., et al. (2017), 'microRNA(miR) subtypes correlates with colorectal cancer(CRC) molecular subtypes: Validation of miR-30b interaction with genes up-regulated in the high-stroma subtype', *Annals of Oncology,* 28, v194-v95.

Perez, D. D., et al. (2020), 'Extracellular vesicle-miRNAs as liquid biopsy biomarkers for disease identification and prognosis in metastatic colorectal cancer patients', *Scientific Reports,* 10 (1).

Petrova, V., et al. (2018), 'The hypoxic tumour microenvironment', *Oncogenesis,* 7 (1), 10.

Pino, M. S. and Chung, D. C. (2010), 'The chromosomal instability pathway in colon cancer', *Gastroenterology,* 138 (6), 2059-72.

Popat, S., Hubner, R., and Houlston, R. S. (2005), 'Systematic review of microsatellite instability and colorectal cancer prognosis', *J Clin Oncol,* 23 (3), 609-18.

Populo, H., Lopes, J. M., and Soares, P. (2012), 'The mTOR signalling pathway in human cancer', *Int J Mol Sci,* 13 (2), 1886-918.

Porkka, N., et al. (2019), 'Epidemiological, clinical and molecular characterization of Lynch-like syndrome: A population-based study', *Int J Cancer,* 145 (1), 87-98.

Poulsen, L. O., et al. (2015), 'Review on adjuvant chemotherapy for rectal cancer - why do treatment guidelines differ so much?', *Acta Oncol,* 54 (4), 437-46.

Povero, D., et al. (2020), 'Characterization and Proteome of Circulating Extracellular Vesicles as Potential Biomarkers for NASH', *Hepatol Commun,* 4 (9), 1263-78.

Qu, J. L., et al. (2009), 'Gastric cancer exosomes promote tumour cell proliferation through PI3K/Akt and MAPK/ERK activation', *Dig Liver Dis,* 41 (12), 875-80.

Rai, A., et al. (2019), 'Exosomes Derived from Human Primary and Metastatic Colorectal Cancer Cells Contribute to Functional Heterogeneity of Activated Fibroblasts by Reprogramming Their Proteome', *Proteomics,* 19 (8), e1800148.

Raimondo, S., et al. (2020), 'Emerging Insights on the Biological Impact of Extracellular Vesicle-Associated ncRNAs in Multiple Myeloma', *Noncoding RNA,* 6 (3).

Raimondo, S., et al. (2019), 'Multiple myeloma-derived exosomes are enriched of amphiregulin (AREG) and activate the epidermal growth factor pathway in the bone microenvironment leading to osteoclastogenesis', *J Hematol Oncol,* 12 (1), 2.

Raposo, G. and Stoorvogel, W. (2013), 'Extracellular vesicles: exosomes, microvesicles, and friends', *J Cell Biol,* 200 (4), 373-83.

Reita, D., et al. (2019), 'Synergistic Anti-Tumor Effect of mTOR Inhibitors with Irinotecan on Colon Cancer Cells', *Cancers (Basel),* 11 (10).

Ren, D., et al. (2017), 'Maintenance of cancer stemness by miR-196b-5p contributes to chemoresistance of colorectal cancer cells via activating STAT3 signaling pathway', *Oncotarget,* 8 (30), 49807-23.

Rentsch, M., et al. (2016), 'Surgery for Colorectal Cancer - Trends, Developments, and Future Perspectives', *Visc Med,* 32 (3), 184-91.

Robinson, H., et al. (2021), 'Caveolin-1-driven membrane remodelling regulates hnRNPK-mediated exosomal microRNA sorting in cancer', *Clin Transl Med,* 11 (4), e381.

Rodríguez-Fraile, M., et al. (2020), 'FDG PET/CT in colorectal cancer', *Revista Española de Medicina Nuclear e Imagen Molecular (English Edition),* 39 (1), 57-66.

Rodriguez-Martinez, A., et al. (2019), 'Exosomal miRNA profile as complementary tool in the diagnostic and prediction of treatment response in localized breast cancer under neoadjuvant chemotherapy', *Breast Cancer Research,* 21.

Royo, F., et al. (2013), 'Transcriptome of extracellular vesicles released by hepatocytes', *PLoS One,* 8 (7), e68693.

Rubin, G. and Weller, D. (2013), 'Improving survival in colorectal cancer: what role for general practice?', *Br J Gen Pract,* 63 (609), 179-80.

Sabatini, David M., et al. (1994), 'RAFT1: A mammalian protein that binds to FKBP12 in a rapamycin-dependent fashion and is homologous to yeast TORs', *Cell,* 78 (1), 35-43.

Sagar, Surendra Kumar (2021), 'miR-106b as an emerging therapeutic target in cancer', *Genes & Diseases*.

Sancho-Albero, M., et al. (2020), 'Isolation of exosomes from whole blood by a new microfluidic device: proof of concept application in the diagnosis and monitoring of pancreatic cancer', *J Nanobiotechnology,* 18 (1), 150.

Sankaranarayanan, Rengaswamy, et al. (2010), 'Cancer survival in Africa, Asia, and Central America: a population-based study', *The Lancet Oncology,* 11 (2), 165-73.

Santasusagna, S., et al. (2018), 'Prognostic Impact of miR-200 Family Members in Plasma and Exosomes from Tumor-Draining versus Peripheral Veins of Colon Cancer Patients', *Oncology,* 95 (5), 309-18.

Sarver, A. L., et al. (2009), 'Human colon cancer profiles show differential microRNA expression depending on mismatch repair status and are characteristic of undifferentiated proliferative states', *Bmc Cancer,* 9.

Sato, Y., et al. (2020), 'Circulating extracellular vesicle-encapsulated microRNA as screening biomarkers for intraductal papillary mucinous neoplasm', *Oncol Lett,* 20 (6), 315.

Saxton, R. A. and Sabatini, D. M. (2017), 'mTOR Signaling in Growth, Metabolism, and Disease', *Cell,* 168 (6), 960-76.

Sayagues, J. M., et al. (2016), 'Genomic characterization of liver metastases from colorectal cancer patients', *Oncotarget,* 7 (45), 72908-22.

Schreuders, E. H., et al. (2015), 'Colorectal cancer screening: a global overview of existing programmes', *Gut,* 64 (10), 1637-49.

Semenza, G. L. (2011), 'Hypoxia. Cross talk between oxygen sensing and the cell cycle machinery', *Am J Physiol Cell Physiol,* 301 (3), C550-2.

Sforza, V., et al. (2016), 'Mechanisms of resistance to anti-epidermal growth factor receptor inhibitors in metastatic colorectal cancer', *World J Gastroenterol,* 22 (28), 6345-61.

Shan, G., et al. (2020), 'Cancer-associated fibroblast-secreted exosomal miR-423-5p promotes chemotherapy resistance in prostate cancer by targeting GREM2 through the TGF-beta signaling pathway', *Exp Mol Med,* 52 (11), 1809-22.

Shang, J., et al. (2014), 'MicroRNA-23a antisense enhances 5-fluorouracil chemosensitivity through APAF-1/caspase-9 apoptotic pathway in colorectal cancer cells', *J Cell Biochem,* 115 (4), 772-84.

Shao, C., et al. (2018a), 'Role of hypoxia-induced exosomes in tumor biology', *Mol Cancer,* 17 (1), 120.

Shao, Y., et al. (2018b), 'Colorectal cancer-derived small extracellular vesicles establish an inflammatory premetastatic niche in liver metastasis', *Carcinogenesis,* 39 (11), 1368-79.

Sheldon, H., et al. (2010), 'New mechanism for Notch signaling to endothelium at a distance by Delta-like 4 incorporation into exosomes', *Blood,* 116 (13), 2385-94.

Shen, S., et al. (2021), 'Cancer-derived exosomal miR-7641 promotes breast cancer progression and metastasis', *Cell Commun Signal,* 19 (1), 20.

Shi, Y. F., et al. (2015), 'MiR-548-3p functions as an anti-oncogenic regulator in breast cancer', *Biomedicine & Pharmacotherapy,* 75, 111-16.

Shinohara, H., et al. (2017), 'Regulated Polarization of Tumor-Associated Macrophages by miR-145 via Colorectal Cancer-Derived Extracellular Vesicles', *J Immunol,* 199 (4), 1505-15.

Shiromizu, T., et al. (2017), 'Quantitation of putative colorectal cancer biomarker candidates in serum extracellular vesicles by targeted proteomics', *Sci Rep,* 7 (1), 12782.

Shukuya, T., et al. (2020), 'Circulating MicroRNAs and Extracellular Vesicle-Containing MicroRNAs as Response Biomarkers of Anti-programmed Cell Death Protein 1 or Programmed Death-Ligand 1 Therapy in NSCLC', *J Thorac Oncol,* 15 (11), 1773-81.

Sidhom, K., Obi, P. O., and Saleem, A. (2020), 'A Review of Exosomal Isolation Methods: Is Size Exclusion Chromatography the Best Option?', *Int J Mol Sci,* 21 (18).

Sidhu, S. S., et al. (2004), 'The microvesicle as a vehicle for EMMPRIN in tumor-stromal interactions', *Oncogene,* 23 (4), 956-63.

Siegel, R. L., et al. (2020), 'Colorectal cancer statistics, 2020', *CA Cancer J Clin,* 70 (3), 145-64.

Simon, K. (2016), 'Colorectal cancer development and advances in screening', *Clin Interv Aging,* 11, 967-76.

Smith, S. F., Collins, S. E., and Charest, P. G. (2020), 'Ras, PI3K and mTORC2 - three's a crowd?', *J Cell Sci,* 133 (19).

Song, L., et al. (2017), 'The performance of the SEPT9 gene methylation assay and a comparison with other CRC screening tests: A meta-analysis', *Sci Rep,* 7 (1), 3032.

Song, X., et al. (2016), 'Cancer Cell-derived Exosomes Induce Mitogen-activated Protein Kinase-dependent Monocyte Survival by Transport of Functional Receptor Tyrosine Kinases', *J Biol Chem,* 291 (16), 8453-64.

Soria, J. C., et al. (2019), 'Phase I safety, pharmacokinetic and pharmacodynamic trial of BMS-599626 (AC480), an oral pan-HER receptor tyrosine kinase inhibitor, in patients with advanced solid tumors', *Ann Oncol,* 30 (6), 1020.

Soung, N. K., et al. (2019), 'Mechanism of the natural product moracin-O derived MO-460 and its targeting protein hnRNPA2B1 on HIF-1alpha inhibition', *Exp Mol Med,* 51 (2), 1-14.

Spano, J. P., et al. (2005), 'Impact of EGFR expression on colorectal cancer patient prognosis and survival', *Ann Oncol,* 16 (1), 102-8.

Srinivasan, S., et al. (2019), 'Assessment of methods for serum extracellular vesicle small RNA sequencing to support biomarker development', *J Extracell Vesicles,* 8 (1), 1684425.

Stahler, A., et al. (2020), 'Amphiregulin Expression Is a Predictive Biomarker for EGFR Inhibition in Metastatic Colorectal Cancer: Combined Analysis of Three Randomized Trials', *Clin Cancer Res,* 26 (24), 6559-67.

Stenqvist, A. C., et al. (2013), 'Exosomes secreted by human placenta carry functional Fas ligand and TRAIL molecules and convey apoptosis in activated immune cells, suggesting exosome-mediated immune privilege of the fetus', *J Immunol,* 191 (11), 5515-23.

Stranska, R., et al. (2018), 'Comparison of membrane affinity-based method with size-exclusion chromatography for isolation of exosome-like vesicles from human plasma', *J Transl Med,* 16 (1), 1.

Stuffers, S., et al. (2009), 'Multivesicular endosome biogenesis in the absence of ESCRTs', *Traffic,* 10 (7), 925-37.

Su, Wentao, et al. (2019), 'Microfluidic strategies for label-free exosomes isolation and analysis', *TrAC Trends in Analytical Chemistry,* 118, 686-98.

Sun, L. H., et al. (2020), 'Exosomal miR-21 promotes proliferation, invasion and therapy resistance of colon adenocarcinoma cells through its target PDCD4', *Scientific Reports,* 10 (1).

Szatanek, R., et al. (2015), 'Isolation of extracellular vesicles: Determining the correct approach (Review)', *Int J Mol Med,* 36 (1), 11-7.

Takahara, T., et al. (2020), 'Amino acid-dependent control of mTORC1 signaling: a variety of regulatory modes', *J Biomed Sci,* 27 (1), 87.

Takano, Y., et al. (2017), 'Circulating exosomal microRNA-203 is associated with metastasis possibly via inducing tumor-associated macrophages in colorectal cancer', *Oncotarget,* 8 (45), 78598-613.

Tang, H. L., et al. (2012), 'Expression and clinical significance of miR-23a and metastasis suppressor 1 in colon carcinoma', *Chin J Pathol,* 41 (1), 28-32.

Tang, Y. Y., et al. (2019), 'Tumor-derived exosomal miRNA-320d as a biomarker for metastatic colorectal cancer', *Journal of Clinical Laboratory Analysis,* 33 (9).

Tao, S. C. and Guo, S. C. (2020), 'Role of extracellular vesicles in tumour microenvironment', *Cell Commun Signal,* 18 (1), 163.

Tarpgaard, L. S., et al. (2016), 'A phase II study of Epirubicin in oxaliplatin-resistant patients with metastatic colorectal cancer and TOP2A gene amplification', *BMC Cancer,* 16, 91.

Tauro, B. J., et al. (2012), 'Comparison of ultracentrifugation, density gradient separation, and immunoaffinity capture methods for isolating human colon cancer cell line LIM1863-derived exosomes', *Methods,* 56 (2), 293-304.

Teng, X., et al. (2015), 'Mesenchymal Stem Cell-Derived Exosomes Improve the Microenvironment of Infarcted Myocardium Contributing to Angiogenesis and Anti-Inflammation', *Cell Physiol Biochem,* 37 (6), 2415-24.

Teng, Y., et al. (2017), 'MVP-mediated exosomal sorting of miR-193a promotes colon cancer progression', *Nat Commun,* 8, 14448.

Tepus, M. and Yau, T. O. (2020), 'Non-Invasive Colorectal Cancer Screening: An Overview', *Gastrointest Tumors,* 7 (3), 62-73.

Thery, C., et al. (2006), 'Isolation and characterization of exosomes from cell culture supernatants and biological fluids', *Curr Protoc Cell Biol,* Chapter 3, Unit 3 22.

Thery, C., et al. (2018), 'Minimal information for studies of extracellular vesicles 2018 (MISEV2018): a position statement of the International Society for Extracellular Vesicles and update of the MISEV2014 guidelines', *J Extracell Vesicles,* 7 (1), 1535750.

Thind, A. and Wilson, C. (2016), 'Exosomal miRNAs as cancer biomarkers and therapeutic targets', *J Extracell Vesicles,* 5, 31292.

Thompson, A. G., et al. (2016), 'Extracellular vesicles in neurodegenerative disease - pathogenesis to biomarkers', *Nat Rev Neurol,* 12 (6), 346-57.

Tian, T., Li, X., and Zhang, J. (2019), 'mTOR Signaling in Cancer and mTOR Inhibitors in Solid Tumor Targeting Therapy', *Int J Mol Sci,* 20 (3).

Torres Crigna, A., et al. (2021), 'Inter-Laboratory Comparison of Extracellular Vesicle Isolation Based on Ultracentrifugation', *Transfus Med Hemother,* 48 (1), 48-59.

Tsukamoto, M., et al. (2017), 'Circulating Exosomal MicroRNA-21 as a Biomarker in Each Tumor Stage of Colorectal Cancer', *Oncology,* 92 (6), 360-70.

Valle, L., et al. (2019), 'Genetic predisposition to colorectal cancer: syndromes, genes, classification of genetic variants and implications for precision medicine', *J Pathol,* 247 (5), 574-88.

Valvezan, A. J., et al. (2014), 'Oncogenic mutations in adenomatous polyposis coli (Apc) activate mechanistic target of rapamycin complex 1 (mTORC1) in mice and zebrafish', *Dis Model Mech,* 7 (1), 63-71.

van der Valk, Maxime J. M., et al. (2018), 'Long-term outcomes of clinical complete responders after neoadjuvant treatment for rectal cancer in the International Watch & Wait Database (IWWD): an international multicentre registry study', *The Lancet,* 391 (10139), 2537-45.

van Niel, G., D'Angelo, G., and Raposo, G. (2018), 'Shedding light on the cell biology of extracellular vesicles', *Nat Rev Mol Cell Biol,* 19 (4), 213-28.

van Zijl, F., Krupitza, G., and Mikulits, W. (2011), 'Initial steps of metastasis: cell invasion and endothelial transmigration', *Mutat Res,* 728 (1-2), 23-34.

Vergauwen, G., et al. (2017), 'Confounding factors of ultrafiltration and protein analysis in extracellular vesicle research', *Sci Rep,* 7 (1), 2704.

Veziroglu, E. M. and Mias, G. I. (2020), 'Characterizing Extracellular Vesicles and Their Diverse RNA Contents', *Front Genet,* 11, 700.

Vickers, K. C., et al. (2011), 'MicroRNAs are transported in plasma and delivered to recipient cells by high-density lipoproteins', *Nat Cell Biol,* 13 (4), 423-33.

Villarroya-Beltri, C., et al. (2013), 'Sumoylated hnRNPA2B1 controls the sorting of miRNAs into exosomes through binding to specific motifs', *Nature Communications,* 4.

Vu, B. T., et al. (2018), 'Chick chorioallantoic membrane assay as an in vivo model to study the effect of nanoparticle-based anticancer drugs in ovarian cancer', *Sci Rep,* 8 (1), 8524.

Vu, L. T., et al. (2020), 'microRNA exchange via extracellular vesicles in cancer', *Cell Prolif,* 53 (11), e12877.

Vuik, F. E., et al. (2019), 'Increasing incidence of colorectal cancer in young adults in Europe over the last 25 years', *Gut,* 68 (10), 1820-26.

Wang, B., et al. (2019), 'Colorectal cancer cell-derived exosomes promote proliferation and decrease apoptosis by activating the ERK pathway', *Int J Clin Exp Pathol,* 12 (7), 2485-95.

Wang, H. N., et al. (2020a), 'Targeting mTOR suppressed colon cancer growth through 4EBP1/eIF4E/PUMA pathway', *Cancer Gene Therapy,* 27 (6), 448-60.

Wang, J., et al. (2017a), 'Circulating exosomal miR-125a-3p as a novel biomarker for early-stage colon cancer', *Scientific Reports,* 7.

Wang, J., et al. (2017b), 'Circulating exosomal miR-125a-3p as a novel biomarker for early-stage colon cancer', *Sci Rep,* 7 (1), 4150.

Wang, K., et al. (2012), 'Comparing the MicroRNA spectrum between serum and plasma', *PLoS One,* 7 (7), e41561.

Wang, M., Yang, M., and Deng, B. (2020b), 'miR-548a-3p Weakens the Tumorigenesis of Colon Cancer Through Targeting TPX2', *Cancer Biother Radiopharm*.

Wang, N., et al. (2018), 'microRNA-23a in Human Cancer: Its Roles, Mechanisms and Therapeutic Relevance', *Cancers (Basel),* 11 (1).

Wang, S. J., et al. (2017c), 'MicroRNA-93-5p increases multidrug resistance in human colorectal carcinoma cells by downregulating cyclin dependent kinase inhibitor 1A gene expression', *Oncol Lett,* 13 (2), 722-30.

Wang, T., et al. (2020c), 'RAPTOR promotes colorectal cancer proliferation by inducing mTORC1 and upregulating ribosome assembly factor URB1', *Cancer Med,* 9 (4), 1529-43.

Wang, X., et al. (2020d), 'Exosome-delivered circRNA promotes glycolysis to induce chemoresistance through the miR-122-PKM2 axis in colorectal cancer', *Mol Oncol,* 14 (3), 539-55.

Webber, J. P., et al. (2015), 'Differentiation of tumour-promoting stromal myofibroblasts by cancer exosomes', *Oncogene,* 34 (3), 290-302.

Wei, R., et al. (2020), 'Liquid Biopsy of Extracellular Vesicle-Derived miR-193a-5p in Colorectal Cancer and Discovery of Its Tumor-Suppressor Functions', *Front Oncol,* 10, 1372.

Wheler, J. J., et al. (2013), 'Combining erlotinib and cetuximab is associated with activity in patients with non-small cell lung cancer (including squamous cell carcinomas) and wild-type EGFR or resistant mutations', *Mol Cancer Ther,* 12 (10), 2167-75.

Willms, E., et al. (2018), 'Extracellular Vesicle Heterogeneity: Subpopulations, Isolation Techniques, and Diverse Functions in Cancer Progression', *Front Immunol,* 9, 738.

Willson, J. K., et al. (1984), 'Mitomycin C resistance in a human colon carcinoma cell line associated with cell surface protein alterations', *Cancer Res,* 44 (12 Pt 1), 5880-5.

Wise, D. R. and Thompson, C. B. (2010), 'Glutamine addiction: a new therapeutic target in cancer', *Trends Biochem Sci,* 35 (8), 427-33.

Witjes, C. D. M., et al. (2021), 'Oncological outcome after local treatment for early stage rectal cancer', *Surg Endosc*.

Witwer, K. W., et al. (2013), 'Standardization of sample collection, isolation and analysis methods in extracellular vesicle research', *J Extracell Vesicles,* 2.

Wolpin, B. M., et al. (2013), 'Multicenter phase II study of tivozanib (AV-951) and everolimus (RAD001) for patients with refractory, metastatic colorectal cancer', *Oncologist,* 18 (4), 377-8.

Wu, H. T., et al. (2020a), 'Oncogenic functions of the EMT-related transcription factor ZEB1 in breast cancer', *J Transl Med,* 18 (1), 51.

Wu, J. H., et al. (2018), 'Exosomal miR-196b-5p is a potential diagnostic marker for colorectal cancer with metachronous liver metastasis', *Translational Cancer Research,* 7 (6), 1482-90.

Wu, M., et al. (2020b), 'Role of exosomal microRNA-125b-5p in conferring the metastatic phenotype among pancreatic cancer cells with different potential of metastasis', *Life Sci,* 255, 117857.

Wu, M., et al. (2017), 'Isolation of exosomes from whole blood by integrating acoustics and microfluidics', *Proc Natl Acad Sci U S A,* 114 (40), 10584-89.

Xavier, C. P. R., et al. (2020), 'The Role of Extracellular Vesicles in the Hallmarks of Cancer and Drug Resistance', *Cells,* 9 (5).

Xin, Y., et al. (2020), 'Identification of exosomal miR-455-5p and miR-1255a as therapeutic targets for breast cancer', *Biosci Rep,* 40 (1).

Xu, K. Y., et al. (2020), 'Extracellular vesicles as potential biomarkers and therapeutic approaches in autoimmune diseases', *Journal of Translational Medicine,* 18 (1).

Yagi, T., et al. (2019), 'Plasma exosomal microRNA-125b as a monitoring biomarker of resistance to mFOLFOX6-based chemotherapy in advanced and recurrent colorectal cancer patients', *Molecular and Clinical Oncology,* 11 (4), 416-24.

Yamada, N., et al. (2016), 'Colorectal cancer cell-derived extracellular vesicles induce phenotypic alteration of T cells into tumor-growth supporting cells with transforming growth factor-beta1-mediated suppression', *Oncotarget,* 7 (19), 27033-43.

Yamada, N. O. and Senda, T. (2021), 'Circulating microRNA-92a-3p in colorectal cancer: a review', *Med Mol Morphol*.

Yan, S., et al. (2018), 'MicroRNA-6869-5p acts as a tumor suppressor via targeting TLR4/NF-kappaB signaling pathway in colorectal cancer', *J Cell Physiol,* 233 (9), 6660-68.

Yan, S., et al. (2017a), 'Exosome-encapsulated microRNAs as circulating biomarkers for colorectal cancer', *Oncotarget,* 8 (36), 60149-58.

Yan, S., et al. (2017b), 'Downregulation of circulating exosomal miR-638 predicts poor prognosis in colon cancer patients', *Oncotarget,* 8 (42), 72220-26.

Yan, S., et al. (2017c), 'Exosome-encapsulated microRNAs as circulating biomarkers for colorectal cancer', *Oncotarget,* 8 (36), 60149-58.

Yanez-Mo, M., et al. (2015), 'Biological properties of extracellular vesicles and their physiological functions', *J Extracell Vesicles,* 4, 27066.

Yang, E., et al. (2020), 'Exosome-mediated metabolic reprogramming: the emerging role in tumor microenvironment remodeling and its influence on cancer progression', *Signal Transduct Target Ther,* 5 (1), 242.

Yang, N., et al. (2012), 'TAZ induces growth factor-independent proliferation through activation of EGFR ligand amphiregulin', *Cell Cycle,* 11 (15), 2922-30.

Yoo, J. K., et al. (2013), 'miR-7641 modulates the expression of CXCL1 during endothelial differentiation derived from human embryonic stem cells', *Arch Pharm Res,* 36 (3), 353-8.

Yue, B., et al. (2020), 'Exosome biogenesis, secretion and function of exosomal miRNAs in skeletal muscle myogenesis', *Cell Prolif,* 53 (7), e12857.

Zeng, Z., et al. (2018), 'Cancer-derived exosomal miR-25-3p promotes pre-metastatic niche formation by inducing vascular permeability and angiogenesis', *Nat Commun,* 9 (1), 5395.

Zhang, H., et al. (2019a), 'A panel of seven-miRNA signature in plasma as potential biomarker for colorectal cancer diagnosis', *Gene,* 687, 246-54.

Zhang, H., et al. (2018), 'Identification of distinct nanoparticles and subsets of extracellular vesicles by asymmetric flow field-flow fractionation', *Nat Cell Biol,* 20 (3), 332-43.

Zhang, J., Pavlova, N. N., and Thompson, C. B. (2017a), 'Cancer cell metabolism: the essential role of the nonessential amino acid, glutamine', *EMBO J,* 36 (10), 1302-15.

Zhang, Q., et al. (2019b), 'Transfer of Functional Cargo in Exomeres', *Cell Rep,* 27 (3), 940-54 e6.

Zhang, S., et al. (2017b), 'Exosomes promote cetuximab resistance via the PTEN/Akt pathway in colon cancer cells', *Braz J Med Biol Res,* 51 (1), e6472.

Zhang, Y. J., et al. (2009), 'mTOR signaling pathway is a target for the treatment of colorectal cancer', *Ann Surg Oncol,* 16 (9), 2617-28.

Zhao, B., et al. (2017a), 'Mechanisms of resistance to anti-EGFR therapy in colorectal cancer', *Oncotarget,* 8 (3), 3980-4000.

Zhao, H., et al. (2018), 'The key role of extracellular vesicles in the metastatic process', *Biochim Biophys Acta Rev Cancer,* 1869 (1), 64-77.

Zhao, L., et al. (2017b), 'Isolation and Identification of miRNAs in exosomes derived from serum of colon cancer patients', *J Cancer,* 8 (7), 1145-52.

Zhao, S., et al. (2014), 'Comparison of RNA-Seq and microarray in transcriptome profiling of activated T cells', *PLoS One,* 9 (1), e78644.

Zhao, Y. J., et al. (2019), 'Circulating Exosomal miR-150-5p and miR-99b-5p as Diagnostic Biomarkers for Colorectal Cancer', *Frontiers in Oncology,* 9.

Zhen, Y. and Stenmark, H. (2015), 'Cellular functions of Rab GTPases at a glance', *J Cell Sci,* 128 (17), 3171-6.

Zhou, J. M., et al. (2019), 'High hnRNP AB expression is associated with poor prognosis in patients with colorectal cancer', *Oncol Lett,* 18 (6), 6459-68.

Zhu, M., et al. (2017), 'A panel of microRNA signature in serum for colorectal cancer diagnosis', *Oncotarget,* 8 (10), 17081-91.

Zonneveld, M. I., Keulers, T. G. H., and Rouschop, K. M. A. (2019), 'Extracellular Vesicles as Transmitters of Hypoxia Tolerance in Solid Cancers', *Cancers (Basel),* 11 (2).

Zou, S. L., et al. (2019), 'Downregulation of serum exosomal miR-150-5p is associated with poor prognosis in patients with colorectal cancer', *Cancer Biomarkers,* 26 (1), 69-77.